

NASA TECHNICAL  
MEMORANDUM

NASA TM X-53295

APRIL 1, 1965

NASA TM X-53295

GPO PRICE \$ \_\_\_\_\_

CFSTI PRICE(S) \$ \_\_\_\_\_

Hard copy (HC) \$5.00

Microfiche (MF) 1.00

# 653 July 65

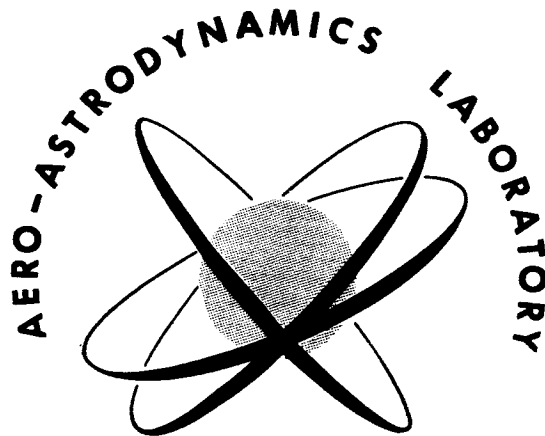
**AERO-ASTRODYNAMICS  
RESEARCH REVIEW NO. 2**

FACILITY FORM 502	<b>N 66 35546</b>	<b>N 66 35558</b>
	(ACCESSION NUMBER)	(THRU)
	<u>156</u>	<u>3</u>
	(PAGES)	(CODE)
	<b>TMX-53295</b>	<b>34</b>
	(NASA CR OR TMX OR AD NUMBER)	(CATEGORY)

AERO-ASTRODYNAMICS LABORATORY  
RESEARCH AND DEVELOPMENT OPERATIONS  
GEORGE C. MARSHALL SPACE FLIGHT CENTER  
HUNTSVILLE, ALABAMA

NASA - GEORGE C. MARSHALL SPACE FLIGHT CENTER

TECHNICAL MEMORANDUM X-53295



RESEARCH REVIEW NUMBER TWO  
July 1, 1964 - December 30, 1964

RESEARCH AND DEVELOPMENT OPERATIONS  
AERO - ASTRODYNAMICS LABORATORY

April 1, 1965

## ACKNOWLEDGEMENTS

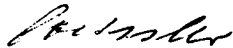
The articles for this review were contributed by various engineers and physicists of the Aero-Astrody-namics Laboratory, reviewed and compiled by William D. Murphree, and edited by Sarah Hightower.

Grateful acknowledgement is given to the Technical Publications Section, Space Systems Information Branch, Management Services Office, MSFC, for preparing the review.

## PREFACE

The topics discussed in this second Aero-Astro-dynamics Research Review cover a variety of subjects. Included are Aerodynamics, Communication Theory, Facilities Research, Flight Evaluation, Instrumentation, Mathematics, and Orbit Theory. Other subjects will be discussed in forthcoming reviews.

It is hoped that these reviews will be interesting and helpful to other organizations engaged in space flight research and related efforts. Criticisms of this review and discussions concerning individual papers with respective authors are invited.



E. D. Geissler  
Director, Aero-Astroynamics Laboratory



# CONTENTS...

	Page
<b>I. AERODYNAMICS</b>	
Newtonian Aerodynamics for General Surfaces by Willi H. Heybey . . . . .	2
A Unified Treatment of Turbulent Fluxes in Multi-Component and Hot Flows by F. R. Krause and M. J. Fisher . . . . .	11
On Quasi-Slender Body Theory for Oscillating Low Aspect Ratio Wings and Bodies of Revolution in Supersonic Flow by M. F. Platzer . . . . .	26
<b>II. COMMUNICATION THEORY</b>	
A New Performance Criterion for Linear Filters With Random Inputs by Mario H. Rheinfurth. . . . .	34
<b>III. FACILITIES RESEARCH</b>	
Variable Porosity Walls for Transonic Wind Tunnels by A. Richard Felix . . . . .	54
<b>IV. FLIGHT EVALUATION</b>	
Automation of Post-Flight Evaluation by Carlos Hagood . . . . .	60
<b>V. INSTRUMENTATION</b>	
Local Measurements in Turbulent Flows Through Cross Correlation of Optical Signals by M. J. Fisher and F. R. Krause . . . . .	66
Hot Wire Techniques in Low Density Flows With High Turbulence Levels by A. R. Hanson, R. E. Larson, and F. R. Krause . . . . .	77
Theory and Application of Long Duration Heat Flux Transducers by S. James Robertson and John P. Heaman . . . . .	92
<b>VI. MATHEMATICS</b>	
A Survey of Methods for Generating Liapunov Functions by Commodore C. Dearman . . . . .	114
An Orthonormalization Procedure for Multivariable Function Approximation by Hugo Ingram . .	133

## VII. ORBIT THEORY

Analysis of the Influence of Venting and Gas Leakage on Tracking of Orbital Vehicles by

A. R. McNair and P. E. Dreher. . . . . 140

## VIII. PUBLICATIONS AND PRESENTATIONS

A. Publications . . . . . 150

B. Presentations . . . . . 166

## I. AERODYNAMICS

# NEWTONIAN AERODYNAMICS FOR GENERAL SURFACES

by  
Willi H. Heybey

## SUMMARY

In the hypersonic regime the Newtonian flow model, especially in its modified form, has been known for some time to produce satisfactory results regarding a number of basic body shapes. It may reasonably be expected to also work well with more complicated body geometries as presented, e. g., by re-entry vehicles. Because of its simplicity, the components of the aerodynamic force and the location of the centroid can be calculated in a relatively easy manner. The mathematics pertaining to the unmodified approach are developed here for a general surface given in analytic terms. Applications are made to the elliptic cone, first without, then with, an attached rear cylinder, to a conoid of biparabolic cross sections, and to a drop-like blunt body. The modification merely amounts to the changing of a constant; it is described in the last section where a survey of results as compared with otherwise known data is also given.

## INTRODUCTION

In recent times Newton's impact theory, especially in its modified form, has been proved a useful tool in high Mach number flow. The results it yielded in a number of test cases came surprisingly close to observed or more exactly derived aerodynamical data, such as pressure distributions, force components, and shock angles at the nose of wedges or circular cones. Since any space vehicle, on returning to earth, will for some time be embedded in hypersonic flow, the impact flow approach is of considerable interest, offering as it does a comparatively easy method for force and moment computations. The pertaining mathematics have been developed so far for basic surfaces only (e. g., flat plates, wedges and diamonds, spheres, right circular cones, capped circular cylinders). The agreement found here with otherwise known data was often excellent, indicating that the impact model of a moving fluid in some measure depicts physical reality in the hypersonic regime, perhaps by error cancellation, while long ago it had to be discarded in hydrodynamics and aerodynamics, both subsonic and moderately supersonic. It is not unreasonable to expect that, in hypersonics, impact theory will work satisfactorily with other and more complicated surfaces such as are offered by re-entry bodies. In this paper the Newtonian

expressions will be derived for an unspecified general surface which is allowed to be composite; however, the stipulation is made that all its parts can be described by analytic equations. The general method will be set down in mathematical detail because it is fundamental. In the four applications given, the treatment will be largely confined to the communication of results; a more elaborate account can be found in a forthcoming Technical Memorandum.

## IMPACT FLOW MATHEMATICS IN GENERAL

In the Newtonian flow concept, minute inelastic particles all move in the same direction and at constant speed. On contact with a material object they transfer their momentum component normal to the surface at the point of impact. The force experienced by the body is in the direction of the local interior normal since the tangential component is carried off without effect on the body. Surfaces with concave parts might be hit again by the deflected stream. Such occurrences are not considered here. The simple Newtonian model obviously does not consider forces acting on shielded areas (shadow zones), nor does it contemplate the formation of a shock. The results can often be improved by a correction to the local pressure coefficient based on shock transition relations of which more will be said at the end of the paper.

The physical concepts set forth above can be used to calculate the pressure coefficient at an impact point; it is found as

$$C_P = \frac{p - p_\infty}{q_\infty} = 2 \cos^2 \alpha', \quad (1)$$

where  $p$  is the local pressure;  $p_\infty$  and  $q_\infty$  are the static and dynamic pressures in the undisturbed flow (both assumed as prescribed). The factor 2 characterizes the simple theory and, in the modified form, will be replaced by a different constant which introduces a Mach number dependence not yet present here. The angle  $\alpha'$  is made by the flow direction and the interior surface normal. In expression (1) its complement,

the local angle of attack,  $\alpha_{loc} = \frac{\pi}{2} - \alpha'$  is often used.

This angle must be distinguished from the overall angle of attack,  $\alpha$ , made by the flow direction and a line chosen within the body, usually the body's axis if such an

axis can be defined. The unit vector,  $\underline{v}$ , in flow direction will as a rule contain certain trigonometric functions of  $\alpha$  which cannot be obtained before a particular flow-body configuration has been introduced. At this station, we therefore write, in general,

$$\underline{v} = \alpha_1 \underline{i} + \alpha_2 \underline{j} + \alpha_3 \underline{k}, \quad (2)$$

where  $\underline{i}$ ,  $\underline{j}$ ,  $\underline{k}$  are unit vectors in the three axis directions of a rectangular ( $x$ ,  $y$ ,  $z$ ) system of coordinates, and the  $\alpha_i$  must be considered as known quantities obeying the relation

$$\alpha_1^2 + \alpha_2^2 + \alpha_3^2 = 1.$$

From the surface equation, taken at first as analytic in the variables  $x$ ,  $y$ ,  $z$ , the interior normal,  $\underline{n}$ , can be obtained at any point as

$$\underline{n} = n_1(x, y, z) \underline{i} + n_2 \underline{j} + n_3 \underline{k}, \quad (3)$$

with

$$(n_1^2 + n_2^2 + n_3^2) = 1.$$

Since  $\cos \alpha'$  is the scalar product of the two vectors  $\underline{v}$  and  $\underline{n}$ , the local pressure coefficient (1) can now be set into the form

$$C_p = 2(\underline{v} \cdot \underline{n})^2, \quad (4)$$

which links it immediately to the surface equation. However, the general calculation of  $C_p$  requires the means of the differential geometry of surfaces in which symmetric and lucid relations are obtained when replacing the Cartesian surface equation by a pointwise representation:

$$x = \psi_1(\sigma, \tau), \quad y = \psi_2(\sigma, \tau), \quad z = \psi_3(\sigma, \tau). \quad (5)$$

The variables  $\sigma$  and  $\tau$  will move within certain "natural" intervals for the triplets  $x$ ,  $y$ ,  $z$  to exactly embrace the surface points. There may be various equally attractive ways in which to introduce  $\sigma$  and  $\tau$ . The surface representation (5) offers the advantage that, on assigning parametric values to  $\sigma$  or to  $\tau$ , it describes two sets of surface curves (in terms of  $\tau$  or  $\sigma$ ) creating a net of curvilinear (not necessarily orthogonal) coordinate lines by which one may orient oneself on the surface.

The components  $n_i$ , now functions of  $\sigma$  and  $\tau$ , are obtained as

$$n_i = \frac{1}{\pm N} \frac{\partial(\psi_j, \psi_k)}{\partial(\sigma, \tau)} \equiv \frac{N_i}{\pm N},$$

where

$$N = \left| \sqrt{N_1^2 + N_2^2 + N_3^2} \right|, \quad (6)$$

The indices  $\bar{i}, j, k$  denote the cyclic sequences (1, 2, 3), (2, 3, 1), and (3, 1, 2). The sign must be chosen such that the surface normal points toward the interior of the body; this can be done without difficulty when the functions  $\psi_i$  are known explicitly.

Since the elemental surface area may be written as

$$dS = N d\sigma d\tau,$$

the expression for the second order local elemental force, which is in the direction (3), emerges as

$$\begin{aligned} d^2 \underline{P} &= 2q_\infty (\underline{v} \cdot \underline{n})^2 N \underline{n} d\sigma d\tau \\ &\equiv i d^2 X + j d^2 Y + k d^2 Z, \end{aligned} \quad (7)$$

where  $X$ ,  $Y$ ,  $Z$  are the rectangular components of the total force,  $\underline{P}$ . They can be found by integration over the proper  $\sigma$ - and  $\tau$ - intervals (which, if the surface (5) is fully exposed to the flow, are the natural intervals of these variables, otherwise narrower than these). The integrals  $X$ ,  $Y$ ,  $Z$  can sometimes be evaluated in closed form; if not, we must resort to numerical methods.

The drag force, being the component of  $\underline{P}$  in the direction  $\underline{v}$ , is given by

$$\underline{D} = (\underline{P} \cdot \underline{v}) \underline{v} = (\alpha_1 X + \alpha_2 Y + \alpha_3 Z) \underline{v} \equiv D \underline{v}, \quad (8)$$

while the lift force follows as

$$\begin{aligned} \underline{L} &= \underline{P} - \underline{D} = i(X - \alpha_1 D) + j(Y - \alpha_2 D) \\ &\quad + k(Z - \alpha_3 D) \end{aligned} \quad (9)$$

with the absolute value  $L = \sqrt{P^2 - D^2}$ .

In addition to the resulting force  $\underline{P}$  there will be a resulting moment of the elemental forces:

$$\underline{M} = \int \int [\underline{r} \times d^2 \underline{P}] d\sigma d\tau, \quad (10)$$

where

$$\underline{r} = i\psi_1 + j\psi_2 + k\psi_3$$

is the lever arm from the origin to the point  $R$  on the surface where the force element is attacking.

The moment balance condition,

$$[\underline{r}^* \times \underline{P}] = \underline{M}, \quad (11)$$

permits the computation of the arm

$$\underline{r}^* = ix^* + jy^* + kz^*$$

of the resulting force. From equation (4),  $\underline{r}^*$  is not uniquely determinable because the vector product may have the value  $\underline{M}$  with infinitely many vectors  $\underline{r}^*$ . Mechanically, this reflects the movability of a force along its line of attack. Mathematically, one of the  $\underline{r}^*$  - components remains arbitrary. An additional condition,

$$f(x^*, y^*, x^*) = 0, \quad (12)'$$

may be introduced which, with symmetrical bodies, usually follows from the desire to locate the point of attack (centroid) on the body axis of which  $\underline{r}^*$  then is a directed part.

### INTEGRATION LIMITS

While the foregoing formulas are perfectly general and directly applicable to any analytic surface (or surface part), the determination and correct employment of shielded areas often require painstaking detail work, especially if there are several such areas (which may or may not overlap). The problem remains simple when the shadow is a single point or an open line (enclosed area zero), because then the reduction in force is a zero quantity, and the natural  $\sigma$ - and  $\tau$ -intervals can still be used when integrating.

Two types of shielded areas can be distinguished: those created by the bulk of the body as it opposes itself to the stream, and those caused by a sharp edge or rim existing on the surface (cast shadow).

With the first type, the flow vector touching the surface is a true tangent so that it obeys the condition

$$(\underline{v} \cdot \underline{n}) = 0. \quad (13)$$

This relationship of  $\sigma$  and  $\tau$ , if written as  $\tau = \varphi(\sigma)$  and introduced into equation (5), defines the points of the tangential shadow curve,  $s_t$ , in terms of  $\sigma$ . Along the boundary  $s_t$  the pressure coefficient is zero as follows from expression (4). The integration will be performed first over  $\tau$  since the function  $\varphi(\sigma)$  will call for at least one limit of  $\tau$  in terms of  $\sigma$ . The area bounded by  $s_t$  may affect part of the natural  $\sigma$ -interval; the subsequent integration with respect to  $\sigma$  must then be carried out over a narrower interval. In simple cases, a solution to equation (13) may not exist (full exposure) or may be found as a constant  $\tau = \tau_t(\varphi(\sigma) = \text{const})$ . The integration scheme as sketched assumes that  $s_t$  is the only shadow boundary. Even then the  $(\sigma, \tau)$ -domain must often be split in two or more areas over which we will have to integrate separately (cf. fourth example).

Along a sharp edge the flow vector as a rule is not in a tangential plane, and condition (13) cannot apply. Let the coordinates of the rim be written, e.g., in terms of the variable  $\zeta$ :

$$x_r = f_1(\zeta), \quad y_r = f_2(\zeta), \quad z_r = f_3(\zeta). \quad (14)$$

Part of the edge may not be exposed to the flow. As far as it is, the straight lines

$$\frac{x - x_r}{\alpha_1} = \frac{y - y_r}{\alpha_2} = \frac{z - z_r}{\alpha_3} \quad (15)$$

in flow direction define the surface of a shadow cylinder; their intersections with other portions of the surface form a shadow boundary,  $s_e$ , which often will co-exist with a tangential shadow line. In such cases, the proper handling of integration limits requires close attendance (second example). If the rim is part of the surface itself, as with truncated bodies, the variable  $\zeta$  can be taken either as  $\sigma$  or  $\tau$ .

In the following illustrations, four applications of the theory are given.

### THE ELLIPTICAL CONE IN SYMMETRICAL SIMPLE IMPACT FLOW

With the tip of the cone at the origin and its axis coinciding with the  $x$ -axis (Fig. 1), its equation can be written as

$$x = a\sigma,$$

$$y = b\sigma \cos \tau,$$

$$z = c\sigma \sin \tau.$$

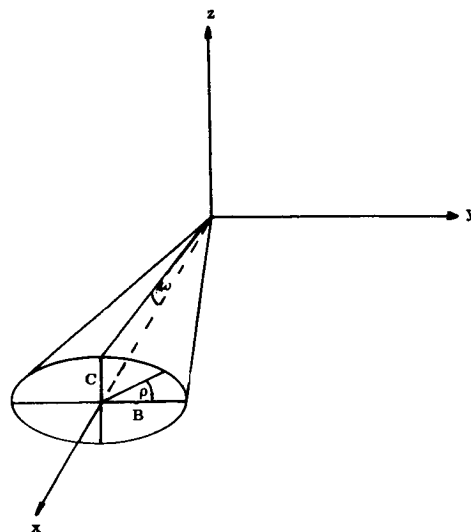


FIGURE 1. ELLIPTICAL CONE

The major and minor half axes of the elliptic cross sections are all proportional to  $b$  and  $c$ , respectively ( $b > c$ ). Their lengths at the base are denoted by  $B$  and  $C$ . Because the variable  $\sigma$  counts the distance  $x$  from the origin in terms of the unit  $a$ , its natural range is

$$0 \leq \sigma \leq \sigma_b,$$

where  $x_b = a\sigma_b$  is the length of the cone axis, and  $B = b\sigma_b$ ,  $C = c\sigma_b$ . The variable  $\tau$  is related to the angle  $\rho$  indicated on Figure 1 through the equation

$$b \tan \rho = c \tan \tau,$$

so that the natural interval for  $\tau$  may be chosen as

$$-\pi \leq \tau \leq \pi.$$

The parametric curves  $\sigma = \text{const.}$  are the cross-sectional ellipses, and the lines  $\tau = \text{const.}$  ( $\rho = \text{const.}$ ) are the cone's generating lines of which three are indicated on Figure 1, the uppermost making the angle  $\omega$  with the cone axis.

If the flow is parallel to the vertical ( $z, x$ ) plane arriving in that plane from below and behind, the configuration is symmetric; the overall angle of attack, taken at the origin, may be smaller than, equal to, or larger than the angle  $\omega$ . The representative unit vector (2) becomes

$$\underline{v} = i \cos \alpha + k \sin \alpha. \quad (16)$$

No shadow evidently is cast on the cone by its elliptical base rim. But a tangential shadow boundary may exist. Equation (13), here independent of  $\sigma$ , defines a constant  $\tau = \tau_t$  as it assumes the form

$$\sin \tau_t = \tan \omega \cotg \alpha.$$

It has no solution when  $\alpha < \omega$ ; the cone is then fully exposed to the incident flow. With  $\alpha > \omega$  there are two solutions in the first and second quadrants. They define a triangular area on the top of the cone enclosed by the two generating lines  $\tau = \tau_t$  and  $\tau = \pi - \tau_t$ . This is the cone zone shielded from impact.

On introducing the numerical eccentricity

$$\epsilon = \sqrt{\frac{b^2 - c^2}{b^2}},$$

and the quantity

$$q = \epsilon^2 \cos^2 \omega,$$

the pressure coefficient (4) may be written as

$$C_p = 2 \frac{(\cos \alpha \sin \omega - \sin \alpha \cos \omega \sin \tau)^2}{1 - q \cos^2 \tau}. \quad (17)$$

The pressure depends on  $\tau$  alone and, therefore, is constant along the generating lines. It exhibits extrema at the boundaries of the  $\tau$ -domain, and may have a third extremum within it. The pressure distribution around the right half of a cross-sectional ellipse ( $-\frac{\pi}{2} \leq \tau \leq +$

$\frac{\pi}{2}$ ) is shown on Figure 2, which is based on  $\omega = 10^\circ$ ,  $\alpha = 14^\circ$ ,  $q = 2/3$ . The shadow boundary  $s_t$  is at  $\tau \approx 45^\circ$  ( $C_p = 0$ ), and a maximum of  $C_p$  exists at  $\tau \approx -45^\circ$ .

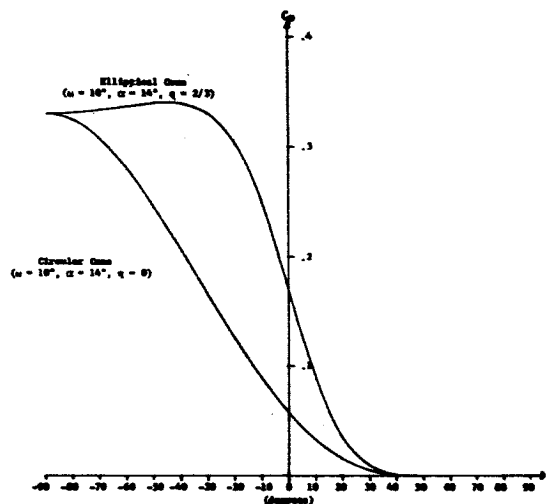


FIGURE 2. PRESSURE DISTRIBUTION ON TWO PARTIALLY IMPACTED CONES.

For comparison, the pressure distribution on the circular cone obtained by setting  $q = 0$  (same  $\omega$ ) is also indicated; for such a cone an extremum inside the  $\tau$ -domain never occurs. The pressures on it are generally smaller, as can be seen from expression (17).

The force components can be obtained in closed form whether or not there is a shielded area. The expressions are relatively simple in the case  $\alpha \leq \omega$  for which they will be written here. If the force coefficients refer to the area ( $\pi BC$ ) of the base ellipse, one finds that

$$\left. \begin{aligned} C_X &= 2 \left( \frac{1 - \sqrt{1 - q}}{q} \cos^2 \omega \sin^2 \alpha + \frac{\sin^2 \omega \cos^2 \alpha}{\sqrt{1 - q}} \right) \\ C_Y &= 0 \\ C_Z &= 4 \sin \alpha \cos \alpha \cos^2 \omega \frac{1 - \sqrt{1 - q}}{q} \end{aligned} \right\} \quad (18)$$

The (known) expressions for the circular cone evolve on putting  $q = 0$ . Drag and lift coefficients are

$$C_D = C_X \cos \alpha + C_Z \sin \alpha$$

$$C_L = -C_X \sin \alpha + C_Z \cos \alpha.$$

A polar for the case  $\cos \omega = 0.75$ ,  $\epsilon = 0.8$  is supplied in Figure 3, where of necessity  $\alpha \leq \omega \approx 41^\circ 20'$  since otherwise expressions (18) do not apply. With  $\alpha$  sufficiently large,  $C_L$  becomes negative.

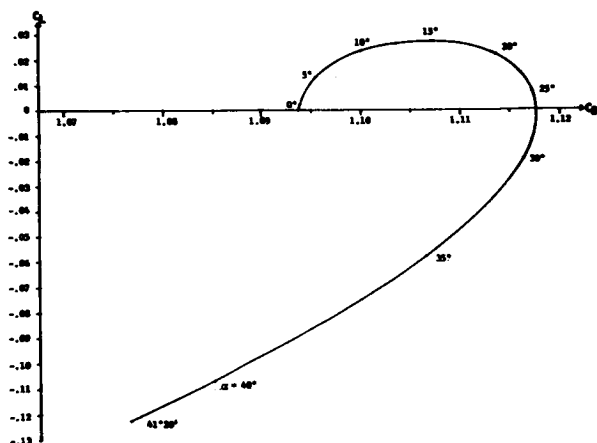


FIGURE 3. POLAR FOR FULLY IMPACTED ELLIPTICAL CONE ( $\cos \omega = 0.75$ ,  $\epsilon = 0.8$ ).

The evaluation of the moment equation (11) can be done with no restriction on  $\alpha$ . It shows that  $y^*$  must be zero. The lever arm of the resultant force  $\underline{P}$  is therefore in the  $(z, x)$  plane and can be chosen as part of the  $x$ -axis, condition (12) taking on the simple form  $z^* = 0$ . The center of pressure is then found at

$$x^* = \frac{2}{3} \frac{x_b}{\cos^2 \omega}, \quad y^* = z^* = 0,$$

i. e., for small angles  $\omega$  at approximately 2/3 of the cone length counted from the tip. With  $\omega \approx 35^\circ$  it already rests near the center of the base, and with still larger values it moves outside the body (in the preceding example  $x^* = \frac{32}{27} x_b$ ). The same formula holds for circular cones. The term  $\cos^2 \omega$  is often absent in the literature when, in computing the moment (10), the normal force elements alone are considered instead of the total force elements.\*

\* The author, who at first had adopted this practice, is indebted to Mr. E. Linsley for pointing out to him the existence of an additional term he had obtained from the chordwise forces acting on the circular cone.

## CONE WITH CYLINDRICAL APPENDAGE

The surface becomes composite if, e. g., a coaxial elliptical cylinder is affixed to the cone base. Let its cross-sectional semi-axes,  $\tilde{B}$  and  $\tilde{C}$ , be parallel to, but neither large than nor necessarily proportional to,  $B$  and  $C$ . In describing the cylindrical surface, the earlier variables  $\sigma$  and  $\rho$  can be used where, as before,  $\rho$  will be linked to a more convenient variable  $\tilde{\tau}$ . The natural ranges are

$$\sigma_b \leq \sigma \leq \sigma_c, \quad -\pi \leq \tilde{\tau} \leq \pi$$

when  $a\sigma$  is the total length of the composite body. The variable  $\tilde{\tau}$  is identical with  $\tau$  in the special case where  $\tilde{B} : \tilde{C} = B : C$ .

With the symmetrical flow vector (16) it suffices to study the right half of the cylinder ( $-\frac{\pi}{2} \leq \tilde{\tau} \leq \frac{\pi}{2}$ ).

The top part of it is bounded by the tangential shadow line  $\tilde{\tau} = 0$  and is not impacted. In addition, the rim of the cone's base will cast a shadow on the lower part. The shadow curve  $s_e$  will start out at some point,  $\sigma = \sigma_1$ , on the cylinder generatrix  $\tilde{\tau} = 0$ , then move downward to a point,  $\sigma = \sigma_2$ ,  $\tilde{\tau} = -\frac{\pi}{2}$  on the nethermost generatrix which it may or may not reach, depending on the cylinder's length. The curve  $s_e$  is plotted schematically in Figure 4 (together with  $s_t$ ).

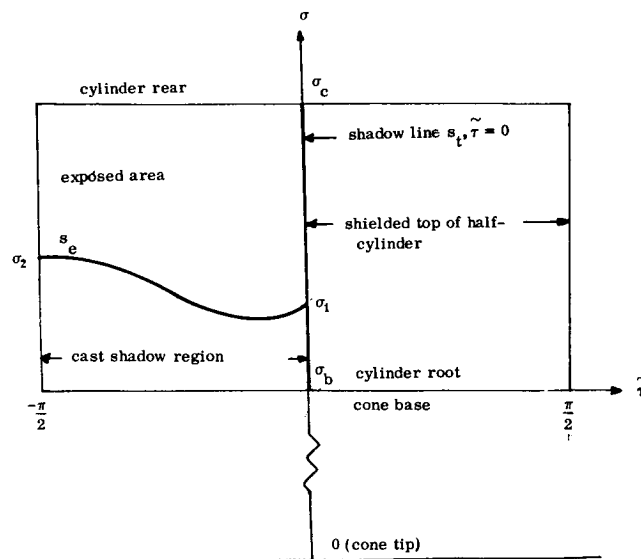


FIGURE 4. SHADOW GEOMETRY ON ATTACHED CYLINDER

Its shape depends on  $B$ ,  $C$ ,  $\tilde{B}$ ,  $\tilde{C}$  and the angle of attack,  $\alpha$ . The length factor  $\sigma_1$  is not necessarily smaller than  $\sigma_2$ , and the midcourse minimum may not exist. If  $\sigma_c$  is not larger than the smallest of the values of  $\sigma$



along  $s_e$ , the cylinder is completely shielded from impact and does not contribute to the forces (a trivial example:  $\alpha = 0$ ). It can be shown that the total force acting on the cylinder is  $P = Z$ . The integration is relatively easy with a circular cylinder (radius  $R$ ) where the shadow curve  $s_e$  is monotonically ascending from  $\sigma = \sigma_2$  to  $\sigma = \sigma_1$ . The outcome depends on whether or not the curve  $s_e$  is cut off by the rear end of the cylinder (length  $h$ ). It is not if

$$h \geq \frac{C}{B} \sqrt{B^2 - R^2} \cotg \alpha. \quad (19)$$

In this case, with  $\beta = R/B$ ,  $\gamma = \frac{R}{C} (\geq \beta)$ ,

$$C_Z = \frac{4}{\pi} \beta \sin^2 \alpha \left\{ \frac{2}{3} \frac{h}{C} + \cotg \alpha \left[ \frac{3}{16} \pi \gamma - \frac{2}{3} + \frac{\beta^2}{15} + \frac{\beta^4}{160} + o(\beta^6) \right] \right\}. \quad (20)$$

where the cone base again is the reference area. The approximation should be good for almost any value  $\beta < 1$ . (With  $\beta = \frac{1}{2}$  the value of the bracket differs in the fifth significant figure only from the exact value). It is seen that the force decreases with decreasing cylinder radius, angle of attack, and cylinder length. The latter remains subject to the condition (19); otherwise, expression (20) assumes a different form.

The circular cylinder is completely impact-free if

$$h \leq (C - R) \cotg \alpha.$$

Evidently, complete shielding (at  $\alpha \neq 0$ ) is precluded if  $R = C$  (the cylinder touching the minor axis vertices of the base ellipse).

With elliptic cylinders, comparatively simple expressions emerge if  $\tilde{B} = B$  (the cylinder touching the major axis vertices of the base ellipse); the curve  $s_e$  is then monotonically descending from  $\sigma = \sigma_2$  to  $\sigma = \sigma_1 \equiv \sigma_b$ . Here again, complete shielding cannot occur. The expression for  $C_Z$  simplifies considerably if with  $\tilde{C} = 0$  the cylinder degenerates into a rectangular plate of length  $h_p$  (width  $2B$ ). On condition that

$$h_p \geq C \cotg \alpha,$$

the entire shadow boundary  $s_e$  finds room on the plate which then contributes the force

$$Z_p = B q_\infty \sin^2 \alpha (4h_p - \pi C \cotg \alpha) \geq BC q_\infty \sin 2\alpha \left(2 - \frac{\pi}{2}\right).$$

For comparison, the  $Z$ -component for a fully impacted circular cone follows from the system (18) as

$$Z = BC q_\infty \sin 2\alpha \cos^2 \omega$$

so that, if  $\alpha$  is moderately small and the plate sufficiently long, the lift of the composite body will be noticeably larger than that of the cone alone. The drag is less affected, although enlarged, too.

## THE BIPARABOLIC CONOID

With an elliptical cone, the expressions for the force components grow unpleasantly lengthy if  $\alpha > \omega$ . More concise formulations can be presumably achieved in the same flow if, in the  $(x, y)$  plane, a sharp edge exists on the surface. For example, a body may be constructed whose cross sections parallel to the plane  $x = 0$  are bounded by two symmetric finite parabolic areas facing each other and intersecting in the ground plane  $z = 0$ . If, with the upper sign holding for the upper parabola, its equation is written as

$$y^2 = 2a (x \tan \omega \mp z),$$

the areas enclosed by the arcs will taper off toward a tip at the origin. The body is then roughly similar to the cone (Fig. 1), with which it will be compared. It intersects with the vertical  $(z, x)$  plane in two straight lines which form the angle  $\omega$  with the  $x$ -axis, connect the parabola vertices, and are the only straight lines on the surface. The planform (in the plane  $z = 0$ ) is the rim parabola

$$y^2 = 2ax \tan \omega. \quad (21)$$

The body is somewhat bulkier than a cone with its triangular planform.

When using again the flow vector (16), examination of the conditions for tangential and edge shadow lines reveals rather simple impact geometries. If  $\alpha \leq \omega$  the whole of the curved surface is exposed to the stream, its lower half alone if  $\alpha > \omega$ . In the latter case there is no  $\alpha$ -dependent shadow line  $\tau = \tau_t$  as exists on the cone; it is replaced by the fixed body rim (21).

The force components emerge in a concise form if they are written with the abbreviations

$$\left. \begin{aligned} m^2 &\equiv \frac{x_b}{a} \sin 2\omega \\ A &= \frac{(m^2 + 1) \operatorname{arctg} m - m}{m^3} \end{aligned} \right\}, \quad (22)$$

where  $x_b$  is the body length.

When  $\alpha \leq \omega$ , the force coefficients become

$$\left. \begin{aligned} C_X &= 3A (\sin^2 \omega \cos^2 \alpha + \sin^2 \alpha \cos^2 \omega) \\ C_Y &= 0 \\ C_Z &= 3A \sin 2\alpha \cos^2 \omega \end{aligned} \right\}, \quad (23)$$

referring to the base area  $\frac{4}{3} \frac{a^2 m^3}{\cos^3 \omega}$ . One may compare relations (23) to the corresponding expressions (18) of an equivalent elliptical cone (same base area, same  $\omega$ ). As a rule,  $C_X$  for the conoid is found smaller, and  $C_Z$  is found larger than for the cone. The lift coefficient (another difference) is positive at least up to  $\omega = 45^\circ$ , i. e., in all practical cases.

For all  $\alpha > \omega$  the shadow boundary (the rim) remains immovable, and the drag and lift coefficients assume a particularly compact form:

$$\begin{aligned} C_D &= \frac{3}{2} A \frac{\sin^3 (\alpha + \omega)}{\sin \omega} \\ C_L &= \frac{3}{2} A \frac{\sin^2 (\alpha + \omega) \cos (\alpha + \omega)}{\sin \omega} \end{aligned}$$

A comparison with the (much more complex) cone expressions has not been made.

The location of the center of pressure is independent of the angle of attack as it is with the cone. The exact expression (not set down here) shows that, in the limit  $\omega = 0$ ,

$$x^* = \frac{3}{5} x_b,$$

which compares with  $x^* = \frac{2}{3} x_b$  for the cone. When  $\omega$  increases from  $\omega = 0$  on, the center of pressure at first moves slowly toward the tip, but afterwards it recedes and is located at the base cross section when  $\omega = 45^\circ$ . The overall trend is the same as was found with the cone.

#### A BLUNT-NOSED BODY

The drop-like surface sketched on Figure 5 the right half of a Bernoulli lemniscate rotated about its axis of symmetry. Its equation may be given as

$$x = a \sqrt{\cos 2\sigma} \cos \sigma$$

$$y = a \sqrt{\cos 2\sigma} \sin \sigma \cos \tau$$

$$z = a \sqrt{\cos 2\sigma} \sin \sigma \sin \tau$$

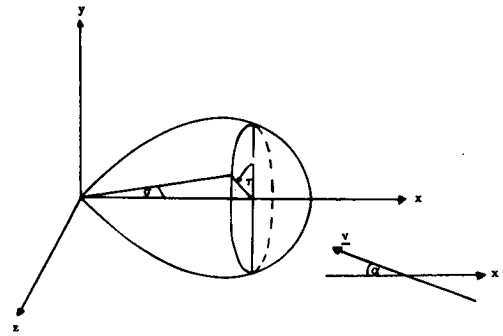


FIGURE 5. LEMNISCATIC SURFACE

where  $a$  is the body length. The angle  $\sigma$  is  $45^\circ$  at the tip,  $0^\circ$  at the blunt end, so that it moves in the natural interval

$$0 \leq \sigma \leq \frac{\pi}{4},$$

while that of  $\tau$  is

$$0 \leq \tau \leq 2\pi.$$

The curves  $\sigma = \text{const.}$  and  $\tau = \text{const.}$  are the circles of constant latitude and the meridians, respectively.

The flow is taken as parallel to the  $(x, y)$  plane arriving from the lower right, so that

$$\underline{v} = -i \cos \alpha + j \sin \alpha. \quad (24)$$

Condition (13) for tangential incidence then assumes the form

$$\cos \tau = \cotg \alpha \cotg 3\sigma. \quad (25)$$

This relation between  $\tau$  and  $\sigma$  defines the shadow boundary  $s_t$  which is not a simple parametric line  $\tau = \text{const.}$  as it was with the cone. The curve  $s_t$  can have two distinct forms. Both appear as a kind of three-dimensional loop that, near the blunt end, intersects with the uppermost meridian at right angles and does so with the nethermost at a point closer to the tip, provided that  $\alpha \leq 45^\circ$ . Otherwise, the loop is pointed at the origin where it sets out in two meridional directions given, according to the  $s_t$ -relation (25), by  $\cos \tau = -\cotg \alpha$ . Both types of loops cross over from the body's upper to its lower part at the latitude circle of largest radius ( $\sigma = 30^\circ$ ). Figure 6 shows their general course on the front side of the body ( $z \geq 0$ ,  $0 \leq \tau \leq \pi$ ). It is seen that an area near the blunt end is impacted in the full natural  $\tau$ -interval. On integrating over  $\tau$ , the upper limit is always  $\tau = \pi$ , while the lower limit is either  $\tau = 0$  or, on  $s_t$ ,  $\tau = \text{arc cos}$

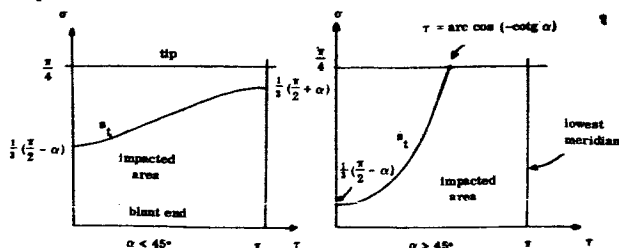


FIGURE 6. SHADOW BOUNDARIES ON LEMNISCATIC DROP

$(\cotg \alpha \cotg 3\sigma)$ , so that two different forms of the integral arise. Owing to the symmetric incidence, the force component  $Z$  is found as zero. The remaining two components cannot be given in explicit form, because, on integrating over  $\sigma$ , one integrand contains the awkward second lower limit of  $\tau$ .

Closed solutions are possible with  $\alpha = \pi/2$  and  $\alpha = 0$ , where the  $s_t$  - curves degenerate into  $\tau = \pi/2$  and  $\sigma = \pi/6$ , respectively. Also, an approximation can be made for small angles  $\alpha$ ; the force coefficients then become

$$C_X = -\frac{19}{20} + 0(\alpha^2)$$

$$C_Y = \frac{21}{20} \alpha + 0(\alpha^3),$$

if the area,  $\frac{1}{8} \pi a^2$ , of the largest circle of latitude serves as reference. As indicated by the sign of  $C_X$ , the chordwise forces push to the left. With  $\alpha = 0$ ,  $C_D \equiv -C_X = \frac{19}{20}$ , which value compares with  $C_D = 1$  for the half-sphere under like circumstances.

For small angles  $\alpha$ , the center of pressure is found at

$$x^* \approx 0.65a,$$

and is thus located near the blunt nose center of curvature which is at

$$x = \frac{2}{3} a.$$

The body shape roughly resembles that of the Apollo capsule; however, the latter's cap has less curvature so that the centroid is likely to be moved toward the left.

#### MODIFICATION OF THE NEWTONIAN $C_p$ - EXPRESSION

With some bodies of plane or axial symmetry and with the circular cylinder in symmetric cross-flow, the Newtonian results have been shown to improve if one sees to it that the pressure coefficient assumes

the exact value at the stagnation point where it is usually (because relatively easily) computed for  $\alpha = 0$ . It may be expected that the expression thus gained will also hold good for small angles of attack. At least one corroboration of this surmise exists in the pressure distribution around a circular cone ( $\omega = 10^\circ$ ,  $\alpha = 6.7^\circ$ ) where the modification amounts to a 4 percent increase in values that are already satisfactory on the whole when computed from shockless impact theory.

With the overall angle of attack zero, the angle  $\omega$ , at the stagnation point, will be the local angle of attack so that  $\omega = \frac{\pi}{2} - \alpha'_{\text{stag}}$ . The modified formula then will be written as

$$C_p = C_p^* \frac{\cos^2 \alpha'}{\sin^2 \omega} = C_p^* \frac{(\mathbf{y} \cdot \mathbf{n})^2}{\sin^2 \omega}, \quad (26)$$

where  $C_p^*$  is the pressure coefficient at the stagnation point. If  $\alpha' = \alpha'_{\text{stag}}$ ,  $C_p = C_p^*$ , as desired. The value of  $C_p^*$  can be calculated from shock transition relations and depends on the ratio of specific heats ( $\gamma$ ) in the gas and on the Mach number,  $M_\infty$ , of the undisturbed flow.

In the case of blunt bodies (for which expression (26) was first suggested by Lester Lees)  $\sin \omega = 1$  and

$$C_p^* = \frac{2}{\gamma} \frac{1}{M_\infty^2} \left[ \left( \frac{\gamma+1}{2} M_\infty^2 \right)^{\frac{\gamma}{\gamma-1}} \left( \frac{\gamma+1}{2\gamma M_\infty^2 - \gamma + 1} \right)^{\frac{1}{\gamma-1}} - 1 \right]. \quad (27)$$

With infinite Mach number in a diatomic gas,  $C_p^* = 1.84$ , which figure then replaces the factor 2 of simple impact theory. The values decrease with decreasing Mach number ( $C_p^* = 1.64$  for  $M_\infty = 2$ ), at first very slowly; in the hypersonic region  $M_\infty > 6$  the figure 1.84 may be used throughout with a small error in the second decimal place ( $\gamma = 1.4$ ). Very satisfactory results have been obtained regarding the sphere, ellipsoid and sphere-capped circular cylinders, and a sphere blunted circular cone; they were somewhat less accurate with the cylinder in crossflow. In all cases, however, they surpassed those obtained by another method (Busemann's pressure relief approach).

With plane symmetric bodies having a sharp leading edge to which the shock is attached, one may use the zero incidence stagnation pressure of the wedge which, although it cannot in general be written down explicitly, assumes a convenient form when the cosine of the shock-body angle is sufficiently close to unity.

Expression (26) then emerges as

$$C_p =$$

$$\left[ \frac{\gamma+1}{2} + \sqrt{\left(\frac{\gamma+1}{2}\right)^2 + \frac{4}{M_\infty^2 \sin^2 \omega}} \right] (\underline{v} \cdot \underline{n})^2. \quad (28)$$

If the Mach number approaches infinity, the bracket approaches  $(\gamma+1)$ ; the factor 2 is then replaced by 2.4 in a diatomic gas.

With  $\gamma = 1.4$  the formula (28) worked well and better than Busemann's method for the wedge itself and for a symmetrical pointed airfoil profile. With the latter and  $\gamma = 1.05$ , however, the modified Newtonian formula gave pressure values that were consistently too high and that were inferior to the pressure relief approach (which resulted in figures somewhat too small).

The surface of a pointed body of revolution may, near the tip, be approximated by that of a circular cone with the same half opening angle  $\omega$ . The latter's relation to the angle  $\sigma_s$  of the attached shock is involved. As a rule, numerical calculations are necessary, unless both  $\omega$  and  $\sigma_s$  are small. In this case the approximate expression

$$\frac{C_p^*}{\omega^2} \approx \frac{4}{\gamma+1} (K_s^2 - 1) + 2 (K_s - K)^2 \frac{\gamma+1}{(\gamma-1) + \frac{2}{K_s^2}} \quad (29)$$

is derived in the literature\*, the relationship of  $K = M_\infty \omega$  and  $K_s = M_\infty \sigma_s$  being given as

$$\frac{K_s}{K} = \frac{\gamma+1}{\gamma+3} + \sqrt{\left(\frac{\gamma+1}{\gamma+3}\right)^2 + \frac{2}{\gamma+3} \frac{1}{K^2}}. \quad (30)$$

If  $M_\infty \rightarrow \infty$ ,  $C_p^* \rightarrow 2 \frac{(\gamma+1)(\gamma+7)}{(\gamma+3)^2} = 2.08$  with  $\gamma = 1.4$

The excess over 2 is markedly less than in two dimensions. For the circular cone itself and  $\gamma = 1.405$ , the approximation of  $C_p$  is very good up to  $\omega = 20^\circ, 30^\circ,$

$40^\circ$ , if  $K \geq 2, \geq 3, = \infty$ . It breaks down rapidly for  $K < 2$ , the error amounting to -8 percent at  $K = 1$  and  $\omega = 5^\circ$ . Expression (30) offers an equally satisfactory approximation of the ratio  $\sigma_s/\omega$  in terms of  $K$ ; with  $\omega$  up to  $10^\circ$ , it is close even with  $K = 1$ .

A check was also made with an ogive ( $\omega = 16.26^\circ$ ,  $M_\infty = 8$ ,  $\gamma = 1.4$ ). The zero incidence meridional pressure distributions as computed from Newton's modified formula and from the (more exact) numerical method of characteristics were practically identical.

For bodies like the elliptical cone and the biparabolic conoid which are not of rotational symmetry, the modification of the factor 2 must be judged on the basis of the wedge and circular cone results. The flatter these more irregular bodies become at a given value of  $\omega$ , the more one may be inclined to cautiously upgrade the relative low cone correction. The blunt lemniscatic body induces no uncertainty; the modified pressure coefficient will here be smaller in accordance with the general expression (27).

\* See G. G. Chernyi, *Introduction to Hypersonic Flow*, translated and edited by R. F. Probstein, Academic Press, New York and London, 1961. Much of the factual information assembled in the last section is taken from this work.

# A UNIFIED TREATMENT OF TURBULENT FLUXES IN MULTI-COMPONENT AND HOT FLOWS

by

F. R. Krause

George C. Marshall Space Flight Center

and

M. J. Fisher

Illinois Institute of Technology Research Institute

## SUMMARY

A unified treatment of turbulent fluxes has been developed to establish a basis for currently planned experimental and analytical programs aimed at the prediction of these fluxes in hot and multi-component flows around launch vehicles.

The unified treatment is achieved by writing all equations of motion in terms of a single conservation law for fluid particles. This law contains a free parameter describing a velocity-dependent conservative property which can be carried by individual molecules. The macroscopic volume concentrations and the molecular fluxes of this property are then obtained by an ensemble average over the velocity distribution function of a single molecule. Thus, all properties which appear in the usual equations of motion can be calculated once the species concentration and the temperature are known inside the fluid particle. Since all of these can be established by spectroscopic analysis, the general conservation law is particularly adapted to optical measurements.

The usual system of turbulent fluxes is found by time-averaging the equations of motion. Applying the same procedure to the general conservation law, one finds that all turbulent fluxes are special cases of a unified turbulent flux which is defined as the time covariance between the velocity fluctuation of a fluid particle and the macroscopic volume concentrations of conservative properties as observed inside the fluid particle. In this way, it is easy to extend the usual discussions of turbulent fluxes that have been given for incompressible and/or one component compressible flows to multi-component and hot flows.

In compressible flows, most turbulent fluxes are estimated from the "driving" concentration gradient and the spreading rate of the concentration profiles.

By writing the general conservation law as a diffusion equation in a moving frame of reference, it is shown that the same procedure can be used in multi-component and hot flows on the condition that (1) volume concentrations are used instead of mass fractions, (2) all concentration profiles are self similar, and (3) all temporal fluctuations are convected as an almost frozen pattern and appear relatively small.

The above conditions are violated in regions where the rms fluctuation levels are comparable to the mean value, for instance, in the separation and reattachment areas of transonic and supersonic shear layers. In these areas we propose to estimate turbulent fluxes directly from measured fluctuations instead of indirectly using point injections and spreading rates. Species concentrations and temperature can be, and some information about velocity fluctuations might be, obtained from local light absorption coefficients. A suitable optical method is now being tested, and the results will be given in the near future.

## LIST OF SYMBOLS

Symbol	Definition
(a) <u>Coordinates</u>	
$\vec{x}_k = (x_1, x_2, x_3)$	curvilinear coordinates
$\vec{x} = (x, y, z)$	Cartesian point vector in space fixed frame
$\vec{\xi} = (\xi, \eta, \zeta)$	Cartesian point vector in moving frame
$t =$	time
$T$	integration time or period of observation

# LIST OF SYMBOLS (Cont'd)

Symbol	Definition		
$\tau$			shear stress
$\vec{q}$			molecular flux of internal energy or heat flux
$V$	volume enclosed by control surface	$\alpha$	molecular exchange coefficients
$M$	total mass enclosed by control surface	$A$	turbulent exchange coefficients
$\vec{c}$	velocity of individual molecule in space fixed reference	$D$	diffusion coefficient
$\vec{u}$	velocity of fluid particle in space fixed reference	$\Gamma$	turbulence level
$\vec{U} = \vec{c} - \vec{u}$	molecular velocities relative to fluid particles	$b$	root mean square spread around injection point streamline
$\vec{C} = \vec{c} - \vec{u}_A$	molecular velocity relative to surface element $dA$ of a fluid particle	$M$	Mach number
		$Re$	Reynolds number
(b) <u>Properties</u>		(c) <u>Operators</u> (including superscripts)	
$m$	mass of individual molecule	—	ensemble average over many realizations of a single molecule or one realization of many molecules
$T$	temperature or statistical parameter of a Boltzmann distribution	$\rightarrow$	vector
$k$	Boltzmann's constant and summation index	$\frac{d}{dt}$	rate of change in moving reference
$E$	internal energy	$\frac{\partial}{\partial t}$	rate of change in space fixed reference
$e$	specific internal energy (internal energy per unit mass)	$\text{div}$	net flow rate or divergence in space fixed and/or moving references
$h$	specific enthalpy	$*$	time average in space fixed reference
$p$	pressure	$+$	time average in moving reference
$\rho$	density	$/$	fluctuation around time average
$n$	number density of molecules	$\oint$	integral over closed control surface
$N$	number of molecules inside fluid particle	(d) <u>Subscripts</u>	
$F$	velocity distribution function of a single molecule	$i$	species "i"
$\phi_i$	velocity dependent conservative property carried by individual molecules	$j, k, l, m$	summation indices
$\rho_\phi$	volume concentration of $\phi_i$	$v$	rigid control surface
$\vec{j}_\phi$	molecular flux of $\phi_i$		

## LIST OF SYMBOLS (Concluded)

### DEFINITION OF SYMBOLS

Symbol	Definition
M	continuously deformed control surface enclosing the same mass
A	element of control surface
o	stagnation and/or injection
$\infty$	jet centerline
a	ambient flow

### INTRODUCTION

The development of modern launch vehicles presents the aerodynamic engineer with unusual problems since the main emphasis is on structural integrity rather than on minimum drag. Highly turbulent and partially separated flows are produced by injections, sharp edges and protuberances. In these areas, an accurate knowledge of turbulent fluxes is needed. For example, turbulent mass fluxes determine the fuel mixing in combustion chambers and supersonic ram jets, the dispersion of turbine exhausts (afterburning), retrorocket exhausts (communication blackout), and cryogenic discharge ( $H_2$  during stage separation). Turbulent heat fluxes are responsible for the high heat transfer rates at the heat shield and the flame deflector. Turbulent momentum fluxes (stresses) act as powerful noise sources in jets (launch), separated flows (supersonic flight), and oscillating shocks (transonic flight). Additional applications are anticipated in air-augmented advanced engines, in supersonic combustors, and in thrust vector control.

The basic difficulty in analytical approaches is that turbulent fluxes appear as additional unknowns in the time-averaged equations of motion. They cannot be calculated since the detailed information about turbulent fluctuations was lost when time averaging the equations. In principle, this information could be retained by solving the time dependent equations of motion and by applying the time averaging procedures to these solutions instead of the equations. However, a review of numerical [1] and statistical [2] methods reveals that it is unlikely that reliable flux estimates can be obtained in spite of the tremendous numerical effort.

The analytical problems have been avoided in the "semi-empirical" approach where the time averaged equations are made determinate by using empirical

relations between turbulent fluxes and driving gradients. Turbulent fluxes are then estimated from the spreading rates of the concentration profiles. For one-component incompressible flows, a good summary is given by Rotta [3]. The statistical interpretation of these fluxes through the random walk of a single fluid particle has been given by G. I. Taylor [4] for uniform flows and by G. K. Batchelor [5] for non-uniform flows. Empirical relations for cold supersonic air flows have been introduced by Gooderum, Wood and Brevoort [6] and Ting and Libby [7].

A unified treatment of turbulent fluxes is now given to establish (a) the conditions that have to be met if the usual flux estimates from concentration profiles and spreading rates is to be extended to hot and multi-component flows and (b) an analytical basis for experimental and analytical work in those areas where these conditions are violated.

### FLUID PARTICLES AND CONSERVATION LAWS

Turbulent fluxes describe the transport of mass, heat and momentum which are produced by the unsteady motion of fluid particles relative to a space-fixed control surface. These fluid particles are enclosed within a small control surface which is continuously deformed and travels with the mass average velocity  $u$  of the enclosed molecules. Because fluid particles are hard to envisage, they will be discussed in detail before they are applied to turbulent flux calculations.

The concept of fluid particles is the main tool in deriving the equations of motion. Qualitative discussions of their surface characteristic are given by Prandtl and Tietjens [8] and by Frenkiel [9]. Some quantitative discussions of their surface characteristics are given by Chapman and Cowling [10] and Becker [11, 12]. Such surface elements will now be combined to a closed control surface in order to derive the macroscopic conservation laws for mass, heat, and the momentum of translational motion.

Though conservation laws might be written for any arbitrary control surface, a special choice is necessary if one wants to retain the thermodynamic and caloric equations of state besides the conservation laws. The reason is that the equations of state relate various ensemble averages which are based on universal velocity distribution functions. These functions have been worked out by the general principles of statistical mechanics [12]. They describe that fraction of all molecules whose velocity is to be expected in a chosen velocity interval. In a stagnant mixture of ideal gases, a first approximation is given by the Maxwellian distribution which shows that such distribution will be different for each species.

$$F_i(\vec{u}) = \left( \frac{m_i}{2\pi kT} \right)^{3/2} e^{-\frac{m_i U^2/2}{kT}} \quad (1)$$

The ensemble average or macroscopic volume concentration of any property  $\phi_i(\vec{U})$  which is a function of the velocity of individual molecules has therefore to be established from the velocity distributions  $F_i(\vec{U})$  and the number densities  $n_i$  belonging to species "i". This average is

$$\overline{\rho_\phi} = \overline{n_i \phi_i(\vec{U})} = \iiint \sum_i \phi_i(\vec{U}) n_i F_i(\vec{U}) d\vec{U} \quad (2)$$

where the overbar denotes the operator

$$\overline{(\quad)} = \iiint \sum_i (\quad) F_i(\vec{U}) d\vec{U}.$$

The equations of motion can use equation (2) in flows, regardless of the fact that the universal velocity distributions have been derived in stagnant media only. However, this requires a special moving observer such that the motion of the surrounding molecules appears to him like the thermal motion of a stagnant gas. According to Chapman and Cowling, a gas is called stagnant if the net mass flux through a surface element  $dA$  is zero. The same result applies to the moving observer if he travels with the mass average velocity of the surrounding molecules. To describe the measurements of such an imaginary observer, the following velocity notation will be used:

Small letters describe the velocity components relative to a fixed reference frame.

$\vec{c}$  = velocity of individual molecule

$\vec{u}_A$  = velocity of surface element  $dA$

$\vec{u}$  = velocity of the center of gravity as determined by the molecules inside the fluid particle

Capital letters describe the velocity relative to moving observers. For each surface element, one would find

$$\vec{C} = \vec{c} - \vec{u}_A, \quad (3)$$

whereas the relative motion inside the fluid particle is described by

$$\vec{U} = \vec{c} - \vec{u}. \quad (4)$$

All moving observers are thus attached to the center

of gravity of the surrounding fluid particles. It is well known that their motion will not be influenced by the internal forces between molecules [11]. Therefore, the average number of crossing particles might be calculated on the assumption that each molecule moves along a straight line. During the time  $dt$ , the velocity interval  $d\vec{C}$  then contributes all particles which are located inside an oblique cylinder of volume  $\vec{C} dA$  (Fig. 1). The number density of these particular particles is given by  $\sum_i n_i F_i(\vec{C}) d\vec{C}$  and the flux of the property  $\phi$  becomes

$$\vec{j}_\phi = \iiint \sum_i n_i F_i(\vec{C}) \phi_i(\vec{C}) \vec{C} d\vec{C} = \overline{n_i \phi_i(\vec{C}) \vec{C}}, \quad (5)$$

where the overbar denotes the operator defined previously in equation (2). If the property  $\phi_i$  is set equal to  $m_i$  in order to represent the mass flux, then this must vanish by definition of the fluid particle, and equation (5) can be solved to calculate the observer motion

$$\vec{u}_A = \frac{1}{\rho} \overline{n_i m_i \vec{c}} = \iiint \sum_i \frac{\rho_i}{\rho} F_i(\vec{C}) \vec{c} d\vec{C}. \quad (6)$$

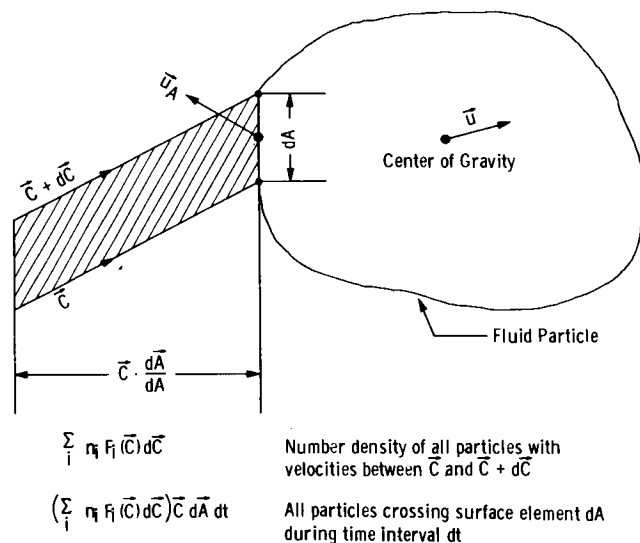


FIGURE 1. ILLUSTRATION OF MACROSCOPIC AVERAGES OF VOLUME CONCENTRATIONS AND MOLECULAR FLUXES

After these preparations, it is possible to state the general macroscopic conservation law which says that the enclosed property  $\iiint_V \rho_\phi d\vec{x}$  changes at a rate which is balanced by the net molecular flux



$$\frac{d}{dt} \left( \iiint_V \rho_\phi(\vec{\zeta}, t) d\vec{\zeta} \right) = - \iint \vec{J}_\phi dA = - \iint_{A(t)} n_i \phi_i(\vec{C}) \vec{C} dA. \quad (7)$$

At this point it is assumed that the fluid particles can be chosen so small that the macroscopic averages are evenly, that is, linearly distributed. In this case, the volume integral is directly proportional to the volume concentration as measured in the center of gravity  $\vec{\zeta} = \vec{x}$ ;

$$\frac{1}{V} \frac{d}{dt} \left( \iiint_V \rho_\phi(\vec{\zeta}, t) d\vec{\zeta} \right) = \frac{1}{V} \frac{d}{dt} (\rho_\phi(\vec{x}, t) \cdot V). \quad (7a)$$

Within the same accuracy the area integral is related to the divergence operator,

$$\text{div}(\vec{C}) = \lim_{V \rightarrow 0} \frac{1}{V} \iint (\vec{C}) dA, \quad (8)$$

which once again has to be evaluated at the center of gravity where the relative molecular velocities are expressed by  $\vec{U}$  instead of  $\vec{C}$ .

We therefore get the conservation law of fluid particles.

$$\frac{1}{V} \frac{d}{dt} (\rho_\phi V) = - \text{div} n_i \phi_i(\vec{U}) \vec{U}. \quad (9)$$

In the first term, the inverse mass density  $\frac{1}{\rho} = \frac{V}{M}$  may be substituted for the volume  $V$  since the mass inside of a fluid particle is constant per definition of its surface elements. This gives

$$\rho \frac{d}{dt} \left( \frac{\rho_\phi}{\rho} \right) = - \text{div} n_i \phi_i(\vec{U}) \vec{U}. \quad (10)$$

Both time derivative and divergence operator must be applied to the moving observer. However, most experiments are made with space-fixed probes. The comparison between experiment and theory therefore requires a space-fixed control surface.

We consider a small and rigid control surface fixed around the position  $\vec{x}$ . The rate of change at this position is then given by the partial time derivative  $\partial/\partial t$  and the volume  $V$  is constant, whereas the mass  $M$  will vary in time. The right side of equation 7a might therefore be approximated by  $\partial \rho_\phi / \partial t$ .

The definition of the surface flux, equation (5), has to be changed. Obviously, all velocity distribu-

tion functions must still be evaluated inside fluid particles, since only then can one expect a universal result. However, these functions might be communicated to an imaginary observer sitting on the rigid control surface. He will find that all molecules belonging to the  $d\vec{C}$  velocity interval can cross his surface element  $dA$ , during the time  $dt$ , which are inside an oblique cylinder aligned parallel to the velocity  $\vec{C} + \vec{u}_A$ . The flux through a space-fixed control surface is therefore given by

$$\vec{j}_{\text{fixed}} = n_i \phi_i(\vec{C}) (\vec{C} + \vec{u}_A); \quad (11)$$

that is, the velocity  $\vec{u}$  has to be added under the divergence operator. The conservation law for a space-fixed control surface becomes

$$\begin{aligned} \frac{\partial \rho}{\partial t} &= - \text{div} n_i \phi_i(\vec{U}) (\vec{U} + \vec{u}) \\ &= - \text{div} \left\{ n_i \phi_i(\vec{U}) \vec{U} + \vec{u} n_i \phi_i(\vec{U}) \right\} \\ &= - \text{div} (n_i \phi_i(\vec{U}) \vec{U} + \rho_\phi \vec{u}), \end{aligned} \quad (12)$$

showing that the rate of volume concentration change is equal to the molecular fluxes across the surface of the moving fluid particles plus the flux of the macroscopic averages across the space-fixed control surface.

The main assumption of the previous section was that the fluid particles are sufficiently small such that the ensemble averages  $\vec{u}$  and  $\rho_\phi$  are linearly distributed inside the particle. In theory, ensemble averages are obtained from a large number of flow realizations or flashlight images. Since the velocity distribution function used in this paper is based on a single molecule, the fluid particle could be of molecular size. However, experimental verification of the ensemble averages requires that a "true" estimate of the ensemble averages be found in only one realization. Therefore, the number of statistical degrees of freedom, that is, the number of molecules, should be so large that the standard deviation taken over all molecules is still below the resolving power of the measuring instrument. This conditions leads to a finite lower limit on the size of fluid particles.

Let us consider a cube of side  $d$  which is filled with a mixture of ideal gases at partial pressures  $p_i$  and temperature  $T$ . The average number of enclosed "i" molecules follows from Avogadro's number

$$N_i = 2.69 \cdot 10^{19} p_i [\text{atm}] \frac{273}{T[^\circ\text{K}]} d^3 [\text{cm}^3]. \quad (13)$$

The actual number will fluctuate around this average in a fashion that can be described by the normal distribution. The corresponding mean square fluctuations of specific density  $\rho_i$  and internal energy  $E_i$ , derived in the kinetic theory of gases [11], are

$$\left(\frac{\Delta\rho_i}{\rho_i}\right)^2 = \frac{3}{2} \left(\frac{\Delta E_i}{E_i}\right)^2 = \frac{1}{N_i}. \text{ "molecular fluctuations"} \quad (14)$$

Assuming that the resolving power of the measuring instrument stays below  $\frac{\rho}{\Delta\rho} \approx \frac{E}{\Delta E} \leq 10^4$ , the combination of equations (13) and (14) gives the following lower limit of particle size:

$$d [\text{cm}] \geq \left\{ \frac{10^{-19}}{2.69 p [\text{atm}]} \frac{T[^\circ\text{K}]}{273} \left(\frac{\Delta\rho_i}{\rho_i}\right)^2 \right\}^{1/3} \\ = \frac{3.4 \cdot 10^{-3} (T/273)^{1/3}}{(p [\text{atm}])^{1/3}}. \quad (15)$$

For partial pressures of  $10^{-3}$  atm and hot flows, this is already in the mm range, and the thermodynamic properties of these hot, low pressure flows may not be evenly distributed inside a fluid particle of this size. It follows that a "one shot" instrumentation may be incompatible with the equations of motion.

### THE EQUATIONS OF MOTION

The concept of fluid particles has the benefit that the thermodynamic and caloric equations of state might be tested in stagnant media. The vast amount of information about real and rarefied gas effects, chemical reactions, radiation, etc., that has been accumulated in these stagnant media might thus be used in reacting and radiating compressible flows, provided that the range of thermodynamic properties is the same for the flow and the stagnant medium. Therefore, the conservation law, equation (10) or (12), does summarize the complete equations of motion for multi-component systems as listed by Byrd, Stewart and Lightfoot [13] and provides in addition an accurate definition of all ensemble averages involved.

The mass balance for species  $l$  can be derived by setting

$$\phi_i = m_l \delta_{il} = \begin{cases} 0 & \text{for } l \neq i \\ m_i & \text{for } l = i \end{cases}. \quad (16)$$

The volume concentration follows from equation (2):

$$\rho_\phi = \overline{n_i m_i \delta_{il}} = \rho_l. \quad (17)$$

The conservation law of fluid particles,

$$\rho \frac{d(\rho_l/\rho)}{dt} = -\text{div } \vec{j}_l, \quad (18)$$

leads then to the definition of the mass flux

$$\vec{j}_l = \overline{n_i m_i \delta_{il} \vec{U}} = \int \int \int_{-\infty}^{+\infty} \sum_i n_i m_i \delta_{il} \vec{U} F_i(\vec{U}) d\vec{U} \\ = \rho_l \int \int \int_{-\infty}^{+\infty} \vec{U} F_l(\vec{U}) d\vec{U}. \quad (19)$$

This flux does not vanish in multi-component flows, since the average velocity of the " $l$ " particles might be different from the mass average  $\vec{U} = 0$  taken over all species.

The momentum balance considers the translational momentum of single molecules in a spaced-fixed reference frame:

$$\phi_i = m_i \vec{c} \quad (20)$$

This leads to three conservation equations, one for each component  $m_i c_i$ ,  $i = 1, 2, 3$ . The volume concentration,

$$\rho_\phi = \overline{n_i m_i c_i} = \int \int \int_{-\infty}^{+\infty} \sum_i n_i m_i (\vec{U}_i + \vec{u}_i) F_i(\vec{U}) d\vec{U} \\ = u_i \sum_i \rho_i \int \int \int_{-\infty}^{+\infty} F_i(\vec{U}) d\vec{U} = \rho u_i \quad (21)$$

is then related to the divergence of a momentum flux tensor

$$\rho \frac{du_l}{dt} = -\text{div } \overline{n_i m_i c_i \vec{U}} = \sum_k \frac{\partial}{\partial x_k} \left( \overline{\rho_i c_i U_k} \right), \quad (22)$$

the components of which are customarily split into normal stresses and shear stresses;

$$P \delta_{kl} + \tau_{kl} = \overline{\rho_i c_i U_k} = \rho_i (\overline{U_l + u_l}) U_k \\ = \int \int \int_{-\infty}^{+\infty} \sum_i \rho_i (U_l + u_l) U_k F_i(\vec{U}) d\vec{U} \\ = \sum_i \rho_i \int \int \int_{-\infty}^{+\infty} U_l U_k F_i(\vec{U}) d\vec{U}. \quad (23)$$

For a spherical symmetric velocity distribution, the shear stresses  $l \neq k$  vanish. It is the deviations from the spherical symmetry that lead to "shearing action."

The conservation of energy takes into account the kinetic energy in the fixed coordinate system and the total potential energy  $\mu_i$  which is communicable and stored in the various energy levels of the individual molecules.

$$\phi_i = m_i \frac{\vec{u}^2}{2} + \mu_i = \frac{m_i}{2} (\vec{U} + \vec{u})^2 + \mu_i = \frac{m_i}{2} \vec{U}^2 + \mu_i + m_i \left( \frac{\vec{u}^2}{2} + \vec{u} \vec{U} \right) = E_i + m_i \left( \frac{\vec{u}^2}{2} + \vec{u} \vec{U} \right). \quad (24)$$

The volume concentration of this energy,

$$\rho_\phi = n_i \{ E_i + m_i \left( \frac{\vec{u}^2}{2} + \vec{u} \vec{U} \right) \} = \overline{n_i E_i} + \frac{\vec{u}^2}{2} \overline{n_i m_i} = \rho \left( e + \frac{\vec{u}^2}{2} \right), \quad (25)$$

is the sum of the specific internal energy as seen by the moving observer

$$e = \frac{1}{\rho} \overline{n_i E_i} = \frac{1}{\rho} \int \int \int \sum_i n_i \left( \frac{m_i}{2} \vec{U}^2 + \mu_i \right) F_i(\vec{U}) d\vec{U} \quad (26)$$

and the kinetic energy  $\rho \frac{\vec{u}^2}{2}$  associated with the center of gravity. Its change is related to the divergence of two molecular fluxes:

$$\rho \frac{d}{dt} \left( e + \frac{\vec{u}^2}{2} \right) = - \operatorname{div} n_i \{ E_i + m_i \left( \frac{\vec{u}^2}{2} + \vec{u} \vec{U} \right) \} \vec{U} = - \operatorname{div} n_i E_i \vec{U} + \rho_i (\vec{u} \vec{U}) \vec{U}. \quad (27)$$

The first describes the transport of internal energy or heat through the surface of the fluid particle

$$q = \overline{n_i E_i \vec{U}} = \int \int \int \sum_i n_i E_i \vec{U} F_i(\vec{U}) d\vec{U}. \quad (28)$$

Once again, it will vanish for a spherical symmetric velocity distribution.

The divergence of the second is customarily interpreted as work of the pressure tensor:

$$\operatorname{div} \rho_i (\vec{u} \vec{U}) \vec{U} = \operatorname{div} \left( \sum_l \rho_i u_l U_l \right) \vec{U} = \sum_k \frac{\partial}{\partial x_k} \left( \sum_l \rho_i U_l U_k \cdot u_l \right) = \operatorname{div} \left( p \delta_{kl} + \tau_{kl} \right) \begin{pmatrix} u_1 \\ u_2 \\ u_3 \end{pmatrix}. \quad (29)$$

Thus, all equations of motion have been derived from the conservation laws, equation (10) or (12). They are valid as long as there are no external sources. Thus, investigations of condensation effects, excitation, ionization and self-generated radiation are covered. However, species generating chemical reactions, momentum generating electromagnetic or gravitational external force fields, and heat generation by incident radiation are to be excluded.

### TURBULENT FLUXES

The main characteristic of turbulent flows is the rapid and random unsteady motion of fluid particles. This paper considers stationary flows where all temporal mean values like

$$\vec{u}^* = \lim_{T \rightarrow \infty} \frac{1}{T} \int_t^{t+T} \vec{u}(\vec{x}, t) dt \quad (30)$$

are independent against a translation in time.

$$\vec{u}^* = \vec{u}^*(x, y, z) \quad (31)$$

Subclasses of stationary flows are customarily established by considering the velocity fluctuations [14]:

$$\vec{u}' = \vec{u}(x, y, z, t) - \vec{u}^*(x, y, z). \quad (32)$$

In turbulent flows, the turbulence level

$$\Gamma = \frac{\sqrt{\frac{1}{3} \overline{(\vec{u}')^2}}}{|\vec{u}^*|} \quad (33)$$

always exceeds 4 percent and values as high as 20 percent are not uncommon in free shear layers [15]. Besides, these fluctuations occur at very high frequencies, mostly between 1000 and 50,000 cps depending on the mean velocity profile and the shear layer thickness. As a result, a very high flux of mass, heat, and momentum is to be expected.

The relation between turbulent fluxes and turbulent fluctuations follows directly from equation (12). We consider the flux of macroscopic averages  $\rho_\phi$  which have been communicated from the passing fluid particles to the space-fixed control surface. This flux was given as  $\rho_\phi \vec{u}$ . It will fluctuate in time since the en-

semble averages  $\rho_\phi$  and  $\vec{u}$  are obtained from only one flashlight image of many molecules (and/or realizations). Subsequent flashlight images might lead to different mean values as has already been noted for the velocity fluctuations. However, in most applications, one is interested only in the time average flux,

$$(\rho_\phi \vec{u})^* = \rho_\phi^* \vec{u}^* + (\rho_\phi' \vec{u}')^*, \quad (34)$$

which consists of two parts. The first describes the transport of a hypothetical "time averaged" motion, that is, the flux of the time average volume concentrations  $\rho_\phi^*$  which are convected with the time average mass velocity  $\vec{u}^*$ . This hypothetical flow is the only one which can be measured by most instruments. The second term  $(\rho_\phi' \vec{u}')^*$  is called the "apparent turbulent flux" or just turbulent flux. It describes the transport of heat, mass, and momentum across a space-fixed control surface by the temporal cross correlation function between the velocity fluctuation  $\vec{u}$  of a passing fluid particle and the volume concentration fluctuation  $\rho_\phi$  as observed inside this fluid particle. This is the covariance between the convecting and convected property as measured simultaneously at the same spot by a space-fixed and by a moving observer.

$$(\rho_\phi' \vec{u}')^* = \lim_{T \rightarrow \infty} \frac{1}{T} \int_0^T \rho_\phi'(\vec{x}, t) \vec{u}'(\vec{x}, t) dt \quad (35)$$

Equation (35) can be written for any velocity-dependent property  $\phi_i$  that can be carried by individual molecules. Possible choices include the mass  $m_i$ , the translational momentum  $m_i \vec{c}$ , and the energy  $m_i \frac{\vec{c}^2}{2} + \mu_i$  as given in equations (16) through (29).

The largest turbulent fluxes are to be expected whenever (a) the velocity fluctuations or turbulence

level  $\sqrt{(\frac{1}{3} \vec{u}^2)^*} / |\vec{u}|$  is large, (b) the fluctuations of the volume concentration  $(\rho_\phi'^2)^*^{1/2}$  are large, and (c) both fluctuations are correlated in time. Since all volume concentrations are ensemble averages over the same velocity distribution functions, all volume concentrations are correlated with each other. It follows that a high correlation coefficient,

$$\frac{(\rho_\phi' \vec{u}')^*}{\sqrt{(\rho_\phi'^2)^*} \sqrt{(\vec{u}^2)^*}} = r_\phi, \quad (36)$$

is to be expected for any thermodynamic property  $\phi$  once it has been found for a particular one. There-

fore, high heat and mass fluxes will occur simultaneously as soon as their turbulence level,

$$\frac{\sqrt{(\rho_\phi'^2)^*}}{\rho_\phi^*} = \Gamma_\phi, \quad (37)$$

is large enough. Furthermore, a correlation between heat fluctuations and momentum component fluctuations is to be expected, since their volume concentrations  $\rho \vec{u}$  and  $\rho(e + \frac{\vec{u}^2}{2})$  are based on the same densities and velocities. Thus, a high turbulent shear stress always indicates a high correlation coefficient  $r_\phi$  as well as high velocity fluctuations.

Comparing flows with the same level of turbulence, one therefore has to expect the highest turbulent fluxes in the region of high turbulent shear stresses.

The problem with turbulent fluxes is that they cannot be calculated from measurable time averaged properties. Since the turbulent flux is a time average, any relation between turbulent fluxes and time averaged properties has to be based on the time averaged equations of motion.

$$\lim_{T \rightarrow \infty} \frac{1}{T} \int_0^T \frac{\partial \rho_\phi}{\partial t} dt = \lim_{T \rightarrow \infty} \frac{\rho_\phi(T) - \rho_\phi(0)}{T} =$$

$$0 = - \operatorname{div} \{ n_i \phi_i (\vec{U}) \vec{U}^* + (\rho_\phi \vec{u})^* \}, \quad (38)$$

which leads to one equation

$$\operatorname{div} (\rho_\phi^* \vec{u}^*) = - \operatorname{div} \{ n_i \phi_i (\vec{U}) \vec{U}^* + (\rho_\phi \vec{u})^* \} \quad (39)$$

for each volume concentration  $\rho_\phi^*$  (including of course  $\vec{u}^*$ ). The molecular fluxes do depend only on the universal velocity distribution functions and may be related to the  $\rho_\phi^*$  in a known manner. However, the turbulent fluxes appeared as additional unknowns, since the information about the individual fluctuations  $\rho_\phi'$  and  $\vec{u}'$  has been lost during the time averaging procedures. As a result, one has more unknowns than equations, the system of equation 39 cannot be solved, and a general relation between turbulent fluxes and time average properties does not exist.

Obviously, the information about turbulent fluctuations is not lost, if one solves the time dependent equations of motion as represented by equation (12).

The turbulent fluxes may then be found by applying the time averaging procedure (covariance, equation (35)) to these now time-dependent solutions and not to the differential equations. Such solutions can be found numerically in a series of stepwise advances in time solving an initial value problem at each step [17]. Modern digital computation facilities offer storage capacity and a computation speed which makes a direct solution feasible in spite of the tremendous numerical effort involved. Two-dimensional turbulent flow fields are presently calculated by modifying a computer program that gives the visco-elastic behavior of soils and rocks due to an atomic blast [18]. However, there is a fundamental limit on spatial resolution. The flow has to be uniform over distances larger than the speed of sound multiplied by the time interval between steps [1]. Thus, only low frequency fluctuations can be obtained. High frequency and/or high spatial resolution cannot be resolved inside the "fluid particles" which constitute the numerical mesh.

Unfortunately, the high frequency fluctuations and the high spatial resolution of cross correlation coefficients are very important, since these fluctuations determine the conversion of the turbulent kinetic energy into heat [3]. The alternative to direct solutions is then to establish some hopefully universal velocity distribution functions for fluid particles. A universal distribution has been found for high temporal and spatial frequencies (wave number) considering the spatial Fourier transform of the two-point product mean values between the velocity components of  $\vec{u}$  [2]. This distribution shows how the kinetic energy  $\vec{u}^2/2$  is distributed in the wave number space. However, the energy-bearing wave number components often reflect specific mechanism of turbulence generation and are often outside the range of the universal distribution.

It appears that the velocity fluctuations of fluid particles cannot be described by a universal distribution function that covers the complete wave number range of interest. In separated flows, the mechanism of turbulent energy transfer is not even a local effect but does depend on the upstream conditions in an unknown manner [13]. Besides, the statistical approach has been applied to incompressible flows only. In compressible flows and especially multi-component flows, concentration and temperature fluctuations appear besides velocity fluctuations, and the associated fluxes still cannot be predicted, even if a universal velocity distribution could be established.

### EXCHANGE COEFFICIENTS

Analytical problems have been avoided in "semi-empirical" approaches, where the missing relations between turbulent fluxes and time average volume concentrations are provided from experiments. However,

with very few exceptions [20], these experiments did not cross-correlate turbulent fluctuations, since the simultaneous measurement of convecting and convected properties proved to be too difficult. Rather, it was assumed that the turbulent fluxes are proportional to driving gradients in analogy to molecular diffusion.

The ratio between turbulent fluxes and driving gradients is called the turbulent exchange coefficient and has been estimated from the spreading rate of the concentration profiles. For one-component incompressible flows, a good summary of empirical data is given by J. C. Rotta [3]. The statistical interpretation through the random walk of a single fluid particle has been given for uniform flows by G. I. Taylor [4] and for non-uniform flows by Batchelor [5]. Empirical relations for cold supersonic flows have been introduced by H. H. Korst [22] and P. A. Libby [7]. The general conservation law is now rewritten in terms of the Fickian diffusion equation to establish the conditions that have to be met in multi-component and hot flows, such that the turbulent fluxes might still be estimated from the spreading rate of concentration profiles.

We consider a rigid frame of reference, the center of which travels along a streamline of the time-averaged motion. Every point  $\xi$  inside this frame is related to space-fixed Cartesian coordinates

$$\vec{\xi} = \vec{x} - \vec{x}_0(t) \quad (40)$$

as measured against the position

$$\vec{x}_0(t) = \vec{x}_0 + \int_0^t \vec{u}_0(t) dt \quad (41)$$

of the origin  $\vec{\xi} = 0$  traveling with the velocity

$$\vec{u}_0(t) = \frac{d\vec{x}_0(t)}{dt} = \vec{u}^*(\vec{x}_0(t)) \quad (42)$$

along the streamline that passes through the reference or injection point  $\vec{x}_0$ .

The general conservation law for a rigid and fixed control surface has already been given in equation (10). Repeating the same analysis for a small volume element of our moving frame, we get

$$\frac{d}{dt} \rho_\phi(\vec{\xi}, t) = - \text{div} (\vec{n}_1 \phi_1(\vec{U}) \vec{U} + \Delta \vec{u} \rho_\phi), \quad (43)$$

where  $\Delta \vec{u}$  denotes the relative motion of the fluid particles on the moving frame.

$$\Delta \vec{u}(\xi, t) = \vec{u}(\vec{x}, t) - \vec{u}_0(t). \quad (44)$$

At the origin,  $\vec{\xi} = 0$ , this relative velocity is identical with the velocity fluctuation  $\vec{u}'$  relative to the streamline through  $x_0$ . A time average of equation (43) will therefore be used to obtain some information about turbulent fluxes. However, the moving frame is subjected to accelerations such that the fluctuation  $\Delta \vec{u}$  is no longer a stationary process, and the time average

$$\rho_{\phi}^{+} = \lim_{T \rightarrow \infty} \frac{1}{T} \int_{t'=t}^{t'=t+T} \rho_{\phi}(\vec{\xi}, t') dt' \quad (45)$$

is not independent against a translation in time

$$\rho_{\phi}^{+} = \rho_{\phi}^{+}(\vec{\xi}, t). \quad (46)$$

The time average of equation (43) therefore retains a time derivative

$$\frac{d}{dt} \rho_{\phi}^{+}(\vec{\xi}, t) = - \text{div}_i n_i \phi_i(\vec{U}) \vec{U} + (\Delta u \rho_{\phi})^{+}. \quad (47)$$

Equation (47) can now be converted to the Fickian diffusion equation,

$$\frac{d}{dt} (\rho_{\phi}^{+}) = D_{\phi}(t) \text{div grad } \rho_{\phi}^{+}(\vec{\xi}, t) = D_{\phi}(t) \Delta \rho_{\phi}^{+}, \quad (48)$$

on the condition that both the molecular exchange coefficient,

$$\alpha_{v\phi} = - \frac{n_i \phi_i(\vec{U}) \vec{U}}{\text{grad } \rho_{\phi}^{+}} = \alpha_{v\phi}(t), \quad (49)$$

and the turbulent exchange coefficient,

$$A_{v\phi} = - \frac{(\rho \Delta u)^{+}}{\text{grad } \rho_{\phi}^{+}} = A_{v\phi}(t), \quad (50)$$

are constant within the moving frame. A diffusion coefficient  $D_{\phi}$  is then introduced as the sum of the two:

$$D_{\phi}(t) = \alpha_{vM}(t) + A_{vM}(t). \quad (51)$$

Equation (48) has the particular solution

$$\rho_{\phi}^{+}(\vec{\xi}, t) = \frac{\phi(x_0, t_0)}{b^3(t) \pi^{3/2}} e^{-\frac{\vec{\xi}^2}{b^2(t)}} \quad (52)$$

describing now how an injection of the conservative property

$$\phi(\vec{x}_0, t_0) = \int_{-\infty}^{+\infty} \rho_{\phi}^{+}(\vec{\xi}, t) d\vec{\xi} \quad (53)$$

at time  $t_0$  and space-fixed point  $x_0$  spreads in the moving frame. The length scale  $b(t)$  is directly proportional to the root mean square spread as weighted with the volume concentration

$$\frac{3}{2} b_{\phi}^2(t) = \frac{\int_{-\infty}^{+\infty} \int_{-\infty}^{+\infty} \int_{-\infty}^{+\infty} \vec{\xi}^2 \rho_{\phi}^{+}(\vec{\xi}, t) d\vec{\xi}}{\int_{-\infty}^{+\infty} \int_{-\infty}^{+\infty} \int_{-\infty}^{+\infty} \rho_{\phi}^{+}(\vec{\xi}, t) d\vec{\xi}}. \quad (54)$$

Its value can then be used to calculate the diffusion coefficient since the particular solution requires that

$$D_{\phi}(t) = \frac{1}{2} b_{\phi}(t) \frac{db_{\phi}}{dt} = \frac{1}{4} \frac{db_{\phi}^2(t)}{dt}. \quad (55)$$

Equation (55) shows how to obtain the diffusion coefficient from measured spreading rates. However,  $b(t)$  is related to the density  $\rho_{\phi}^{+}$  as seen by the moving observer, whereas most instruments are space-fixed; that is, they measure the density  $\rho_{\phi}^{*}$ . The difference between the two time averages is now established by communicating the results from the moving to the fixed frame.

We consider the simplest of all cases where the streamline of interest is straight.

$$\vec{u}_0(t) = (u^*(\vec{x}_0(t)); 0, 0) = \left(\frac{dx}{dt}, 0, 0\right) \quad (56)$$

If at time  $t$  the moving cross section  $\xi = 0$  occupies the position  $x_0(t) = x_0 + x(t)$ , this cross section will advance to the position  $x_0 + x(t')$  at the later time  $t'$ . At this later time, the space-fixed cross section  $x$  is then identical with the moving cross section  $\xi = - (x(t') + x(t))$ .

The instantaneous communication from the moving to the fixed frame therefore gives

$$\rho_{\phi}(x, y, z, t') = \rho_{\phi}(\xi = x(t) - x(t'); \eta = y - y_0, \zeta = z - z_0, t'), \quad (57)$$

and the difference between the time averages is equal to

$$\begin{aligned} \rho_{\phi}^{+}(x, y, z, t) - \rho_{\phi}^{+}(\xi = 0, \eta, \zeta, t) \\ = \lim_{T \rightarrow \infty} \frac{1}{T} \int_{t'=t}^{t'=t+T} \rho_{\phi}(x(t) - x(t'); \eta, \xi, t') - \rho_{\phi}(0, \eta, \zeta, t') dt'. \end{aligned} \quad (58)$$

This difference becomes small if we assume that (a) the communicated densities appear as small temporal fluctuations to the space-fixed observer

$$\frac{|\rho_\phi(x(t) - x(t'); \eta, \xi, t) - \rho_\phi(x(t) - x(t'); \eta, \xi, t)|}{\rho_\phi^+(0, \eta, \xi, t)} \ll 1 \quad (59)$$

and (b) that they are convected as a frozen pattern

$$\rho_\phi(x(t) - x(t'); \eta; \xi; t) \approx \rho_\phi(0, \eta, \xi, t'). \quad (60)$$

The approximation

$$\begin{aligned} \rho_\phi^*(x, y - y_0, z - z_0) &= \rho_\phi^+(0, \eta, \xi, t) \\ &= \frac{\phi(\vec{x}_0, t_0)}{\pi^{3/2} b^3(x)} e^{-\frac{(y-y_0)^2 + (z-z_0)^2}{b^2(x)}} \end{aligned} \quad (61)$$

is therefore valid in almost frozen patterns of turbulence. Although the relative amplitude of the fluctuations is small, their space gradients  $\partial\rho/\partial\eta$  and their frequencies could be quite considerable.

The profiles of a two-dimensional jet or line source follow by an integration over  $z_0$ .

$$\rho_\phi^*(x, y - y_0) = \int_{-\infty}^{+\infty} \rho(x, y, z - z_0) dz_0 = \frac{\phi(x_0, y_0, z_0)}{b^2(x)\pi} e^{-\frac{(y-y_0)^2}{b^2(x)}} \quad (62)$$

Shear layer profiles across the main region of both axisymmetric and plane jets should therefore be self similar and resemble the error curve  $e^{-(y/b)^2}$ . The scale factor  $b(x)$  and the spreading rate  $db/dx$  follow most easily from the "half concentration width," as indicated in Figure 2. Evaluating  $b(x)$  at several

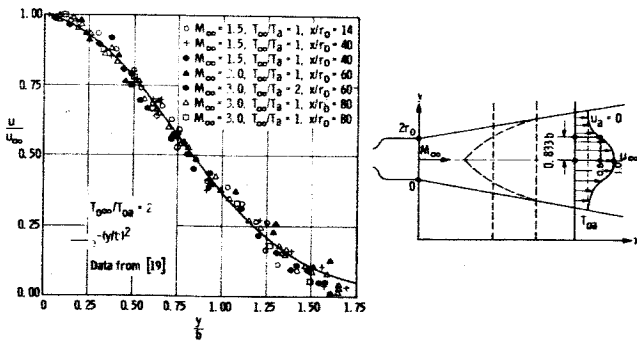


FIGURE 2. VELOCITY PROFILES IN THE MAIN REGION OF SUPERSONIC JETS

cross sections, the diffusion coefficient can then be given as

$$D_\phi = \frac{1}{4} \frac{db^2}{dt} = \frac{1}{2} b \frac{db}{dx} \frac{dx}{dt} = \frac{1}{2} b_\phi(x) \vec{u}^* (x, y_0, z_0) \frac{db}{dx} \quad (63)$$

The shear layer profiles across the initial portion of a jet are obtained by treating the jet as straight-line sources parallel to the  $z$  direction. The contribution of each line is then given by equation (62). The total volume concentration follows by integrating over all line sources

$$\rho_\phi^*(x, y) = \int_{y_0=0}^{y_0=\infty} \rho_\phi^*(x, y - y_0) dy_0 = \frac{\phi(x_0, t_0)}{\sqrt{\pi} b(x)} \frac{1}{2} (1 - \operatorname{erf} \frac{y}{b(x)}). \quad (64)$$

Accordingly, the shear layer profiles across the initial region of jets should resemble the error integral. The spreading scale  $b(x)$  and the spreading rate  $db/dx$  may then be obtained from a sample straight-line approximation as shown in Figure 3.

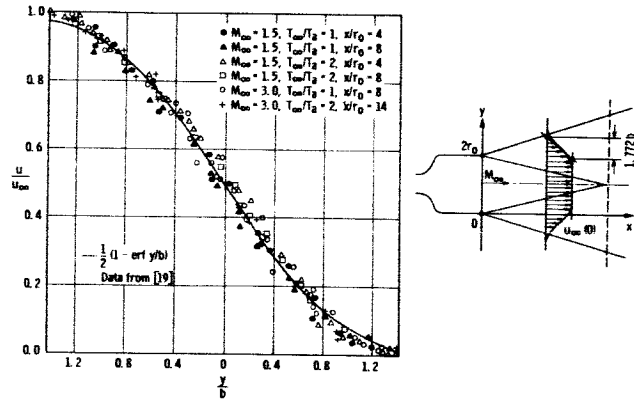


FIGURE 3. VELOCITY PROFILES IN THE INITIAL REGION OF SUPERSONIC JETS

The diffusion equation (equation (48)) was obtained from the general conservation law, and its solutions should therefore be valid in multi-component and hot flows, as long as the assumptions of turbulent exchange coefficients, equations (49) and (50), and almost frozen patterns of turbulence, equations (59) and (60), are justified. The shear layer profiles of all volume concentrations like species density,  $\rho_i$ , stream density,  $\rho u$ , and internal energy,  $\rho c_v T_0$ , are similar, and for each property the diffusion coefficient can be found by establishing the lateral scale factor  $b(x)$  as outlined in Figure 2 and equation (63). These diffusion coefficients might then be multiplied with  $\operatorname{grad} \rho_\phi^*$  to obtain an estimate of the combined molecular and turbulent fluxes along the injection streamlines. At other positions, this estimate will be less accurate since the relative velocity  $\Delta u$  and the velocity fluctuation  $u'$  might differ appreciably.

The present treatment of turbulent diffusion is somewhat unusual, since it is based on volume concentrations instead of mass fractions. This is suggested by Batchelor's treatment of turbulent diffusion where the volume concentration  $\rho_\phi^*(\xi, t)$  of a conser-

vative property is associated with the probability that a single fluid particle be displaced to position  $\xi$ . On the other hand, turbulent exchange coefficients are customarily defined by the gradients of mass fractions instead of volume concentrations. It seems therefore necessary to discuss why volume concentrations have been used in this paper.

Mathematically, the choice of volume concentration  $\rho_\phi$  or mass fraction  $\rho_\phi/\rho$  follows from the choice of the control surface. Fluid particles conserve their mass; therefore, the mass fraction  $\rho_\phi/\rho$  appears in the conservation law, equation (10), and a diffusion equation can be obtained only by defining the exchange coefficient with a mass fraction gradient.

$$\rho^+ \alpha_{M\phi} = - \frac{n_i \phi_i (\vec{U}) \vec{U}^+}{\text{grad} (\rho_\phi/\rho)^+} \quad (65)$$

The coefficient  $\alpha_{M\phi}$  which will be called molecular diffusivity, unifies the standard definition of mass diffusivity  $\alpha_{M_1}$ , thermal diffusivity  $\alpha_{M_e}$ , and dynamic viscosity  $\alpha_{M_u}$ .

The customary definition of turbulent exchange coefficients is strictly analogous:

$$\rho^+ A_{M\phi} = - \frac{(\rho_\phi' u')^*}{\text{grad} (\rho_\phi/\rho)^*} \quad (66)$$

However, in this case the diffusion equation cannot be obtained. To demonstrate, we choose a continuously deformed control surface such that the net mass flux of the time averaged motion is zero. The conservation law would then assume the form

$$\rho \frac{d\rho_\phi/\rho}{dt} = - \text{div} \left\{ n_i \phi_i (\vec{U}) \vec{U} + \vec{u}' \rho_\phi \right\} \quad (67)$$

provided that the divergence operator and all velocity components are expressed in curvilinear coordinates following the time-averaged motion streamlines. Time averaging equation (67) and assuming that  $\rho^+ A_{M\phi}$  is of function of time only leads to the equation

$$\frac{d(\rho_\phi/\rho)^*}{dt} = A_{M\phi} \text{div grad} (\rho_\phi/\rho)^* \quad (68)$$

This is not a diffusion equation since  $A_{M\phi}$  will depend on the space coordinates like  $1/\rho$ . Besides, the system of curvilinear coordinates is not even orthogonal

in shear layers where the stream density  $\rho u$  varies from stream tube to stream tube.

In view of these difficulties, the exchange coefficient  $A_{M\phi}$  is mostly used in Cartesian coordinates, and the spreading angle  $db/dx$ , as well as the exchange coefficients  $A_{M\phi}$ , is obtained by curve-fitting meas-

ured mass fractions  $\rho_\phi^*/\rho$  with the error curve  $e^{-y^2/b^2}$  or the error function. Some examples are given in Figures 2 through 5, showing the velocity and stagnation temperature profiles in the initial and main regions of supersonic jets. However, as soon as the density gradients are appreciable, the diffusion equation is violated, and its general statistical interpretation by the random walk of a single fluid particle does not apply. It seems doubtful that the exchange coefficients  $A_{M\phi}$ , which have been measured in simple flows, are sufficiently general such that they might be extrapolated to more complicated flow fields.

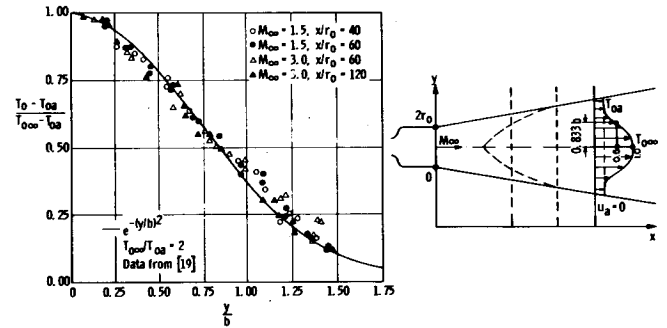


FIGURE 4. STAGNATION TEMPERATURE PROFILES IN THE MAIN REGION OF SUPERSONIC JETS

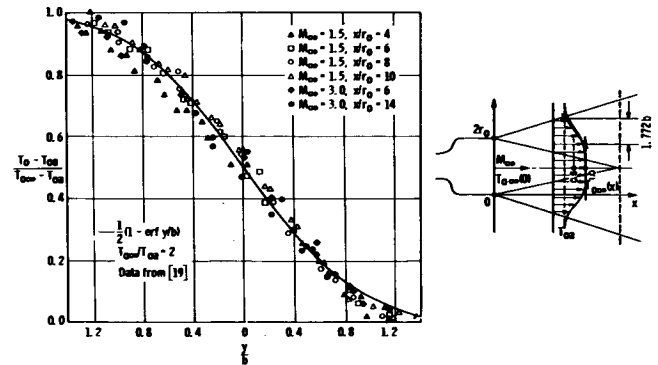


FIGURE 5. STAGNATION TEMPERATURE PROFILES IN THE INITIAL REGION OF SUPERSONIC JETS



A comparison between the exchange coefficients  $A_{M\phi}$  and  $A_{V\phi}$  has been made for the initial region of supersonic jets at constant stagnation temperature. Since both coefficients are supposed to give the same turbulent flux at the streamline, we have the general relation

$$\frac{A_{V\phi}}{A_{M\phi}} = \frac{\rho^* \frac{\partial}{\partial y} \left( \frac{\rho \phi}{\rho} \right)}{\frac{\partial}{\partial y} (\rho^* \phi)} \quad \left| \quad \vec{u} = \vec{u}^* (x, y_0, z_0) \right. \quad (69)$$

In isoenergetic and isobaric flows, densities and velocities are related by

$$\rho(\vec{u}) = \frac{\rho_\infty a_\infty^2}{a_0^2 - \frac{\gamma-1}{2} \vec{u}^2} \quad (70)$$

For shear layers with linearly increasing thickness, this leads to

$$\frac{A_{V\phi}}{A_{M\phi}} = \left( \frac{b_u}{b_{\rho u}} \right)^2 = 1 + \left( \frac{u}{\rho} \frac{d\rho}{du} \right)_{u=u_\infty/2} = 1 + \frac{0.4 M_\infty^2}{1 + 0.15 M_\infty^2} \quad (71)$$

This ratio has been used to convert the spreading rates  $(db/dx)_u$  of measured velocity profiles to the spreading rates  $(db/dx)_{\rho u}$  that would have been measured for stream density profiles. The results are plotted on Figure 6. They indicate that the spreading rates of the volume concentration  $\rho u$  are Mach number independent. Apparently, the use of the incompressible value,  $A_{\rho u}(M_\infty = 0)$  would have been an accurate extrapolation to compressible flows.

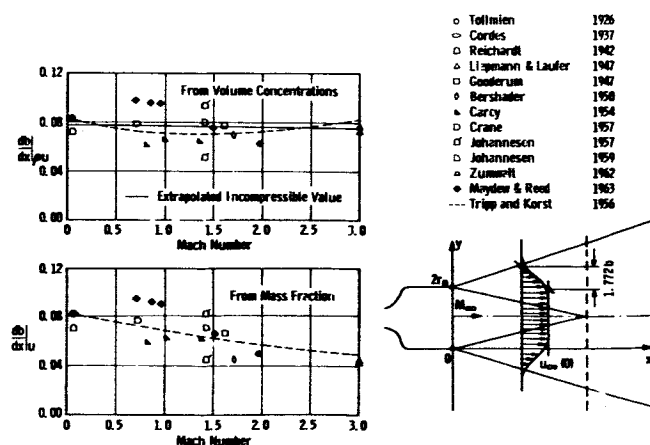


FIGURE 6. THE ROOT MEAN SQUARE SPREAD ANGLE  $db/dx$  IN THE INITIAL PORTION OF SUPERSONIC JETS

## DESIRABLE FLUCTUATION MEASUREMENTS

The estimate of turbulent fluxes from volume concentration profiles and spreading rates has been quite successful in incompressible free shear layers [23] and the above unified treatment indicates that a similar success might be expected in multi-component and hot free shear layers. However, the diffusion equation always predicts self similar profiles and does not account for deviations from similarity. In fact, Batchelor has shown that the moving observer will find uniform exchange coefficients only if self similar profiles do exist. In dissimilar flows, the whole diffusion concept becomes questionable. Furthermore, in regions of intense turbulent mixing, the turbulent fluctuations are no longer small relative to their mean values and the "pattern of turbulence" might decay sufficiently rapid such that the assumption of almost frozen behavior becomes invalid. Therefore, the indirect estimate of turbulent fluxes from measured spreading rates is very questionable in the most interesting regions with high turbulence levels, and direct fluctuation measurements are very desirable.

Experimental evidence suggests that the highest turbulence levels and the highest turbulent fluxes are associated with flow separation [24], reattachment [25] and oscillating shocks [26].

High wall pressure fluctuations in front of a forward-facing step are shown on Figure 7. The static pressure distribution indicates a large dead air region, and the root mean square pressure fluctuations indicate high intensity peaks in the separation and reattachment areas. The peak values are twice as big as those below the recirculated flow and one order of magnitude bigger than those below the attached turbulent boundary layer upstream.

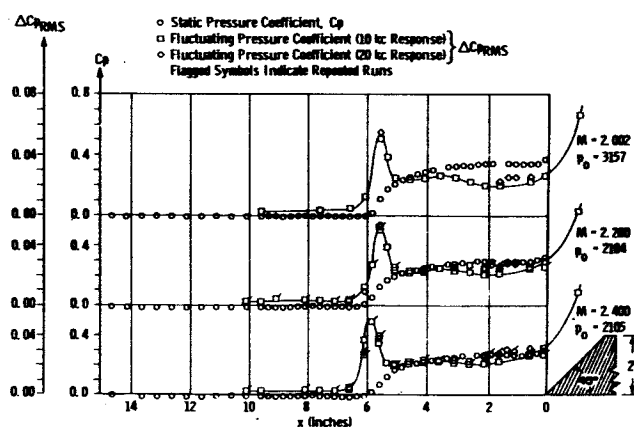


FIGURE 7. FLUCTUATION LEVELS IN SEPARATION AND REATTACHMENT AREAS [25]

High fluxes have been observed in the reattachment zone of turbulent free shear layers. At a free stream Mach number of 3.51 and  $Re/ft = 3 \cdot 10^6$ , a 2.8-inch diameter cylinder swept forward at 45 degrees induced a wake pattern with a closed separation bubble [27]. The highest heat transfer rates were measured at the downstream end of the separation bubble where the flow reattaches. At this point the heat transfer increased to seven times the value that has been measured in absence of the protruding cylinder. This is about three times higher than all heat transfer rates that were measured simultaneously at the rest of flow field where the flow was steady as indicated by a fine structure of the oil flow pattern. Charwart made a similar observation on a rectangular cavity [28]. The flow separated at the upstream edge, and a free shear layer attached at the downstream recompression step of the cavity. Again the highest heat transfer rates were measured in this area. They were about twice as great as those measured in absence of the cavity and about four times greater than the heat transfer at the bottom of the cavity.

Though the above experimental evidence is very limited, some qualitative considerations indicate that it might be of a general nature. Let us consider a turbulent flow where the molecular shear stresses and heat fluxes are negligible relative to their turbulent counterparts. The conservation law of fluid particles, equation (10), then shows that the stagnation enthalpy,

$$h_o = C_p T + \frac{\overline{u^2}}{2} = e + \frac{p}{\rho} + \frac{\overline{u^2}}{2}, \quad (72)$$

will remain constant inside each particle. Therefore, each fluctuation  $(\overline{u^2})'$  of the particle speed is balanced by a correspondent temperature change. Both fluctuations are "in phase"; that is, they are correlated and will produce a heat flux. Furthermore, the temperature fluctuation indicates a related fluctuation of the velocity distribution function, which in turn produces a correlated fluctuation of all other thermodynamic state variables.

Consequently, we get turbulent fluxes that are approximately proportional to the mean square velocity fluctuations, regardless of whether there is a driving gradient or not. In fact, the driving gradients seem to be rather a consequence of the turbulent fluxes and not the cause.

High fluxes are anticipated whenever the mean square velocity is large. The question arises, "Where are the highest velocity fluctuations to be expected?" Obviously not in self similar shear layers since the preservation of profile shapes seems to be a property

of almost frozen flows with relatively small fluctuations. Rather the above experimental evidence leads one to speculate that local regions of high subsonic flow adjacent to a dead air region might produce one of the dominant instabilities. Such flows are produced by certain portions of a supersonic shear layer during a shock-induced separation or during the flow reversal in a reattachment area. Their high instability has been observed again and again during the operation of transonic wind tunnels.

H. F. Vessey offered a simple physical model that did explain the observations [29]. Consider a local velocity decrease adjacent to the porous tunnel wall. In subsonic flows, this produces a pressure rise which will produce a lateral mass flux or outflow in transonic flows. The following fluid particles are expanded; this leads to a further decrease in velocity, thereby amplifying the initial perturbation. In slightly supersonic flows, the subsequent expansion will increase the velocity, thereby stabilizing the original perturbation. Thus, the instabilities are limited to a narrow range of high subsonic local Mach numbers.

There is very little difference between the oscillating outflow across a porous wall and the turbulent mass transport across the time-average position of an interface bounding a dead air region. Therefore, the same mechanism might be responsible for the concentration of high turbulence levels in separation and reattachment areas.

## REFERENCES

1. Trulio, J. G.: The Strip Code and the Jetting of Gas Between Plates, Chap. 3 in Methods in Computational Physics, B. Alder, S. Fernbach, M. Rotenberg, eds., New York, Academic Press, 1964.
2. Batchelor, G. K.: The Theory of Homogeneous Turbulence, students' edition, Cambridge, University Press, 1960.
3. Rotta, J. C.: Turbulent Boundary Layers in Incompressible Flow, Chap. 1 in Progress in Aeronautical Sciences, Vol. 2, A. Ferri, D. Kuchemann, L. H. G. Sterne, eds., New York, Pergamon Press, 1962.
4. Taylor, G. I.: Diffusion by Continuous Movements, Proc. London Math. Soc. Series A, Vol. 20 (1921) pp 196-211.

5. Batchelor, G. K.: Diffusion in Free Turbulent Shear Flows, *Journal of Fluid Mechanics*, Vol. 3 (1957), pp 67-80.
6. Gooderum, P. B., G. P. Wood and M. J. Brevoort: Investigation with an Interferometer of the Turbulent Mixing of a Free Supersonic Jet, NACA Report 963 (1950).
7. Ting, L., P. A. Libby: Remarks on the Eddy Viscosity in Compressible Mixing Flows, *Journal of Aeronautical Sciences*, Vol. 27 (1960), pp 797-798.
8. Tietjens, O., L. Prandtl: Hydro and Aeromechanik, ed. 1, Berlin, Springer, 1929, Vol. 1, Chap. 1.
9. Frenkiel, F. N.: Turbulent Diffusion, Chap. 3 in Advances in Applied Mechanics, Vol. III, von Mises, R., Th. von Karman eds, New York, Academic Press, 1953.
10. Chapman, S., T. G. Cowling: The Mathematical Theorie of Non-Uniform Gases, 2nd ed., Cambridge, The University Press, 1960.
11. Becker, R.: Vorstufe zur theoretischen Physik, Göttingen, Springer, 1950.
12. Becker, R.: Theorie der Wärme, Göttingen, Springer, 1961.
13. Bird, B. R., W. E. Stewart, E. M. Lightfoot: Transport Phenomena, New York, J. Wiley & Sons, 1960.
14. Schlichting, H.: Grenzschicht-Theorie, Karlsruhe, G. Braun, 1951.
15. Fisher, M. J., P. O. A. L. Davies: Correlation Measurements in a Non-Frozen Pattern of Turbulence, *Journal of Fluid Mechanics*, Vol. 18 (1963), pp 97-116.
16. Corcos, G. M.: The Structure of the Turbulent Pressure Field in Boundary Layer Flows, *Journal of Fluid Mechanics*, Vol. 18 (1964).
17. Richtmyer, R. D.: Difference Methods for Initial Value Problems, New York, Wiley, 1957.
18. Trulio, S. G.: Computational Analytical Study of the Shedding of Vortices in the Subsonic Flow Around a Two-Dimensional Rigid Cylinder, Contract NAS8-11400, F. Y. 1964.
19. Abramovich, G. N., The Theory of Turbulent Jets, translated from the Russian, Cambridge, Mass., The MIT Press. 1963.
20. Ellison, T. H.: Atmospheric Turbulence, Chap. 10 in Surveys in Mechanics, G. K. Batchelor and R. M. Davies, eds., Cambridge, The University Press, 1956.
21. Batchelor, G. K., A. A. Townsend: Turbulent Diffusion, Chap. 9 in Surveys in Mechanics, G. K. Batchelor, R. M. Davies, eds., Cambridge, The University Press, 1956.
22. Korst, H. H., R. H. Page, M. E. Childs, Compressible Two-Dimensional Jet Mixing at Constant Pressure, Univ. of Illinois, ME-TN-392-1, OSR-TN-54-82, Contract A. F. 18(6000) 392, Apr. 1954.
23. Reichardt, H., "Gesetzmässigkeiten der freien Turbulenz, Verein deutscher Ingenieure, Forschungsheft 414, 1942.
24. Kistler, A. L.: The Fluctuating Pressure Field in a Supersonic Turbulent Boundary Layer, Fluid Dynamics Panel of AGARD, Rhode St. Genese, Belgium, Apr. 1-5, 1963.
25. Unpublished data from an investigation in progress at Ames Research Center.
26. Krause, F.: Preliminary Results of SA-4 Acoustic Flight Tests, NASA-MSFC Office Memorandum, M-AERO-A-48-63 (1963).
27. Burbank, P. B., Newlander, R. A., Collins, I. K.: Heat Transfer and Pressure Measurements on a Flat Plate Surface and Heat Transfer Measurements on Attached Protuberances on a Supersonic Turbulent Boundary Layer at Mach Numbers of 2.65, 3.51 and 4.44, NACA TN-D-1372 (Dec. 1962).
28. Charwart, A. F., Dewey, C. F., Roos, J. N., Nilt, J. A., An Investigation of Separated Flows - Part II: Flow in the Cavity and Heat Transfer, *Journal of Aerospace Sciences*, Vol. 28 (1961), pp 513-527.
29. Vessey, H. F.: Transonic Wind Tunnel Testing Techniques: Historical and General Introduction, *Journal of Roy. Aeron. Society*, Vol. 62 (1958), pp 1-6.

# ON QUASI-SLENDER BODY THEORY FOR OSCILLATING LOW ASPECT RATIO WINGS AND BODIES OF REVOLUTION IN SUPERSONIC FLOW

by

M. F. Platzer

## SUMMARY

The paper presents a new formulation of quasi-slender body theory for oscillating low aspect ratio wings and bodies of revolution making use of concepts introduced first by K. Oswatitsch and F. Keune to analyze the steady flow field around low aspect ratio wings at zero angle of attack.

It also presents a new elementary approach to quasi-slender body theory for slowly oscillating bodies of revolution showing the interrelationship between the methods of W. H. Dorrance and Adams-Sears.

The range of validity of quasi-slender body theory is examined by comparing it with an exact solution of the linearized unsteady potential equation. Such a solution is found for the infinitely long oscillating cylinder.

## LIST OF SYMBOLS

Symbol	Definition
$a$	$\sqrt{(y-\eta)^2 + z^2}$
$c$	Free stream velocity of sound
$E^{[n]}(x, y, z)$	Sum of source-moments of n-th order over the cross-section
$\hat{E}^{[0]}(x)$	Sum of dipoles over the cross-section
$H_1^{(1)} = J_1 + i Y_1$	Hankel function of first kind and first order
$H_1^{(2)} = J_1 - i Y_1$	Hankel function of second kind and first order
$i$	Imaginary unit
$K_1$	Modified Besselfunction of second kind and first order
$k_{2\nu}$	$\frac{1}{2^{2\nu} (\nu!)^2}$

## Symbol

## Definition

$M$	Free-stream Mach number
$m^{[n]}$	Source-moment of n-th order
$q(\xi, \eta)$	Source Distribution
$\hat{q}(\xi, \eta)$	Dipole Distribution
$s(x)$	Half span of wing
$U$	Free-stream velocity
$x, y, z$	Cartesian coordinates Fig. 1
$x, r, \theta$	Cylindrical coordinates Fig. 2
$\mathcal{Y}(x, \theta)$	Amplitude of oscillation
$\hat{w}(x, y)$	Downwash distribution
$\bar{\alpha}$	$\frac{\omega}{c(M+1)}$
$\alpha'$	$\frac{\omega}{c(1-M)}$
$\alpha''$	$\frac{\omega}{c(M-1)}$
$\cot \alpha$	$\sqrt{M^2 - 1}$
$\beta$	$\sqrt{1 - M^2}$
$\gamma$	Wave-number of oscillation
$\phi(x, y, z)$	Amplitude of pulsating wing potential
$\phi_q(x, y, z)$	Cross-flow potential of pulsating wing
$\phi_R(x, y, z)$	Spatial influence of pulsating wing
$\hat{\phi}(x, y, z)$	Amplitude of oscillating wing potential

# LIST OF SYMBOLS (Cont'd)

Symbol	Definition
$\hat{\phi}_q(x, y, z)$	Cross-flow potential of oscillating wing
$\hat{\phi}_R(x, y, z)$	Spatial influence of oscillating wing
$\kappa$	$\frac{\omega}{c \cot^2 \alpha}$
$\mu$	$\frac{\omega U}{c^2 \cot^2 \alpha}$
$\kappa_{2\nu}$	$= \frac{1}{1} + \frac{1}{2} + \dots + \frac{1}{\nu}$ for $\nu \geq 1$ $= 0$ for $\nu = 0$
$\omega$	Circular frequency
$\xi, \eta$	Dipole coordinates

## I. INTRODUCTION

The problem of steady linearized subsonic, transonic, and supersonic flow over bodies of low aspect ratio at small angle of attack has been treated by M. Munk [1], H. S. Tsien [2], R. T. Jones [3], G. N. Ward [4], M. J. Lighthill [5], and M. C. Adams - W. R. Sears [6]. It is shown in these papers that the disturbance flow pattern of slender bodies can be regarded as incompressible and two-dimensional in planes normal to the main stream. The lift forces then can be obtained by simple momentum considerations (Munk - Jones slender body theory). An extension of these results to not-so-slender bodies was obtained by M. C. Adams - W. R. Sears [6] using Laplace or Fourier transform methods. Subsequently, it was shown by I. E. Garrick [7] and J. W. Miles [8] that the Munk-Jones hypothesis retains considerable usefulness also for harmonically oscillating slender pointed wings and bodies. Thus, the velocity potential of the transverse flow pattern satisfies in both cases, steady and unsteady flow, Laplace's equation in two dimensions. However, for unsteady flow the condition of sufficiently low reduced frequency must be fulfilled in addition to the condition of very low slenderness ratio.

The present investigation is based upon the linearized unsteady potential equation. The time dependence is assumed to be purely harmonic. An approximation theory based upon this equation was first de-

veloped by F. Hjelte [9], M. Landahl [10], G. Zartarian - H. Ashley [11] which extends the range of validity of pure slender body theory. This method generalizes the Adams - Sears theory for steady flow [6] to oscillating flow; i.e., it uses Laplace or Fourier transform methods.

In [12] a general approximation theory for pulsating wings was developed extending F. Keune's and K. Oswatitsch's results for steady flow [13, 14] to this unsteady flow case. It was seen that the leading term of the expanded velocity potential consists of a cross flow and a spatial influence. An equivalence rule was found for configurations having the same total source strength in each cross section. The higher order terms of the expanded velocity potential were also shown to consist of a generalized cross flow and a generalized spatial influence.

This paper shows that this basic buildup of the flow field holds also for oscillating bodies. However, the leading term now is given by a cross flow only, namely, the Munk - Jones potential. The second approximation may be interpreted as consisting of a further cross flow and a spatial influence. Quite analogous to the spatial influence of pulsating low aspect ratio bodies, this part of the flow potential does not depend on the individual dipole distribution, but only on the overall dipole strength in a given cross section.

These general results are further substantiated by developing a particularly simple theory for the case of the slowly oscillating body of revolution which simultaneously shows the interrelationship between the approaches of W. H. Dorrance [15] and Adams-Sears [6].

Finally, this approximation theory is applied to configurations for which exact solutions of the linearized potential equation can be found. These exact solutions are discussed in more detail.

## II. APPROXIMATION THEORY FOR OSCILLATING LOW ASPECT RATIO WINGS AND BODIES OF REVOLUTION IN SUPERSONIC FLOW

The developments of Reference 12 for pulsating wings can be used quite conveniently to formulate an approximation theory also for oscillating flow. Introducing after Keune [14] higher order source moments

$$m^{[n]}(x, y, z, \eta) = q(x, \eta) \cdot a^n = q(x, \eta) [(y-\eta)^2 + z^2]^{\frac{n}{2}} \quad (2.1)$$

and the sum of these source moments over the cross section

$$E^{[n]}(x, y, z) = \int_{-s(x)}^{+s(x)} q(x, \eta) [(y-\eta)^2 + z^2]^{\frac{n}{2}} d\eta, \quad (2.2)$$

it was stated in Reference 12 that each term in the series expansion of the pulsating wing potential consists of a cross flow and a spatial influence. In this expansion

$$\begin{aligned} \varphi(x, y, z) &= \varphi^{[0]}(x, y, z) + \varphi^{[II]}(x, y, z) + \\ &+ \dots \varphi^{[2\nu]}(x, y, z) \dots, \quad \nu = 0, 1, 2 \end{aligned} \quad (2.3)$$

one has

$$\varphi^{[0]}(x, y, z) = \varphi_q^{[0]}(x, y, z) + \varphi_R^{[0]}(x) \quad (2.3a)$$

$$\varphi^{[II]}(x, y, z) = \varphi_q^{[II]}(x, y, z) + \varphi_R^{[II]}(x, y, z) \quad (2.3b)$$

and so on,

where

$$\varphi_q^{[2\nu]}(x, y, z, \eta) = \frac{k_{2\nu}}{2\pi} \left( \cot^2 \alpha \frac{\partial^2}{\partial x^2} + \frac{2i\omega U}{c^2} \frac{\partial}{\partial x} - \frac{\omega^2}{c^2} \right) \int_{-s(x)}^{+s(x)} m^{[2\nu]}(x, y, z, \eta) \ln \sqrt{(y-\eta)^2 + z^2} d\eta \quad (2.3c)$$

and

$$\begin{aligned} \varphi_R^{[2\nu]}(x, y, z) &= \frac{k_{2\nu}}{2\pi} \left( \cot^2 \alpha \frac{\partial^2}{\partial x^2} + \frac{2i\omega U}{c^2} \frac{\partial}{\partial x} - \frac{\omega^2}{c^2} \right) \left( E^{[2\nu]}(x, y, z) \left( \ln \frac{\cot \alpha}{2} - \epsilon_{2\nu} \right) \right. \\ &- \frac{1}{2} \left( \frac{\partial}{\partial x} + \frac{1}{M+1} \right) \int_0^x E^{[2\nu]}(\xi, y, z) e^{-i \frac{\omega(x-\xi)}{c(M+1)}} \ln(x-\xi) d\xi \\ &\left. + \frac{1}{2} \left( \frac{\partial}{\partial x} + \frac{1}{M-1} \right) \int_0^x E^{[2\nu]}(\xi, y, z) e^{-i \frac{\omega(x-\xi)}{c(M-1)}} \ln(x-\xi) d\xi \right) \quad (2.3d) \end{aligned}$$

Considering now a pointed wing oscillating in supersonic flow (Fig. 1), the velocity potential in this case is given by

$$\Phi(x, y, z) = -\frac{1}{4} \frac{\partial}{\partial x} \int_0^x \int_{-s(\xi)}^{+s(\xi)} \frac{\partial \{L(\xi)\} \cos \left[ \frac{\omega}{c} \sqrt{(x-\xi)^2 - \cot^2 \alpha (y-\eta)^2 - \cot^2 \alpha \cdot z^2} \right] e^{-i\mu(x-\xi)} d\eta d\xi \quad (2.4)$$

Therefore,

$$\Phi(x, y) = -\frac{1}{4} \frac{\partial^2}{\partial x^2} \int_0^x \int_{-s(\xi)}^{+s(\xi)} \frac{\partial \{L(\xi)\} \cos \left[ \frac{\omega}{c} \sqrt{(x-\xi)^2 - \cot^2 \alpha (y-\eta)^2 - \cot^2 \alpha \cdot z^2} \right] e^{-i\mu(x-\xi)} d\eta d\xi \quad (2.5)$$

is an integral equation for the velocity potential on the wing surface when the downwash distribution is known or prescribed.

Generally valid exact solutions of this integral equation have not been found. We could try to integrate equation (2.5) numerically, but so far as is known, no such approach has been developed. Instead, only that integral equation which is based on the con-

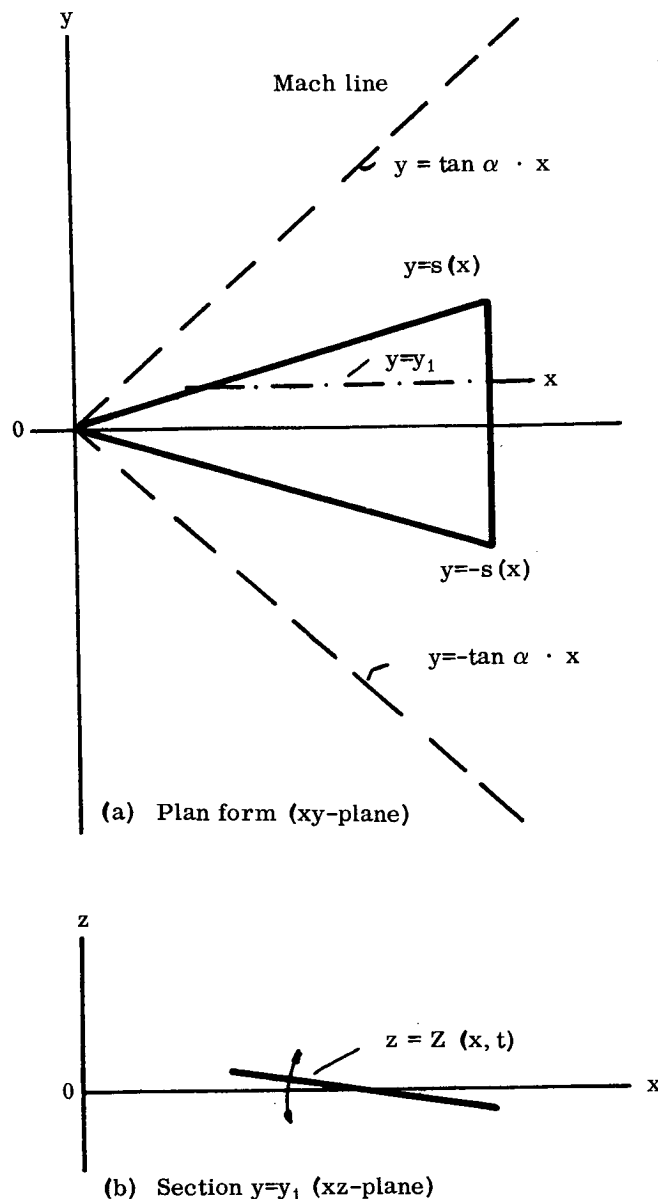


FIGURE 1. OSCILLATING LOW ASPECT RATIO WING

cept of the pressure potential (see C. E. Watkins, Three Dimensional Supersonic Theory, AGARD Manual on Aeroelasticity, Vol. II, p. 31) has been treated numerically.

A decisive simplification of equation (2.4) results only for the case of very low aspect ratio bodies (slender body theory). The assumption of a plane, incompressible cross-flow--originally introduced by Munk [1] and R. T. Jones [3]--holds true also for oscillating flow (Garrick [7], Miles [8]) and leads to a surprisingly simple theory. An appropriate solution of the Laplace equation for the oscillating low aspect ratio wing is

$$\hat{\phi}(x, y, z) = \frac{z}{2\pi} \int_{-s(x)}^{+s(x)} \frac{\hat{q}(x, \eta) d\eta}{(y-\eta)^2 + z^2} + \hat{\phi}_R(x). \quad (2.6)$$

Because of the antisymmetry condition,

$$\hat{\phi}(x, y, z) = -\hat{\phi}(x, y, -z), \quad (2.7)$$

there can be no spatial influence; thus

$$\hat{\phi}_R(x) = 0. \quad (2.8)$$

Similarly, we have for the oscillating body of revolution

$$\hat{\phi}(x, r, \theta) = \frac{\hat{q}(x)}{2\pi r} \cos \theta. \quad (2.9)$$

This slender body theory allows a rapid estimation of the aerodynamic forces on missiles and low aspect ratio wings. Its extension to higher values of aspect ratio and reduced frequency has been achieved by applying the Adams-Sears method to oscillating flow [9, 10, 11]. We will show here another formulation which makes use of the concepts found for pulsating flow and generalizes them to oscillating flow.

Replacing the double integral in equation 2.4 (where the distribution function is now proportional to the velocity potential on the wing surface) by the series expansion equation 2.3 for the pulsating wing and performing the differentiation with respect to  $z$  leads to a similar expansion for the oscillating wing,

$$\hat{\phi}(x, y, z) = \frac{\partial}{\partial z} \left[ \phi^{[0]}(x, y, z) + \phi^{[II]}(x, y, z) + \dots \right] = \phi^{[0]}(x, y, z) + \phi^{[II]}(x, y, z) + \dots \quad (2.10)$$

where the first term

$$\hat{\phi}^{[0]} = \frac{z}{2\pi} \int_{-s(x)}^{+s(x)} \frac{\hat{q}(x, \eta)}{(y-\eta)^2 + z^2} d\eta \quad (2.11)$$

is the well known slender body result (no spatial influence) and the second term

$$\hat{\phi}^{[II]}(x, y, z) = \hat{\phi}^{[II]}(x, y, z) + \hat{\phi}_R^{[II]}(x, y, z) \quad (2.12)$$

$$\hat{\phi}_q^{[II]}(x, y, z) = \frac{z}{8\pi} \left( \cot^2 \alpha \frac{\partial^2}{\partial x^2} + 2 \frac{i\omega U}{c^2} \frac{\partial}{\partial x} - \frac{\omega^2}{c^2} \right) \int_{-s(x)}^{+s(x)} \hat{q}(x, \eta) \left[ 1 + 2 \ln \sqrt{(y-\eta)^2 + z^2} \right] d\eta \quad (2.13)$$

$$\begin{aligned} \hat{\phi}_R^{[II]}(x, y, z) = & \frac{z}{4\pi} \left( \cot^2 \alpha \frac{\partial^2}{\partial x^2} + \frac{2i\omega U}{c^2} \frac{\partial}{\partial x} - \frac{\omega^2}{c^2} \right) \left\{ \hat{E}^{[0]}(x) \left( \ln \frac{\cot \alpha}{2} - 1 \right) \right. \\ & - \frac{1}{2} \left( \frac{\partial}{\partial x} + \frac{i\omega}{M+1} \right) \int_0^x \hat{E}^{[0]}(\xi) e^{-i \frac{\omega(x-\xi)}{c(M+1)}} \ln(x-\xi) d\xi \\ & \left. - \frac{1}{2} \left( \frac{\partial}{\partial x} + \frac{i\omega}{M-1} \right) \int_0^x \hat{E}^{[0]}(\xi) e^{-i \frac{\omega(x-\xi)}{c(M-1)}} \ln(x-\xi) d\xi \right\} \end{aligned} \quad (2.14)$$

consists again of a cross flow  $\hat{\phi}_q^{[II]}(x, y, z)$  and a spatial influence  $\hat{\phi}_R^{[II]}(x, y, z)$ . In equation (2.14)  $\hat{E}^{[0]}(x)$  represents the sum of the dipole elements over the cross section; thus,

$$\hat{E}^{[0]}(x) = \int_{-s(x)}^{+s(x)} \hat{q}(x, \eta) d\eta. \quad (2.15)$$

In a similar way, the following expansion for the oscillating body of revolution is obtained

$$\begin{aligned} \hat{\phi}(x, r, \theta) = & \hat{\phi}_q^{[0]}(x, r, \theta) + \hat{\phi}_q^{[II]}(x, r, \theta) \\ & + \hat{\phi}_R^{[II]}(x, r, \theta), \end{aligned} \quad (2.16)$$

where

$$\hat{\phi}^{[0]}(x, r, \theta) = \frac{\hat{q}(x)}{2\pi r} \cos \theta \quad (2.17)$$

is again the well known slender body result, and the second term reads

$$\hat{\phi}^{[II]}(x, r, \theta) = \hat{\phi}_q^{[II]}(x, r, \theta) + \hat{\phi}_R^{[II]}(x, r, \theta) \quad (2.18)$$

$$\begin{aligned} \hat{\phi}_q^{[II]}(x, r, \theta) = & \frac{r \cos \theta}{8\pi} \left( \cot^2 \alpha \frac{\partial^2}{\partial x^2} + \frac{2i\omega U}{c^2} \frac{\partial}{\partial x} - \frac{\omega^2}{c^2} \right) \hat{q}(x) \left[ 1 + 2 \ln r \right] \\ \hat{\phi}_R^{[II]}(x, r, \theta) = & \frac{r \cos \theta}{4\pi} \left( \cot^2 \alpha \frac{\partial^2}{\partial x^2} + \frac{2i\omega U}{c^2} \frac{\partial}{\partial x} - \frac{\omega^2}{c^2} \right) \left\{ \hat{q}(x) \left( \ln \frac{\cot \alpha}{2} - 1 \right) \right. \\ & - \frac{1}{2} \left( \frac{\partial}{\partial x} + \frac{i\omega}{M+1} \right) \int_0^x \hat{q}(\xi) e^{-i \frac{\omega(x-\xi)}{c(M+1)}} \ln(x-\xi) d\xi \\ & \left. - \frac{1}{2} \left( \frac{\partial}{\partial x} + \frac{i\omega}{M-1} \right) \int_0^x \hat{q}(\xi) e^{-i \frac{\omega(x-\xi)}{c(M-1)}} \ln(x-\xi) d\xi \right\} \end{aligned} \quad (2.19)$$

$$- \frac{1}{2} \left( \frac{\partial}{\partial x} + \frac{i\omega}{M-1} \right) \int_0^x \hat{q}(\xi) e^{-i \frac{\omega(x-\xi)}{c(M-1)}} \ln(x-\xi) d\xi \quad (2.20)$$

The result of equation (2.12) for the oscillating wing has previously been obtained by F. Hjelte [9] using the Adams-Sears procedure [6]. The present formulation shows that the concept of cross flow and spatial influence---originally introduced by K. Oswatitsch [13] -- retains considerable usefulness also for oscillating flow problems. Comparing the spatial influences for the oscillating wing, equation (2.14), and the oscillating body of revolution, equation (2.20), one recognizes that the flow in front of a given cross section approaches that around a body of revolution. The equivalent body of revolution, however, is now defined as that body having the same total dipole strength in all cross sections.

### III. SPECIAL CASE: THE SLOWLY OSCILLATING BODY OF REVOLUTION

The general results of the previous section can be substantiated by developing a particularly simple theory for the case of the slowly oscillating body of revolution which simultaneously shows the interrelationship between the methods of W. H. Dorrance [15] and Adams-Sears [6].

Restricting his analysis to slow oscillations, W. H. Dorrance expands the general velocity potential of the oscillating body of revolution for  $M > 1$ ,

$$\hat{\phi}(x, r, \theta) = -\frac{\cos \theta}{2\pi} \frac{\partial}{\partial r} \int_0^{x-r \cot \alpha} \frac{\hat{q}(\xi) \cos(\xi \sqrt{(x-\xi)^2 - \cot^2 \alpha \cdot r^2})}{\sqrt{(x-\xi)^2 - \cot^2 \alpha \cdot r^2}} e^{-i\mu(x-\xi)} d\xi \quad (3.1)$$

with respect to the frequency, and retains only terms up to the first power of the frequency; thus,

$$\hat{\phi}(x, r, \theta) = \cos \theta \frac{\partial}{\partial r} \left[ -\frac{1}{2\pi} \int_0^{x-r \cot \alpha} \frac{\hat{q}(\xi) [1-i\mu(x-\xi)]}{\sqrt{(x-\xi)^2 - \cot^2 \alpha \cdot r^2}} d\xi \right] \quad (3.2)$$

Zartarian and Ashley [11], on the other hand, arrive at a theory for the oscillating body of revolution by applying Fourier transform methods to the unsteady potential equation.

We will show that the results of Zartarian and Ashley [11] can be obtained from Dorrance's equation (3.2) in a quite elementary way [20]. For this purpose we split equation (3.2) into a stationary part,

$$\hat{\phi}_{\text{Stat.}} = \cos \theta \cdot \frac{\partial}{\partial r} \left[ -\frac{1}{2\pi} \int_0^{x-r \cot \alpha} \frac{\hat{q}(\xi) d\xi}{\sqrt{(x-\xi)^2 - \cot^2 \alpha \cdot r^2}} \right] \quad (3.3)$$

which represents the potential of the pointed body of revolution at angle of attack, and into an unsteady part,

$$\hat{\phi}_{\text{Unst.}} = \cos \theta \frac{\partial}{\partial r} \left[ \frac{1}{2\pi} \int_0^{x-r \cot \alpha} \frac{\hat{q}(\xi) (x-\xi) d\xi}{\sqrt{(x-\xi)^2 - \cot^2 \alpha \cdot r^2}} \right] \quad (3.4)$$

For  $\hat{\phi}_{\text{Stat.}}$  we can immediately make use of F. Keune's expansion for the body of revolution at zero angle of attack [21]. This author shows that the velocity potential can be expanded into

$$\phi_0(x, r) = -\frac{1}{2\pi} \int_0^{x-r \cot \alpha} \frac{\hat{q}(\xi) d\xi}{\sqrt{(x-\xi)^2 - \cot^2 \alpha \cdot r^2}} = \phi_0^{[0]} + \phi_0^{[II]} + \dots \quad (3.5)$$

where

$$\phi_0^{[0]} = \frac{q(x)}{2\pi} \ln r + \frac{q(x)}{2\pi} \ln \cot \alpha - \frac{1}{2\pi} \int_0^x q'(\xi) \ln [2(x-\xi)] d\xi \quad (3.5a)$$

$$\phi_0^{[II]} = \frac{\cot^2 \alpha}{8\pi} r^2 q''(x) [\ln(r \cot \alpha) - 1] - \frac{\cot^2 \alpha}{8\pi} r^2 \frac{\partial^2}{\partial x^2} \int_0^x q'(\xi) \ln [2(x-\xi)] d\xi \quad (3.5b)$$

Inserting this expansion into equation (3.3) and differentiating with respect to  $r$ , we have

$$\hat{\phi}_{\text{Stat.}} = -\frac{\cos \theta}{2\pi r} \hat{q}(x) + \frac{\cos \theta}{4\pi} r \cot^2 \alpha \left[ \hat{q}'(x) \left( \ln \frac{\cot \alpha \cdot r}{2x} - \frac{1}{2} \right) + \int_0^x \frac{\hat{q}''(\xi) (x-\xi) d\xi}{x-\xi} \right] \quad (3.6)$$

For the unsteady part  $\hat{\phi}_{\text{Unst.}}$  we first make use of the relation valid for pointed bodies

$$\frac{\partial}{\partial r} \int_0^{x-r \cot \alpha} \frac{\hat{q}(\xi) (x-\xi) d\xi}{\sqrt{(x-\xi)^2 - \cot^2 \alpha \cdot r^2}} = -\frac{\partial}{\partial x} \int_0^{x-r \cot \alpha} \frac{\hat{q}(\xi) \cot^2 \alpha \cdot r d\xi}{\sqrt{(x-\xi)^2 - \cot^2 \alpha \cdot r^2}} = -\cot^2 \alpha \cdot r \frac{\partial^2}{\partial x^2} \int_0^{x-r \cot \alpha} \frac{\hat{q}(\xi) \cosh^{-1} \frac{x-\xi}{\cot \alpha \cdot r} d\xi} \quad (3.7)$$

This expression can again be approximated for small  $r$  and we obtain for

$$\hat{\phi}_{\text{Unst.}} = \frac{1}{2\pi} \cot^2 \alpha \cdot r \cos \theta \left[ \hat{q}'(x) \ln \frac{\cot \alpha \cdot r}{2} + \int_0^x \frac{\hat{q}''(\xi) (x-\xi) d\xi}{x-\xi} \right] \quad (3.8)$$

Therefore, the velocity potential for the slowly oscillating body of revolution in supersonic flow can be written as

$$\hat{\phi}(x, r, \theta) = \cos \theta \frac{\partial}{\partial r} \left[ -\frac{1}{2\pi} \int_0^{x-r \cot \alpha} \frac{\hat{q}(\xi) (1-i\mu(x-\xi)) d\xi}{\sqrt{(x-\xi)^2 - \cot^2 \alpha \cdot r^2}} \right] - \frac{\cos \theta}{2\pi r} \hat{q}(x) + \frac{\cos \theta}{4\pi} r \cot^2 \alpha \left[ \hat{q}'(x) \left( \ln \frac{\cot \alpha \cdot r}{2x} - \frac{1}{2} \right) + \int_0^x \frac{\hat{q}''(\xi) (x-\xi) d\xi}{x-\xi} \right] + \frac{1}{2\pi} \frac{\partial}{\partial x} \int_0^x \hat{q}'(\xi) \ln \frac{\cot \alpha \cdot r}{2x} d\xi + \int_0^x \frac{\hat{q}''(\xi) (x-\xi) d\xi}{x-\xi} \quad (3.9)$$

Similar results can be obtained for subsonic flow [17]. Using equation (3.4), stability derivatives have been calculated by G. Hoffman (Lockheed Missiles and Space Co., Huntsville, Alabama) for a convex and concave parabolic ogive and a cone. This work shows the dependence of the aerodynamic forces on Mach number, pitch axis location, body shape and thickness ratio [18]. The range of validity of this solution is checked for the steady case by comparing it with J. L. Sims'



linearized angle of attack method of characteristics solution of the full rotational axisymmetric equation of motion [19].

#### IV. COMPARISON WITH EXACT SOLUTIONS

Consider an infinitely long tube which performs a harmonic oscillation in the plane  $\theta = 0$  (compare Fig 2).

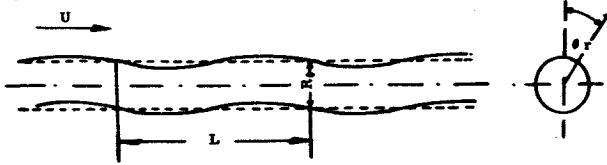


FIGURE 2. INFINITELY LONG OSCILLATING CYLINDER

In cylindrical coordinates, the problem is described by the equation

$$(1-M^2) \hat{\phi}_{xx} + \hat{\phi}_{rr} + \frac{1}{r} \hat{\phi}_r + \frac{1}{r^2} \hat{\phi}_{\theta\theta} - 2 \frac{i\omega M}{c} \hat{\phi}_x + \frac{\omega^2}{c^2} \hat{\phi} = 0 \quad (4.1)$$

and the deflection of the body axis is assumed to be

$$Z(x, \theta) = Z_0 \sin \gamma x \cdot \cos \theta \quad (4.2)$$

In Ref. 12, we found, for the pulsating tube, equation (3.5) as solution to the problem. Therefore, we assume an analogous buildup of the potential function also for the oscillating tube and write

$$\hat{\phi}(x, r, \theta) = \hat{q}_1 e^{i\gamma x} \cos \theta \cdot P_3(r) + \hat{q}_2 e^{-i\gamma x} \cos \theta \cdot P_4(r) \quad (4.3)$$

with  $\hat{q}_1$  and  $\hat{q}_2$  as dipole distributions which are to be determined from the proper boundary condition.

After inserting the potential function equation (4.3) into equation (4.1), we obtain the following solutions:

$$\begin{aligned} P_3(r) &= H_1^{(2)} \left[ r \beta \sqrt{(\bar{\alpha} + \gamma)(\alpha' - \gamma)} \right] \quad \alpha' > \gamma \\ &= K_1 \left[ r \beta \sqrt{(\bar{\alpha} + \gamma)(\gamma - \alpha')} \right] \quad \alpha' < \gamma \\ P_4(r) &= H_1^{(2)} \left[ r \beta \sqrt{(\bar{\alpha} - \gamma)(\alpha' + \gamma)} \right] \quad \bar{\alpha} > \gamma \\ &= K_1 \left[ r \beta \sqrt{(\gamma - \bar{\alpha})(\alpha' + \gamma)} \right] \quad \bar{\alpha} < \gamma \end{aligned} \quad (4.4)$$

and

$$\begin{aligned} P_3(r) &= H_1^{(2)} \left[ r \cot \alpha \sqrt{(\bar{\alpha} + \gamma)(\alpha'' + \gamma)} \right] \\ P_4(r) &= H_1^{(2)} \left[ r \cot \alpha \sqrt{(\bar{\alpha} - \gamma)(\alpha'' - \gamma)} \right] \quad \begin{matrix} \bar{\alpha} > \gamma \\ \alpha'' > \gamma \end{matrix} \\ &= H_1^{(1)} \left[ r \cot \alpha \sqrt{(\gamma - \bar{\alpha})(\gamma - \alpha'')} \right] \quad \begin{matrix} \gamma > \bar{\alpha} \\ \gamma > \alpha \end{matrix} \\ &= K_1 \left[ r \cot \alpha \sqrt{(\gamma - \bar{\alpha})(\alpha'' - \gamma)} \right] \quad \begin{matrix} \gamma > \bar{\alpha} \\ \alpha'' > \gamma \end{matrix} \end{aligned} \quad (4.5)$$

A comparison with the approximation theory as developed in Section 2 is easily achieved by series expansion of the exact solution of equations (4.4) and (4.5).

Expanding the Bessel functions,

$$H_1^{(1)}(u) = -i \frac{2}{\pi u} + \frac{u}{2} + i \frac{2}{\pi} \left[ (C + \ell n \frac{u}{2}) \frac{u}{2} - \frac{u}{4} \right] + \dots \quad (4.6a)$$

$$H_1^{(2)}(u) = i \frac{2}{\pi u} + \frac{u}{2} - i \frac{2}{\pi} \left[ (C + \ell n \frac{u}{2}) \frac{u}{2} - \frac{u}{4} \right] + \dots \quad (4.6b)$$

$$K_1(u) = \frac{1}{u} + \frac{u}{2} (C + \ell n \frac{u}{2}) - \frac{u}{4} + \dots \quad (4.6c)$$

and keeping only the leading term, we obtain the well known slender body result, equation (2.9). Retention of the second order terms in equations (4.6) leads to the quasi-slender body theory equations (2.18) to (2.20) and results in a considerable improvement over slender body theory [16]. A detailed comparative study will be published soon.

Finally, we mention that a further exact solution can be obtained also for the oscillating infinitely long ribbon of constant span because chordwise integration can be performed also in this case which, therefore, leads to a substantially simplified integral equation [16].

#### CONCLUSIONS

A new formulation of quasi-slender body theory for oscillating low aspect ratio wings and slender bodies of revolution is presented. It shows that the "spatial influence" of the wing depends only on the total dipole strength in each cross section, and therefore, reduces this part of the flow field to the flow around its equivalent body of revolution.

In addition, a new elementary approach to quasi-slender body theory for slowly oscillating bodies of revolution is derived which shows at the same time the interrelationship between Dorrance's solution [15] and the extension of the Adams-Sears theory to oscillating bodies [11].

The range of validity of quasi-slender body theory is examined by comparing it with an exact solution of the linearized unsteady potential equation. Such a solution is found for the infinitely long oscillating cylinder.

#### REFERENCES

1. M. M. Munk, The Aerodynamic Forces on Airship Hulls, NACA Report 184, 1923.
2. H. S. Tsien, Supersonic Flow over an Inclined Body of Revolution, J. Aeron. Sci., Vol. V, 1938, p. 430.
3. R. T. Jones, Properties of Low Aspect Ratio Pointed Wings at Speeds below and above the Speed of Sound, NACA Report 835, 1946.
4. G. N. Ward, Supersonic Flow past Slender Pointed Bodies, Quart. J. Mech. Appl. Math., Vol. 2, p. 75-97, 1949.
5. Lighthill, M. J. Supersonic Flow Past Slender Pointed Bodies of Revolution at Yaw. Quarterly Journal Mechanics and Applied Mathematics 1, p. 76, 1948.
6. M. C. Adams, W. R. Sears, Slender Body Theory, Review and Extension, J. Aeron. Sci., Vol. 20, 1953, pp. 85-98.
7. I. E. Garrick, Some Research on High Speed Flutter, 3rd Anglo-American Aeron. Conference, 1951, p. 419.
8. J. W. Miles, On Nonsteady Motion of Slender Bodies, Aeron, Quart. Vol V, Nov. 1950, pp. 183-194.
9. F. Hjelte, Methods for Calculating Pressure Distributions on Oscillating Wings of Delta Type at Supersonic and Transonic Speeds, KTH Aero TN 39, Stockholm 1956.
10. M. T. Landahl, The Flow around Oscillating Low Aspect Ratio Wings at Transonic Speeds, KTH Aero TN 40, Stockholm 1954.
11. G. Zartarian, H. Ashley, Forces and Moments on Oscillating Slender Wing-Body Combinations at Supersonic Speed, AFOSR TN 57-386, 1959.
12. M. F. Platzer, On an Extension of Oswatitsch's Equivalence Rule to Unsteady Flow, Semi-annual Research Review, NASA TMX-53189, Oct. 1964.
13. F. Keune, K. Oswatitsch, Nicht Angestellte Körper kleiner Spannweite in Unter- und Überschallströmung, Z. F. Flugwiss, Vol. I, Nov. 1953, pp. 85-98.
14. F. Keune, Strömung an Körpern nicht mehr kleiner Streckung in auftriebsloser linearer Unter- und Überschallströmung, WGL Jahrbuch 1957, p. 67-82.
15. W. H. Dorrance, Nonsteady Supersonic Flow, J. Aeron, Sci. 18 [1951], p. 501-511.
16. M. Platzer, Doctoral Dissertation, Vienna Institute of Technology, February 1964.
17. M. F. Platzer, unpublished.
18. M. F. Platzer, G. Hoffman, J. L. Sims, to be published.
19. J. L. Sims, unpublished.
20. M. F. Platzer, A Note on the Solution for the Slowly Oscillating Body of Revolution in Supersonic Flow, MTP-AERO-63-28, April 23, 1963.
21. F. Keune, Reihenentwicklung des Geschwindigkeitspotentials der linearen Unter- und Überschallströmung für Körper nicht mehr kleiner Streckung, Z. F. Flugwiss. 5 (1957) p. 243-247.

## II. COMMUNICATION THEORY

38330  
5555  
N 66

# A NEW PERFORMANCE CRITERION FOR LINEAR FILTERS WITH RANDOM INPUTS

by

Mario H. Rheinfurth

## SUMMARY

The paper introduces a new performance criterion for linear statistical filters. Because of its physical significance, the new performance criterion represents a welcome complement to Wiener's performance criterion, and provides for greater flexibility in the design of optimal filters. Application to several typical filter problems reveals its remarkable mathematical simplicity promoting an intuitive physical understanding of its essential features. Another important advantage of the new performance criterion is its applicability to problems involving periodic signals, which affords an interesting comparison with other available filter techniques. The full potential and limitations of the new performance criterion, however, can only be judiciously assessed by further extensive studies that are presently going on.

## I. INTRODUCTION

The development of the classical communication theory is characterized by two basic concepts. One is the description of signals as deterministic functions using Fourier series or Fourier integrals, the other their distortion-free transmission. The latter is supposed to be accomplished by the ideal filter, which avoids any amplitude or phase distortion of the signal (Ref. 1). It is, however, evident that these concepts can only represent idealizations of the real situation encountered in praxis and that they would have to be supplemented or discarded in the further development of the communication theory. This is exemplified in the fundamental paper of N. Wiener (Ref. 2), which introduces new concepts and ideas leading to a new formulation of the basic problem of communication theory.

Recognizing the fact that, as a rule, the transmitted signals are not prescribed functions of time but exhibit random features, we consequently regard them as stochastic processes characterized by adequate statistical quantities. A particularly useful statistical description of these random processes is afforded by the correlation functions and their equivalent spectra. In addition, the principle of distortion-free transmission was replaced by the more realistic

requirement of transmitting the signal with "smallest possible error" or optimal. A precise definition of this new concept is given by a judiciously chosen performance criterion. Since its introduction by C. F. Gauss, the "method of least squares" has proven to be a very effective concept in many areas of the natural sciences. It is therefore not surprising that this criterion played also a central role in the development of modern statistical filter theory and was used by N. Wiener as a criterion for the "quality" of reproducing a message. Intuitively, this criterion avoids the occurrence of strong deviations from the useful signal. Its mathematical advantage becomes apparent in the statistical treatment of the signals, where its application results in mathematical relations containing only correlation functions of second order. Despite these obvious advantages, it is well known that in certain practical situations the mean-square error criterion exhibits deficiencies. Therefore, the question arises quite often whether or not other performance criteria, which avoid these deficiencies, could be introduced. Searching for such a new performance criterion, we must focus attention not only on the physical significance but also on mathematical simplicity in the theory development.

This paper establishes such a new performance criterion and discusses its similarities and differences with respect to the mean-square error criterion. To do this, some new concepts are needed, which are introduced and defined in the following section.

## II. THE DESCRIPTION OF RANDOM PROCESSES

### (1) Correlation Functions

A random process is defined as an ensemble of time functions of infinite duration, whose properties can be characterized only by statistical concepts.

Particularly important statistical characteristics of these random processes are the correlation functions that represent generalizations of the correlation coefficients widely employed in elementary statistics.

In the subsequent analysis, the autocorrelation function shall be defined as the ensemble average

$$\Gamma_{xx}(t, \tau) = \lim_{N \rightarrow \infty} \frac{1}{N} \sum_{k=1}^N x_k(t) x_k(t + \tau) \quad (2.1)$$

$$= \langle x_k(t) x_k(t + \tau) \rangle,$$

and the cross-correlation function as the ensemble average

$$\Gamma_{xy}(t, \tau) = \lim_{N \rightarrow \infty} \frac{1}{N} \sum_{k=1}^N x_k(t) y_k(t + \tau) \quad (2.2)$$

$$= \langle x_k(t) y_k(t + \tau) \rangle,$$

where  $x_k(t)$  and  $y_k(t)$  represent member functions of two different ensembles of random time functions. These correlation functions are, in general, functions of two independent variables  $(t, \tau)$ , where  $t$  shall be referred to as reference time and  $\tau$  as correlation time.

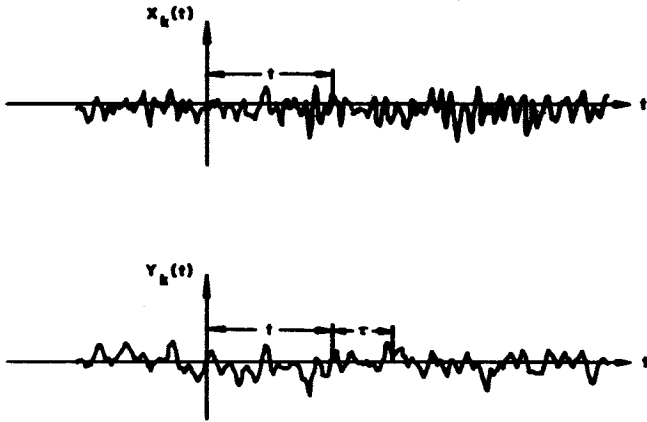


FIGURE 1. DEFINITION OF CORRELATION FUNCTIONS

For certain random processes, we find that their correlation functions become independent of the reference  $t$ ; in other words, they are invariant with respect to time translations such that

$$\Gamma_{xx}(t + t_0, \tau + t_0) = \Gamma_{xx}(t, \tau) \quad (2.3)$$

$$\Gamma_{xy}(t + t_0, \tau + t_0) = \Gamma_{xy}(t, \tau). \quad (2.4)$$

These processes are called stationary. Because their correlation functions depend only on the correlation time  $\tau$ , we may write

$$\Gamma_{xx}(t, \tau) = K_{xx}(\tau) \quad (2.5)$$

$$\Gamma_{xy}(t, \tau) = K_{xy}(\tau) \quad (2.6)$$

for stationary processes.

Stationary processes often exhibit the further property that their ensemble averages taken over a large number of member functions are identical with their corresponding time averages on a single member function; i. e.,

$$K_{xx}(\tau) = \lim_{T \rightarrow \infty} \frac{1}{2T} \int_{-T}^T x_k(t) x_k(t + \tau) dt = R_{xx}(\tau) \quad (2.7)$$

$$K_{xy}(\tau) = \lim_{T \rightarrow \infty} \frac{1}{2T} \int_{-T}^T x_k(t) y_k(t + \tau) dt = R_{xy}(\tau). \quad (2.8)$$

These processes are called ergodic. The question of whether or not a random process is ergodic cannot be answered for most practical cases, because the number of member functions is usually very limited. However, the recorded time of observation is often sufficiently long to obtain a satisfactory time average. Therefore, it is common practice to assume ergodicity of the random process and to replace ensemble averages by time averages wherever they occur in the analysis.

The following analysis exclusively uses correlation functions based on ensemble averages. This affords the possibility of analyzing nonstationary processes and avoids the restriction to ergodic processes.

Several important properties of stationary autocorrelation functions can be directly derived from their definition equations (2.1) and (2.2):

$$K_{xx}(\tau) = K_{xx}(-\tau) \quad (2.9)$$

$$K_{xy}(\tau) = K_{yx}(-\tau). \quad (2.10)$$

The autocorrelation function of a stationary random process is therefore an even function, whereas the cross-correlation function is, in general, neither even nor odd.

Other properties of stationary correlation functions of interest involve their derivatives:

$$\frac{d}{dt} K_{xy}(\tau) = K'_{xy}(\tau) = K_{xy}(\tau) \quad (2.11)$$

$$\frac{d^2}{dt^2} K_{xy}(\tau) = K''_{xy}(\tau) = -K_{xy}(\tau), \quad (2.12)$$

where the dot represents the time derivative of the random time functions. It is worth mentioning that the concept of correlation functions can also be applied to deterministic functions. The subsequent investigation will, however, be restricted to random time functions. They shall also be free from dc or ac components. Intuitively, the correlation functions of these

random processes approach zero as the correlation time  $\tau$  goes to infinity.

## (2) Power Spectra

It is known that problems that present complicated relations in the time domain can often be greatly simplified by a linear integral transformation into the frequency domain. In this connection we recall the powerful usage of the Laplace transform in linear network analysis. Similar simplifications are obtained by a proper transformation of the correlation functions introduced above from the time domain into the frequency domain.

Because the correlation functions of random processes vanish as the argument tends to infinity (dc and periodic components excluded), they are absolutely integrable; i.e.,

$$\int_{-\infty}^{\infty} |\Gamma(t, \tau)| d\tau < \infty. \quad (2.13)$$

As a consequence, it is possible to apply a Fourier transformation to the correlation functions. This frequency domain approach, however, is only advantageous for stationary processes. The value of extending this concept to nonstationary random processes similar to the equivalent description of linear time-varying systems is very doubtful. In the sequel the Fourier transformation will, therefore, be applied only to stationary correlation functions.

The Fourier transforms of the stationary auto- and cross-correlation function are known as power and cross-power spectrum, respectively. They are given by

$$S_{XX}(j\omega) = \int_{-\infty}^{\infty} K_{XX}(\tau) e^{-j\omega\tau} d\tau \quad (2.14)$$

$$S_{XY}(j\omega) = \int_{-\infty}^{\infty} K_{XY}(\tau) e^{-j\omega\tau} d\tau. \quad (2.15)$$

Because the auto-correlation function is an even function, the power spectrum is a real function of  $\omega$ . In addition, it can be shown that the power spectrum assumes only positive values. The cross-power spectrum is, in general, complex. The physical significance of both concepts will not be discussed in this paper.

The inversion integrals corresponding to the definition integrals (2.14) and (2.15) are

$$K_{XX}(\tau) = \frac{1}{2\pi} \int_{-\infty}^{\infty} S_{XX}(j\omega) e^{j\omega\tau} d\omega \quad (2.16)$$

$$K_{XY}(\tau) = \frac{1}{2\pi} \int_{-\infty}^{\infty} S_{XY}(j\omega) e^{j\omega\tau} d\omega. \quad (2.17)$$

## (3) Summation of Power Spectra

Contrary to the factorization of rational spectra in the conventional statistical filter theory, it will be necessary in the sequel to decompose the power spectra into the sum of two one-sided functions. To this effect we write the cross-power spectrum in the form

$$S_{XY}(j\omega) = \int_{-\infty}^0 K_{XY}(\tau) e^{-j\omega\tau} d\tau + \int_0^{\infty} K_{XY}(\tau) e^{-j\omega\tau} d\tau. \quad (2.18)$$

Replacing the correlation time  $\tau$  to  $-\tau$  in the first integral yields

$$S_{XY}(j\omega) = \int_0^{\infty} K_{XY}(-\tau) e^{j\omega\tau} d\tau + \int_0^{\infty} K_{XY}(\tau) e^{-j\omega\tau} d\tau. \quad (2.19)$$

Using the relation (2.10) results in

$$S_{XY}(j\omega) = \int_0^{\infty} K_{YX}(\tau) e^{j\omega\tau} d\tau + \int_0^{\infty} K_{XY}(\tau) e^{-j\omega\tau} d\tau. \quad (2.20)$$

If we introduce, in addition,

$$\begin{matrix} (+) & (-) \\ K_{XY}(\tau) = K_{XY}(\tau) + K_{XY}(\tau), \end{matrix} \quad (2.21)$$

where

$$\begin{matrix} (+) \\ K_{XY}(\tau) = \begin{cases} K_{XY}(\tau) & \text{for } 0 \leq \tau < \infty \\ 0 & \text{for } -\infty < \tau < 0 \end{cases} \end{matrix} \quad (2.22)$$

and

$$\begin{matrix} (-) \\ K_{XY}(\tau) = \begin{cases} 0 & \text{for } 0 \leq \tau < \infty \\ K_{XY}(\tau) & \text{for } -\infty < \tau < 0 \end{cases} \end{matrix} \quad (2.23)$$

we obtain with the introduction of the Fourier transform

$$N_{XY}(j\omega) = \int_{-\infty}^{\infty} K_{XY}^{(+)}(\tau) e^{-j\omega\tau} d\tau, \quad (2.24)$$

the expression (2.20) in the form

$$S_{xy}(j\omega) = N_{xy}(j\omega) + N_{yx}^*(j\omega). \quad (2.25)$$

The asterisk denotes the conjugate complex function.

The new auxiliary functions  $N_{xx}(j\omega)$  and  $N_{xy}(j\omega)$  will be called auto- and cross-correlation spectra, respectively. Representing Fourier transforms of time functions that vanish for negative arguments, their poles are confined to the upper half-plane of the complex frequency plane  $\omega$ . Since the power spectrum itself is non-negative, it follows, in addition, that the real part of the auto-correlation spectrum is

$$\operatorname{Re} \{N_{xx}(j\omega)\} = \frac{1}{2} S_{xx}(j\omega) \geq 0 \quad (2.26)$$

for all  $\omega$ . The auto-correlation spectrum is, therefore, a positive real function (Ref. 4). As a consequence, its zeroes, as well as its poles, are all lying in the upper half-plane of the complex frequency plane. This fact will prove to be of decisive importance in the subsequent investigation of the realizability of the statistical filter optimized with respect to the new performance criterion.

### III. THE DESCRIPTION OF LINEAR SYSTEMS

The input-output relation of a time-varying linear system can be derived by using the principle of superposition. Accordingly, the input  $\varphi(t)$  will be represented as a succession of impulses of magnitude  $\varphi(\tau) d\tau$  (Fig. 2).

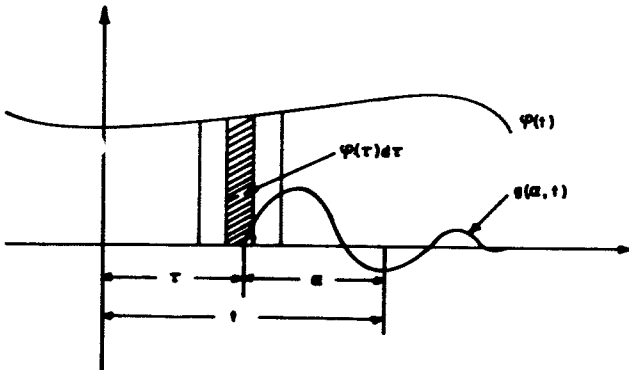


FIGURE 2. SUPERPOSITION INTEGRAL

The function  $g(\alpha, t)$  represents the output of the system at the observation time  $t$  to a unit impulse excitation applied at the earlier time  $\tau = t - \alpha$ . The variable  $\tau$  denotes, physically speaking, the excitation time; the variable  $\alpha$  denotes the "age" of the function  $g(\alpha, t)$ . This function is called the unit-impulse

response (weighting function) of the system. The total output  $x(t)$  is now obtained by summing up the responses of the system to all impulses of magnitude  $\varphi(\tau) d\tau$  during the time of observation and adding the effect of the initial state of the system. This is mathematically expressed as

$$x(t) = \int_0^t g(\tau, t) \varphi(\tau) d\tau + \sum_i a_i(0) \phi_i(0, t). \quad (3.1)$$

A characteristic feature of this relation is that it decomposes the total output of the system in two parts, the first part representing the zero-state response of the system to  $\varphi(t)$ , the second part the zero-input response starting in an initial state characterized by the coefficients  $a_i$ . This is the well-known decomposition property of linear systems. The functions  $\phi_i(0, t)$  depend on the parameters of the system. For stable systems, they tend to zero as time passes, reflecting the finite memory of a physical system.

The input-output relation as given in Equation (3.1) can be put in a more familiar form by setting  $\tau = t - \alpha$ , which yields

$$x(t) = \int_0^t g(\alpha, t) \varphi(t - \alpha) d\alpha + \sum_i a_i(0) \phi_i(0, t). \quad (3.2)$$

The influence of the initial conditions can be eliminated if the effect of the input impulses is summed over an infinite time segment, i.e., from  $\tau = -\infty$  to  $\tau = t$ .

This results in

$$x(t) = \int_0^\infty g(\alpha, t) \varphi(t - \alpha) d\alpha. \quad (3.3)$$

As is seen from Equation (3.1), the unit-impulse response  $g(\alpha, t)$  completely characterizes the zero-state response of a linear system. For a completely controllable and observable system, it gives also complete information regarding its zero-input response. Keeping this restriction in mind, we can specify a linear system by its unit-impulse response. A transformation of this function into the frequency domain is again advantageous only for time-invariant systems. In this case the unit-impulse response depends only on the "age"  $\alpha$ . For stable systems the unit-impulse response is absolutely integrable such that

$$\int_0^\infty |g(t)| dt < \infty. \quad (3.4)$$

Its Fourier transform is given by

$$F(j\omega) = \int_{-\infty}^{\infty} g(t) e^{-j\omega t} dt \quad (3.5)$$

and defines the transfer function of a system. Because each physical system is nonanticipative, i. e.,  $g(t) = 0$  for  $t < 0$ , the transfer function has only poles in the upper half-plane of the complex frequency plane  $\omega$ . This condition is known as the realizability condition of a system. Physically speaking, it means that a system cannot respond earlier than the cause arrives.

#### IV. OPTIMUM LINEAR FILTERS

##### (1) Statement of Problem

The basic problem of filter theory consists in extracting a message that is contaminated by noise. The process of filtering necessarily results in amplitude and phase distortions of the useful signal, which must be kept as small as possible. Depending on the application of the filter to be designed, both types of distortions affect the quality of the message in relatively different magnitude. It is therefore necessary to find an appropriate compromise between these distortions. If the filter is to be used in voice transmission, the phase distortion is not very critical because the human ear has a rather poor phase discrimination. For the transmission of video signals, the situation is just reversed; i. e., the quality of the picture is much more sensitive to phase distortions than to amplitude distortions. In general, however, it is necessary to consider both distortions as equally important and adapt them to the special requirements of the filter problem. The modern statistical filter theory does this by selecting a proper performance criterion. Most of them are based on the idea of minimizing the average value of a positive function of the error, which is defined as

$$\epsilon(t) = x(t) - d(t),$$

where  $x(t)$  denotes the actual output of the filter and  $d(t)$  the desired message. The choice of a positive function of the error avoids the cancellation of individual positive or negative deviations from the true value which would, of course, not show up in the final error of the message. There are, however, a multitude of other performance criteria, whose detailed discussion would be beyond the scope of the present paper. A system that satisfies a performance criterion is said to be optimal with respect to the performance criterion under consideration.

##### (2) Mean-square Error Criterion

The best known performance criterion is the mean-square error criterion. It is relatively mathematically simple and physically logical, because it tries to prohibit the occurrence of large errors. The undesirability of an error, however, increases quadratically with its magnitude, which can result in an unduly heavy penalty of large errors. As a consequence, it may happen that systems that are optimized with respect to the mean-square error criterion are relatively insensitive for small errors. In cases where small errors are just as undesirable as large ones, it may be desirable to resort to another performance criterion. Thus, the mean-square error criterion, like all other performance criteria, is by no means universal. Applied to statistical filter problems, it has, however, proven to afford a rather adequate compromise between amplitude and phase distortion of the useful signal. This is one of its main advantages over other performance criteria employed in designing filters.

The purpose of the subsequent section is to analyze the mean-square error criterion in some detail to assess its effectiveness and limitations. The knowledge gained in this investigation shall then be used to derive a new performance criterion that satisfies the basic postulates of physical reality and mathematical simplicity. Let us determine a linear system which minimizes the mean-square of the ensemble average

$$\langle \epsilon_k^2(t) \rangle = \langle [x_k(t) - d_k(t)]^2 \rangle \quad (4.2)$$

for each time point after starting the system assuming zero initial conditions.

Following the statistical approach to the filter problem, message and noise are treated as random processes whose correlation functions are assumed to be known in advance. The input should be composed of the sum of message  $m(t)$  and noise  $n(t)$  such that

$$\phi(t) = m(t) + n(t) \quad (4.3)$$

The desired output  $d(t)$  is allowed to be the result of a physically realizable operation on the message in the form

$$d(t) = O_p \{ m(t) \} \quad (4.4)$$

where  $O_p$  designates the operator on the message.

Physically realizable operators are those that depend only on the past. We restrict the analysis to the sub-



class of linear operators that are invariant with respect to time translations. Using the superposition integral (3.2) and the fact that the averaging operators commute with the integral operator, we can bring the expression (4.2) in the form

$$\begin{aligned} \langle \epsilon_k^2(t) \rangle &= \langle x_k^2(t) - 2 \langle x_k(t) d_k(t) \rangle + \langle d_k^2(t) \rangle \\ &= \int_0^t g(\alpha, t) \langle \varphi_k(t-\alpha) x_k(t) \rangle d\alpha \\ &\quad - 2 \int_0^t g(\alpha, t) \langle \varphi_k(t-\alpha) d_k(t) \rangle d\alpha + \langle d_k^2(t) \rangle. \end{aligned} \quad (4.5)$$

Introducing the appropriate correlation functions yields

$$\begin{aligned} \langle \epsilon_k^2(t) \rangle &= \int_0^t g(\alpha, t) \Gamma_{\varphi x}(t-\alpha, \alpha) d\alpha \\ &\quad - 2 \int_0^t g(\alpha, t) \Gamma_{\varphi d}(t-\alpha, \alpha) d\alpha + \Gamma_{dd}(t, 0). \end{aligned} \quad (4.6)$$

The problem consists now of finding a unit-impulse response  $g(\alpha, t)$  for which the ensemble average of the squared error becomes a minimum. This problem can be solved by the well known rules of the calculus of variations. However, the final result shall here be derived from a purely statistical consideration. Because message and noise are only known in the form of statistical quantities, it is principally impossible to completely recover the desired message at the output terminal of the filter. We can, however, require that the statistical properties of the output  $x(t)$  be the same as the desired message  $d(t)$ . If the well known method of extracting a signal by cross correlation with the desired message is recalled, the thought comes to mind to require the cross correlation of the output  $x(t)$  with the input signal  $\varphi(t)$  to be identical with that of the desired message  $d(t)$  itself. By virtue of the causality principle, care has to be taken that the output  $x(t)$  is only correlated with input values of an earlier time segment. This complies with the realizability condition of physical systems. The optimal correlation shall, furthermore, be enforced for all time segments within the operating time of the system. The mathematical formulation of this statistical relation yields

$$\Gamma_{\varphi x}(t-\tau, \tau) = \Gamma_{\varphi d}(t-\tau, \tau). \quad 0 \leq \tau \leq t \quad (4.7)$$

It is indeed surprising and worth noticing that this optimum condition, which was obtained by a pure statistical consideration, is equivalent with the postulate of minimizing the mean-square error. This can be directly deduced with the well known input-output cross correlation theorem for linear systems, which

reads

$$\begin{aligned} \Gamma_{\varphi x}(t-\tau, \tau) &= \langle \varphi_k(t-\tau) x_k(t) \rangle \\ &= \int_0^t g(\alpha, t) \langle \varphi_k(t-\tau) \varphi_k(t-\alpha) \rangle d\alpha, \end{aligned} \quad (4.8)$$

and, after introducing the autocorrelation function of the input signal,

$$\Gamma_{\varphi x}(t-\tau, \tau) = \int_0^t g(\alpha, t) \Gamma_{\varphi\varphi}(t-\tau, \tau-\alpha) d\alpha. \quad (4.9)$$

Inserting this equation in the optimal condition (4.7) results in the integral equation for the optimum filter in the form

$$\Gamma_{\varphi d}(t-\tau, \tau) = \int_0^t g(\alpha, t) \Gamma_{\varphi\varphi}(t-\tau, \tau-\alpha) d\alpha. \quad 0 \leq \tau \leq t. \quad (4.10)$$

This integral equation, however, is identical with that of Shinbrot (Ref. 5), which was derived using the mean-square error criterion and applying the conventional methods of the calculus of variations. This confirms the above assertion.

The minimum mean-square error pertaining to (4.10) follows from (4.6) as

$$\langle \epsilon_k^2(t) \rangle_{\text{Min}} = \Gamma_{dd}(t, 0) - \int_0^t g(\alpha, t) \Gamma_{\varphi d}(t-\alpha, \alpha) d\alpha. \quad (4.11)$$

Extending the operating time in equation (4.10) to infinity yields the special case of Booton (Ref. 6):

$$\Gamma_{\varphi d}(t-\tau, \tau) = \int_0^\infty g(\alpha, t) \Gamma_{\varphi\varphi}(t-\tau, \tau-\alpha) d\alpha. \quad 0 \leq \tau < \infty. \quad (4.12)$$

Restricting the analysis to time-invariant systems and stationary random processes finally reduces the integral Equation (4.10) to

$$K_{\varphi d}(\tau) = \int_0^\infty g(\alpha) K_{\varphi\varphi}(\tau-\alpha) d\alpha. \quad \tau \geq 0. \quad (4.13)$$

This is the celebrated Wiener-Hopf integral equation (Ref. 2).

Equation (4.11) shows that the last two special cases minimize the mean-square error only after all transients have subsided.

The above derived integral equations remain to be investigated with respect to existence, uniqueness, and stability of their solution. In most practical situations, these questions have a relatively simple answer by pure physical considerations. A closed-form solution of these integral equations -- even for the Wiener-Hopf type -- is possible only in some simple cases. In general, the solution must be obtained by numerical methods. Although these do not represent major difficulties, they mostly involve rather extensive computational efforts. A disadvantage of this situation is that it is very difficult to interpret numerical results physically or deduce general statements that could afford a deeper insight into the basic features of the filtering process.

## V. CROSS-CORRELATION CRITERION

### (1) Optimum Transfer Function

With the knowledge gained in the preceding section, we now turn our attention to finding a new performance criterion for solving statistical filter problems. To keep the mathematical formalism simple, we restrict the analysis in the sequel to time-invariant systems and stationary random processes. The new performance criterion to be established can, however, easily be extended to the general case of time-varying systems and instationary random processes. The advantage of mathematical simplicity over other existing performance criterion is then essentially lost, because these cases can in practice only be solved by numerical methods.

We bring back in attention the filter which is optimum with respect to the stationary mean-square error criterion (Wiener criterion). This optimum filter (Wiener filter) is uniquely determined by the integral equation

$$K_{\varphi d}(\tau) = \int_0^{\infty} g(\alpha) K_{\varphi \varphi}(\tau - \alpha) d\alpha, \quad \tau \geq 0. \quad (5.1)$$

Comparing the right-hand side of this equation with equation (4.10), we see that the Wiener filter represents the limiting case of the general statistical optimum condition (4.7) for  $t = \infty$ ; i.e.,

$$\Gamma_{\varphi x}(\infty, \tau) = K_{\varphi d}(\tau), \quad \tau \geq 0. \quad (5.2)$$

Restricting the analysis to time-invariant systems, the output  $x(t)$  assumes stationary character after the transients disappear. The instationary cross-correlation function in Equation (5.2) can therefore be replaced by its corresponding stationary correlation function. This results in the well known relation of the Wiener filter theory:

$$K_{\varphi x}(\tau) = K_{\varphi d}(\tau), \quad \tau \geq 0. \quad (5.3)$$

From this it follows that the optimum correlation between output and input of the Wiener filter is attained only after all transients have subsided. This explains the known fact that the Wiener filter, in general, exhibits poor transient behavior (e.g., poor relative stability). To improve this situation, the statistical optimum condition (4.7) shows that it is possible to obtain the optimum correlation immediately after starting the system by setting  $t = \tau$ . This yields the second limiting case:

$$\Gamma_{\varphi x}(0, \tau) = K_{\varphi d}(\tau), \quad \tau > 0 \quad (5.4)$$

Statistically speaking, the relations established in equations (5.2) and (5.4) are equally meaningful and informative. Thus, it seems justified to introduce the relation (5.4) as a new performance criterion for the statistical treatment of filter problems. In the sequel, this performance criterion will be called cross-correlation criterion. A common feature of this new criterion and the Wiener criterion is that they represent limiting cases of the general statistical optimum condition (4.7). As a consequence, they do not achieve the optimum cross correlation between output and input of the filter for all correlation times within the operating time interval. They supplement each other, however, insofar as the Wiener criterion emphasizes the behavior of the filter for the stationary condition, whereas the cross-correlation criterion tries to optimize the transient behavior. Furthermore, it is to be expected that the cross-correlation criterion, by virtue of its well-defined reference time, exhibits a rather strong sensitivity with respect to phase differences. Main applications of the new criterion are, therefore, envisioned in phase-sensitive servosystems and systems where the transient response is the only acceptable measure of system performance.

The new performance criterion can also be represented in the integral form

$$I = \int_0^{\infty} [\Gamma_{\varphi x}(0, \tau) - K_{\varphi d}(\tau)]^2 d\tau. \quad (5.5)$$

Thus, it appears as a modification of the minimum-square-cross-correlation-error criterion introduced by Y. W. Lee (Ref. 7):

$$I_L = \int_{-\infty}^{\infty} [K_{\varphi x}(\tau) - K_{\varphi d}(\tau)]^2 d\tau. \quad (5.6)$$

The integral equation governing the optimum filter follows directly as a special case of (4.10) or can be derived from Equation (5.5) by the calculus of variations. It reads:

$$K_{\varphi d}(\tau) = \int_0^{\tau} g(\alpha) K_{\varphi \varphi}(\tau - \alpha) d\alpha, \quad \tau \geq 0 \quad (5.7)$$

Contrary to the Wiener-Hopf integral equation (5.1), the present integral equation represents a genuine convolution integral. Its solution is directly obtained by the Laplace transformation of Equation (5.7).

The optimum transfer function with respect to the cross-correlation criterion is, therefore,

$$F(s) = \frac{N_{\varphi d}(s)}{N_{\varphi \varphi}(s)}. \quad (5.8)$$

In the sequel this filter will be called correlation filter.

The realizability of the optimum filter is guaranteed by the fact that the auto-correlation spectrum  $N_{\varphi \varphi}(s)$  appearing in equation (5.8) is a positive real function such that its poles and zeros are lying in the negative  $s$ -half plane (upper half plane of complex  $w$ -plane). Because the cross-correlation spectrum contains only poles in the negative  $s$ -half plane, the optimum transfer function (5.8) is free of poles in the right-half of the  $s$ -plane.

In the subsequent section, we will derive some typical examples of filter problems and solve them by applying the new performance criterion. All relations are derived for the complex  $s$ -plane rather than the complex  $w$ -plane, which results in some simplification of notation.

## (2) Pure Delay

We begin with the simplest problem to find an optimum system that reproduces a message  $m(t)$  with a time delay  $\alpha$  in the absence of noise. Therefore, the input is given simply by

$$\varphi(t) = m(t). \quad (5.9)$$

The desired message is

$$d(t) = m(t - \alpha). \quad (5.10)$$

The expressions for the pertaining correlation spectra are

$$N_{\varphi \varphi}(s) = N_{mm}(s) \quad (5.11)$$

$$N_{\varphi d}(s) = N_{mm}(s) e^{-\alpha s}. \quad (5.12)$$

According to Equation (5.8) the optimum transfer function is

$$F(s) = \frac{N_{\varphi d}(s)}{N_{\varphi \varphi}(s)} = e^{-\alpha s}. \quad (5.13)$$

The optimum transfer function is a pure delay element whose amplitude characteristic is constant and whose phase shift is proportional to the frequency. The Wiener theory yields the same result.

## (3) Pure Prediction

Now the message shall be predicted by  $\alpha$  time units in the absence of noise. This can be achieved only by employing an operator that depends on the future. Thus, it is physically not realizable and does not belong to the original class of admissible operators. Because the Wiener theory, however, pays much attention to the prediction problems, we will also discuss it here in some detail. Formally, the solution of the prediction problems is obtained by simple sign change of the delay time  $\alpha$  which yields the transfer function of the correlation filter:

$$F(s) = e^{\alpha s}. \quad (5.14)$$

Approximations of this transcendental transfer function are readily obtained by the first few terms of the Taylor series:

$$F(s) = 1 + \alpha s + \frac{\alpha^2}{2!} s^2 + \dots \quad (5.15)$$

The first approximation to a pure predictor is, therefore, a combination of gain and differentiation. Higher approximations are obtained by considering more terms of the Taylor series. The number of terms that have to be taken for a satisfactory "prediction" naturally depends on the magnitude of the prediction time  $\alpha$ . Similar to the previous problem the optimum transfer function is independent of the statistical

characteristics of the message. On the contrary, the Wiener filter of the prediction problem depends decisively on the statistical nature of the message. For comparison we turn our attention to some concrete examples.

#### Example P-1:

The auto-correlation function of the message is assumed to be

$$K_{mm}(\tau) = e^{-|\tau|} (\cos \tau + \sin |\tau|). \quad (5.16)$$

The corresponding power spectrum reads:

$$S_{mm}(\omega) = \frac{1}{1 + \omega^4}. \quad (5.17)$$

The Wiener theory yields the optimum transfer function in the form (Ref. 2)

$$F_w(s) = e^{-\frac{\alpha}{\sqrt{2}}} \left( \cos \frac{\alpha}{\sqrt{2}} + \sin \frac{\alpha}{\sqrt{2}} \right) + s e^{-\frac{\alpha}{\sqrt{2}}} \sin \frac{\alpha}{\sqrt{2}}. \quad (5.18)$$

Because all practical situations require the restriction to small prediction times, we develop equation (5.18) with respect to  $\alpha$  in a Taylor series and consider only linear terms. This results in

$$F_w(s) = 1 + \alpha s. \quad (5.19)$$

Considering the restrictions which have to be imposed on all practical prediction problems, we can state that the Wiener filter of the present prediction problem is identical with the corresponding correlation filter.

#### Example P-2:

The auto-correlation function of the message is assumed to be

$$K_{mm}(\tau) = (1 + |\tau|) e^{-|\tau|} \quad (5.20)$$

and its power spectrum

$$S_{mm}(\omega) = \frac{1}{(1 + \omega^2)^2}. \quad (5.21)$$

The optimum transfer function of the Wiener filter assumes the form:

$$F_w(s) = e^{-\alpha} [(1 + \alpha) + \alpha s]. \quad (5.22)$$

Developing again in a Taylor series with respect to  $\alpha$  yields the first approximation:

$$F_w(s) = 1 + \alpha s. \quad (5.23)$$

Once more both theories yield the same result.

#### Example P-3:

The auto-correlation function of the message is assumed to be

$$K_{mm}(\tau) = e^{-|\tau|} \quad (5.24)$$

and its corresponding power spectrum

$$S_{mm}(\omega) = \frac{1}{1 + \omega^2}. \quad (5.25)$$

The optimum transfer function of the Wiener theory is

$$F_w(s) = e^{-\alpha}. \quad (5.26)$$

The optimum prediction filter is now simply an attenuator which reduces the amplitude of the message. A differentiation and consequent displacement of the message forward in time are not provided by the Wiener theory. The reason for this seemingly puzzling result is that the class of time functions belonging to the selected auto-correlation function (RC-noise) exhibits such fast fluctuations that their time derivatives can assume infinitely large values. A differentiation of such a time function would, however, lead to infinitely large errors. It is quite natural that the Wiener criterion, which puts a severe penalty on large errors, cannot tolerate a differentiation of these time functions. This precludes a prediction of this class of messages. The cross-correlation criterion is not subjected to this limitation. The same holds true for all types of messages with power spectra, whose denominator is only two degrees higher than the numerator. If, on the other hand, the power spectrum of a message decreases very rapidly (e.g.,  $\sim \omega^{-6}$ ), we can expect that the Wiener criterion allows higher differentiations of the message that would correspond to the consideration of higher terms of the Taylor series (5.15). The question of which of the two performance criteria is more realistic or suitable for prediction seems to be rather academic. We can, however, safely conclude that the new performance criterion yields, in general, the same result as the Wiener theory for the problem of predicting a stationary random process. The mathematical efforts associated with the determination of the optimal Wiener prediction filter are always quite substantial.

#### (4) Delay (prediction) and Filtering

The message  $m(t)$  will, in general, be accompanied by a noise  $n(t)$  such that the total input is given by

$$\varphi(t) = m(t) + n(t). \quad (5.27)$$

The desired message  $d(t)$  is again obtained by delaying (predicting) the message; i.e.,

$$d(t) = m(t \pm \alpha), \quad (5.28)$$

where the positive sign indicates a prediction and the negative sign a delay of the message. The various correlation spectra for this case are then

$$\begin{aligned} N_{dd}(s) &= N_{mm}(s) \\ N_{\varphi d}(s) &= [N_{mm}(s) + N_{nn}(s)] e^{\pm \alpha s} \\ N_{\varphi \varphi}(s) &= N_{mm}(s) + N_{nn}(s) + N_{mn}(s) + N_{nm}(s). \end{aligned} \quad (5.29)$$

The transfer function of the correlation filter reads:

$$F(s) = \frac{N_{mm}(s) + N_{nm}(s)}{N_{\varphi \varphi}(s)} e^{\pm \alpha s}. \quad (5.30)$$

The correlation filter consists, therefore, of a cascade of noise filter and delay (prediction) element (Fig. 3).

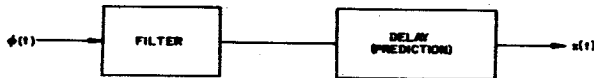


FIGURE 3. DELAY (PREDICTION) AND FILTERING

As a consequence, the problem of filtering and delay (prediction) can be treated in two separate parts. The first part consists of designing a filter with the transfer function,

$$F(s) = \frac{N_{mm}(s) + N_{nm}(s)}{N_{mm}(s) + N_{nn}(s) + N_{mn}(s) + N_{nm}(s)}, \quad (5.31)$$

the second part of designing a lag (lead) element of high precision. The delay element (play-back tape recorder, hi-fi record, etc.) can be constructed completely independent of the statistical nature of the message (e.g., speech, classical music, jazz). It is interesting and advantageous that the new performance criterion automatically separates the deterministic part of the filter problem from its random part. This appears also to be a realistic requirement.

Several special cases of importance can be derived from the general equation (5.31).

Particularly often encountered is the situation in which message and noise are uncorrelated. We obtain then

$$F(s) = \frac{N_{mm}(s)}{N_{mm}(s) + N_{nn}(s)}. \quad (5.32)$$

This relation may be used also in the frequent case that the correlation between message and noise is not known. Of practical importance also is the reproduction of a message in the presence of a high white noise level. In this case, the auto-correlation spectrum of the message can be neglected with respect to that of the noise such that

$$F(s) = \frac{N_{mm}(s)}{N_{nn}(s)}. \quad (5.33)$$

This formula can also be applied if the signal-to-noise power ratio is not known. The filter is then (completely) overmatched (cf., example 4). The relation (5.33) simplifies further for white (or unknown) noise interference. After appropriate normalization the transfer function reads

$$F(s) = N_{mm}(s). \quad (5.34)$$

The optimum filter is, therefore, adapted only to the auto-correlation spectrum of the noise.

#### (5) Periodic Message

Finally, we discuss a filter problem that cannot be treated in the Wiener theory, the important problem of reproducing a periodic message subjected to random noise interference.

The auto-correlation function of a periodic signal of the form

$$m(t) = \frac{C_0}{2} + \sum_{n=1}^{\infty} C_n \cos(n\omega_0 t + \alpha_n) \quad (5.35)$$

reads:

$$K_{mm}(\tau) = \frac{C_0^2}{4} + \frac{1}{2} \sum_{n=1}^{\infty} C_n^2 \cos n\omega_0 \tau, \quad (5.36)$$

The auto-correlation function of a periodic signal is a cosine series with zero initial phase angles.

With the introduction of the new quantity

$$\phi_{mm}(n) = \frac{C_n^2}{4}, \quad (5.37)$$

the expression (5.36) can be transformed into

$$K_{mm}(\tau) = \sum_{n=-\infty}^{\infty} \phi_{mm}(n) \cos n\omega_0 \tau. \quad (5.38)$$

The quantity  $\phi_{mm}(n)$  is known as the power spectrum of the periodic signal  $m(t)$ . The power (density) spectrum of the auto-correlation function (5.36), however, is given by

$$S_{mm}(\omega) = \frac{C_0^2}{4} S(\omega) + \frac{1}{2} \sum_{n=1}^{\infty} C_n^2 S(|\omega| - n\omega_0). \quad (5.39)$$

The power (density) spectrum degenerates, therefore, to a sum of Dirac-functions (Dirac comb). A factorization of such a spectrum as required by the Wiener theory is consequently not possible. The auto-correlation spectrum of equation (5.36) is

$$N_{mm}(s) = \frac{1}{4} \frac{C_0^2}{s} + \frac{1}{2} \sum_{n=1}^{\infty} C_n^2 \frac{s}{s^2 + (n\omega_0)^2}. \quad (5.40)$$

The optimum transfer function shall here be derived only for the (completely) overmatched condition represented by equation (5.33) and with the assumption that the periodic message has no dc-component. This results in

$$F(s) = \frac{1}{2} \frac{\sum_{n=1}^{\infty} C_n^2 \frac{s}{s^2 + (n\omega_0)^2}}{N_{mm}(s)}. \quad (5.41)$$

The optimum transfer function is adapted to the power spectrum of the message and the auto-correlation spectrum of the random noise. The situation is similar to the combfilter technique where the optimum filter (comb filter) is adapted to the amplitude spectrum of the message and the power spectrum of the noise.

For white noise interference  $N_{nn}(s) = \lambda_0^2$ , the correlation filter consists of a series of narrow band-pass systems whose attenuation is tuned to the power spectrum of the periodic message.

The cross correlation criterion affords the possibility of reducing the phase error by appropriate

matching of the signal-to-noise power ratio by employing equation (5.32). The comb filter technique, however, does not provide for a similar consideration of the phase error.

## VI. NUMERICAL EXAMPLES

For further illustration of the significance of the new performance criterion, the subsequent section discusses some typical filter problems and compares them with the corresponding results obtained by applying the Wiener criterion.

### Example 1:

The first example considers the problem of designing a filter for a message that is contaminated by white noise. The message is assumed to have the auto-correlation function

$$K_{mm}(\tau) = \sigma_m^2 e^{-\beta|\tau|} \quad (6.1)$$

and the power spectrum

$$S_{mm}(\omega) = \sigma_m^2 \frac{2\beta}{\beta^2 + \omega^2}. \quad (6.2)$$

The white noise signal has the power spectrum

$$S_{nn}(\omega) = \lambda_0^2. \quad (6.3)$$

The corresponding auto-correlation spectra are

$$N_{mm}(s) = \frac{\sigma_m^2}{\beta + s} \quad (6.4)$$

and

$$N_{nn}(s) = \frac{\lambda_0^2}{2}. \quad (6.5)$$

This particular problem cannot only be solved by the Wiener theory but also by a method of the classical theory of communication. According to the latter we select a low pass filter, whose bandwidth is rather arbitrarily chosen to be the intersection between the power spectrum of the message and the noise. The bandwidth is, therefore, determined by equating Equations (6.2) and (6.3). The result is

$$\omega_1^2 = \frac{\alpha^2}{\lambda_0^2} - \beta,$$

where

$$\alpha^2 = 2\beta \sigma_m^2.$$

(6.6)

The Wiener theory, on the other hand, yields a low pass filter with the bandwidth

$$\omega_2^2 = \frac{\alpha^2}{\lambda_0^2} + \beta^2 = \omega_1^2 + 2\beta^2 \quad (6.7)$$

The bandwidth of the Wiener filter is always higher than the classical filter.

Applying the new performance criterion again yields a low pass, but its bandwidth is now given by

$$\omega_3^2 = \frac{1}{\beta^2} \left( \frac{\alpha^2}{\lambda_0^2} + \beta^2 \right)^2 = \frac{2\omega_2^2}{1 - \omega_1^2/\omega_2^2} \quad (6.8)$$

Comparing with equation (6.7) shows that the correlation filter has a still higher bandwidth than the Wiener filter. For increasing noise level, however, the correlation filter approaches the Wiener filter asymptotically.

The corresponding amplitude and phase characteristics of these three differently designed filters are shown in Figures 4 and 5 for numerical values of  $\alpha = 1$ ,  $\beta = 1$ ,  $\lambda = 0.5$ . It is recognized that, while an increase in bandwidth increases the portion of the noise in the total output of the filter, it also results in a substantial decrease of the phase error in the region of the message. (In the subsequent discussion, the phase error shall be defined as the deviation from the zero value. As such it is to be distinguished from the definition of the phase distortion in the conventional communication theory.) The phase error is smallest for the correlation filter and largest for the conventional filter; the Wiener filter takes an intermediate place in this particular example.

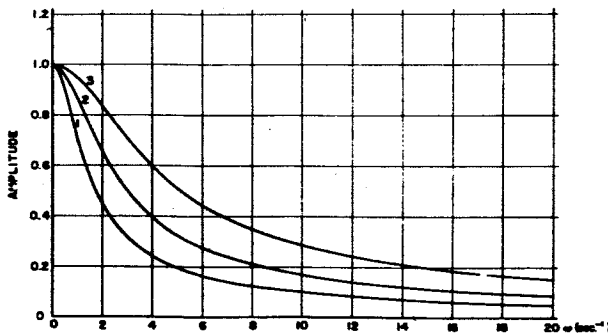


FIGURE 4. NORMALIZED AMPLITUDE CHARACTERISTIC OF CLASSICAL FILTER (1) WIENER FILTER (2), AND CORRELATION FILTER (3)

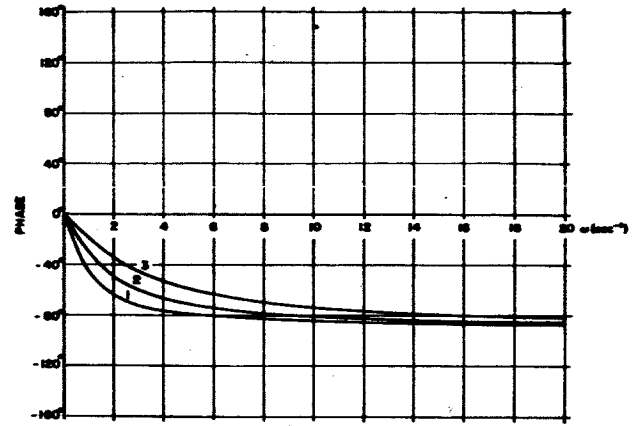


FIGURE 5. PHASE CHARACTERISTIC OF CLASSICAL FILTER (1), WIENER FILTER (2), AND CORRELATION FILTER (3)

#### Example 2:

The task is to filter a message whose autocorrelation function is of the form

$$K_{mm}(\tau) = \sigma_m^2 e^{-a|\tau|} \left( \cos \sqrt{\omega_0^2 - a^2} \tau + \frac{a}{\sqrt{\omega_0^2 - a^2}} \sin \sqrt{\omega_0^2 - a^2} |\tau| \right) \quad (6.9)$$

in the presence of noise whose autocorrelation function is given by

$$K_{nn}(\tau) = \sigma_n^2 e^{-b|\tau|} \quad (6.10)$$

In addition, message and noise should not be correlated. The corresponding power spectra are

$$S_{mm}(\omega) = \sigma_m^2 \frac{4a\omega_0^2}{(\omega^2 - \omega_0^2)^2 + 4a^2\omega_0^2} \quad (6.11)$$

and

$$S_{nn}(\omega) = \sigma_n^2 \frac{2b}{b^2 + \omega^2} \quad (6.12)$$

The corresponding correlation spectra read:

$$N_{mm}(s) = \sigma_m^2 \frac{2a + s}{s^2 + 2as + \omega_0^2} \quad (6.13)$$

and

$$N_{nn}(s) = \sigma_n^2 \frac{1}{b+s} \quad (6.14)$$

The optimum transfer function of the correlation filter is derived from Equation (5.32) as

$$F(s) = \frac{1}{1+R^2} \frac{(b+s)(2a+s)}{s^2 + \frac{2a(1+R^2)+b}{1+R^2}s + \frac{\omega_0^2 R^2 + 2ab}{1+R^2}}, \quad (6.15)$$

where  $R^2 = \sigma_n^2 / \sigma_m^2$  is the noise-to-signal power ratio.

The transfer function of the corresponding Wiener filter cannot be given in closed form. To compare both filters, a numerical example is selected whose pertaining values are given as  $a = 2 \text{ sec}^{-1}$ ,  $b = 1 \text{ sec}^{-1}$ ,  $\omega_0 = 10 \text{ sec}^{-1}$ , and  $R^2 = 1$ . The corresponding correlation functions and power spectra are shown in Figures 6 and 7. The correlation functions are nor-

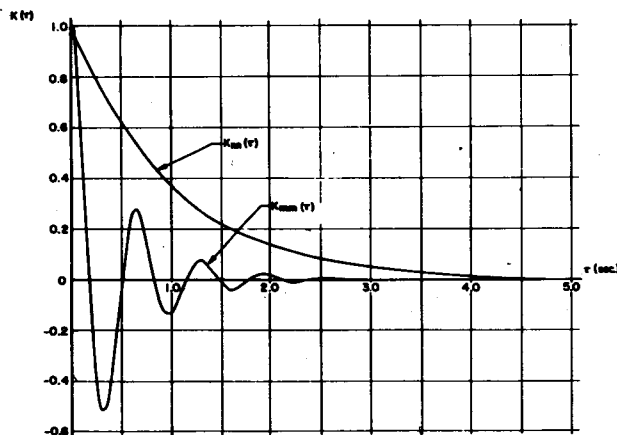


FIGURE 6. NORMALIZED AUTOCORRELATION FUNCTIONS OF MESSAGE AND NOISE, EXAMPLE 2

malized to unity at the origin, whereas the power spectra are normalized such that the areas under their curves are equal according to the noise-to-signal power ratio  $R^2 = 1$ . The transfer function of the correlation filter is

$$F_k(s) = 0.50 \frac{(s+2-9.8j)(s+2+9.8j)}{(s+2.25-6.85j)(s+2.25+6.85j)}, \quad (6.16)$$

and the transfer function of the Wiener filter

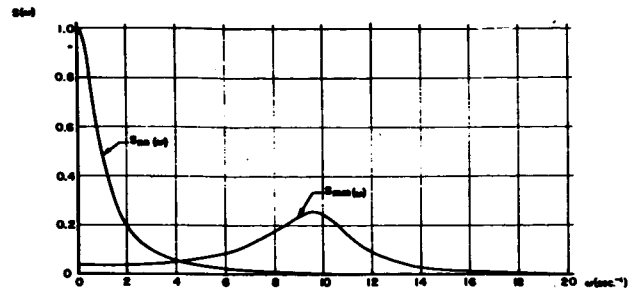


FIGURE 7. NORMALIZED POWER SPECTRA OF MESSAGE AND NOISE, EXAMPLE 2

$$F_w(s) = 0.86 \frac{(s+2-9.8j)(s+2+9.8j)}{(s+8.5)(s+12)} \quad (6.17)$$

In this particular example, the zeros of both filters are identical.

Normalized amplitude and phase characteristics of both filters are depicted in Figures 8 and 9. The correlation filter of this example has better selectivity than the Wiener filter. In the spectrum of the message ( $\omega \approx 10 \text{ sec}^{-1}$ ), however, the Wiener filter exhibits a smaller phase error than the correlation filter.

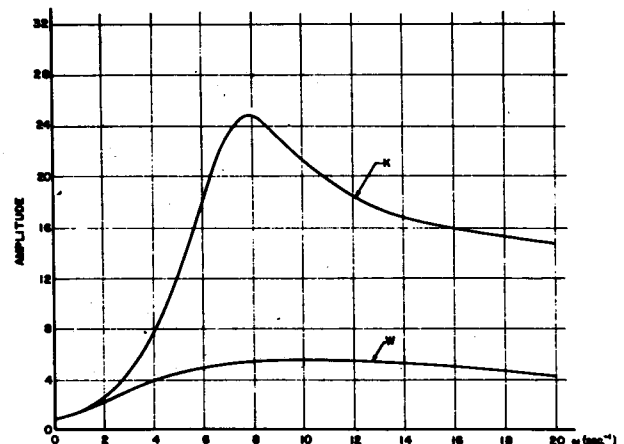


FIGURE 8. NORMALIZED AMPLITUDE CHARACTERISTIC OF CORRELATION FILTER AND WIENER FILTER, EXAMPLE 2

Figure 10 shows an analog computer diagram to demonstrate the performance of both filters when simulated on an analog computer. Message and noise are generated by two independent low-frequency Gaussian noise generators and suitable shaping filters. The power spectrum of the noise generator is constant within 0.4 db in the frequency domain from 0-35 cps.



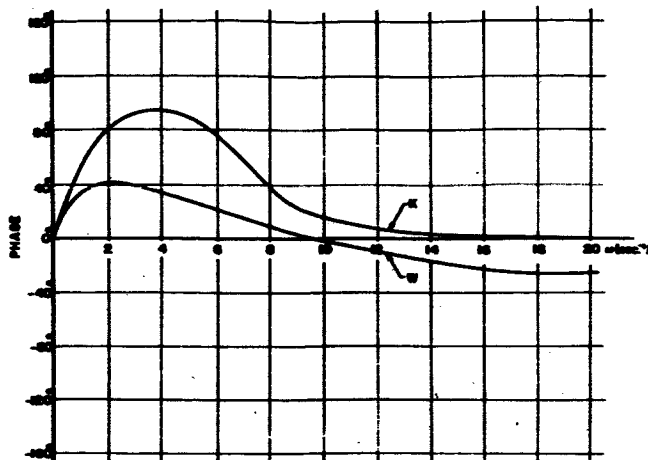


FIGURE 9. PHASE CHARACTERISTIC OF CORRELATION FILTER AND WIENER FILTER, EXAMPLE 2

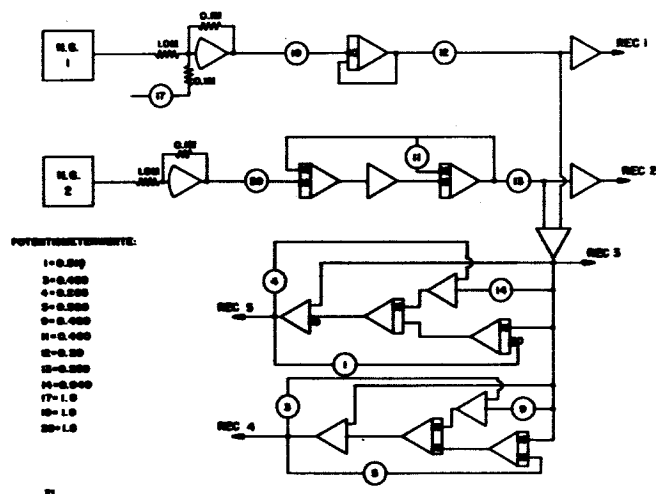


FIGURE 10. ANALOG COMPUTER DIAGRAM FOR SIMULATION OF EXAMPLE 2

The recorder No. 1 records the noise signal (RC-noise), the recorder No. 2 the message as a narrow band random process. Summing message and noise yields the input signal of the filters which is recorded by recorder No. 3. Recorder No. 4 shows the output of the correlation filter, and recorder No. 5 the output of the Wiener filter.

Figure 11 contains all records. In addition, it shows the bandwidth-limited white noise of the noise generator and the time marks with a distance  $\Delta t = 1$  sec. Since Figure 11 is only an optical illustration, it is not suited to appraise the "quality" of the reproduction of the message. Such an appraisal would

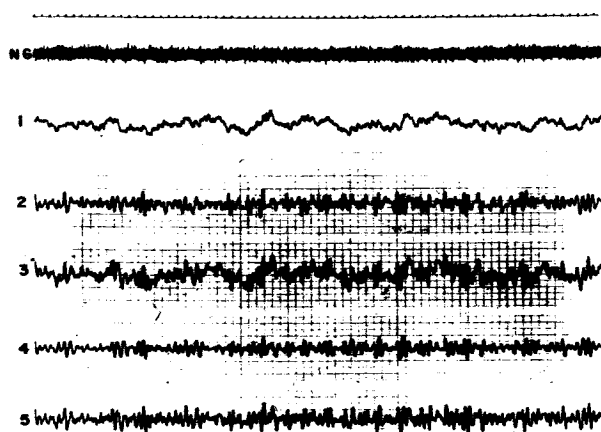


FIGURE 11. ANALOG COMPUTER RECORDS OF EXAMPLE 2

always be limited to the visual evaluation of the records which is much more sensitive to amplitude distortions than to phase errors.

#### Example 3:

In this example, message and signal are just interchanged. The transfer function of the correlation filter is then given by

$$F_k(s) = \frac{1}{1 + R^2} \frac{s^2 + 2as + \omega_o^2}{a^2 + (2a + \frac{R^2}{1 + R^2} b) s + \frac{\omega_o^2 + 2R^2 ab}{1 + R^2}} \quad (6.18)$$

Inserting the appropriate numerical values yields, for the correlation filter, the expression

$$F_k(s) = 0.50 \frac{(s + 1)(s + 4)}{(s + 2.25 - 6.85j)(s + 2.25 + 6.85j)} \quad (6.19)$$

and for the Wiener filter

$$F_w(s) = 0.86 \frac{(s + 1)(s + 114)}{(s + 8.5)(s + 12)} \quad (6.20)$$

The situation is now exactly reversed. According to Figures 12 and 13, the Wiener filter now exhibits better selectivity than the correlation filter, whereas its phase error within the spectrum of the message is larger than that of the correlation filter. The Wiener filter does not allow a phase error in the region of the noise

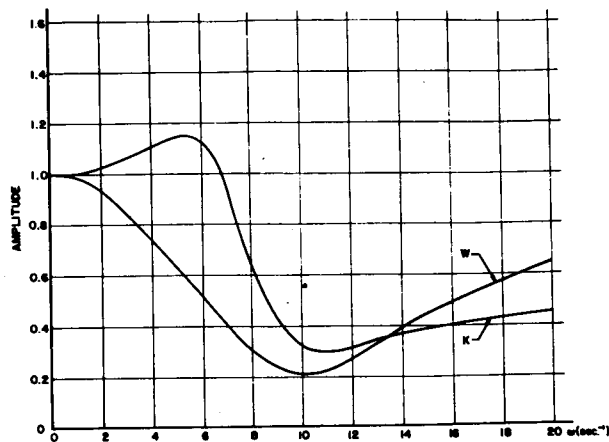


FIGURE 12. NORMALIZED AMPLITUDE CHARACTERISTIC OF CORRELATION FILTER AND WIENER FILTER, EXAMPLE 3

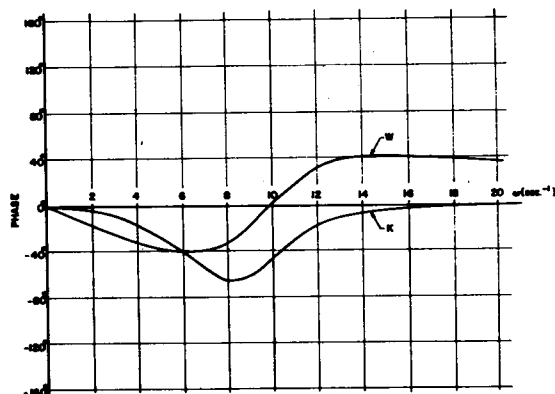


FIGURE 13. PHASE CHARACTERISTIC OF CORRELATION FILTER AND WIENER FILTER, EXAMPLE 3

spectrum ( $\omega \approx 10 \text{ sec}^{-1}$ ) where the attenuation is a maximum. The demonstration of this example on the analog computer is shown diagrammatically in Figure 14 and the resulting records in Figure 15. It is particularly interesting to evaluate the records visually. The Wiener filter appears to be decisively superior to the correlation filter, since it is capable of reproducing also the high frequency content of the message causing a high "similarity" between the output of the Wiener filter and the message. The phase characteristics, however, reveal that this portion of the message suffers a phase error of close to  $40^\circ$ . Although the eye is apparently very insensitive to such

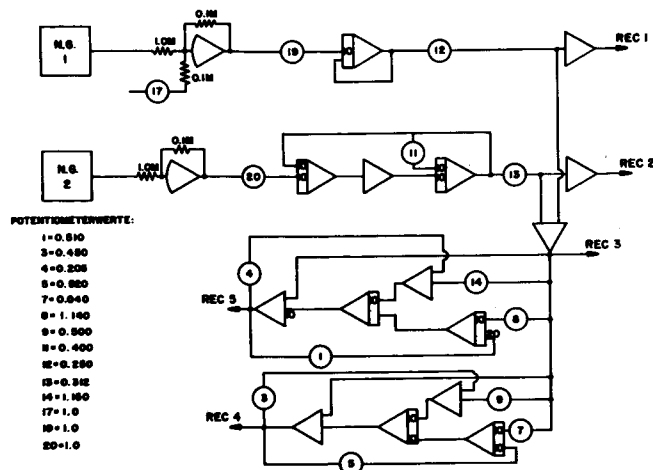


FIGURE 14. ANALOG COMPUTER DIAGRAM FOR SIMULATION OF EXAMPLE 3

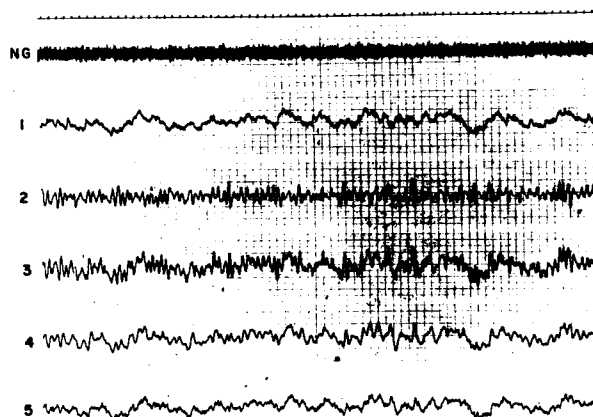


FIGURE 15. ANALOG COMPUTER RECORDS OF EXAMPLE 3

a phase error, it is quite possible that such a performance could be potentially troublesome in a phase-sensitive feedback system.

#### Example 4:

Finally, we will consider dependency of selectivity and phase error on the matching of the noise-to-signal power ratio. A possible correlation between message and noise will not be considered in this particular study. The power spectrum of the message is chosen as

$$S_{mm}(\omega) = \sigma_m^2 \frac{4a_m \omega_m^2}{(\omega^2 - \omega_m^2)^2 + 4a_m^2 \omega_m^2} \quad (6.21)$$

The power spectrum of the noise is assumed to have the same structure:

$$S_{nn}(\omega) = \sigma_n^2 \frac{4a_n \omega_n^2}{(\omega^2 - \omega_n^2) + 4a_n^2 \omega_n^2} \quad (6.22)$$

The corresponding auto-correlation spectra are

$$N_{mm}(s) = \sigma_m^2 \frac{2a_m + s}{s^2 + 2a_m s + \omega_m^2} \quad (6.23)$$

$$N_{nn}(s) = \sigma_n^2 \frac{2a_n + s}{s^2 + 2a_n s + \omega_n^2} \quad (6.24)$$

The optimum transfer function of the correlation filter reads then:

$$F(s) = \frac{(2a_m + s)(s^2 + 2a_n s + \omega_n^2)}{(2a_m + s)(s^2 + 2a_n s + \omega_n^2) + kR^2(2a_n + s)(s^2 + 2a_m s + \omega_m^2)} \quad (6.25)$$

where again  $R^2 = \sigma_n^2 / \sigma_m^2$ .

The match factor  $k$  which is introduced in Equation (6.25) is dimensionless and designates the degree of matching the noise-to-signal power ratio. The value of  $k = 1$  corresponds to the matched condition; for  $k \geq 1$ , the filter operates undermatched or overmatched.

The numerical values of the example are

$$\begin{aligned} a_m &= 1.2 \text{ sec}^{-1} & a_n &= 2.4 \text{ sec}^{-1} & R^2 &= 1. \\ \omega_m &= 6.0 \text{ sec}^{-1} & \omega_n &= 12.0 \text{ sec}^{-1} \end{aligned}$$

The power spectra of both input signals, shown in Figure 16, are normalized to equal areas ( $R^2 = 1$ ). The dependency of amplitude and phase characteristics on the match factor  $k$  is depicted in Figures 17 and 18. It is interesting to see how the selectivity of the filter can be raised by increasing the match factor  $k$ , accompanied, however, by a deterioration of the phase characteristic. Selectivity and phase error are highest for the completely overmatched condition ( $k = \infty$ ).

#### Example 5:

In this example, message and noise are again commuted with respect to the previous example. Am-

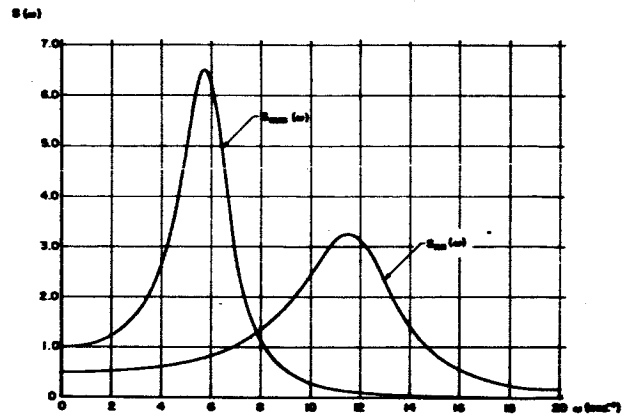


FIGURE 16. NORMALIZED POWER SPECTRA OF MESSAGE AND NOISE, EXAMPLE 4

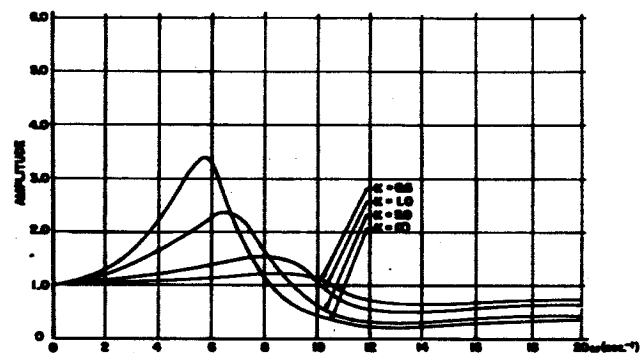


FIGURE 17. NORMALIZED AMPLITUDE CHARACTERISTIC OF EXAMPLE 4 WITH MATCH FACTOR  $k$  AS PARAMETER

plitude and phase characteristics (Figures 19 and 20) show essentially the same behavior as in Example 4. The selectivity is again improving for increasing values of the match factor  $k$  while the phase characteristic deteriorates.

The choice of the proper match factor depends completely on the relative importance of amplitude and phase distortions for the system under consideration. This has to be investigated anew for each concrete case. The purpose of the above example was only to show how a suitable compromise between phase and amplitude distortion can be achieved by varying the matching of the noise-to-signal power ratio.

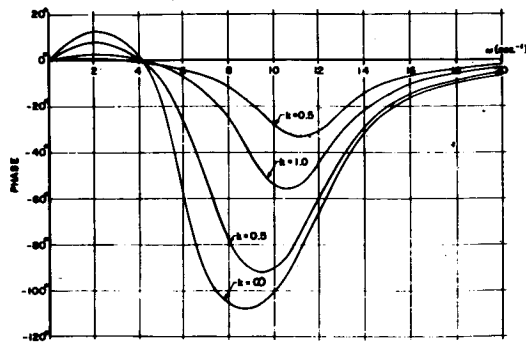


FIGURE 18. PHASE CHARACTERISTIC OF EXAMPLE 4 WITH MATCH FACTOR  $k$  AS PARAMETER

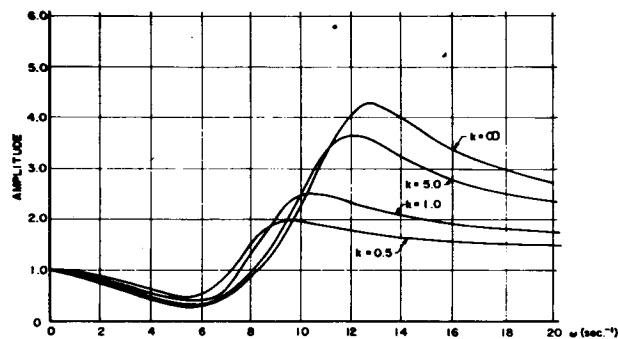


FIGURE 19. NORMALIZED AMPLITUDE CHARACTERISTIC OF EXAMPLE 5 WITH MATCH FACTOR  $k$  AS PARAMETER

## VII. CONCLUSION

Similar to the Wiener performance criterion, the new performance criterion represents a special case of a more general statistical optimality condition. By virtue of its physical significance, it can also be advantageously applied to the statistical treatment of filter problems. In contrast to the Wiener criterion, the new performance criterion attempts to optimize the system during the initial phase of operation. As a consequence, its main applicability is foreseen in systems where transient performance is important and for those which are sensitive to phase differences. A particular advantage of the new performance criterion is its surprisingly simple mathematical treatment. It affords not only a better physical understand-

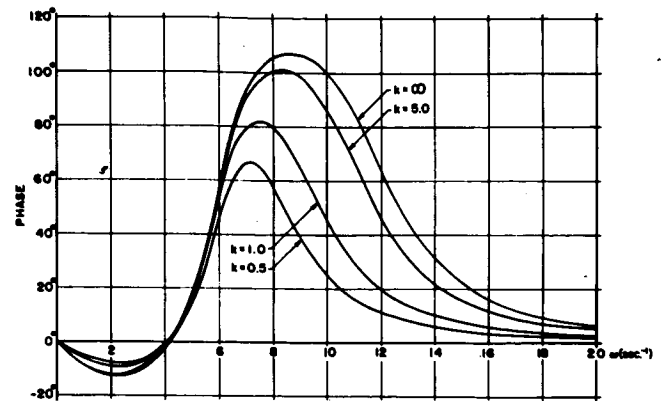


FIGURE 20. PHASE CHARACTERISTIC OF EXAMPLE 5 WITH MATCH FACTOR  $k$  AS PARAMETER

ing of the statistical filter process but also assists in the practical synthesis of networks. In addition, the new criterion can also be used for filter problems involving periodic signals. This opens the possibility of comparing the new criterion with other conventional techniques of filter design in this area. The new performance criterion cannot claim to be universal. Rather, it represents a welcome addition to the already existing performance criteria and enhances the flexibility of optimum filter design. Effectiveness and limitations of the new criterion can be judiciously assessed only by further extensive studies and applications in practice. Because of its mathematical simplicity, it could provide new stimulus for analyzing more complicated filter problems.

## REFERENCES

1. K. Küpfmüller, "Die Systemtheorie der elektrischen Nachrichtenübertragung." Stuttgart, Hinzl 1949.
2. N. Wiener, "The Extrapolation, Interpolation and Smoothing of Stationary Time Series with Engineering Applications." John Wiley & Sons, New York 1949.
3. E. Parzen, "Stochastic Processes." Holden-Day, San Francisco 1962.
4. L. Weinberg, "Network Analysis and Synthesis." McGraw-Hill Book Co., New York 1962.
5. M. Shinbrot, "Optimization of Time-Varying Linear Systems with Nonstationary Inputs." Trans. ASME, Vol. 80, 1958, pp. 457-62.

6. R. C. Booton, "An Optimization Theory for Time-Varying Linear Systems with Nonstationary Statistical Inputs." Proc. I.R.E. Vol. 40, 1952, pp. 977-81.
7. Y. W. Lee, "Statistical Theory of Communication." John Wiley & Sons, New York 1960.
8. H. Schlitt, "Systemtheorie für regellose Vorgänge." Springer Verlag 1960.

### III. FACILITIES RESEARCH

# VARIABLE POROSITY WALLS FOR TRANSONIC WIND TUNNELS

by

A. Richard Felix

## SUMMARY

Variable porosity walls were recently installed in the transonic test section of the 14 by 14-in. Trisonic Tunnel at Marshall Space Flight Center. Evaluation tests have indicated that use of these walls greatly improves the ability of this facility to produce reasonably accurate model pressure distribution data throughout the critical and difficult Mach range from 1.0 to 1.25. The evaluation was accomplished by comparing pressure distributions for a 20° cone-cylinder model with interference-free data for the same model. The range of porosities used is between 0.5 percent and 5.4 percent with the holes being slanted 60°.

## I. INTRODUCTION

Several recent experimental investigations [1, 2, 3,] have established that interference-free pressure distributions in the transonic speed range between  $M = 1.0$  and  $1.3$  cannot be produced in a transonic wind tunnel having a single, fixed-wall porosity. To provide an optimum wave cancellation at the wall, a small porosity is required at Mach numbers near  $1.0$  and a larger porosity at or near  $M = 1.3$ . However, for mechanical simplicity, it has been standard procedure in transonic test sections, including the 14 by 14-in. Trisonic Tunnel at MSFC, to use walls having a single fixed porosity (usually about 6 to 8 percent open area for 60° slanted holes). Such an approach has obvious advantages and is satisfactory except for tests requiring accurate pressure distributions throughout the transonic range. Figure 1 illustrates the magnitude of the errors in model surface pressures which may result from use of a single wall porosity. The symbols represent data taken in the MSFC 14 by 14-in. Trisonic Tunnel when equipped with a single fixed wall porosity of about 7.5 percent using 60° slanted holes. The model is a 20° cone-cylinder with a tunnel blockage ratio of 0.9 percent. Comparison of these data with interference-free results from the 16-ft. Transonic Tunnel at AEDC shows that wall-reflected disturbances produce errors as great as 13 percent.

To minimize these wall interference effects in the Mach number range between  $1.0$  and  $1.3$ , it was decided to design and install a variable porosity wall in

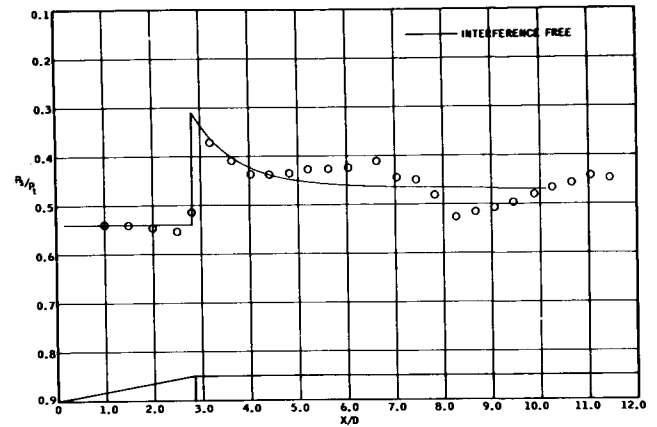


FIGURE 1. CONE-CYLINDER PRESSURE DISTRIBUTION AT  $M = 1.10$  FIXED TUNNEL WALL POROSITY OF 7.5% WITH 60° SLANTED HOLES

the transonic test section of the 14 by 14-in. Trisonic Tunnel. This paper describes these walls and the results achieved from their use.

## II. DESCRIPTION OF FACILITY

The 14 by 14-in. Trisonic Tunnel (Fig. 2) is an intermittent blowdown facility exhausting either to the atmosphere or to vacuum. Stagnation pressure is controlled at values between one and seven atmospheres with stagnation temperatures controllable between 100° and 200° F. Air is stored at 500 psig in a 6000-ft<sup>3</sup> bottle. Vacuum storage field is 42,000 ft<sup>3</sup> evacuated to 1 mm Hg. The Mach number range from 0.2 to 5.0 is achieved by two interchangeable test sections -- one covering the Mach range from 0.2 to 2.5 and the other spanning the range from 2.75 to 5.0. The transonic test section (Fig. 3) uses a set of sonic blocks to produce Mach numbers from 0.2 to 1.3. The portion of this range from 0.2 to 0.85 is set by use of a controllable diffuser. The portion from 0.9 to 1.3 is set by regulating wall porosity, wall angle, and plenum suction. Three sets of discrete blocks produce Mach numbers of 1.5, 2.0, and 2.5.

The Mach range from 2.75 to 5.0 requires installation of the second or supersonic test section. This test section uses fixed contour movable blocks which can be both translated and tilted to produce the desired Mach number.

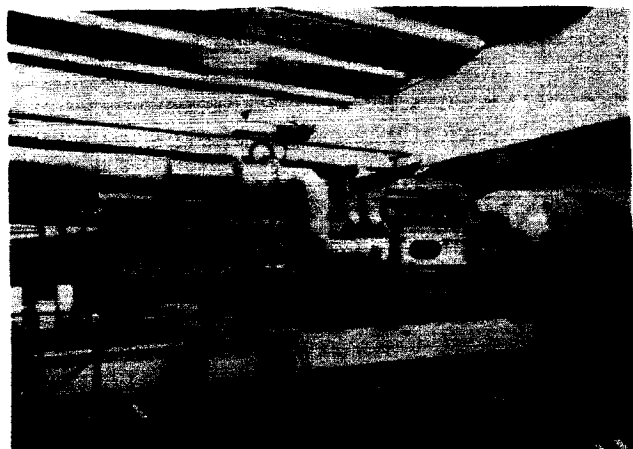


FIGURE 2. PHOTOGRAPH OF 14 X 14 INCH TRANSONIC TUNNEL

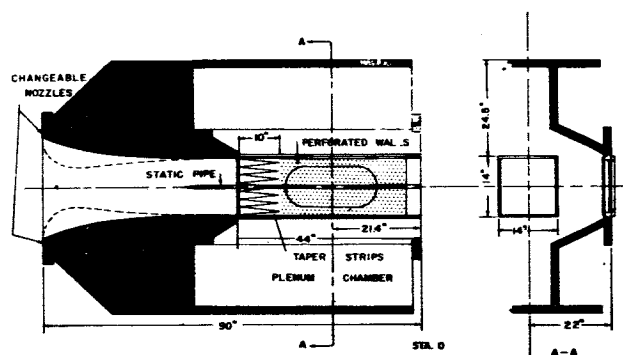


FIGURE 3. SKETCH OF TRANSONIC TEST SECTION

### III. DESIGN AND CONSTRUCTION OF VARIABLE POROSITY WALLS

The design concept (Fig. 4) employed for varying the porosity is very simple. The inner wall nearest the flow is fixed, and the outer wall is movable in the axial direction, thus permitting a continuously variable porosity from zero up to the maximum value determined by the wall configuration.

The maximum porosity for which these walls were designed is 5.4 percent and was determined from in-house research results as well as from AEDC data. The nominal design value was 6 percent but a fabrication error produced the final 5.4 percent. Porosity is defined as hole area based on hole diameter divided by wall area. The fixed wall thickness is .125 in., and the movable wall is .125 in. giving a total wall thickness of .250 in. The hole diameter is 0.156 in. Figure 5 is a sketch of the wall geometry. All four walls are identical with the exception that floor and ceiling wall angle can be varied slightly.

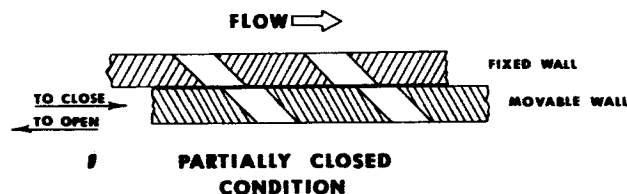
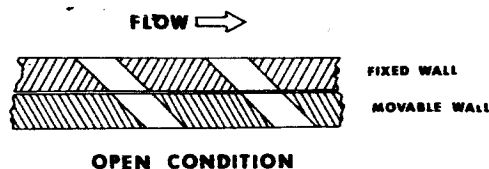


FIGURE 4. SKETCH OF VARIABLE POROSITY CONCEPT

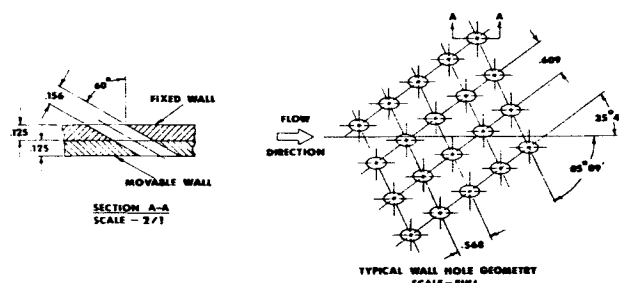


FIGURE 5. SKETCH OF WALL GEOMETRY

Wall movement is provided by a Globe planetary gear motor having an output speed of 15.4 rpm which results in a wall translational speed of 0.64 in/min. This permits a full porosity variation from 0 to 5.4 percent in about 30 seconds. The position of the wall is monitored by a Bourns linear potentiometer. Figures 6 and 7 are photographs of the front and rear of typical wall.

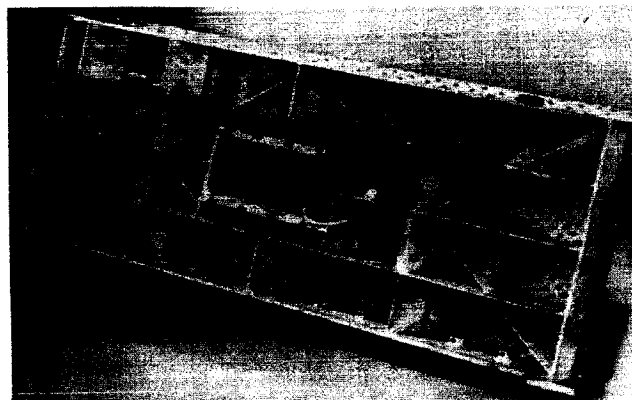


FIGURE 6. PHOTOGRAPH OF REAR OF VARIABLE POROSITY WALL



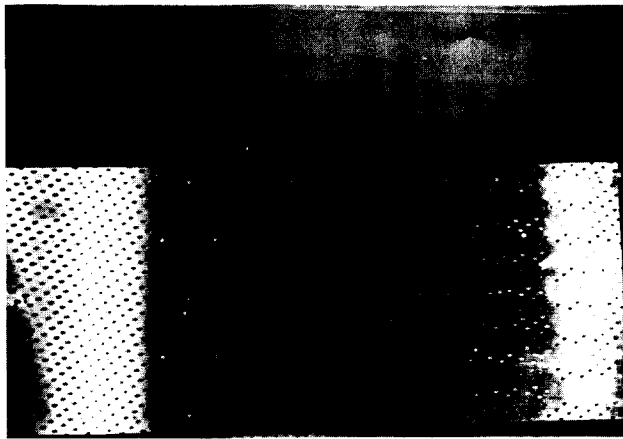


FIGURE 7. PHOTOGRAPH OF FRONT OF VARIABLE POROSITY WALL

#### IV. WALL CALIBRATION PROCEDURE AND MODELS

The method for optimizing the wall settings was chosen comparing pressure distributions for a 20° cone-cylinder model with interference-free data from the 16-ft Transonic at AEDC.

This particular configuration is a severe test of wall cancellation properties because of the strong pressure rise region generated by the cone, immediately followed by the centered expansion field emanating from the cone-cylinder intersection.

When this phase of the investigation was completed and wall porosities and angles optimized, the 20° cone-cylinder was replaced by a static pressure survey pipe so that a longitudinal Mach number survey of the test section might be made.

Figure 8 summarizes the physical dimensions of the 20° cone-cylinder and the survey pipe. The 1.5-in. base diameter of the cone-cylinder produces a tunnel blockage ratio of 0.9 percent. Figure 9 is a photograph of the 20° cone-cylinder in the tunnel.

Except as noted in Figure 11, all data presented herein were run at a tunnel stagnation pressure of 7 psia. The corresponding Reynolds number per foot is about 6.5 by 10<sup>6</sup>.

#### V. RESULTS AND DISCUSSION

A systematic program was conducted to evaluate the effects of wall porosity and wall angle on wave cancellation properties. The range of porosities investigated was from 0 to 5.4 percent, and wall (ceiling and floor) angles from 30 minutes diverged to 30 min-

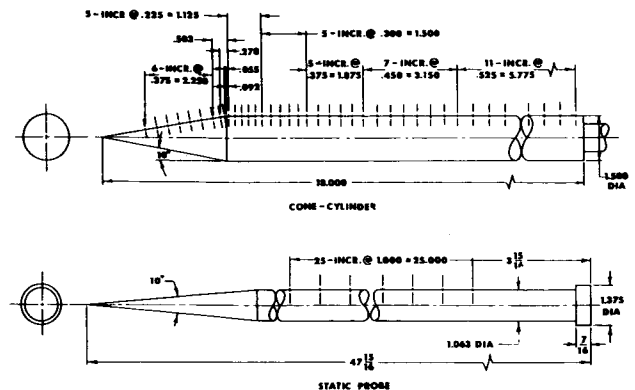


FIGURE 8. SKETCH OF 20° CONE-CYLINDER AND STATIC SURVEY PIPE

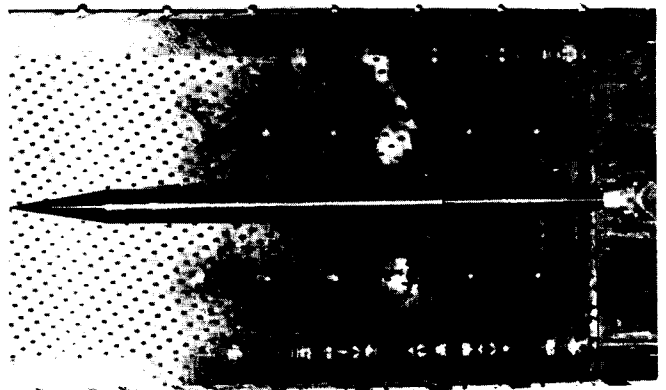


FIGURE 9. PHOTOGRAPH OF 20° CONE-CYLINDER IN TUNNEL

utes converged. In addition to porosity and wall angle, the plenum suction pressure was varied to produce the desired test section Mach numbers. This facility has a controllable diffuser for attaining subsonic Mach numbers up to 0.85, but plenum suction is required for Mach numbers between 0.9 and 1.25. The optimized porosities and wall angles are summarized in Table I.

TABLE I

M	Wall angle, minutes	Wall porosity, %
.9	+ 15	5.40
.95	+ 15	5.40
1.00	- 15	0.50
1.05	- 15	0.75
1.10	- 15	1.60
1.15	- 15	2.50
1.20	- 10	5.40
1.25	0	5.40

(+ indicates diverged, - indicates converged)

As was previously mentioned, the effectiveness of the wall conditions was evaluated by comparing pressure distributions for a 20° cone-cylinder with interference-free data.

Results using the wall conditions presented in Table I are shown in Figure 10. Pressures are presented as a ratio of local static,  $P_s$ , to tunnel stagnation pressure,  $P_t$ . The longitudinal orifice positions are plotted in model diameters,  $X/D$ , measured from the nose of the model. The Mach numbers presented are 0.90, 0.95, 1.00, 1.05, 1.10, 1.15, 1.20, and 1.25. The symbols represent the measured data points, and the solid line on each plot presents the interference-free data, as measured in the 16-ft Transonic Tunnel at AEDC [1].

The agreement between the measured pressures and interference-free data is quite acceptable. No significant reflections are evident as was the case in Figure 1. The maximum error in  $P_s/P_t$  is about  $\pm 0.02$ , representing a percentage error of  $\pm 5$ . Two exceptions are the surface pressures immediately behind the cone-cylinder intersection at  $M = 0.95$  and the cone pressures at  $M = 1.05$ . It is unlikely that either of these disagreements is due to incorrect wall cancellation properties.

Because the model chosen produces a very severe test of wave cancellation, it is felt that pressure distribution errors of less than  $\pm 5$  percent can be achieved when more smoothly contoured configurations such as ogive-cylinders are being tested.

The results of a longitudinal Mach number survey of the test section using the optimized wall settings are included as Figure 11. The abscissa in this plot is the Tunnel Station in inches measured from the downstream end of the test section or Station 0 (Fig. 3). The Mach numbers included in Figure 10 are presented in Figure 11, 0.90, 0.95, 1.00, 1.05, 1.10, 1.15, 1.20, and 1.25. Each of the calibrations was made at two stagnation pressures, 7 psig and 15 psig. The agreement between the data at the two pressure levels was very good, and for the sake of clarity, the 15 psig data points are presented for only two Mach numbers, 0.90 and 1.10.

The normal test area or rhombus in this facility is between Station 12 and Station 26. The Mach number variation in this area is no more than  $\pm 0.02$ . The drop in Mach number near Station 12 in the  $M = 1.05$  plot is thought to be the result of blockage of the chuck which supported the static pipe rather than an actual open tunnel condition.

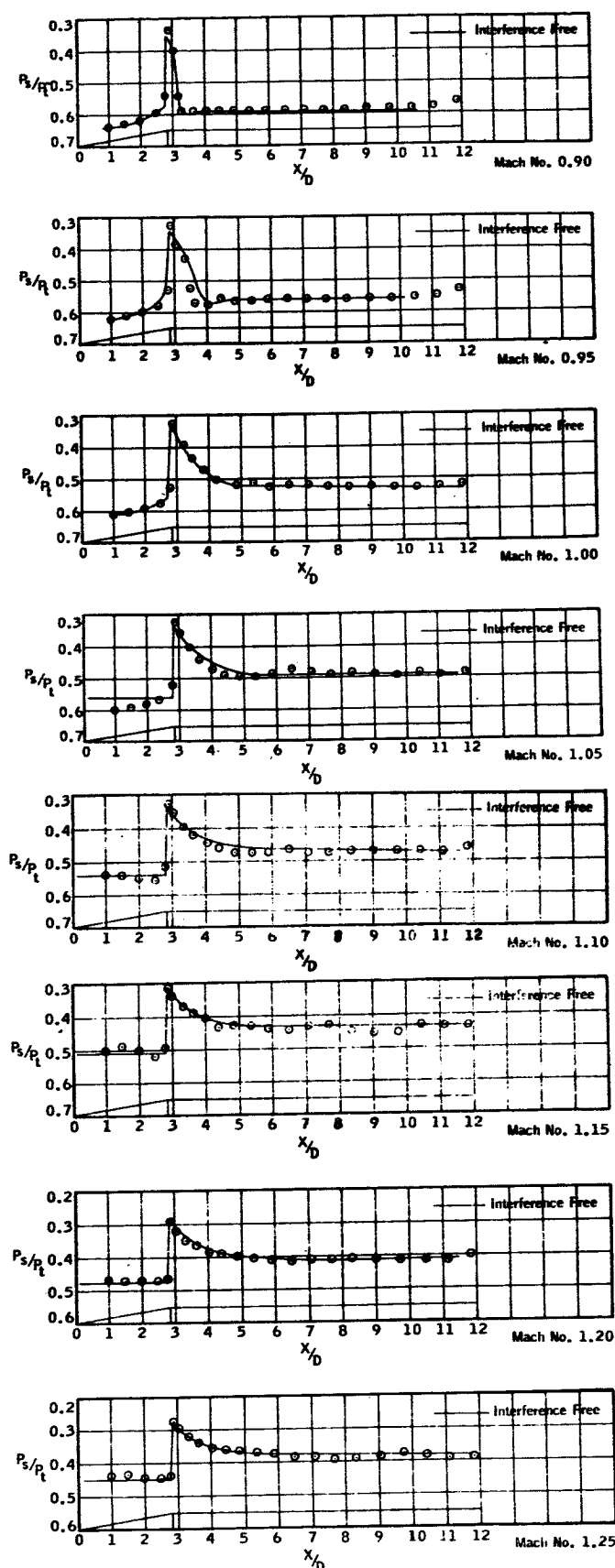


FIGURE 10. CONE-CYLINDER PRESSURE DISTRIBUTION WITH VARIABLE POROSITY WALLS

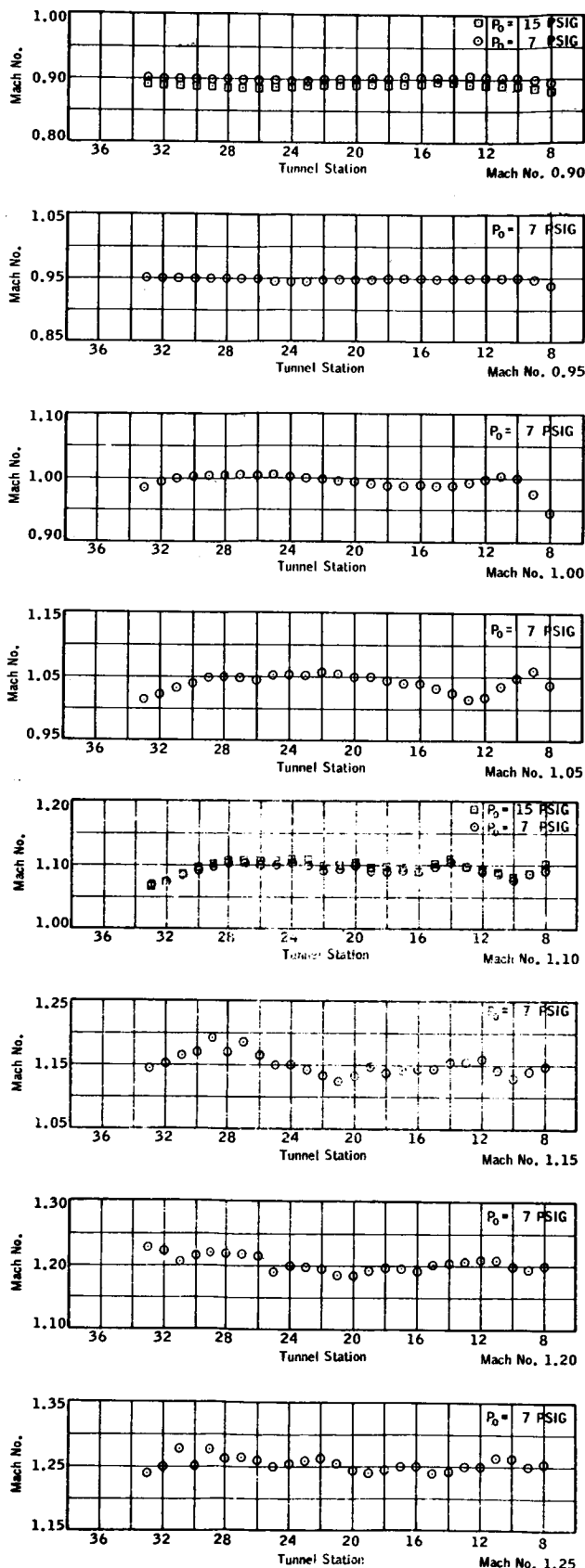


FIGURE 11. TEST SECTION MACH NUMBER DISTRIBUTION WITH VARIABLE POROSITY WALLS

## VI. CONCLUDING REMARKS

The installation of variable porosity walls in the transonic test section of the 14 by 14-in. Trisonic Tunnel at MSFC has greatly enhanced its capability to produce reasonably accurate model pressure distributions through the Mach number range between 1.00 and 1.25.

## REFERENCES

1. Estabrooks, B. B., "Wall Interference Effects on Axisymmetric Bodies in Transonic Wind Tunnels with Perforated Wall Test Section." AEDC-TR-59-12, June 1959, (AD216698).
2. Chew, W. L., "Experimental and Theoretical Studies on Three-Dimensional Wave Reflection in Transonic Test Sections -- Part III: Characteristics of Perforated Test Section Walls with Differential Resistance to Cross-Flow." AEDC-TN-55-44, March 1956, (AD-84158).
3. Goethert, B. H., "Transonic Wind Tunnel Testing." Published for AGARD by Pergamon Press, 1961.

#### **IV. FLIGHT EVALUATION**

# AUTOMATION OF POST-FLIGHT EVALUATION

by

Carlos Hagood

## SUMMARY

The results of a study to determine the feasibility of automating the evaluation of flight test data are considered. While operational results from this program have not been obtained, comparison with data from past flights indicates that the concepts and program design will prove extremely useful. A large number of telemetry measurements can be scanned and useful information obtained in a minimum of computer and analyst time shortly after a launch.

This information will provide early knowledge of minor deviations and malfunctions as well as some insight into the cause of failures. A chronological listing of the deviations are obtained in a timely fashion. This analysis allows a sound decision to be made as to what areas of the vehicle evaluation should be concentrated on and how computer time should be allotted.

Based on results obtained by comparing the automated analysis with the detailed analysis of SA-5, approximately 85 percent of the deviations were detected. It is recognized that some failures cannot be found with this type of analysis, and a detailed inspection of measurements will still be required. However, the number of measurements requiring inspection should be greatly reduced. As additional experience is gained in using this approach, the scheme will be modified to improve its usefulness with respect to the tests performed. Data presentation can be improved also.

## I. INTRODUCTION

With the advent of computers with large data handling capabilities, the ability to perform a preliminary quick-look postflight analysis of the many measurements made on a Saturn vehicle within a few hours has been realized. In the past, this analysis has been accomplished by engineering analysts reviewing in detail all measurements displayed in the form of oscillographs, plots, and digitized data. This type of analysis requires the time of a rather large number of engineers, at considerable expense and time, in determining what, if any, malfunctions or deviations existed in a given flight test. All deviations were correlated by subjective analysis of the observed discrepancies.

This type of analysis can now be done automatically with a digital computer program to obtain a quick assessment of the vehicle performance. This would be done as follows:

1. Locate deviations in measurements from nominal.
2. Determine whether these discrepancies are due to instrumentation or telemetry problems, or whether they do, in fact, represent deviations from the expected flight characteristics.
3. Determine which vehicle system or major subsystem is the initiating cause of the malfunction.
4. Provide chronological histories and information of the deviations in an organized form for the flight analyst.

Such a computer program must be flexible to adjust easily to particular mission profiles, instrumentation changes, or revised analytic requirements. Therefore, the process was divided into a number of functional steps, each of which tends to refine results obtained from previous operations. The program was then constructed in modular form to achieve the desired flexibility. The various parts of the program are discussed in the following sections.

## II. DATA PREPARATION

The source of nominal or predicted data for use in a program of this type varies considerably with the type of system being instrumented. The data in some instances may not be realistic for the first flight test in a block of vehicles. However, after a few flight tests the performance of a vehicle can be reliably predicted, and the quality of results obtained from such a program will be greatly enhanced.

Nominal data, used to compare with actual or telemetered data, are obtained from a variety of sources. These sources may be prototype testing, static testing, wind tunnel testing, laboratory testing of components, or predictions based on mathematical models of the flight configuration. If a given vehicle has been flight tested previously, the information obtained from the flight or flights is used to update or modify previously predicted data. In many instances the only concern is whether a given level or red-line

value is exceeded, which constitutes an upper limit test of a given function. Input of this type of information may be from magnetic tapes, table lookup, polynomials, or constants.

Whatever the source of data to be used for comparisons there exists a set of data for each individually telemetered measurement. Telemetry data from the flight are received in various forms at MSFC. The data have consisted of analog tapes of the telemetry data, partially reduced data, SC-4020 plots, etc. Beginning with the flight of vehicle SA-9, a new mode of data transmission will be used. Data will be recorded at KSC in real time and stored in a data center. Transmission to MSFC will be in near real time within a transmission capability of 40.8 kc. This makes a significant amount of data available to evaluating segments at MSFC immediately after launch. These are the data expected to be used in an automated evaluation.

Certain processing is now required for these data before being input to the program. This processing involves linearization of the data, conversion to engineering units, converting to even time increments for testing, and, finally, writing input tapes. The possibility of eventually using the data in the form in which it arrives from KSC is being explored. If this procedure becomes acceptable, computer time could be further reduced.

Before the comparison of telemetry data with reference data is actually carried out, there are four preparatory steps, each of which may be used or disregarded, in accordance with the requirements of each particular measurement being tested:

1. digital filtering,
2. bias adjustment,
3. in-flight calibration removal,
4. data conversion.

### III. TEST DESCRIPTION

Telemetry and reference data (in various combinations) are input to three basic types of tests;

- a. Nominal tests
  - (1) Quasi-static
  - (2) Oscillatory
- b. Correlation listings
- c. Systems tests

In general, the vehicle and its systems will operate as expected. Therefore, immediately following a flight the volume of measured data confirming this fact is of little immediate concern. Of urgent interest, however, are any measurements that indicate a deviation from the expected performance. The function of the nominal tests is to isolate such measurements, which is done by comparing periodically each individual measurement with its corresponding predicted value (within prescribed limits), which may be constant or variable. Oscillatory components caused by bending or sloshing, for example, may also be tested.

Quasi-static (Q.S.) tests, one form of the nominal tests, are applied to virtually all measurements. In some cases these measurements have been filtered to remove oscillatory components. These measurements are compared with reference data consisting of predicted or allowable values. The Q. S. tests consist of determining at what times, if any, the telemetry data deviate from the reference data by more than a specified tolerance. Deviations outside the tolerance are referred to as test failures and can be caused by: vehicle failure, malfunction, or deviation; invalid telemetry data; incorrect reference data; or unrealistic limits.

The quasi-static test does not differentiate between these possible causes. This is the task of subsequent tests (correlation listings and systems test).

Oscillatory tests are applied to individual measurement affected by bending or sloshing. The tests consist of passing selected telemetered measurements (accelerometers, rate gyros, etc.) through an appropriate digital band-pass filter and comparing the amplitude of the filtered data with a specified tolerance. Data points exceeding this tolerance are classified as "failures" as in the quasi-static tests. For these test to be meaningful, a reasonably high sampling rate of the data is required (0.02 sec intervals for bending detection). The initial data rate from KSC data center to MSFC will not be high enough to perform this test.

Only a few measurements placed at well-selected locations on the vehicle are required to determine the severity of bending and sloshing on a given flight test. It is expected that these tests can be performed on later vehicles. However, the real requirement for this degree of sophistication is still not clearly established.

Nominal tests consisting of quasi-static tests and oscillatory tests are tests of individual measurements. The output, therefore, is time-sequenced groups of data pertaining to measurements which failed these

tests. If for any reason a measurement fails, additional information is obtained by applying additional testing in the form of subsequent correlation listings. Analysis of failures in a given measurement usually involves referencing to related or redundant measurements to determine if they also failed during the same time interval. Such a comparison may yield information regarding the validity and nature of the failure. The purpose of the correlation tests, then, is to correlate related measurements, narrow down the area of malfunctions or deviations to a specific vehicle system or subsystem, or identify the detected failure as a probable instrumentation failure.

The nominal test results usually contain a significant number of failures caused by noise in the telemetered data. To reduce the number of correlation listings, which would be difficult to interpret and are usually of no significance, a persistence criterion is applied to the failed data. Thus, failures are not counted as such for correlation listing unless they persist for a specified time (usually 3 to 6 sec). It is recognized that intermittent type failures will be missed by this type analysis.

The correlation listing printout provides the time interval of the measurement failure and average data during the failure. In addition, all related measurements which fail at any point during this interval are listed. If this information is insufficient, only then would the analyst be required to search the quasi-static printout. If this is needed, his task is made easier by the correlation listing specifying which time records are of interest.

A systems test is a means for providing additional insight into the validity of failures detected in the quasi static tests. These tests consist of inserting telemetered parameters into analytically derived equations to determine if the known physical relationships between these parameters are satisfied within some specified tolerance. The function is, as the name implies, to analyze a given system, such as the control system.

This analysis can be performed by determining, among other things, if the relationship between control equation inputs and the resulting actuator position is satisfied. Additional information is obtained by determining if the sum of the moments and forces acting on the vehicle is zero. Other analytical relations are used in a similar manner and contribute additional information concerning the type or mode of the deviation if one exists.

Systems tests are run only after two failures in a given system have occurred during the same time interval and for as long as the specified persistence (3 to 6 sec). Thus far, systems tests have been developed

only for environmental pressures and dynamics and control areas, but they could be extended to other areas if needed.

#### IV. SA-5 TEST RESULTS

A pilot program was designed by RCA, Burlington, Massachusetts, under contract NAS8-11173. A schematic of the data sources and the flow of the tests is shown in Figure 1. The program was optimized for considerable flexibility by the use of control cards. The flight data from Saturn vehicle SA-5 were used to study the results that could be obtained from a fully implemented automated program. The computer time for running the S-I stage data (approximately 400 measurements) was less than 30 minutes. Also, in most cases the data rate for these runs was higher than is now considered optimum. This will result in reduced computer time for an operational case.

Typical tests were run in propulsion, flight dynamics, electrical, and environmental systems. Table 1 summarizes the number of measurements used, tests performed, data rate, and required computer time. The test time specified in Table I was for 145 seconds of S-I stage data. Also, the correlation listing input data rate is the same as the quasi-static test rate. These times do not include program compilation or printer time. It does include the read-in time for the program control cards and for data input.

Quasi-static tests and correlation listings were performed on all available propulsion data (153 measurements). The computer time required for these tests for 144 seconds of flight was 3.63 minutes. The test was conducted at two-second intervals.

The correlation listings and quasi-static tests identified all the major areas of interest obtained from a detailed analysis which are specified in the Flight Test Evaluation report [1]. Failures or deviations detected and called out were

- a. Failure of all engine-5 instrumentation which was powered by the 22.5-volt measuring system.
- b. Open gauges on LOX pump inlet temperature measurements of engines 2 and 4.
- c. Low initial pressure in LOX tank Number 1.
- d. Low initial pressure at LOX pump inlet.
- e. The control equipment supply pressure decayed out of tolerance toward the end of S-I stage flight.
- f. Hydraulic source pressures were higher than predicted.

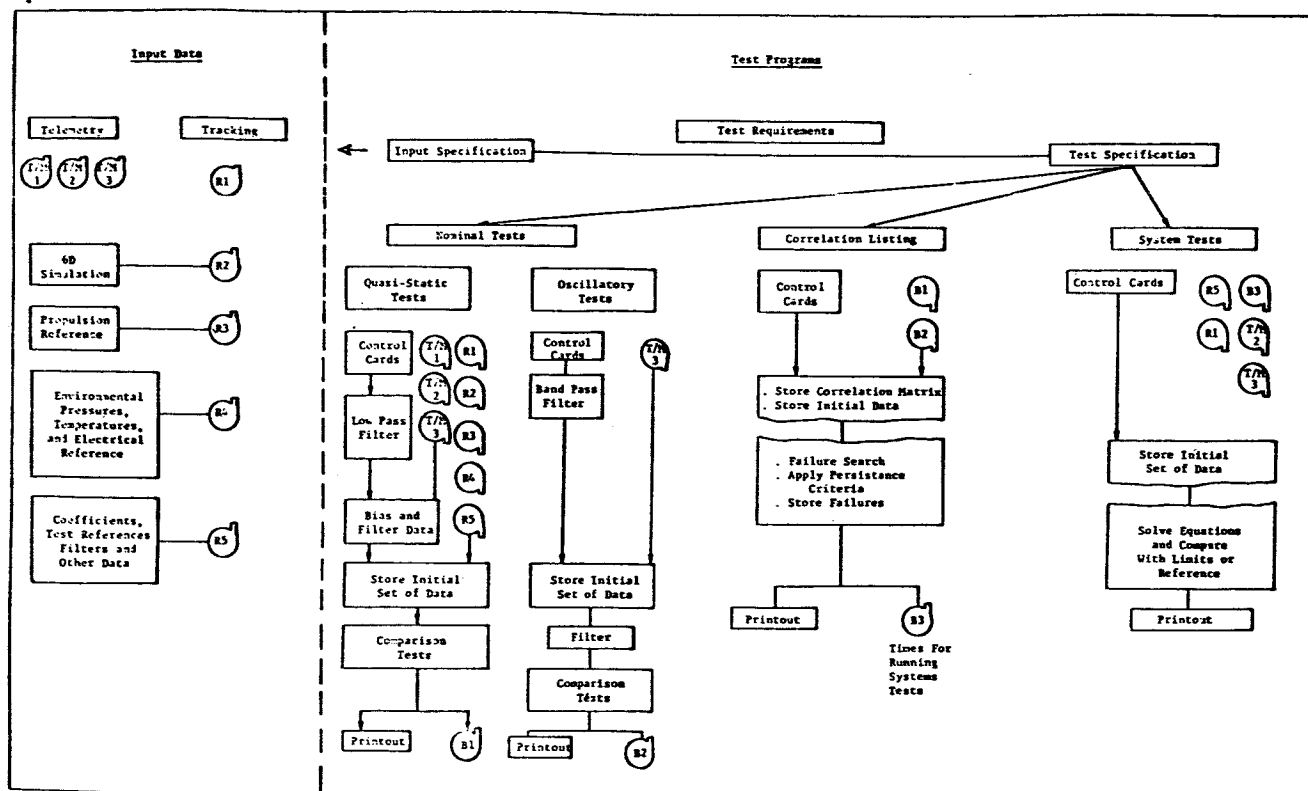


FIGURE 1. SCHEMATIC OF DATA SOURCES AND TESTS

TABLE 1

SUMMARY OF TESTS APPLIED TO SA-5 (S-I STAGE) DATA

SUBJECT	TESTS Quasi-Static (Q.S.) Tests									
	Number of Measurements	Input TM Data Rate (sec)	Q. S. Test Rate (sec)	Computer Time (min)	Number of Measurements	Number of Correlations Checked	Input Data Rate (sec)	C. L. Test Rate (sec)	Persistence Criteria (sec)	Computer Time (min)
Propulsion	153	0.1	2.0	3.01	142	611	2.0	2.0	6.0	0.62
Flight Dynamics	61	86	0.1	12.32	69	348	0.1	1.0	3.0	2.02
Electrical	25				28	172	0.1	1.0	5.0	1.86
Environmental	143	0.1	5.0	3.41	54	171	5.0	5.0	5.0	0.13
Sub-Totals	382			18.74	293	1302				4.63

A persistence criterion of six seconds was applied to the correlation listings before a deviation was called out. A sample of the information in the correlation listing is shown in Table II, which lists the prime measurement and the period of flight in which it was out of tolerance; related measurements and whether or not they are also out of tolerance, and other pertinent information. Results of the quasi-static tests are

available in printout form for additional evaluation purposes if it is deemed necessary after reviewing the results from the correlation listing. Plans are to plot the quasi-static test results as soon as this capability can be added to the program. This will be a definite advantage in using the results of this test because the shape of the deviation is always of interest from an evaluation viewpoint.



TABLE II  
SA-5 CORRELATION PARTIAL LISTING - PROPULSION

Measurements; Prime Correlated	Failure Persistence		Average T/M Value	Average $\left(\frac{T/M - Ref}{Tolerance}\right)$	Tolerance ( $\pm$ )
	From (sec)	To (sec)			
Temp H.S. Pinion Brg 6	4	144	30.3	1.15	100°F
Turbine RPM	Pass				
Press Combustion Chamber	Pass				
Press Fuel Pump Inlet	Pass				
Press LOX Pump Inlet	8	40	91.4	1.35	10 psi
Temp Turbine Shaft Bearing 7	4	144	12.2	-1.38	100°F
Turbine RPM	Pass				
Press Combustion Chamber	Pass				
Press Fuel Pump Inlet	Pass				
Press LOX Pump Inlet	8	40	91.4	1.35	10 psi
Temp Gas Gen. Chamber 2	0	144	1162	-10.1	50°F
Press Combustion Chamber	Pass				
Turbine RPM	0	144	6396	-3.44	100 rpm
Press Turbine Inlet	Pass				
Temp. Gas Gen. Chamber 3	0	144	1157	-10.3	50°F
Press Combustion Chamber	Pass				
Turbine RPM	90	100	6742	1.33	100 rpm

T/M = Telemetered

#### REFERENCES

1. Results of the Fifth Saturn I Launch Vehicle Test Flight, MPR-SAT-FE-64-15, April 1, 1964, Marshall Space Flight Center.
2. Automation of Post Flight Evaluation, Phase II Final Report, Contract NAS8-5280, Radio Corporation of America, Burlington, Massachusetts, CR588-127, Dated 31 December, 1963.
3. Automation of Post Flight Evaluation Phase III Final Report, Contract NAS8-11173, Radio Corporation of America, Burlington, Massachusetts, CR588-132, (To Be Published by May 1965).

## V. INSTRUMENTATION

N66 35553

# LOCAL MEASUREMENTS IN TURBULENT FLOWS THROUGH CROSS CORRELATION OF OPTICAL SIGNALS

by

M. J. Fisher

Illinois Institute of Technology Research Institute

and

F. R. Krause

NASA - MSFC - Fluid Mechanics Research Office

## SUMMARY

The cross correlation of optical signals is developed to provide the necessary inputs for the statistical analysis of responses like rigid body motions, unsteady forces, elastic deformations, as well as heat, mass, and momentum fluxes. For model tests of globally or locally generated turbulent fluctuations, this crossed beam correlation is the only known method which combines the necessary linear and time invariant frequency response with a sufficiently high temporal and spatial resolution and is capable of withstanding hot and burning flows.

The method estimates local power spectra, turbulence scales, convection velocities, and eddy lifetimes with the same data reduction procedures that have been developed for conventional two-point measurements with standard probes. In addition, an area integral of the space time correlation can be obtained so that "one shot" estimates of forcing functions and true three-dimensional wave number components become possible, avoiding the prohibitive by expensive translation of point probes across the source area of interest.

Because the optical wave length can be chosen from any portion of the electromagnetic spectrum, the crossed beam correlation method offers a versatility and/or selectivity not available with any standard solid probe.

## I. INTRODUCTION

Turbulent fluctuations are used as an input for the statistical analysis of responses like rigid body motions (control systems and vibration stability), unsteady forces (buffeting, instrument failure), elastic deformations (structural failure), as well as heat, mass, and momentum fluxes (aerodynamic and base

heating, jet noise). The measurement of turbulent fluctuations therefore represents one of the major problems in the development of launch vehicles [1].

The problem with fluctuation measurements is to find suitable instruments which have such a sufficiently high temporal and spatial resolution that the fluctuations are not integrated out. In supersonic flows, additional difficulties are introduced by the probe shocks which might destroy the fluctuation to be measured. We therefore propose to measure turbulent fluctuations optically.

## II. INSTRUMENTATION PROBLEMS WITH STANDARD PROBES

This paper is concerned with model tests of globally or locally generated turbulent fluctuations in transonic and supersonic flows with emphasis on fluctuation levels which are comparable to the mean values. Table 1 classifies the turbulent fluctuations around launch vehicles into three categories, each of which has its own range of independent variables. These ranges suggest the instrumentation and computational tools, and must be covered in dynamic calibration tests. They are listed in Table 1 for full scale Saturn IB and Saturn V vehicles. In wind tunnel tests, the frequencies depend mostly on the stagnation conditions (maximum escape velocity) and the shear layer thickness. The values of Table 1 are based on the largest models which can be installed in existing continuous transonic and supersonic wind tunnels without causing blockage.

The record length of a fluctuation sample is given by the smallest correlation coefficients to be measured and by the bandwidth requirements of the spectral analysis. The values in the figures of Tables 1 are based on the applications presently planned.

TABLE 1. INSTRUMENTATION AND CALIBRATION REQUIREMENTS

Type of Turbulence	Flow	Dynamic Range rms	Center Frequencies	Record Length T	Dynamic Calibration
Convected (up-stream disturbances)	Atmosphere 4 km to 15 km	Amplitudes: $\pm 15$ db Mean square levels: $\pm 30$ db	$2 \cdot 10^{-4}$ to $2 \cdot 10^{-2}$ cycles/km	15 min. to 10 hrs.	1. The average power transfer $ H(f) $ function as function of frequency $f$ and amplitude
	ground winds 0 to 500 ft.	Amplitudes: $\pm 15$ db Mean square levels: $\pm 30$ db	$10^{-4}$ to 10 cps		
Generated Globally (vortex shedding oscillating shocks wake impingement)	flight	Amplitudes: $\pm 15$ db Mean square levels: $\pm 30$ db	.5 to 50 cps	2 sec. to 5 sec.	2. The average phase shift $\Delta\phi$ between each pair of data transmitting elements as function of frequency and amplitude
	wind tunnel	Amplitudes: $\pm 15$ db Mean square levels: $\pm 30$ db	5 to 500 cps	1 min. to 30 min.	
Generated Locally (closed separation bubbles)	flight	Amplitudes: $\pm 15$ db Mean square levels: $\pm 30$ db	10 cps to 5,000 cps	2 sec. to 5 sec.	3. The standard deviations of $ H $ and $\Delta\phi$ as a function of frequency, amplitude, and record length
	wind tunnel	Amplitudes: $\pm 15$ db Mean square levels: $\pm 30$ db	150 cps to 50,000 cps	5 sec. to 500 sec.	

All statistical response calculations require elimination of the signal distortions, which have been introduced by the measuring instrument. To eliminate systematic signal distortions in the above range of independent variables, one needs a linear and time invariant frequency response up to 50,000 cps in a dynamic range of 30 db. Besides, the instrument must be exposed to pressures between 1 and 800 mm Hg and temperatures between 100 and 3000°K. Obviously, no solid probe is capable of handling all these ranges.

Dynamic signal distortions, like timing errors, shifts in reference (zero) levels, or phases, cannot be corrected. They have to be kept to a minimum. Their measurement leads to unusual extensive dynamic calibrations tests, which are also outlined in Table 1.

The hot wire is customarily used for limited investigations of cold subsonic flows. However, it is well known [4] that the interpretation of the hot wire signal is extremely difficult for the relatively high fluctuation levels of interest.

Interpretation problems are increased by an order of magnitude if other solid probes such as pitot tubes, thin film thermometers, and piezoelectric crystals are used in a high speed shear layer. These probes are very large compared to hot wires and will produce shock waves which not only distort the fluctuations, but may be of sufficient strength and extent that they will appreciably alter even the mean value properties of the flow.

### III. FLUCTUATION MEASUREMENTS USING OPTICAL TECHNIQUES

Obviously, the disturbance caused by measuring instruments can be avoided if the turbulent fluctuations are measured optically<sup>[5]</sup>. The major disadvantage of

standard optical methods, such as Schlieren, shadowgraph, or interferometry techniques, is that the measured output depends on an integral of the flow properties along the entire light path. This must normally extend through the entire test section while the technique required should give information on the local conditions existing at some point within this test section.

Local fluctuation measurements, using an optical technique, have been made successfully using a viewing technique [6]. The basis of such a technique is to focus the image of a powerful light source at the point of interest in the flow. This image is then viewed at an angle to the optical system producing it. In this way the detector system collects only light which is scattered from the point of interest, and the measured intensity can then be related to the number density of the scattering particles as shown in Figure 1.

In the example referenced, a fog tracer technique was employed to scatter visible light. Obviously, however, the use of a tracer is not necessary if secondary emission can be stimulated from species already available in the flow with radiation of shorter wavelength or electron beams [7].

Mean value measurements with viewing techniques are possible. However, the interpretation is very difficult because:

a) The light intensity (power/area, solid angle wavelength interval) is modified by polarization and extinction in the detector's field of view.

b) Scattering at large liquid and/or solid particles might contribute so much to the intensity that the contaminations are detected rather than the gas properties.

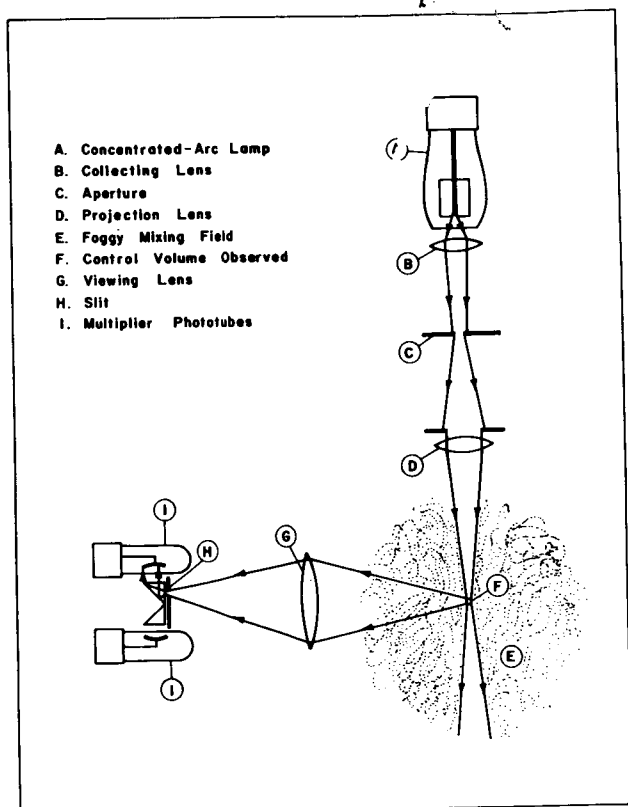


FIGURE 1. VIEWING TECHNIQUE USING OIL FOG [6]

c) Scattered radiation exhibits continuous optical spectra. Isolated lines or molecular bands are missing so that a resolution into species concentration and temperatures is very difficult.

d) Velocity measurements from Doppler shifts have been successful on laminar flows; however, the much higher velocities in turbulent flows could not be measured. It appears that bandwidth damping and wave front distortions through turbulent fluctuations of the refractive index result in a severe loss of the heterodyne signal power [5].

Fluctuation measurements are subjected to the same difficulties plus an additional one, which is caused by the power-fluctuations inside the sensitive volume [8]. Light is scattered not only at the position of interest, but also at all points between this position and the source. Thus, fluctuations of number density at any point along this path will cause the light available for scattering at the investigated point to vary. This introduces fluctuations in the scattered radiation detected which is not the result of turbulence. A possible solution to this problem is offered if the scattering process is very weak so that only a small percentage of the incident radiation is scattered from the path of the incident beam. However, because it is the same

process which is responsible for scattering both on this path and at the point of interest, this reduces the amount scattered into the detector system to a very small value. Thus, extremely powerful sources or sensitive detectors would be required merely to detect the mean value of the scattered light. The detection of small fluctuations superimposed on this mean value will increase the power requirements by another order of magnitude.

Most of the above problems are associated with the scattering process and might be avoided by using primary signals that are transmitted or emitted into the detector's field of view. This leads to the "optical cross correlation method" which measures fluctuations, but sacrifices mean value information.

Two collimated beams of radiation are crossed at the point of investigation, and the power loss of each beam, because of its passage through the flow is measured with two independent photo-detectors (Fig. 2).

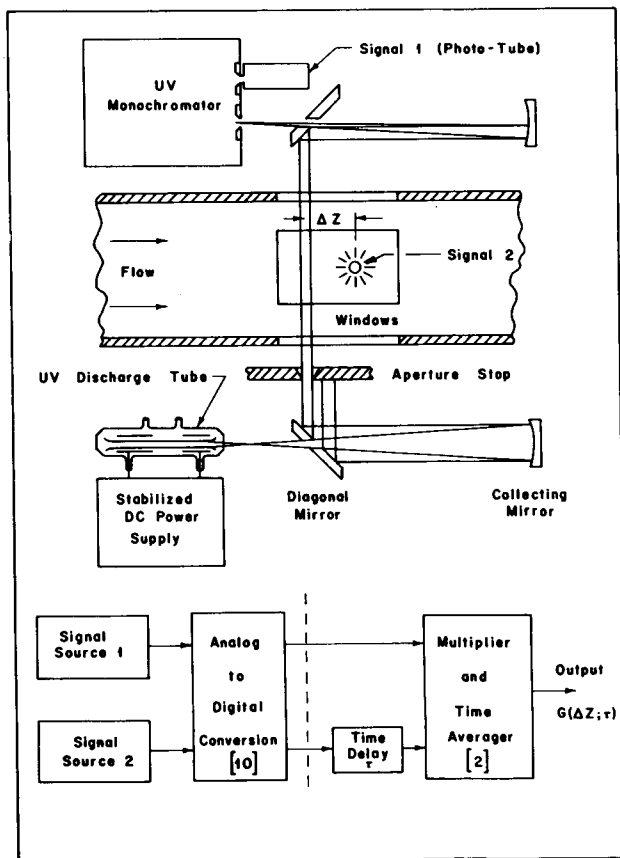


FIGURE 2. THE FIRST CROSSED BEAM CORRELATOR

Each detector alone yields only an integrated effect along the entire beam path. However, succeeding sections of this paper will indicate how forming a cross correlation between the two detector signals removes the unwanted portions of the signals and yields local information about the turbulent properties instead.

An additional interesting possibility offered by the technique is that of measuring the correlation between either different thermodynamic properties or different species concentrations. This, in principle, can be achieved by arranging one beam to be sensitive to one property, while the second detects fluctuations of the other.

The following sections give the analytical formulation of the optical cross-correlation method. For reasons of convenience, the optical signal is identified with light intensity. Very similar considerations hold for wave lengths or, in fact, any signal that can integrate flow properties such as ultrasonic waves along the line of sight.

#### IV. ANALYTICAL DESCRIPTION OF THE OPTICAL CROSS CORRELATION METHOD

The basic experimental procedure can best be described with the aid of Figure 3. A turbulent flow region is supposed to be contained within the area ABCD. The mean velocity of this flow is assumed to be perpendicular to the plane of the paper, in the Z direction.

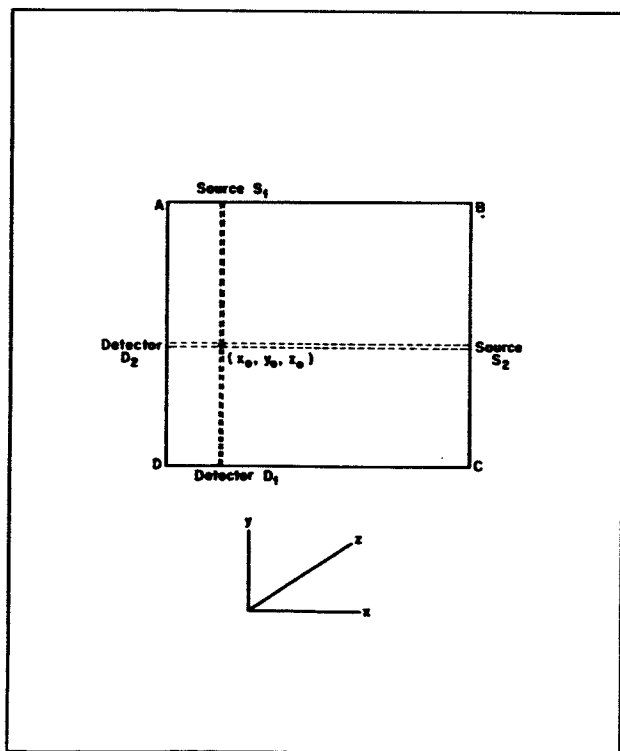


FIGURE 3. SCHEMATIC DIAGRAM OF CROSSED BEAM CORRELATION TECHNIQUE

$S_1$  and  $S_2$  are sources of electromagnetic radiation which pass collimated beams of radiation across the flow region. The intensity of the beams, after their passage through the flow, are registered by detectors  $D_1$  and  $D_2$ , respectively. The coordinate system will be such that the beam  $S_1D_1$  travels along the line  $(x, y_0, z_0)$ , while  $S_2D_2$  travels along  $(x_0, y, z_0)$ .

Let us consider initially the beam  $S_1D_1$ . The loss of intensity of this beam in passing through a small segment of the flow of length  $dx$  will be directly proportional to both the intensity of the beam incident on the segment and to the segment length. Thus, this loss can be written

$$dI(x, y_0, z_0) = -KI(x, y_0, z_0) dx,$$

where  $K$  is a constant of proportionality for which we shall coin the term "extinction coefficient." We notice here that  $K$  is used to account not only for true absorption, that is, classically at least, the conversion of electromagnetic radiation into other forms of energy, but also for any other process which may reduce the beam intensity as seen by the detector. In many applications, other intensity-reducing phenomena can be considered negligible, and the two terms then become synonymous. However, with the narrow beams to be used in the present application, as well as possible applications to "dirty flows," other processes might conceivably become appreciable, and the term extinction coefficient is used to cover those eventualities.

Electromagnetic theory shows that the value of  $K$  is a function of the local thermodynamic properties. Throughout this paper, for the sake of generality, we shall speak of fluctuations of the extinction coefficient. However, these fluctuations will always reflect changes of a flow property so that the terms should be considered synonymous. Because all thermodynamic properties will be functions of only position and time in a turbulent flow, the extinction coefficient will be similarly dependent. In addition, the value of  $K$  will also be a function of the wave length of the radiation. For the purpose of this discussion, however, we shall assume the radiation to be monochromatic, and dependence will not be explicitly shown.

Integrating along the entire path from the source to the detector, we can write the intensity received at the detector,  $D_1$ , at some arbitrary time  $t$  as

$$I_1(t) = I_0 e^{-\int K(x, y_0, z_0, t) dx}, \quad (1)$$

where  $I_0$  represents the source intensity (energy per area, solid angle, time and wave length interval).

If the extinction coefficient is now written as the sum of its time-averaged mean value and a fluctuating component, i. e.,

$$K(x, y_0, z_0, t) = \langle K \rangle(x, y_0, z_0) + k(x, y_0, z_0, t), \quad (2)$$

equation (1) can be written

$$I_1(t) = I_0 \exp \left[ - \int \langle K \rangle(x, y_0, z_0) dx - \int k(x, y_0, z_0, t) dx \right]. \quad (3)$$

We now arrange the value of the extinction coefficient (i. e., choose a suitable wave length for the radiation) so that its integrated fluctuation becomes small relative to one.

$$\int k(x, y_0, z_0, t) dx \ll 1 \quad (4)$$

This assumption is not very restrictive because the integration is to be performed over fluctuations that will be to some extent spatially incoherent. Thus, the value will always tend to be small, even if the first integral in equation (3) is not. Equation (3) can be written

$$I_1(t) = I_0 e^{- \int \langle K \rangle(x, y_0, z_0) dx} \left\{ 1 - \int k(x, y_0, z_0, t) dx \right\}. \quad (5)$$

Averaging this equation with respect to time, we obtain the time-averaged value of the intensity at the detector.

$$\langle I_1 \rangle = I_0 e^{- \int \langle K \rangle(x, y_0, z_0) dx}. \quad (6)$$

Thus, equation (5) can be written

$$I_1(t) = \langle I_1 \rangle \left\{ 1 - \int k(x, y_0, z_0, t) dx \right\}. \quad (7)$$

The fluctuating signal, relative to the mean value at the detector, is

$$I_1'(t) = I_1(t) - \langle I_1 \rangle = \langle I_1 \rangle \int k(x, y_0, z_0, t) dx. \quad (8)$$

$$* \langle K \rangle = \frac{1}{T} \int_0^T K(t) dt$$

If a similar analysis is now performed for the second beam of radiation  $S_2 D_2$ , which is assumed to be along the line  $(x_0, y, z_0)$ , the fluctuating signal at this detector is given by

$$I_2'(t) = \langle I_2 \rangle \int k(x_0, y, z_0, t) dy. \quad (8')$$

Forming next the product of these two signals and subsequently estimating the time-averaged value of this product  $G(x_0, y_0, z_0)$ , we obtain

$$G(x_0, y_0, z_0) = \frac{1}{T} \int_0^T I_1'(t) I_2'(t) dt = \langle I_1 \rangle \langle I_2 \rangle \frac{1}{T} \int_0^T \int_y \int_x k(x, y_0, z_0, t) k(x_0, y, z_0, t) dx dy dt. \quad (9)$$

Next, reversing the order of integration, this can be written

$$G(x_0, y_0, z_0) = \langle I_1 \rangle \langle I_2 \rangle \int_y \int_x \frac{1}{T} \int_0^T k(x, y_0, z_0, t) k(x_0, y, z_0, t) dt dx dy. \quad (10)$$

Thus, to summarize, taking the fluctuating portions of the signals from the two detectors and measuring their covariance, we obtain the result represented by equation (10).

## V. SPATIAL RESOLUTION OF COVARIANCES AND MEAN SQUARE VALUES

Let us now proceed to review this result in more detail by considering initially only the inner integral, i. e.,

$$R_k = \frac{1}{T} \int_0^T k(x, y_0, z_0, t) k(x_0, y, z_0, t) dt. \quad (11)$$

This term, obviously, is merely the covariance existing between the extinction coefficient fluctuations at the points  $(x, y_0, z_0)$  and  $(x_0, y, z_0)$ . If these two points are separated in space by a "large" distance (i. e., one or both are far from the point of beam intersection), then the turbulent fluctuations, and hence the fluctuations of extinction coefficient at the points, will in all probability be mutually random. Hence, the value of expression (11) for two such remote points will be zero, and these fluctuations will not contribute to the value of  $G(x_0, y_0, z_0)$ . In fact, rewriting expression (11) in terms of the root mean square values of the fluctuations at the two points and a space correlation coefficient  $R(x, y)$   $x_0, y_0, z_0$ , i. e.,

$$R_k = \left\{ \overline{k^2(x, y_0, z_0)} \overline{k^2(x_0, y, z_0)} \right\}^{\frac{1}{2}} R(x, y), \quad x_0, y_0, z_0 \quad (11')$$

indicates that only points contained in the correlated area around the point of beam intersection contribute to  $G(x_0, y_0, z_0)$ . This is because once one point is outside this area  $R(x, y)$  will be zero. Judging from previous turbulence investigations,  $R(x, y)$  will decrease continuously as the point separation is increased, and predominant contributions to the space integrals of equation (10) will come from positions close to the beam intersection point.

In an ideal situation in which  $R(x, y)^*$  is a delta function, having a finite value only when the points considered are coincident, then equation (10) becomes

$$G(x_0, y_0, z_0) = \langle I_1 \rangle \langle I_2 \rangle \overline{k^2(x_0, y_0, z_0)}, \quad (12)$$

and we see that the measured product of the two detector signals is directly proportional to the intensity of turbulent fluctuations at the point of beam intersection.

Alternately, if it is assumed that within a typical eddy length around the intersection point the turbulent intensity does not vary appreciably, equation (10) becomes

$$G(x_0, y_0, z_0) = \langle I_1 \rangle \langle I_2 \rangle \overline{k^2(x_0, y_0, z_0)} \int_y \int_x R(x, y) dx dy. \quad (12')$$

Once more the measured covariance is directly proportional to the intensity of the fluctuations although the absolute value is additionally a function of the turbulent scales. In fact if the variables are separable, i. e., if  $R(x, y)$  can be written the double integral of

$$R(x, y) = R_x(x-x_0) R_y(y-y_0),$$

equation (12') merely reduces to the product of the integral length scales in the  $x$  and  $y$  directions. These length scales are

$$L_x = \int_{-\infty}^{\infty} R(x, y=y_0) dx = \int_{-\infty}^{\infty} R(x-x_0) d(x-x_0).$$

Direct interpretation of the measured quantity  $G(x_0, y_0, z_0)$  is still possible even when the intensity of the fluctuations varies appreciably across the correlated area, as long as the variable separation assumption is still reasonable. In this case equation (10) can be written

$$G(x_0, y_0, z_0)$$

$$= \langle I_1 \rangle \langle I_2 \rangle \int_y \left\{ \overline{k^2(x_0, y, z_0)} \right\}^{\frac{1}{2}} R_y(y-y_0) dy \cdot \int_x \left\{ \overline{k^2(x, y_0, z_0)} \right\}^{\frac{1}{2}} R_x(x-x_0) dx.$$

Each separate integral can be regarded as the product of the average root mean square intensity over an integral length scale and the length scale itself. To obtain the intensity from the measured quantity, it is necessary to divide by the product of the integral length scales in the beam directions.

Apparently a good approximation to the turbulent intensity can be obtained either in the case where the turbulent scales are small (i. e., the delta function approximation) or when they are large, if the separation of variables represents a good assumption. The case not covered, that is, large scales where separation cannot be assumed, is unlikely to occur. Large lateral scales indicate that there are relatively few wave number components involved in the turbulent processes, while separation of variables assumes that the wave number components in the  $x$  and  $y$  directions do not interact appreciably. Thus, the case not covered would demand a strong interaction between a few wave number components that is not communicated to other regions of wave number space. That such a process can exist seems very unlikely.

## VI. TWO-POINT SPACE TIME CORRELATIONS

Let us next consider the result obtained if one beam is displaced from the other in the streamwise ( $Z$ ) direction, and, in addition, a time delay,  $\tau$ , is introduced between them before estimating the time-averaged cross product.

If this result is denoted by  $G(x_0, y_0, z_0 + \Delta z, \tau)$ , the result can be written formally by inspection of equation (10).

$$G(x_0, y_0, z_0 + \Delta z, \tau) = \langle I_1 \rangle \langle I_2 \rangle \int_y \int_z \frac{1}{T} \int_0^T k(x, y_0, z_0, t) k(x_0, y, z_0 + \Delta z, t + \tau) dt dx dy. \quad (13)$$

The interpretation of any one term within the double space integral is straightforward. It is the cross correlation existing between the points  $(x, y_0, z_0)$  and  $(x_0, y, z_0 + \Delta z)$  for the particular value of time delay  $\tau$ . The double space integration represents the fact that what is actually measured is an average of such correlations for all points on the beams contained within

\* Hereafter, the subscripts  $x_0, y_0, z_0$  are suppressed.



the correlated region surrounding their line of minimum separation.

The way in which the result is strongly weighted toward the properties of fluctuations at points close to this line of minimum separation is most clearly appreciated by the definition of a cross-correlation coefficient defined

$$R(x, y, \Delta z, \tau) \equiv \frac{k(x, y_0, z_0, t) k(x_0, y, z_0 + \Delta z, t + \tau)}{\sqrt{k^2(x, y_0, z_0)} \sqrt{k^2(x_0, y, z_0)}} \quad (14)$$

Equation (13) can then be rewritten

$$G(x_0, y_0, z_0 + \Delta z, \tau) = \langle I_1 \rangle \langle I_2 \rangle \int_y \int_x \left\{ \frac{k^2(x, y_0, z_0) k^2(x_0, y, z_0 + \Delta z)}{R(x, y, \Delta z, \tau)} \right\}^{\frac{1}{2}} R(x, y, \Delta z, \tau) dx dy \quad (15)$$

Let us now write this correlation coefficient as the product of two functions

$$R(x, y, \Delta z, \tau) = R(x, y) R'(x, y, \Delta z, \tau) \quad (16)$$

Here  $R(x, y)$  represents the space correlation coefficient existing between the points  $(x_0, y, z_0)$  and  $(x, y_0, z_0)$ .  $R'(x, y, \Delta z, \tau)$  is a function which relates this coefficient to the cross-correlation coefficient between the points  $(x_0, y, z_0)$  and  $(x, y_0, z_0 + \Delta z)$  for the value of time delay  $\tau$ . As long as  $R'(x, y, \Delta z, \tau)$  is not a very rapidly varying function of  $x$  and  $y$  over the region for which  $R(x, y)$  is finite, the double space integral of equation (15) will receive large contributions only from pairs of points for which  $R(x, y)$  is large, that is, points close to the line of minimum beam separation. This spatial resolution is even stronger if this line is in a region of high turbulent intensity because the intensity terms contained in equation (15) will additionally strengthen the weighting.

In view of these considerations, we can rewrite equation (16) in the form

$$R(x, y, \Delta z, \tau) = R(x, y) R'(\Delta z, \tau), \quad (17)$$

neglecting the weak  $(x, y)$  dependence of  $R'(x, y, \Delta z, \tau)$  over this limited range completely. Equation (15) can then be written

$$G(x_0, y_0, z_0 + \Delta z, \tau) = \langle I_1 \rangle \langle I_2 \rangle R(\Delta z, \tau) \int_y \int_x \left\{ \frac{k^2(x, y_0, z_0) k^2(x_0, y, z_0 + \Delta z)}{R(x, y)} \right\}^{\frac{1}{2}} R(x, y) dx dy \quad (18)$$

The significance of  $R(\Delta z, \tau)$  can now be made apparent by considering the special case of equation (17) for which  $x = x_0$  and  $y = y_0$  so that  $R(x, y) = 1$ . Thus, by definition of  $R(x, y, \Delta z, \tau)$ ,  $R(\Delta z, \tau)$  is the cross-correlation coefficient existing for time delay  $\tau$  between the points  $(x_0, y_0, z_0)$  and  $(x_0, y_0, z_0 + \Delta z)$ . This is the parameter normally measured in subsonic flows, using hot wire anemometers, from which the convection velocity and eddy lifetime is estimated.

We are now in a position to write down, by inspection, some special cases of equation (18) and to discuss how additional parameters of the turbulent field can be estimated by combination of the measured quantities represented by these equations.

#### a. Convection Velocity and Eddy Lifetimes.

Consider first the particular case of equation (18) corresponding to zero beam separation and time delay (i. e.,  $\Delta z = \tau = 0$ ). This can be written

$$G(x_0, y_0, z_0) = \langle I_1 \rangle \langle I_2 \rangle \int_y \int_x \left\{ k^2(x, y_0, z_0) k^2(x_0, y, z_0) \right\}^{\frac{1}{2}} R(x, y) dx dy \quad (19)$$

This is merely an alternative form of equation (10) from which a good estimate of the turbulent intensity can be obtained.

Comparing equations (18) and (19), we find

$$\frac{G(x_0, y_0, z_0 + \Delta z, \tau)}{G(x_0, y_0, z_0)} = R(\Delta z, \tau) \quad (20)$$

From previous discussion, however, we have identified  $R(\Delta z, \tau)$  as the cross-correlation coefficient. From the variation of this parameter as a function of beam separation and time delay, therefore, the convective properties of the turbulence can be estimated. Thus, equation (20) indicates that this correlation coefficient can be found experimentally by dividing the covariance measured between the detector signals when the beams are separated in space and in time by the covariance measured for zero separation in both space and time.

#### b. Integral Scales of Turbulence

Following equation (12) the integral length scale in  $z$  direction can be expressed by

$$L_z = \int_{-\infty}^{\infty} R(\Delta z) dz,$$

where  $R(\Delta z)$  is the space correlation coefficient. Equation (20) then indicates immediately how the required space correlation coefficient is measured. Obviously, space scales in the remaining two directions can be similarly estimated by reorientation of the beams. Further, as we have seen previously, it is these scales which we require to relate the measured value of  $G(x_0, y_0, z_0)$  to the value of the turbulent intensity.

### c. Power Spectra

It is a well established fact that the frequency spectrum and auto-correlation functions of a signal constitute a Fourier transform pair. Thus, if the auto-correlation function of a signal is known, its frequency spectrum can be determined, with the converse also being true.

Further, the auto-correlation coefficient, (i.e., the nondimensional form of the auto-correlation) is a second special case of the cross correlation coefficient, namely, its value for zero spatial separation.

$$R(0, \tau) = \frac{G(x_0, y_0, z_0, \tau)}{G(x_0, y_0, z_0)}.$$

The frequency spectrum can then be determined by Fourier transformation of the resulting function. If  $A(w)$  denotes the spectral density at frequency  $w$ , then  $A(w)$  can be written

$$A(w) = \frac{1}{\sqrt{2\pi}} \int_{-\infty}^{\infty} R(0, \tau) e^{-i w \tau} d\tau.$$

Thus, the spectral content of the signals can be estimated from the measured variation of  $G(x_0, y_0, z_0, \tau)$  as a function of the time delay  $\tau$ .

## VII. AREA INTEGRALS OF THE SPACE TIME CORRELATION FUNCTION

In the previous sections of this paper, we have indicated the way in which the various quantities measured, using a crossed beam correlation system, can be combined to yield estimates of the pointwise turbulent properties. However, it has become apparent that the technique in practice measures an integral over a correlation area surrounding the point of interest, and point properties are obtained only with the aid of some simplifying assumptions. In many important applications the space integrals over correlation areas are wanted instead of two-point correlations. In these cases the integration along the beams is wanted, and the simplifications are unnecessary.

### a. Forcing Functions

Let us consider the problem of estimating the mean square load on an infinitely long flat plate due to a distributed pressure field of the type found under a turbulent boundary layer. If the pressures are represented by  $p(x, y, t)$ , then the load at time  $t$  is

$$L(t) = \int_x \int_y p(x, y, t) dy dx.$$

We can obtain the mean square value of this load and its spectral distribution from its auto-correlation functions. This function can conveniently be written in the form

$$\overline{L(t) L(t+\tau)} = \int_x \int_y \int_{\epsilon} \int_{\eta} \overline{p(x, y, t) p(x+\epsilon, y+\eta, t+\tau)} d\eta d\epsilon dy dx. \quad (21)$$

The contribution to this integral of a small area around the point  $(x_0, y_0)$  is

$$L(x_0, y_0, \tau) = \int_{\epsilon} \int_{\eta} \overline{p(x_0, y_0, t) p(x_0 + \epsilon, y_0 + \eta, t + \tau)} d\eta d\epsilon. \quad (22)$$

It is apparent therefore that even to estimate the contribution of a small region of turbulence to the total, we need a knowledge of the cross correlation existing between the fluctuations at one point in the region and all other points with which a correlation exists.

Obviously, the exact evaluation of equation (22) from point measurement is not physically possible. Normally, simplifying assumptions are employed to reduce the amount of data required. For example, if complete homogeneity of the turbulent field is assumed, a line of transducers extending in one direction over the correlation area will suffice. Even in such a case the amount of data reduction required to obtain just one value of the auto-correlation function is still very large.

Consider next the comparison of equation (22) with equation (13). By putting  $\Delta z = 0$ , rewriting the space variables in equation (13) in the form

$$x = x_0 + \epsilon$$

$$y = y_0 + \eta,$$

and replacing the time integral by the overbar notation of equation (22), we obtain

$$G(x_0, y_0, z_0, \tau) =$$

$$\langle I_1 \rangle \langle I_2 \rangle \int \int_{\eta \in} \overline{k(x_0 + \epsilon, y_0, z_0, t) k(x_0, y_0, z_0, t + \tau)} d\epsilon d\eta. \quad (23)$$

Obviously, there is a strong resemblance and, with one additional assumption, the functional similarity can be made complete. We assume that there exists one direction along which the turbulence is homogeneous. Let this be the x direction so that we can write

$$\begin{aligned} \overline{k(x_0 + \epsilon, y_0, z_0, t) k(x_0, y_0 + \eta, z_0, t + \tau)} &= \\ &= \overline{k(x_0, y_0, z_0, t) k(x_0 - \epsilon, y_0 + \eta, z_0, t + \tau)}. \end{aligned}$$

In this case equation (23) becomes

$$\begin{aligned} G(x_0, y_0, z_0, \tau) &= \\ &= \langle I_1 \rangle \langle I_2 \rangle \int \int_{\eta \in} \overline{k(x_0, y_0, z_0, t) k(x_0 - \epsilon, y_0 + \eta, z_0, t + \tau)} d\epsilon d\eta, \quad (24) \end{aligned}$$

which is now exactly the wanted point load  $L(x_0, y_0, \tau)$

It is to be emphasized immediately that, although we have demonstrated this similarity in terms of a specific example, chosen more for its well-known nature rather than its particular applicability to light absorption measurement, there is a wide range of problems in which integrals over a correlation area or volume need to be evaluated. In Lighthill's [11] theory of aerodynamic noise production, an integral of a stress tensor over a correlated volume is involved, while Williams [12] has shown that this "should be replaced by an integration over the correlation area normal to the radiation direction in association with an integration over the moving axis time scale, whenever Mach waves are under study." F. Krause [3] showed recently that the forcing functions of dangerously large skin vibrations below free shear layers and oscillating shocks can be obtained from the area integral of the pressure cross correlation function. For the easier case of homogeneous turbulence, A. Powell [13] has shown that the generalized forces can be obtained directly from the wave number components of the pressure fluctuations which will be discussed in the subsequent section.

These considerations indicate that not only can we obtain estimates of pointwise turbulent properties from the crossed beam correlation method, but, with the assumption of flow homogeneity in only one direction, the directly measured quantities are those required in situations where we wish to estimate the strength of the turbulence as a forcing function. This is normally

the practical application of any turbulence investigation. In cases where the forcing function is represented by an integral over a correlated area, the cross correlation of the detector signals is exactly the required quantity. If a volume integral is involved, the technique performs two of the space integrations automatically, while the third is obtained by successive beam displacement. The reduction in experimental effort and data reduction, compared with that which would be necessary if pointwise measurement were employed, is obviously still very considerable.

#### b. Measurement of the Three-Dimensional Wave Number Spectrum

We shall now conclude this section with consideration of the way in which the crossed beam correlation technique can be employed to measure a very fundamental and useful property of any turbulent field, namely, its three-dimensional wave number spectrum.

Fourier or wave number components have to be used to resolve the energy of the turbulent fluctuations into a number of additive components or "energy levels" such that the general concepts of statistical mechanics might be used to infer general results for complicated flows from simple model tests. Quoting Batchelor [14], Fourier's analysis corresponds to a general resolution into components of the motion of different linear size. It also gives a definite meaning to the idea of the different degrees of freedom possessed by the fluid. Large scale and small scale components of the motion are not attached to limited portions of the fluid in the way that different degrees of freedom of a simple gas are attached to different molecules; nevertheless, we can think of turbulent motion as consisting of a large number of different sized eddies or wave number components which make additive contributions to the total energy and which interact with each other in a way demanded by the nonlinear term in the equations of motion.

The problem with true wave number components is that they represent a mean square "amplitude" averaged over a wave front of infinite size. This cannot be measured with point probes since they catch only the fluctuation along one line. Because the crossed beam correlation provides an area integral over a plane "wave front," however, it can be used to measure a true three-dimensional wave number component propagated normal to the beam intersection plane, that is, along the line of minimum beam separation.

We consider the definition of wave number components as given by Hinze [4]. Using the notation of this paper, and, assuming the process to be statistically stationary, we can write

$$E(k_1, k_2, k_3)$$

$$= \frac{1}{8\pi^3} \int \int \int_{-\infty}^{\infty} v(x_0, y_0, z_0, t) v(x_0 + \epsilon, y_0 + \eta, z_0 + \zeta, t)$$

$$\exp[-i(k_1\epsilon + k_2\eta + k_3\zeta)] d\epsilon d\eta d\zeta,$$

where  $v(x_0, y_0, z_0, t)$  and  $v(x_0 + \epsilon, y_0 + \eta, z_0 + \zeta, t)$  represent turbulent fluctuations occurring at time  $t$  at the points  $(x_0, y_0, z_0)$  and  $(x_0 + \epsilon, y_0 + \eta, z_0 + \zeta)$ . The terms  $k_1, k_2$  and  $k_3$  represent wave number components in the  $x, y$ , and  $z$  directions, respectively.

Consider now the value of  $E(0, 0, k_3)$  given by

$$E(0, 0, k_3) =$$

$$\frac{1}{8\pi^3} \int \int \int v(x_0, y_0, z_0, t) v(x_0 + \epsilon, y_0 + \eta, z_0 + \zeta, t) e^{-ik_3\zeta} d\epsilon d\eta d\zeta$$

Combining equation (13), (putting  $\tau = 0$ ), the definitions of  $\epsilon, \eta$ , and  $\zeta$ , i. e.,

$$x = x_0 + \epsilon$$

$$y = y_0 + \eta$$

$$z = z_0 + \zeta,$$

and assuming flow homogeneity in the  $x$  direction, this equation can be written

$$E(0, 0, k_3) = \frac{1}{8\pi^3} \int G(x_0, y_0, z_0 + \Delta z) e^{-ik_3\Delta z} dz.$$

We have already seen that  $G(x_0, y_0, z_0 + \Delta z)$  is merely the covariance between the detector signals when they are displaced by a distance  $\Delta z$ . Thus, a number of determinations of this covariance as a function of  $\Delta z$  will permit the integration to be performed, and the  $k_3$  wave number spectrum can be determined. Also, reorientation of the beams will allow other spectra,  $E(k_1, 0, 0)$  and  $E(0, k_2, 0)$ , to be determined, although to determine all three, we do need two directions of homogeneity.

## CONCLUSIONS

Our discussion has shown that the cross correlation of optical signals does not strictly yield point properties of the flow, but rather an average value of such properties over a correlated area surrounding the point of beam intersection is measured. However, the strong weighting of this average toward the values

at the point of beam intersection indicates that acceptable spatial resolution of turbulent properties will be obtained.

Although there is a strong tendency to attempt to characterize a turbulent field in terms of such properties, this is not always necessary or experimentally desirable. When we wish to evaluate the effectiveness of a turbulent region as a forcing function, a considerable amount of integration of pointwise properties over a correlated region is normally necessary. The bulk of information necessary to make such an evaluation from pointwise determined quantities is very considerable, and certain simplifying assumptions are normally introduced to reduce it to a manageable amount. The crossed beam correlation method, on the other hand, performs a considerable amount of the required integration automatically, and the measured quantities often resemble very closely the required integrals. Thus, exact evaluation of the effects of a region of turbulence are much more practical using this method than would be the case if only point probe information were available.

It appears that for those flows where point probes cannot be employed the crossed beam correlation technique offers for the first time a method from which local statistical properties of the flow can be estimated. In those problems in which the effects of a region of turbulent flow are of interest, the technique offers a comparatively direct method for evaluation of the required functions, offering an advantage over point probe methods.

Finally, it is emphasized that the radiation to be absorbed can be chosen from any portion of the electromagnetic spectrum. Thus, a versatility and/or selectivity is offered by this method which is not available with many standard measuring systems.

## REFERENCES

1. Geissler, E. D.: Appointment of Working Group for the Statistical Analysis of Turbulent Fluctuation, NASA-MSFC Office Memorandum R-AERO-DIR, dated March 31, 1964.
2. NASA, George C. Marshall Space Flight Center: The Vibration Manual (1st ed 1964)
3. Krause, F.: Wall Pressure Fluctuations and Skin Vibrations with Emphasis on Free Shear Layers and Oscillating Shocks, NASA TMX 53189, Oct. 1964.

4. Hinze, J. O., Turbulence, An Introduction to its Mechanism and Theory, McGraw-Hill Book Company (1959).
5. Krause, F.: Flow Diagnosis with Scattered Light. NASA-MSFC Office Memo, R-AERO-AM-65-2.
6. Becker, H. A., 1961, Concentration Fluctuations in Ducted Jet Mixing, Ph.D. Thesis Massachusetts Institute of Technology, (1961).
7. Krause, F.: Optical Measurements of Temperature and Density with High Temporal and Spatial Resolution, NASA-MSFC Office Memo, M-AERO-A-66-63, July 1963.
8. Fisher, M. J. (1964), Optical Measurement with High Temporal and Spatial Resolution, IIT Research Institute Progress Report N6092-5, Contract No. NAS8-11258.
9. Fisher, M. J., (1963), Measurement of Local Density Fluctuation in a Turbulent Shear Layer, IIT Research Institute, Proposal No. 64-603N.
10. Contract NAS8-1125, Progress Report N6092-6, Dec. 15, 1964.
11. Lighthill, M. J. (1954), On Sound Generated Aerodynamically II: Turbulence as a Source of Sound, Proc. Roy. Soc. 222A.
12. Williams, J. E., Ffand Maidanik, C., The Mach Wave Field Radiated by Supersonic Turbulent Shear Flows, Bolt Beranek and Newman Rept. (1964).
13. Powell, A.: On the Response of Structures to Random Pressures and to Jet Noise in Particular, Chapt. 8 in Random Vibration, Vol. 1, St. H. Crandall ed, Cambridge: MIT Press 1958.
14. Batchelor, G. K.: The Theory of Homogeneous Turbulence, Students ed., Cambridge, The University Press, 1960.

# HOT WIRE TECHNIQUES IN LOW DENSITY FLOWS WITH HIGH TURBULENCE LEVELS

by

A. R. Hanson,\* R. E. Larson\*, and F. R. Krause\*\*

## SUMMARY

Large turbulence levels in the separation and re-attachment regions of free shear layers produce severe heat fluxes and acoustical loads on launch vehicles. The direct investigation of these phenomena requires an instrument that combines a high temporal and spatial resolution with a highly linear and time invariant frequency response. This paper summarizes extensive static and dynamic calibrations of modern hot-wire systems that might be used in low density flows with high relative fluctuation levels.

A review of the hot-wire heat loss equations indicated that a time invariant frequency response can be obtained at high turbulence levels only if the probes are operated at constant temperature. The static calibration of two modern constant-temperature hot-wire systems (a modified Kovasznay circuit and the DISA anemometer) combined with hot-wire and hot-film sensors showed:

1) Significant changes of the calibration constants at low densities (approximately 1 percent of atmospheric).

2) A large increase of wall proximity effects at low densities. At a pressure of approximately 0.1 atm, the effect of a wall at room temperature is detectable at a distance of roughly 1000 hot-wire radii.

3) Considerable changes occur in the slope of the wire-resistance temperature relation, especially at low temperatures. These changes are attributed to small impurities and the mechanical drawing process which make it necessary to repeat the resistance-temperature calibration for each batch of wire.

The dynamic calibration showed that the temporal resolution is insufficient. Relative to the center frequencies of observed narrow-band components, the cut-off frequency (3 db down) is an order of magnitude

lower at atmospheric density, while it is two orders of magnitude lower at low densities. This means that the results can be only of a qualitative nature.

To obtain measurements which warrant a quantitative cross-correlation analysis, it is proposed to:

1) keep the density levels always above 10 percent of the atmospheric value.

2) modify the electronic circuits to allow precise neutralization of reactive impedances, which limit the maximum usable frequency.

3) simulate a higher stream velocity by replacing the hot wire by a hot film with an internal coolant flow which can be controlled.

4) lower the thermal inertia of the film by decreasing the film thickness and using new film materials with higher  $C_w/\alpha$  values.

## DEFINITION OF SYMBOLS

Symbol	Definition
M	u/a mach number
U	stream velocity
a	local sound speed
$\rho$	density
$T_e$	equilibrium (recovery) temperature of unheated wire
$T_t$	total temperature
$T_w$	average hot-wire temperature
$\eta$	$\frac{T_e}{T_t}$ (temperature recovery ratio)
$\mu_t$	viscosity of air at stagnation point
$C_p$	specific heat of air
k	thermal conductivity of air

\* This work was partially performed by the Applied Science Division of Litton Systems, Inc., under Contract NAS8-11299.

\*\* George C. Marshall Space Flight Center

Pr	$\frac{C_p \mu}{k}$ (Prandtl number)
Re	$\frac{\rho U D_w}{\mu}$ (Reynolds number based on wire diameter)
$D_w$	diameter of wire
$l$	length of hot wire
$A_w$	$\pi D_w l$ (surface area of hot wire)
$I$	$\sqrt{I^2}$ + i wire current
$R$	$\langle \bar{R} \rangle + r$ wire resistance
$H$	$I^2 R$ total rate of heat loss from hot wire
Nu	$\frac{h D_w}{k}$ (Nusselt number)
$h$	$\frac{H}{A_w (T_w - T_e)}$ (heat transfer coefficient)
Kn	$\frac{\lambda}{D_w}$ (Knudsen number)
$\lambda$	mean free path

## I. INTRODUCTION

There is an urgent need for a technique which will allow experimental determination of turbulent properties of both attached and free supersonic shear layers. The prediction of heat, mass, species, and momentum fluxes in the environment of rocket launch vehicles and a more detailed understanding of aerodynamic noise production by supersonic jet and rocket exhausts, to mention only two, both require a knowledge of the associated turbulent field.

In particular, flow phenomena and heat transfer have been studied behind a blunt trailing edge in a two-dimensional, supersonic stream ( $M = 3$ ) with a turbulent forebody boundary layer [1]. Extensive pitot tube traverses, hot-wire traverses, and heat transfer measurements suggest that a new type of shear layer might exist below the base recirculation zone, and that "resonance vibrations" might be superimposed [2], such that the current models of base heating and base pressure fluctuation may have to be modified.

The surest way to arrive at definite conclusions about the suspected new type of shear layer is through a correlation of velocity and temperature fluctuations.

One-point correlations would show the structure of the sublayer and the spectral content, whereas two-point correlations are needed to disentangle sound radiation and turbulent convection. All these measurements require a linear and time-invariant instrument with a high temporal and spatial resolution, such that a relative cross correlation estimate can be obtained [3] without integrating out the fluctuations which are to be correlated.

The hot wire is the only instrument that has been applied successfully to turbulence investigations in shear layers [4]. However, the proposed measurements are unusual since the rms levels in the recirculation zones of interest might very well be so large that they are comparable to the mean values. It is well known [5] that the interpretation of hot-wire signals is then difficult, even at atmospheric densities. The densities around transonic and supersonic wind tunnel models are sometimes much lower than atmospheric, so additional frequency response problems are to be expected. This paper gives the results of careful static and dynamic calibrations of modern hot-wire systems in low density flows with high turbulence levels. These results may be useful in future investigations of separating and reattaching free shear layers.

## II. REVIEW OF WIRE HEAT LOSS IN TURBULENT FLOWS

The heat loss equation relates the flow properties such as velocity, pressure, and temperature to the electrical power dissipated in a heated wire, which is detectable from measurement of the wire resistance  $R_w$  and wire current  $I$ .

For steady and incompressible flows, the heat loss equation was established by King [6]. His work has been continued by the authors cited in References 7 through 14. Their findings affirm the approximate heat loss relationship

$$Nu_m = A + B \cdot Re^{1/2} = 0.32 + 0.43 Re^{1/2}, \quad (1)$$

where  $Nu_m$  is the Nusselt number based on uncorrected measured values of heat loss  $H$ .

$$Nu_m = \frac{H}{\pi l k_t (T_w - T_e)} = \frac{I^2 R_w}{\pi l k_t (T_w - T_e)} \quad (2)$$

In this paper the empirical relation (equation 2) is written in terms of the mass flux component  $\rho U$  as

$$\frac{I^2 R_w}{T_w - T_e} = A' + B' (\rho U)^{1/2}. \quad (3)$$

In this case, the empirical factors

$$A' = A \pi l k_t$$

and

$$B' = B \pi l k_t \sqrt{\frac{D_w}{\mu}}$$

depend on temperature only. In equations (1) through (5), all quantities are to be taken as averaged in time and over the length of the wire. Moreover, A and B are not accurately given by theory, and must therefore always be obtained experimentally [5].

Equations (3) through (5) are the basis of the usual hot-wire applications. Unfortunately, they will be erroneous at low densities, where the mean free path  $\lambda$  becomes as large as the wire diameter ( $Kn = \lambda/D_w \approx 1$ ) [15] through [18].

The density behind the present two-dimensional base model [1] is so low that slip flow effects have to be considered. The operational regime is shown in Figure 1. Therefore, a careful calibration study was conducted with emphasis on low pressures. The results are given in Sections IV and V.

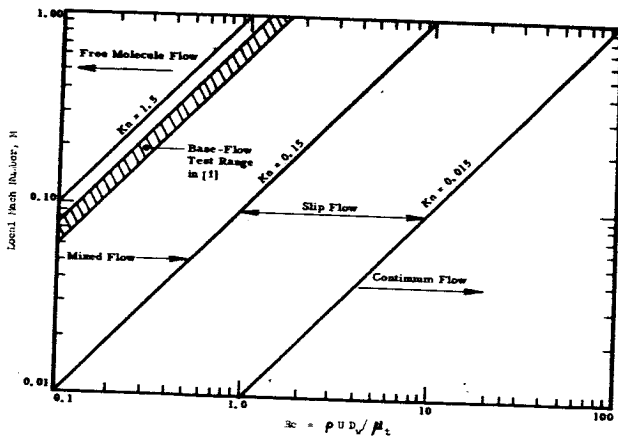


FIGURE 1. HOT-WIRE OPERATIONAL REGIME IN THE BASE FLOW REGION

The values of A' and B' are customarily obtained in calibration ducts with a smooth flow, where the fluctuations are very small. The results of this "static" calibration are then applied to fluctuation measurements, where neither the frequency nor the rms levels is small. Analytically, this procedure amounts to the assumption of a "quasi-steady" heat transfer; that is, the velocity fluctuations

$$\begin{aligned} (\rho U)' &= \rho U(t) - \lim_{T \rightarrow \infty} \frac{1}{T} \int_0^T \rho U(t) dt \\ &= \rho U(t) - \overline{\rho U}, \end{aligned} \quad (6)$$

the current fluctuation

$$i = I(t) - \bar{I}, \quad (7)$$

and the resistance fluctuations

$$r_w = R_e - \bar{R}_w \quad (8)$$

are treated as differentials. Applying the differential operator

$$d = \left( \frac{\partial}{\partial R_w} \right) \bigg|_{R_w = \bar{R}_w} r_w + \left( \frac{\partial}{\partial I} \right) \bigg|_{I = \bar{I}} i \quad (9)$$

to the left-hand side of equation (3) we obtain the dynamic response relation

$$\begin{aligned} \frac{\bar{I}^2}{(\bar{T}_w - T_e)^2} (\bar{T}_w - T_e - \frac{\bar{R}_w}{\partial R_w / \partial T_w}) r_w \\ + \frac{2 \bar{I} \bar{R}_w}{\bar{T}_w - T_e} i = \frac{B'}{2 \sqrt{\rho U}} (\rho U)'. \end{aligned} \quad (10)$$

A direct measurement of mass flux fluctuations is then possible in two alternate ways

1) The wire is operated at constant current ( $i=0$ ). The mass flux fluctuations are then calculated from the resistance fluctuations  $r_w$ .

2) The wire is operated at constant resistance ( $r_w=0$ ), that is, at constant temperature. The mass flux fluctuations are then related to the current fluctuations  $i$ .

Hinze [5] has shown that the constant-temperature method is really superior for the following reasons:

1) The values of A' and B' are true constants even for large fluctuations.

2) The thermal inertia (effect of finite heat capacity) can be reduced such that the quasi-steady response relation may be applied at frequencies which are one to two orders of magnitude higher than those that would give the same dynamic error in an uncorrected constant-current hot-wire set. Therefore, the quasi-steady response relation is mostly used on constant-temperature sets without correcting for thermal inertia.

3) The nonlinear signal distortions of the constant-temperature method are about three times



smaller than those on the constant current set. Moreover, it is possible to use two squaring circuits whose amplitude characteristics balance the nonlinear behavior of the hot-wire response, shown by equation (3) such that a practically linear relation between output voltage and velocity can be realized even for relatively large fluctuations.

4) The wire is self-protecting, since catastrophically high temperatures are avoided by its mode of operation.

In view of these considerations, the present investigations have been performed with constant-temperature systems.

The above heat loss relations are restricted to incompressible flows. In compressible shear layers, the entropy mode will add new temperature fluctuations. However, the Mach number of the recirculated flow seldom exceeds a value of 0.6; therefore, it is reasonable to assume that velocity fluctuations produce a much stronger signal than temperature fluctuations. A test of this assumption in the base recirculation zone requires the separation of temperature and velocity fluctuations. Kovaszny [9] has shown that this may be accomplished by operating the hot-wire at three overheats. When the overheat is very small, the wire is predominantly temperature sensitive; but as the overheat is increased, the response to velocity fluctuations also increases. The velocity and temperature fluctuations might thus be separated by comparing the hot-wire signals for the different overheats.

### III. FACILITIES

The electronic equipment required for constant-temperature operation is much more complicated than that used in the constant-current application, such that the constant-temperature method is usually used only when large fluctuations have to be recorded. In fact, the constant-temperature circuits have been plagued by unstable oscillation, and only after World War II have carrier wave systems with sufficiently stable feedback become available which give the equipment adequate stability [5].

#### A. Circuits

Mean velocity measurement in the base recirculation zone and probe calibrations were initially performed with a constant-temperature manually balanced set (Fig. 2). Voltages were accurately measured with a Fluke Model 821A precision differential voltmeter which can measure voltages to  $\pm 0.01$  percent (of 10  $\mu$ V.) Probe resistances were measured with a Leeds and Northrup Model 4760 Wheatstone bridge which has a reading accuracy of  $\pm 0.01$  ohm.

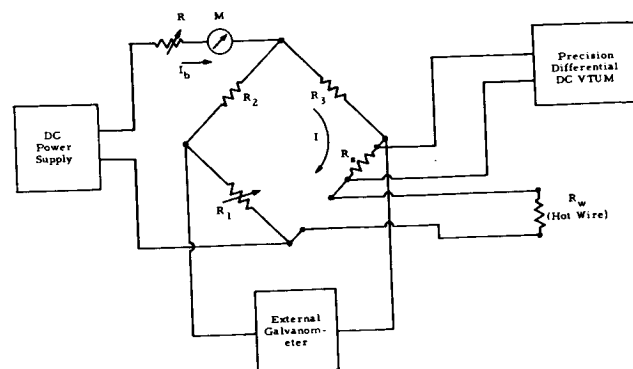


FIGURE 2. SCHEMATIC OF MANUALLY BALANCED HOT-WIRE BRIDGE

Fluctuating velocities were measured by a constant-temperature anemometer with a frequency response from dc to approximately 15 kc/sec, the instrument was constructed according to a circuit developed by Kovaszny [20]. The basic features of this circuit are shown in Figure 3. An electronic control circuit senses bridge unbalance, and through negative feedback adjusts  $I_w$  to balance the bridge against fluctuations in mass flux  $\rho U$  over a frequency range of 0 to 15 kc/sec. The linearizing circuit performs two squaring operations, with zero offset, to make  $E_{LO}$  proportional to  $\rho U$ . This linear relation is particularly convenient for calibration and measurement.

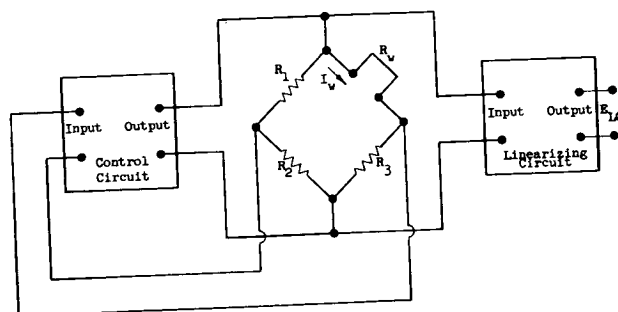
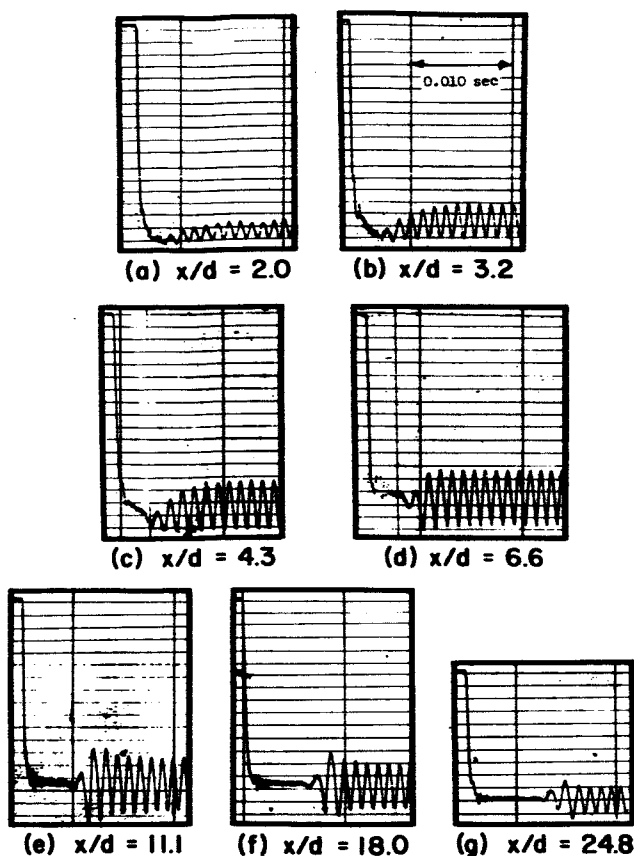


FIGURE 3. HOT-WIRE CIRCUIT FOR CONSTANT-TEMPERATURE OPERATION WITH LINEARIZED OUTPUT

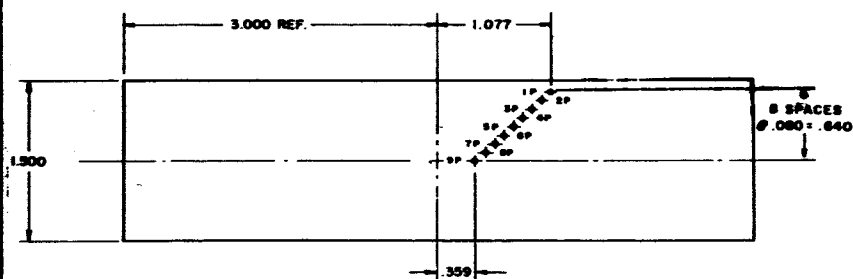
Karlsson [21], who used Kovaszny's apparatus, has reported its frequency response as approximately flat from dc to 17 kc/sec. Measurements made on the present equipment confirmed the flat response from dc to about 15 kc/sec. In this work, voltages from a signal generator were injected into the hot-wire bridge. Further evidence of the response of the present equipment has been obtained from some shock tube studies of vortex shedding from a circular cylinder carried out by Hanson and Strom [22]. Figure 4 shows typical records of the signal from the hot-wire anemometer when the probe is placed in the wake of the cylinder.



CYLINDER DIAMETER,  $d = 0.022$  in.

(Modified Kovasznay Circuit;  $x$  is Distance of Probe Downstream of Cylinder Axis).

FIGURE 4. HOT-WIRE TRACE SHOWING VORTEX SHEDDING FROM CIRCULAR CYLINDER IN SHOCK TUBE.



REAR VIEW OF MODEL

FIGURE 5. HOT-WIRE TRAVERSE OF TWO-DIMENSIONAL BASE BOUNDARY LAYER

These records were made with a Model 1108 Honeywell Visicorder equipped with moving coil galvanometers. Although the flat galvanometer response extends only to 5 kc/sec, it is evident from Figure 4 that the hot-wire anemometer circuit is compensating in a way to record steep wave fronts associated with higher frequencies.

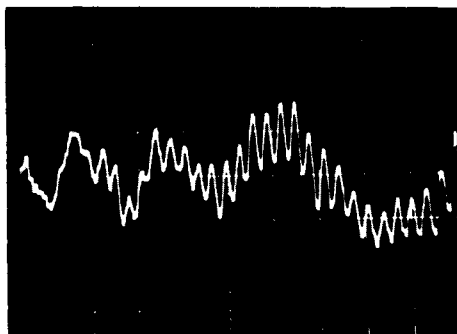
Unfortunately, a frequency cut-off at 15 kc/sec is too low. A hot-wire traverse of a two-dimensional base boundary layer, as shown in Figure 5, indicates that the velocity fluctuations have narrow band components with center frequencies around 6 and 23 kc/sec. A typical oscilloscope trace is shown in Figure 6. To extend the range of measurable frequencies, the DISA 55A01 constant-temperature anemometer was purchased. Staritz [23], using an earlier version of this instrument, reports upper frequency limits of 6.5 kc/sec at zero velocity and 25 kc/sec at 66 ft/sec. These values were obtained at atmospheric densities.

The circuit diagram of the DISA anemometer is shown in Figure 7. It is possible to read voltages to an accuracy of  $\pm 1$  percent. This solution was found to be adequate for the wind tunnel measurements, but the Fluke differential voltmeter was used for probe calibrations. Velocity fluctuation data, in the form of rms values, were read on the DISA meter and on a Ballantine Model 320 true rms electronic voltmeter. Traces of the fluctuating velocities were recorded from a Tektronix Model 561A oscilloscope using a polaroid camera.

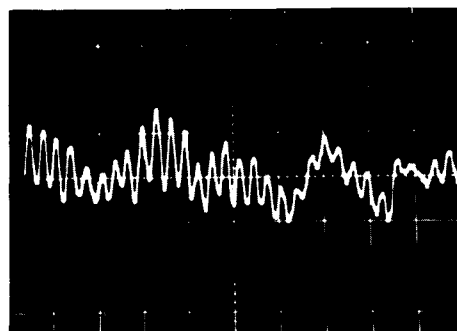
#### B. Probes

Because of the thinness of the base velocity boundary layer (of the order of 0.05 in.), the hot-wire

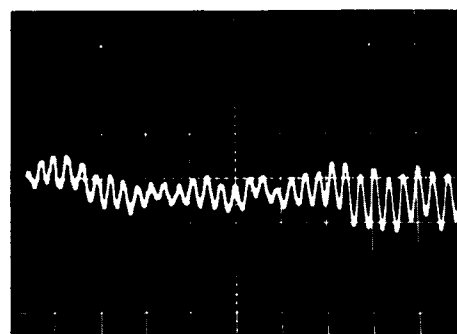
$x = 0.016$  in  
 $y = 0.45$  in  
 $\bar{e} = 33.4$  mv  
 $\Delta T = 400$  °C



$x = 0.016$  in  
 $y = 0.45$  in  
 $\bar{e} = 24.0$  mv  
 $\Delta T = 200$  °C



$x = 0.016$  in  
 $y = 0.45$  in  
 $\bar{e} = 17.7$  mv  
 $\Delta T = 100$  °C



(DISA Anemometer; sweep rate, .5 m sec/cm; sensitivity, 50 m V/cm).

FIGURE 6. OSCILLOSCOPE TRACES OF TURBULENT VELOCITY FLUCTUATIONS.

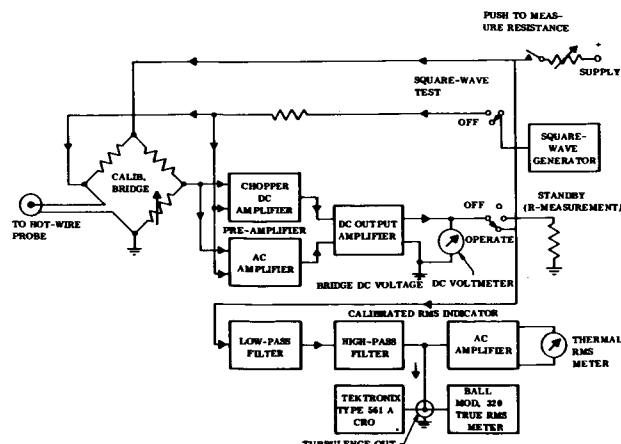


FIGURE 7. BLOCK DIAGRAM OF DISA CONSTANT-TEMPERATURE ANEMOMETER AND ACCESSORY EQUIPMENT

probes used in this investigation were necessarily smaller than those used in normal wind tunnel applications. For probings in an attached boundary layer, only the size of the probe near the sensing element is critical. Disturbances introduced into the boundary layer by the probe holder can be minimized by streamlining and by proper sweep. In the present application the probe holder can interfere with the recirculatory flow processes and modify the base boundary layer development [1].

The major design objective was to minimize disturbances by miniaturizing the sensing element and the probe-holder combination. The studies reported in Reference 1 indicate that minimum disturbance of the flow field results when the probe is inserted into the recirculation zone through the base plate. The probes protruded from the base plate through openings similar to static pressure taps. Nine probing positions were provided in a slanted array to minimize disturbances of the boundary layer flow and to allow probings at various vertical stations (Fig. 5). The probe holders were made of stainless steel tubing with a 0.32-inch diameter; the tubing slides within a stainless steel sleeve of 0.035-inch inside diameter. Figure 8 shows details of the probe installation.

Two major probe designs were used for these studies. In the first design, the sensing element was made of 0.00025-inch diameter platinum-irridium (80 Pt-20 Ir) shown in Figure 9. Variations of this design

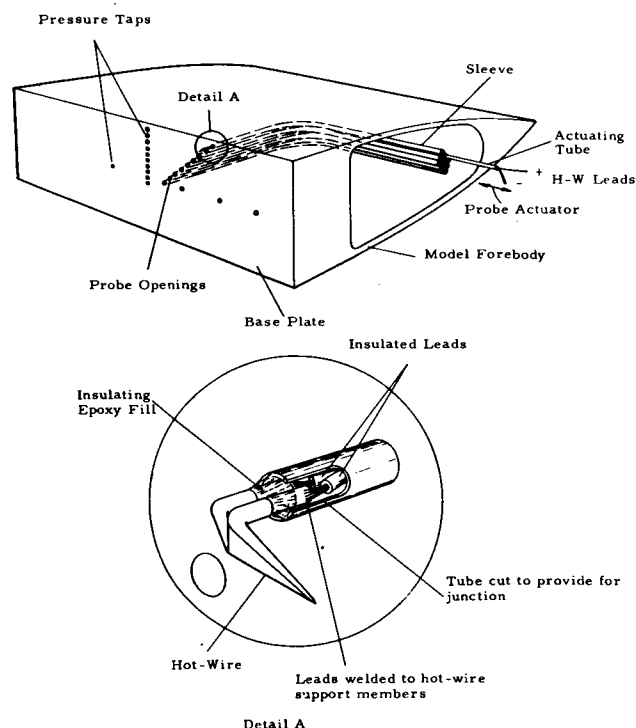


FIGURE 8. SCHEMATIC OF HOT-WIRE PROBE INSTALLATION OF MODEL BASE PLATE

incorporated a bent probe for boundary layer measurements (Fig. 10) and a straight version for probings in the recirculation zone. In the second design, a hot-film probe was formed of a 0.001-inch diameter quartz rod (Fig. 11); a platinum film 1000 Å thick was deposited on the rod as the sensing element. These hot-film probes were manufactured to our specifications by Thermo-Systems, Inc., of Minneapolis, Minnesota. Magnified photographs of both types of probes are shown in Figure 12.

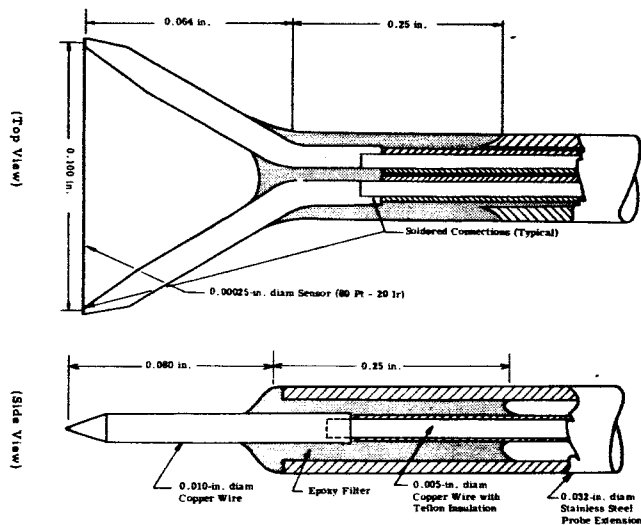


FIGURE 9. DETAIL OF STRAIGHT PROBE TIP WITH HOT-WIRE SENSOR

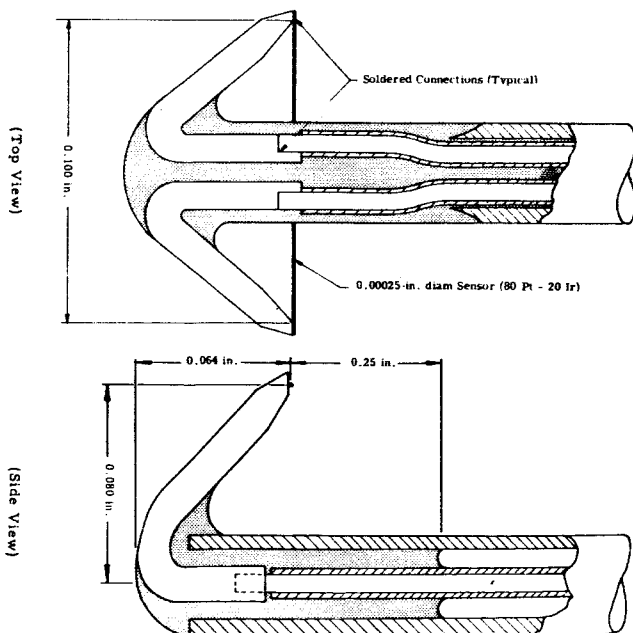


FIGURE 10. DETAIL OF BENT PROBE TIP WITH HOT-WIRE SENSOR

In an early version of the hot-wire probe, the insulated positive lead was passed through the 0.032-inch diameter stainless steel tubing, while the ground or negative connection was made by silver soldering the remaining lead to the wall of the tube. Slight changes in the contact pressure between the hot-wire actuating tube and the enclosing sleeve produced changes in shunting resistances. These problems were eliminated by enclosing both insulated leads in the actuating tube. To facilitate removal and insertion of new probes into

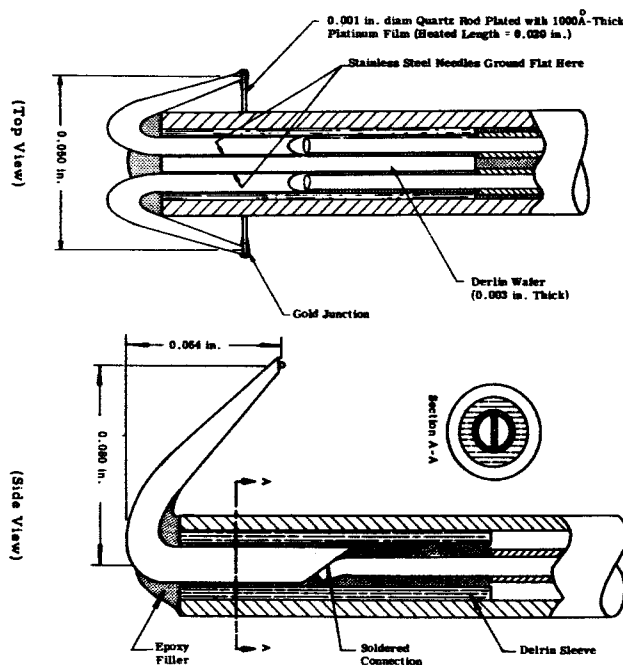


FIGURE 11. DETAIL OF BENT PROBE TIP WITH HOT-FILM SENSOR

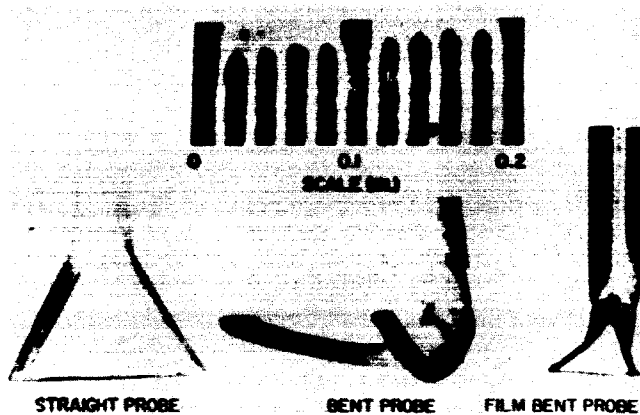


FIGURE 12. PHOTOGRAPH OF HOT-WIRE AND HOT-FILM PROBES

the different probing positions, various connector designs were tried. In cooperation with Thermo-Systems, Inc., a micro-miniature coaxial probe connector was designed and fabricated. A photograph and schematic of this design are shown in Figure 13.

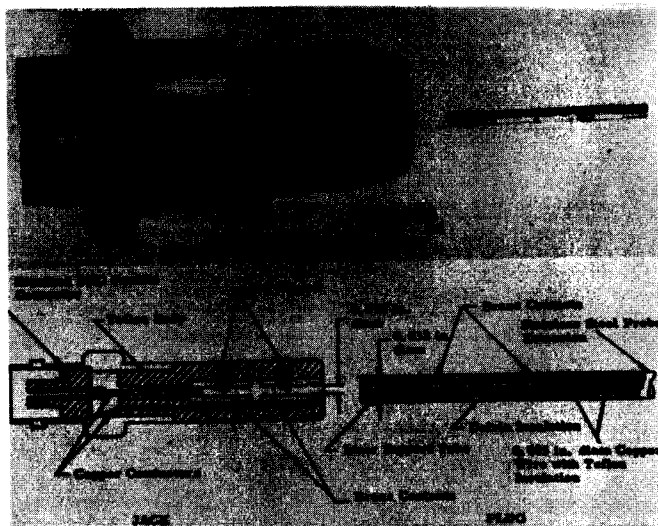


FIGURE 13. PHOTOGRAPH AND DETAIL SKETCH OF MICROMINIATURE CABLE CONNECTOR FOR HOT-WIRE PROBE

#### C. Calibration Ducts

The initial hot-wire probe calibrations were performed in a low speed wind tunnel at atmospheric density conditions. The tunnel is powered by a small centrifugal blower and can be controlled to provide test section velocities of 0 to 40 ft/sec; it is well suited for probe calibration studies at low velocities and ordinary densities. Low free-stream turbulence levels result from damping screens in the settling chamber. The test section is circular and has a 4-inch diameter.

To simulate density conditions in the base-flow regions, the majority of the calibrations were performed in a small free-jet wind tunnel. This tunnel is powered by a vacuum pump capable of producing pressures as low as 60  $\mu$  Hg. Room air is drawn into a 6-inch diameter stagnation chamber through a precision throttling valve. The flow is smoothed by passing through a filter and screen assembly formed of two porous steel plates and a layer of fine-gauge screening. Test section velocity and static pressure levels are controlled by adjusting the upstream throttling valve and the downstream vacuum valve. This allows probe calibration over a wide range of densities; velocity variations from several ft/sec to sonic speeds can be obtained.

During the static calibration, all velocities were obtained from measured static and stagnation pressures. Figure 14 gives the measurement accuracies required for the resolution of mean and fluctuating velocities at atmospheric pressure and at the low test pressure of 4.5 inch oil. It was found that conventional oil manometers are not accurate enough and special micromanometers must be used. The manometer board fluid used for the wind tunnel studies and the probe calibrations was Dow Corning Series 200 silicone oil, whose density is 0.9345 g/cm<sup>3</sup> at 25°C. However, zero-velocity hot-wire probe data were obtained in a bell jar. We found that a straight-line fairing of the probe calibration data could be extrapolated through the zero velocity point obtained in the bell jar. A near-zero velocity setting of the tunnel could also be obtained by properly positioning the valves, although this was not as accurate as the bell jar method. To improve the low-velocity accuracy, future studies will be performed using a calibrated hot-wire probe as the velocity sensor.

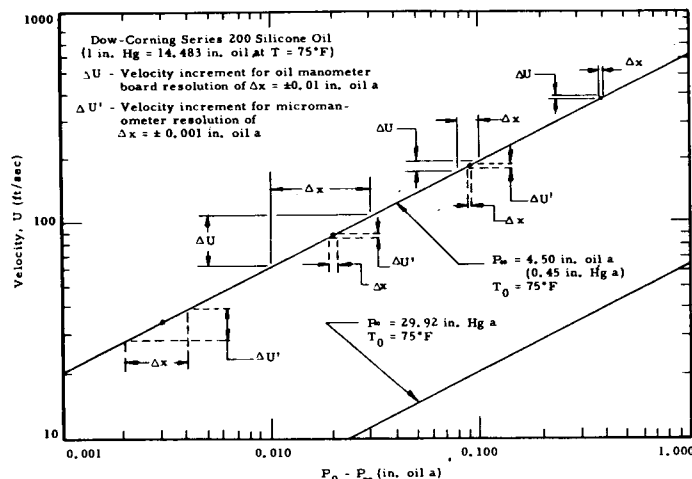


FIGURE 14. ILLUSTRATION OF PRESSURE REQUIREMENTS

#### IV. STATIC CALIBRATION

The aim of the static calibration is to provide values of A' and B'. These may be obtained from a straight-line fit of the hot-wire output  $I^2 R_w / (T_w - T_e)$  as plotted against values of  $(\rho U)^{1/2}$  that have been calculated from measured pressures.

The calibrated probes are listed on Table I.

TABLE I. CALIBRATED PROBES

Probe	Hot-Wire Material		Pt 80-Ir 20	
	Nominal Length, $l$	Nominal Diameter, $D_w$	Temperature Coeff., $\alpha$	
			0.10 in.	$2.5 \times 10^{-4} \text{ in.}^{-1}$
			$8.39 \times 10^{-4} \text{ } ^\circ\text{C}^{-1}$	
	Lead Resistance $R_l$ (ohm)	$R_e$ (ohm)	$\Delta T = 200^\circ\text{C}$ $R_v$ (ohm)	$\Delta T = 400^\circ\text{C}$ $R_v$ (ohm)
1GA	1.66	22.15	25.80	29.60
2G	1.66	24.08	28.10	32.20
3G	1.66	23.71	27.65	31.65
4G	1.66	22.14	25.80	29.58
5G	1.71	22.84	26.67	30.50
5GC	1.71	23.67	27.61	31.58
7G	1.70	27.45	32.05	36.70
7GA	1.70	26.56	30.97	35.47
2	1.70	23.50	27.50	31.50

For reasons of convenience, the temperature difference  $T_w - T_e$  was replaced with the more accessible resistance difference  $R_w - R_e$ . This assumes a linear resistance-temperature relationship. The linearity was checked with simple apparatus consisting of a small, highly polished stainless steel container which is instrumented with thermocouples. It contains a wire sample that is inserted in reference baths of various temperatures. The variation of resistance with temperature, as measured by a Wheatstone bridge capable of resolving 0.01 ohm, yielded resistance coefficients which range from  $\alpha = 8.6 \times 10^{-4} \text{ } ^\circ\text{C}^{-1}$  at  $0^\circ\text{C}$  and above to  $10.1 \times 10^{-4} \text{ } ^\circ\text{C}^{-1}$  at  $-188^\circ\text{C}$ .

Lowel [10] measured the resistance of several samples of platinum-irridium wire over a temperature range of  $20^\circ\text{C}$  to  $700^\circ\text{C}$ . Three samples yielded resistance coefficients of  $6.53 \times 10^{-4}$ ,  $7.34 \times 10^{-4}$ , and  $9.76 \times 10^{-4} \text{ } ^\circ\text{C}^{-1}$ , with an average value of  $7.88 \times 10^{-4} \text{ } ^\circ\text{C}^{-1}$ . The information required to measure wire equilibrium temperature for cool wall conditions was not included.

In the calibration tests, the temperature difference  $\Delta T = T_w - T_e$  was mostly set at  $200^\circ\text{K}$ . It never exceeded  $400^\circ\text{K}$ . Within these intervals the resistance-temperature curve was sufficiently linear, allowing use of a constant  $\alpha$ .

#### A. Atmospheric Density

Although our primary interest was in probe calibration at low densities, there are certain advantages in making preliminary measurements under continuum flow conditions. First, low velocities can be easily and accurately measured using standard micro-manometric techniques. Secondly, these continuum measurements afford a convenient method of checking the performance of novel probe designs under well-known flow conditions.

All calibration studies were performed with the manual balancing set. Calibration data for a typical probe are shown in Figure 15. As theory predicts, the data points fall well on a straight line.

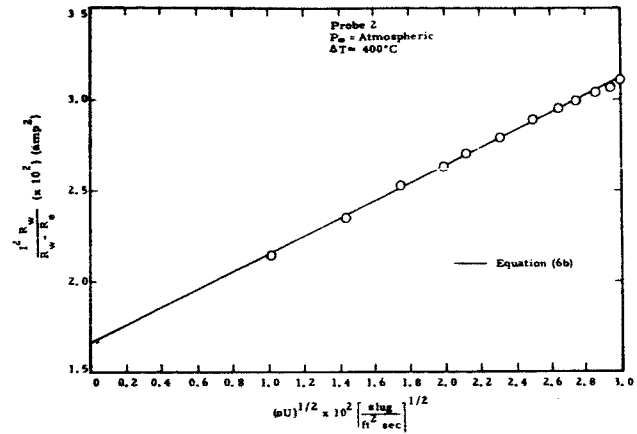


FIGURE 15. MEAN VELOCITY CALIBRATION AT ATMOSPHERIC PRESSURE

#### B. Low Densities

All the probes were calibrated at a density level corresponding to that in the base-flow recirculation zone. The probings were performed at a stagnation pressure of 40 psia, which results in a base pressure of 7 mm Hg. Because the recirculation zone temperatures are approximately  $60^\circ\text{F}$  colder than normal room temperatures (depending on tunnel stagnation temperature, which is strongly affected by the outside ambient temperature), probe calibrations were performed at 7 and 8 mm Hg.

The results indicate that the basic heat loss as represented by equation (3) is still valid, even at this low density.

Typical straight-line approximations are shown in Figure 16 for the largest temperature difference. The approximation is generally good, although some small deviations from linearity usually occur at the highest mass fluxes. At smaller temperature differences, the linearity should be even better.

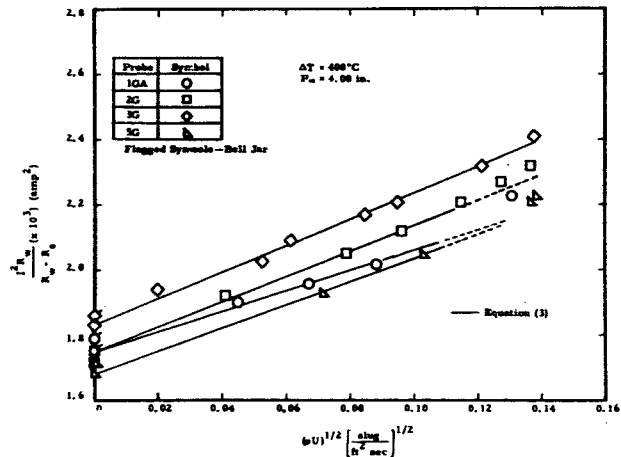


FIGURE 16. MEAN VELOCITY CALIBRATION RESULTS (4.00 in. oil a)

The variation of King's law "constants" with overheat and density is shown in Figure 17. It shows both density and overheat strongly affect the values of the "constants". The variation of these constants is not explicitly predicted by equations (7) and (8). In particular, the expression for  $A'$  shows no dependence on density, because  $k_t$  is a function of free-stream total temperature only. An alternative is to evaluate  $k$  at the mean film temperature as discussed by Hinze [5]. However, because  $k$  depends largely on temperature, this procedure still does not explain the dependence on density.

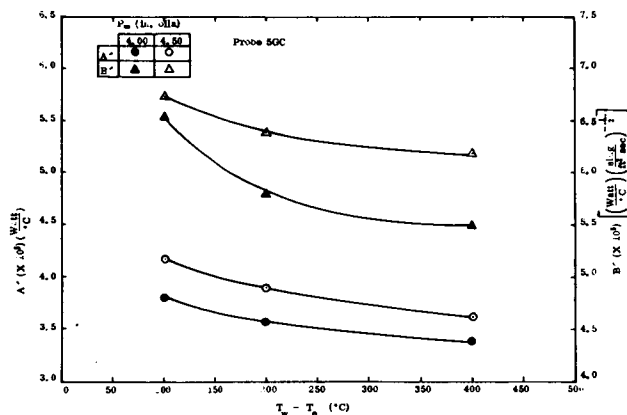


FIGURE 17. VARIATION OF KING'S LAW "CONSTANTS" WITH OVERHEAT AND DENSITY

A closer correlation between the values of the constants at various densities and overheats could be obtained if probe correction for end effects and slip flow were made. However, these procedures are not well established, and individual calibration of probes at the desired overheats and densities are required to obtain reliable results.

### C. Wall Proximity

The effects of wall proximity on hot-wire mean velocity indications have been studied at ambient densities, but apparently little work has been done at low densities. It is known that a boundary wall can influence temperature and velocity fields around the hot-wire probe and thus affect the heat loss from a wire. As the hot-wire probe approaches the wall, heat losses for a given flow velocity are larger than those encountered in calibration of the hot-wire probe. This gives a heat loss indication which is too high and which tends to distort the inner portion of the velocity profile. Earlier investigations [24, 25] of wall effect show that the errors encountered are appreciable and extend a considerable distance from the wall. In the present investigation, where the density is on the order of 0.01 atm, the wall effect is even more severe; it is

sufficient to overpower the decreasing velocity in the inner portion of the profile and to indicate an increasing velocity as the wall is approached.

Some of the earlier studies of wall effect were performed by Van der Hegge Zijnen [24] and Dryden [26]. They measured heat losses from the hot wire at various distances from the wall under still-air conditions. They also derived an equation which relates heat loss with (1) the distance from the wall, and (2) the temperature difference between the hot-wire and the wall. These still-air calibrations were used to correct velocity profile data. Van der Hegge Zijnen reported that in some cases this correction procedure resulted in an S-shaped distortion of the velocity profile. Dryden noted this difficulty and recommended that no correction be made for heat loss when the flow is laminar and when the velocity is greater than 3 ft/sec.

Dryden applied the above method to correct the root-mean-square velocity fluctuation measurements. This correction resulted in an increase in the turbulence intensity  $u'/U$ .

Piercy, Richardson and Winny [27] theoretically and experimentally investigated wall effects at low velocities. They performed a two-dimensional analysis assuming an inviscid incompressible fluid. Their theory showed that the wall proximity effect is a strong function of flow velocity over the hot wire; thus, for a given error, the probe can be moved closer to the wall as the velocity is increased. They verified their theory by whirling a hot wire through still air near the surface of a large brass cylinder. Heat losses were measured for various wire velocities and distance from the cylinder. Velocity ranged from 1/6 to 2 ft/sec; an optical positioning technique permitted the wire to be placed within approximately 0.005 inch of the cylinder wall.

The most recent work on the problem seems to be that of Wills [25], who made an experimental study of heat loss from hot wires near one wall of a narrow, parallel walled channel. These measurements were made for a condition of laminar, fully developed pipe flow; but he showed that some of the relationships between velocity and distance from the wall could be obtained in laminar and turbulent boundary layer flow. Wills also showed that wall effect is strongly velocity dependent.

The wall proximity effect was experimentally studied in the present investigation by two methods. The first method was performed under actual base flow conditions. Here, the hot-wire probe was traversed through the model base boundary layer, and velocity indications were obtained at various overheats

ranging from 50 to 400°C. Interpretation of these data is difficult because of the unknown characteristics of the boundary layer. The second method involved measurements under still-air conditions in the wind tunnel and in a bell jar using a simulated model surface. Measurements in the bell jar were performed for densities ranging from ambient to 0.01 atm. Our measurements at ambient density generally agreed with those of Wills [25] and Piercy et al [27]. The results of the low-density measurements are presented in Figure 18, which shows the effects of wire overheat. Most measurements were performed with the plate horizontal; but one set of data, showing very little effect, was taken with the plate vertical.

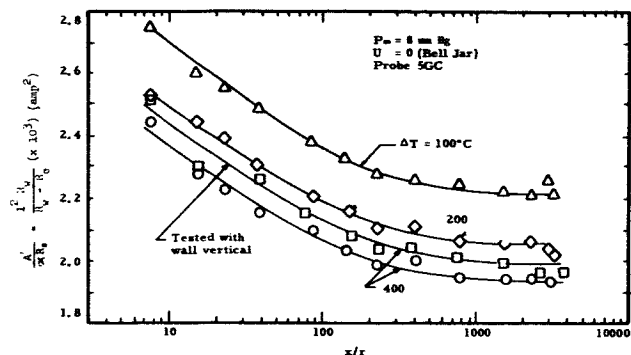


FIGURE 18. WALL PROXIMITY DATA AT VARIOUS WIRE OVERHEAT TEMPERATURES AT LOW DENSITY

Because of the strong influence of velocity on wall effect, zero-velocity calibrations are not sufficiently accurate to correct wind tunnel test data. Since the nature of the base boundary layer is unknown, it is not presently possible to perform a calibration under simulated flow conditions at low densities. Thus, we are faced with the problem of performing a calculation which requires prior knowledge of the velocity distribution. As mentioned previously, this problem is not too severe for near-ambient density conditions; but at low densities in the recirculation zone, the wall effect correction is sufficiently large to completely distort the indicated velocity profile and to prevent a meaningful correction. This problem requires further investigation before definite conclusions can be reached.

#### D. Resistance Thermometer

Since the velocities in the boundary layer are low (roughly  $U < 100$  ft/sec), the unheated probe can be used as a resistance thermometer to measure  $T_e$ , which is essentially the local static temperature. At ambient densities, adequate bridge sensitivity is easily obtained without significant wire heating. However, at low densities--where the wire heat loss is much

smaller--this same current would appreciably heat the wire; this would falsify the wire resistance and therefore the temperature indication. Bell jar experiments were made to select a proper bridge indication voltage. The results are shown in Figure 19.

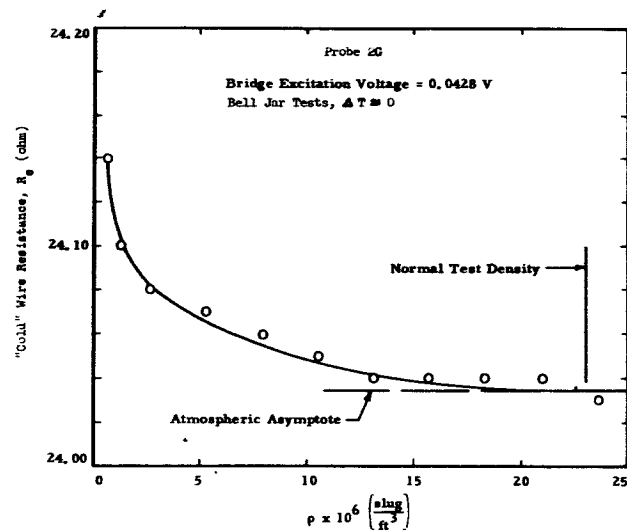


FIGURE 19. EFFECT OF DENSITY LEVEL ON HOT-WIRE "COLD" RESISTANCE

The linear resistance-temperature relation is an approximation to a more general relation

$$R = R_0 [1 + \alpha (T - T_0) + \beta (T - T_0)^2 + \dots], \quad (11)$$

where  $\alpha, \beta, \dots$  are temperature coefficients of resistance. For the metals used in hot-wire sensing elements,  $\beta/\alpha \approx 10^{-4}$ ; thus, for moderate values of  $T$  one can omit the higher order terms from equation (11) and simply write it as

$$R = R_0 [1 + \alpha (T - T_0)]. \quad (12)$$

From equation (12)

$$T = \frac{R - R_0 (1 - \alpha T_0)}{\alpha R_0}, \quad (13)$$

which may be used to calculate temperatures from measured values of  $R$ .

The use of equation (13) to find a temperature  $T$  from a measured value of  $R$  depends upon knowing  $\alpha$  with sufficient accuracy. Handbook values are not good enough for precise work because  $\alpha$  is sensitive to small amounts of impurities and is influenced by the mechanical drawing process used to make fine wires.

For greatest accuracy,  $\alpha$  must be determined for each batch of wire.



## V. DYNAMIC CALIBRATION

Preliminary theoretical calculations, guided by existing shear layer data, indicate the likelihood of velocity fluctuations in the recirculation zone and base boundary layer with frequencies up to 30 kc/sec and higher. This has been confirmed by our recent measurements in which bursts of periodic fluctuations were observed in the 6 to 23 kc/sec frequency range. In the base boundary layer, the mean velocities range from zero at the wall to values of the order of 100 ft/sec at the edge of the boundary layer. It becomes important in this section to consider the frequency response of the hot-wire apparatus, especially since the velocity fluctuations are sometimes comparable in magnitude to the mean flow velocity.

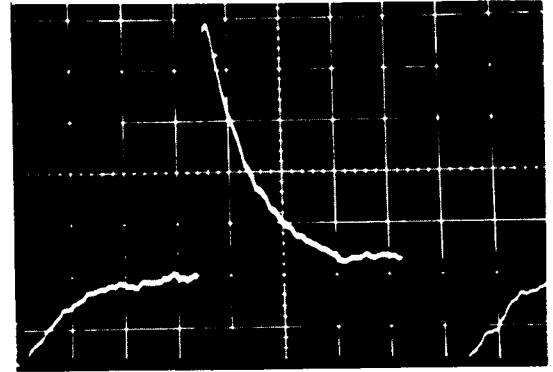
The accurate estimate of cross correlation coefficients requires that the instrument be as linear and time invariant as possible. In this case, systematic distortions like thermal inertia can be eliminated using the time average frequency response function [28]. However, dynamic signal distortions like timing errors, shifts in reference (zero) levels or phases cannot be corrected [3]. They have to be kept to a minimum. A realistic tolerance would be to require that the relative dynamic error of the power transfer function  $\Delta |H^2| / |H^2|$  and the dynamic phase shifts between the outputs of two hot-wires does not exceed 2 percent. Therefore, the ideal dynamic calibration program should establish the standard deviations of the frequency response functions besides their average values [3].

### A. Square Wave Excitation

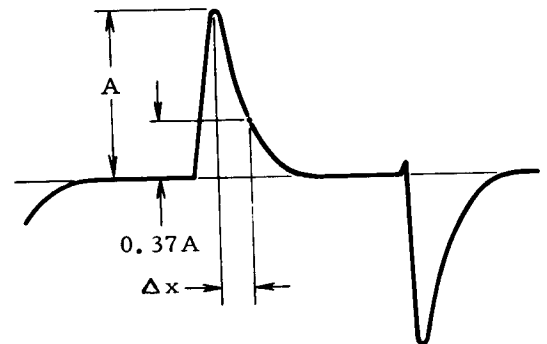
The problem with dynamic calibration is that there are no calibration tunnels which can produce stationary mass flux fluctuations with prescribed ranges of frequency and amplitude. It is planned to use the vortices which are shed from heated wires. However, this method is in the early stages of development [29], and therefore dynamic calibration had to be based on the simpler square wave excitation as proposed in the DISA operational manual.

Instead of keeping the wire at a constant temperature in a known mass flux fluctuation, the wire is placed in the smooth flow of the static calibration duct and driven by a stepwise heating current such that its temperature changes stepwise in time. It is then assumed that the output of the wire resembles the unit step response of the hot-wire system. In this case a crude estimate of the frequency response function  $H(f)$  could be obtained from the Fourier transform of the output signal time history. In practice, however, it is as accurate to assume that the constant-temperature hot-wire system behaves like a highly

damped harmonic oscillator, the unit step response of which is known. Figure 20 gives an example of this "idealized wave form." The corresponding frequency response functions are plotted in Figure 21. They are sufficiently flat up to a certain "cut-off frequency"  $f_u$ , where the response to a hypothetical harmonic calibration input will have dropped 3 db below the expected quasi-steady value (power transfer function  $|H^2| = 1/2$  of its static value). This cut-off frequency may be read directly from the square wave response as shown in Figure 20. This is the only dynamic property that has been measured to the present, and the results will now be used for a qualitative discussion of the frequency response function.



Actual Wave Form



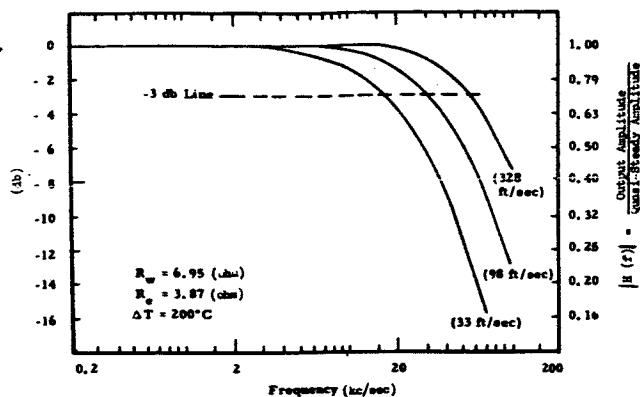
Idealized Wave Form

$$\Delta t (\mu \text{ sec}) = \Delta x (\text{cm}) \cdot \text{sweep rate } (\mu \text{ sec/cm})$$

$$f_u = \frac{1}{2\pi \Delta t}$$

FIGURE 20. SQUARE-WAVE METHOD OF MEASURING CUT-OFF FREQUENCY  $f_u$

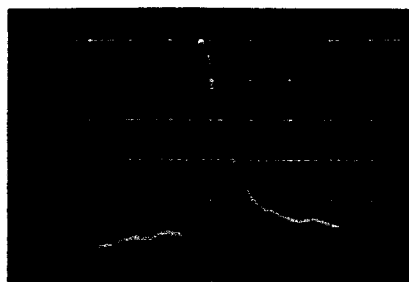
All dynamic calibration work was performed with the DISA constant-temperature system using probes 7GA and 5GA. Some representative samples of the square wave response are given in Figure 22. One



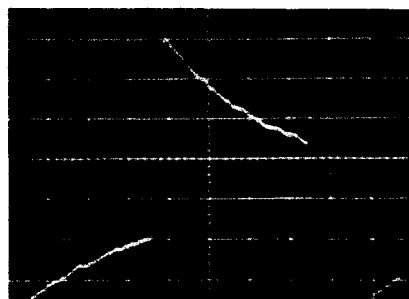
(After DISA Operating Manual, Model 55A01)

FIGURE 21. FREQUENCY RESPONSE ESTIMATE FOR THREE MEAN STREAM VELOCITIES AT ATMOSPHERIC CONDITIONS

$U = 0 \text{ ft/sec}$   
 $f_u = 3.64 \text{ kc/sec}$   
 $\Delta t = 43.7 \mu\text{sec}$   
 $P_\infty = \text{atmospheric}$



$U = 0 \text{ ft/sec}$   
 $f_u = 0.66 \text{ kc/sec}$   
 $\Delta t = 208.0 \mu\text{sec}$   
 $P_\infty = 0.311 \text{ in.Hg a}$



$U = 273 \text{ ft/sec}$   
 $f_u = 0.76 \text{ kc/sec}$   
 $\Delta t = 210.0 \mu\text{sec}$   
 $P_\infty = 0.311 \text{ in.Hg a}$

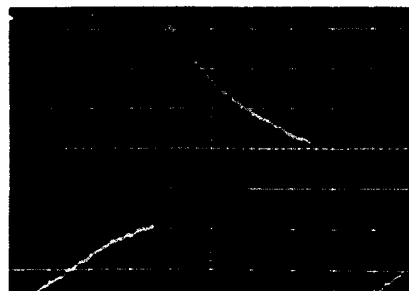


FIGURE 22. OSCILLOSCOPE TRACES SHOWING SQUARE-WAVE RESPONSE OF DISA ANEMOMETER

sees immediately that the cut-off frequencies are lowered by about 80 percent if the pressure level is decreased from one atmosphere to 0.31 inch Hg. A slight improvement can be obtained by raising the velocity level. Both effects have therefore been studied separately.

### B. The Zero Velocity Cut-Off Frequency

The largest frequency response limitations are to be expected at near-zero velocities and low densities. Therefore, the zero velocity frequency response has been studied as a function of pressure level. The results are shown in Figure 23. At atmospheric densities the near-zero velocity frequency response is flat up to 4 kc/sec. This is already one order of magnitude smaller than required. Lowering the pressure to the values which are anticipated on base heating tests reduces the cut-off frequencies by another order of magnitude. Thus, the present hot-wire systems are incapable of resolving the fluctuations near the reattachment region of free shear layers, where the largest fluctuations are anticipated.

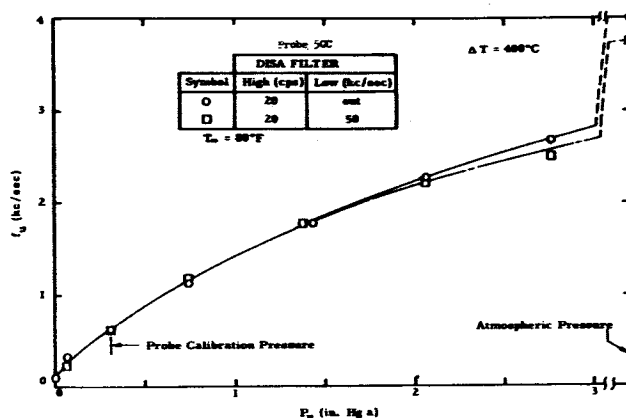


FIGURE 23. ZERO VELOCITY CUT-OFF FREQUENCY  $f_u$  (3 db down) FOR VARIOUS PRESSURE LEVELS

### C. Frequency Response at Nonzero Velocities

At atmospheric pressures, Staritz [23] showed that the usable frequency range can be improved by a factor of 5 by raising the velocity from zero to several hundred ft/sec. Similar results are also shown in Figure 21. A similar, but smaller, effect has been found at low pressures. Figure 24 gives the velocity dependence of the cut-off frequency for a pressure level of 8 mm Hg. Raising the velocity from 0 to 800 ft/sec will increase the cut-off frequency by roughly a factor of 2. However, this increase cannot be used in flow where the fluctuation levels are comparable to the mean values, since a velocity dependent

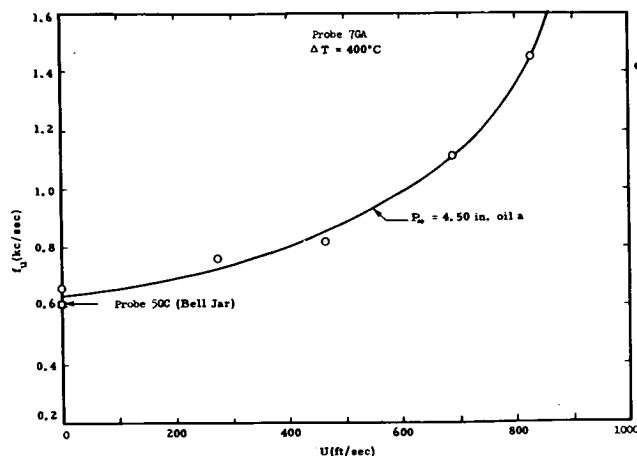


FIGURE 24. UPPER FREQUENCY LIMIT AS A FUNCTION OF FLOW VELOCITY

frequency response violates the basic requirement that the instrument has to be time invariant. Thus, a correlation analysis of turbulent fluctuations can be performed only for those frequencies that do not appreciably exceed the cut-off frequency for near-zero velocity.

The above results indicate that even the advanced constant-temperature hot-wire systems, such as the Kovasznay circuit or the DISA anemometer, are unable to resolve relatively high turbulent fluctuations in the reattachment region of free shear layers. The flat frequency response might be extended to 2 kc/sec by raising the density levels to approximately 10 percent of the atmospheric value.

Further improvements are only possible by redesigning both the circuitry and the probes. We propose:

- 1) To modify the electronic circuits to allow precise neutralization of reactive impedances, which limit the maximum usable frequency. In addition, special precautions must be taken in the construction of the hot-wire bridge to minimize stray capacitance and inductance.

- 2) To raise the tolerable heating current at near-zero velocity by replacing the wire with an internally cooled film sensor. This will increase the total heat loss from the sensor, which in effect simulates a higher stream velocity. An accurate velocity measurement is then obtained through precise calibration and control of the coolant flow.

- 3) To lower the thermal inertia of the film by decreasing the film thickness and using materials having lower  $C_w/\alpha$  values which previously could not be drawn into thin wires. New sputtering techniques now allow deposition of practically any material on a wide variety of substrates.

## VI. ACKNOWLEDGEMENTS

The authors are pleased to acknowledge the valuable guidance provided by Werner K. Dahm of the George C. Marshall Space Flight Center. Particular thanks are extended to Mr. Sheldon Vick of the University of Minnesota, Aero-Hypersonic Laboratory, for his valuable assistance in the entire wind tunnel program. Mr. Donald M. Monson and Mr. Arthur R. Kydd of the Applied Science Division, Litton Systems, Inc. deserve our thanks and recognition for capable assistance in measurements and data reduction.

## VII. REFERENCES

1. Larson, R. E. et al. Turbulent Base Flow Investigation at Mach No. 3, University of Minnesota, Rosemount Aeronautical Laboratories, Research Report No. 183 (July 1963).
2. Thornton, R., F. R. Krause. Pressure and Heat Transfer Rate Fluctuations in the MSFC Base Flow Facility, S-1 model. NASA-MSF, Office Memorandum R-AERO-AM-64-4.
3. Krause, F. Wall Pressure Fluctuations and Skin Vibrations with Emphasis on Free Shear Layers and Oscillating Shocks. NASA-TMX53189, Oct. 1964.
4. Schlichting, H. Grenzschicht-Theorie, Karlsruhe, G. Braun, 1951.
5. Hinze, J. O. Turbulence, N. Y., McGraw-Hill, 1959.
6. King, L. V. On the Convection of Heat from Small Cylinders in a Stream of Fluid: Determination of the Convective Constants of small platinum Wires with Application to Hot-wire Anemometry. Phil. Trans, Roy. Soc. London, Ser. A 214: 373-432 (1914).
7. McAdams, W. H. Heat Transmission, 3rd ed. N. Y., McGraw-Hill, 1954.
8. Foltz, F. W. Hot-wire Heat-loss Characteristics and Anemometry in Subsonic Continuum and Slip Flow. NASA TND-773 (1961).
9. Spangenberg, W. G. Heat-loss Characteristics of Hot-wire Anemometry at Various Densities in Transonic and Supersonic Flow. NACA TN 3381 (1955).

10. Lowell, H. H. Design and Applications of Hot-wire Anemometers for Steady-State Measurements at Transonic and Supersonic Airspeeds. NACA TN 2117 (1950).
11. Baldwin, L. W. Slip-flow Heat Transfer from Cylinders in Subsonic Airstreams. NACA TN 4369 (1958).
12. Cybulski, R. J., and Baldwin, L. V. Heat Transfer from Cylinders in Transition from Slip Flow to Free-Molecule Flow. NASA Memo. 4-27-59E (1959).
13. Laurence, J. C. and Sandborn, V. A. Heat Transfer from Cylinders in Symposium on Measurement in Unsteady Flow, American Society of Mechanical Engineers, Hydraulic Division of Conference, May 21-23, 1962, Proceedings. N. Y., ASME, 1962. pp. 36-43.
14. Sandborn, V. A., and Laurence, J. A. Heat Loss from Yawed Hot-wires at Subsonic Mach Numbers. J. Fluid Mech. 6:357-84 (1959).
15. Collis, D. C., and Williams, M. J. Two-Dimensional Convection from Heated Wires at Low Reynolds Numbers. J. Fluid Mech. 6:357-84 (1959).
16. Collis, D. C., and Williams, M. J. Molecular and Compressibility Effects on Forced Convection of Heat from Cylinders. Australian Defense Scientific Service, Aeronautical Research Laboratories, Report A. 110 (July 1958).
17. Levey, H. Heat Transfer in Slip Flow at Low Reynolds Number. J. Fluid. Mech. 6:386-91 (1959).
18. Webb, W. H. Hot-wire Heat Loss and Fluctuation Sensitivity for Incompressible Flow. Princeton University, Department of Aeronautical Engineering, Report No. 596 (1962).
19. Kovasznay, L. S. G. Turbulence in Supersonic Flow. J. Aeronaut. Sci. 20:657-74, 682, (1953).
20. Kovasznay, L. S. G., Miller, L. T., and Vasudeva, B. R. A Simple Hot-wire Anemometer. Johns Hopkins University, Project Squid Technical Report JHU-22-P (July 1963).
21. Karlsson, S. F. K. An Unsteady Turbulent Boundary Layer. J. Fluid. Mech. 5:622-636 (1959).
22. Hanson, A. R. and Strom, R. O. Paper in Preparation.
23. Staritz, R. F. Die elektronische Messung der Stroemungsgeschwindigkeit and der Turbulenz. FDI-Zeit. 102:94-97 (1960).
24. Van der Hegge Zijnen, B. G. Measurements of the Velocity Distribution in the Boundary Layer Along a Plane Surface. Thesis, Delft (1924).
25. Wills, J. A. B. The Corrections of Hot-wire Readings for Proximity to a Solid Boundary. J. Fluid Mech. 12: 388-96 (1962).
26. Dryden, H. L. Air Flow in the Boundary Layer Near a Plate. NACA Technical Report No. 562 (1936).
27. Piercy, N. A. V., Richardson, E. G., and Winny, H. F. On the Convection of Heat From a Wire Moving Through Air Closed to a Cooling Surface. Proc. Phys. Soc. (London), Ser. B 69:371-42 (1956).
28. Crandall, S. H., W. D. Mark. Random Vibration in Mechanical Systems. Academic Press (1963) New York, N. Y.
29. Applied Science Division Div. of Litton Industries, Proposal no. 2226. Periodic Fluctuating Flow Studies, by A. R. Hanson and R. E. Larson. (May 1964).

THEORY AND APPLICATION OF LONG DURATION  
HEAT FLUX TRANSDUCERS

by

S. James Robertson\* and John P. Heaman

SUMMARY

Presented in this paper are various devices and techniques for the measurement of heat flux. The principles of operation of the slug type sensor and the steady-state sensor are discussed, and certain design parameters for these sensors are presented. Special considerations for the application of both radiation and convection measuring devices, and the various types of heat flux simulators used in calibrating heat flux transducers are discussed.

SECTION I. INTRODUCTION

The extreme thermal environments encountered in the base region and other areas of large rocket powered vehicles have created special design problems which require a knowledge of the intensity of the heat transfer to be expected. To acquire this knowledge, heat transfer measurements have been made during scale model tests and flight tests of these vehicles.

During the early scale model "hot flow" testing of Saturn I at Lewis Research Center and Arnold Engineering Development Center, the lack of existing knowledge and experience in heat flux measurements resulted in the accumulation of base heating data which was difficult, if not impossible, to analyze. To help overcome this lack of knowledge and experience, a study program was initiated by Aeroballistics Division (now Aero-Astroynamics Laboratory) of MSFC in September 1961. This program, performed under contract by Heat Technology Laboratory, Inc., of Huntsville, Alabama resulted in the development of instrumentation employing the latest state-of-the-art concepts for heat flux measurements.

The purpose of this note is to present an outline of the theory and application of the various types of heat flux transducers used to measure the "long duration variety; that is, they are used in tests of more than a second's duration.

\* HEAT TECHNOLOGY LABORATORY, INC.  
Huntsville, Alabama

ACKNOWLEDGEMENTS

Several of the personnel of the Aerodynamics Division have contributed in various ways to the accumulation and presentation of the information contained herein.

SECTION II. THEORY OF BASIC SENSING DEVICES

The basic heat transfer equation which applies to all of the sensors described herein is

$$Q = Q_{\text{storage}} + Q_{\text{loss}}, \quad (1)$$

where  $Q$  is the rate of heat input into a sensor and  $Q_{\text{storage}}$  and  $Q_{\text{loss}}$  are the components which are stored in the sensor or lost.

Most heat flux sensors fall into two general categories depending on which term of equation (1) is used in the measurement:

1. Slug type - the storage term
2. Steady-state type - the loss term

A. The Slug Type Sensor

Until recently, the most widely used heat flux measuring device was the slug type heat flux transducer. The "slug" is a relatively thermally isolated heat-receiving mass with provision for continuous measurement of its temperature.

1. The Slug Heat Transfer Equation. The heat flux measured by a perfectly thermally isolated slug is related to the time rate of change of slug temperature  $dT/dt$  according to the following equation:

$$dT/dt = q/K, \quad (2)$$

where  $q$  is the heat flux and  $K$  is a calibration constant depending on (1) the fraction of the heat flux actually absorbed by the slug and (2) the thermal capacitance of the slug.

Normally, the slug cannot be sufficiently thermally isolated for heat losses to be considered negligible. These losses primarily consist of conduction losses and are generally assumed to be proportional to the temperature difference,  $\Delta T$ , between the slug and its surroundings. Adding the "loss" term to equation (2) yields the slug transducer equation

$$dT/dt = q/K - \theta \Delta T \quad (3)$$

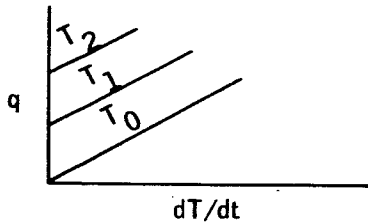
or

$$q = K dT/dt + K\theta \Delta T,$$

where  $\theta$  is a calibration constant depending only on the thermal resistance between the slug and its surroundings and the thermal capacitance of the slug. The fraction of the heat flux actually absorbed by the slug does not influence the value of this constant. Equation (3) is derived in Appendix A.

2. Calibrating the Slug Transducer. Equation (3) indicates that the heat flux measured by a slug transducer can be considered a function of the temperature-time derivative of the slug with the slug temperature as a parameter. This is based on the assumption that the "loss" term depends only on the instantaneous magnitude of the slug temperature.

Based on the above hypothesis, one method for calibrating the slug transducer is to expose the transducer to several values of a known constant heat flux and plot this heat flux as a function of the slug temperature-time derivative with slug temperature,  $T$ , as a parameter. A typical calibration plot is shown below.



$T_0$  is the initial slug temperature.

Another method of calibrating the slug transducer depends on directly determining the value of the calibration constants  $K$  and  $\theta$  in equation (3). This is done by first exposing the transducer to known values of a constant heat flux, as in the previous method. If the value of the calibration constants  $K$  and  $\theta$  may be assumed to be constant and the temperature difference,  $\Delta T$ , assumed to be equal to the temperature rise of the slug, the calibration constants may be obtained from the following equations:

$$K = q / (dT/dt)_i, \quad (4)$$

$$\theta = \frac{(dT/dt)_i - dT/dt}{\Delta t},$$

where  $(dT/dt)_i$  is the initial slope of the temperature-time curve.

Another method for determining the loss coefficient,  $\theta$ , is through the use of the following equation:

$$Z = \frac{\Delta TK}{q} = \frac{1}{\theta} (1 - e^{-\theta t}). \quad (5)$$

Equation (5), obtained by integrating equation (3), is graphed parametrically in Figure 1. The principal advantage in using this method is that the loss coefficient,  $\theta$ , may be determined directly from the temperature rise,  $\Delta T$ , thus avoiding the possibility of introducing large errors in determining the slope,  $dT/dt$ , by graphical techniques.

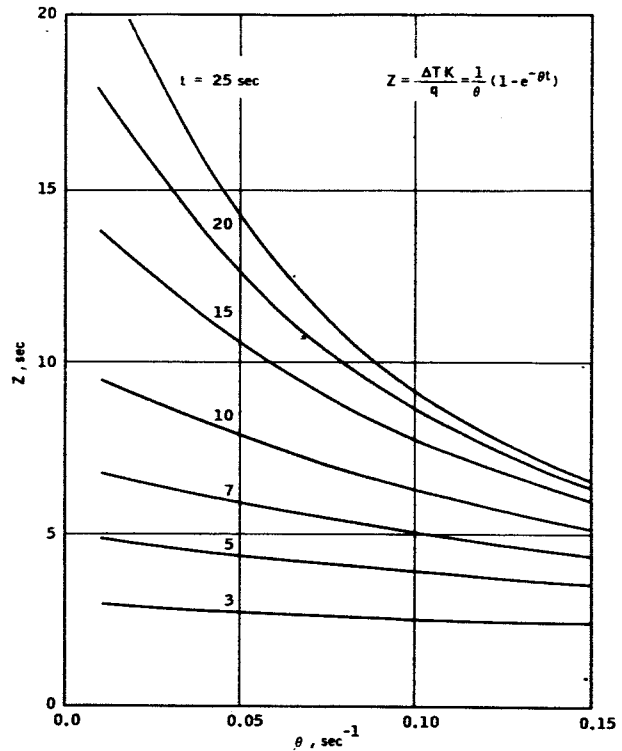


FIGURE 1. PARAMETRIC REPRESENTATION OF THE EQUATION USED IN DETERMINING THE LOSS COEFFICIENT.

All the above described calibration techniques, in which the instrument is calibrated before the test, have some inherent error, because the heat losses are not point functions of the slug temperature, but depend on

the history of the heating rate to the slug. Thus, an exact point calibration applicable for every possible heat flux history is not possible. Therefore, the heat flux history to a slug transducer is sometimes determined by exposing a similar transducer to a varying heat flux such that the temperature history of the original transducer is duplicated. The resulting heat flux history is then taken to be the same as that of the original transducer. This method is useful only for slowly varying heat fluxes, because radical changes in heat flux will result in relatively small changes in the magnitude of the slug temperature over a small period of time.

Whether the transducers are to be used in measuring radiation or convection must be considered during calibrating. Generally, the calibrating heat source is radiation whether the transducers are used for convection or for radiation measurements because it is much easier to supply radiation of known intensity than convection of known intensity. When a transducer to be used in measuring convection is calibrated in a radiant heat source, the sensing surface must be coated with a material of high absorptivity for thermal radiation. The absorptivity must then be considered in determining the heat flux to the transducer.

3. Response Time. The response time,  $t^*$ , for a lossless slug transducer is obtained from the following equation:

$$t^* = 0.203 \delta^2 / \alpha, \quad (6)$$

where  $\delta$  is the slug thickness and  $\alpha$  is the thermal diffusivity of the slug material. This equation is presented graphically in Figure 2. Equation (6), derived in Appendix B, is defined as the time required for the slope of the back surface temperature-time curve to reach approximately 75 percent of quasi-steady-state after a step change in heat flux.

4. Thermal Capacitance. In designing a slug type transducer, the thickness of the slug affects not only the response time but also the duration for which the transducer may be exposed to a given thermal environment.

The slug thickness,  $\delta$ , required for a specified integrated heat flux history  $\int_0^t q dt$  can be estimated from the following equation:

$$\delta = \frac{\int_0^t q dt}{\rho C \Delta T} \quad (7a)$$

or

$$\delta = \frac{qt}{\rho c \Delta T}, \quad (7b)$$

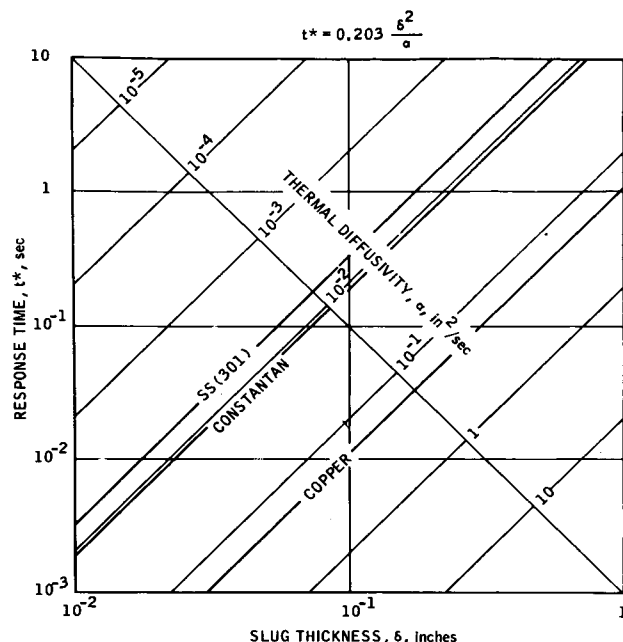


FIGURE 2. RESPONSE TIME,  $t^*$ , OF A SLUG CALORIMETER AS A FUNCTION OF SLUG THICKNESS,  $\delta$ , AND THERMAL DIFFUSIVITY,  $\alpha$ .

for a constant heat flux,  $q$ , where  $\Delta T$  is the maximum allowable temperature rise of the slug and  $\rho$  and  $c$  are the density and specific heat, respectively, of the slug. Losses are neglected. This equation is presented as a nomogram in Figure 3 for a constant heat flux.

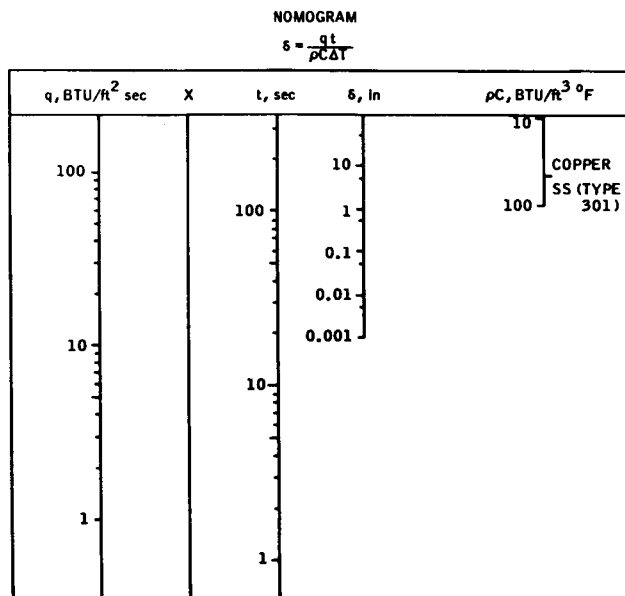


FIGURE 3. NOMOGRAM FOR DETERMINING THE SLUG THICKNESS,  $\delta$ , OF A SLUG-TYPE CALORIMETER EXPOSED TO A CONSTANT HEAT FLUX,  $q$ , FOR A MAXIMUM TEMPERATURE RISE,  $\Delta T$ , OF 600° F.

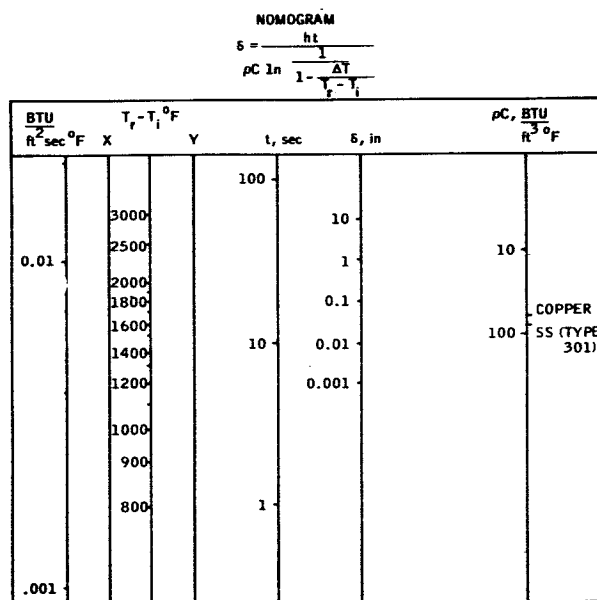
A slug exposed to convective heat flux will respond according to

$$h(T_r - T) = \rho c \delta \, dT/dt, \quad (8)$$

where  $h$  is the film coefficient for convective heat transfer,  $T_r$  is the recovery temperature of the convective gases, and  $\rho$ ,  $c$ , and  $\delta$  are the density, specific heat, and thickness, respectively, of the slug. Again, losses are neglected. Upon integrating equation (8), the following expression for slug thickness is obtained:

$$\delta = \frac{ht}{\rho c \ln \left( \frac{1}{1 - \frac{\Delta T}{T_r - T_i}} \right)}, \quad (9)$$

where  $h$  and  $T_r$  are assumed constant,  $\Delta T$  is the maximum allowable temperature rise of the slug, and  $T_i$  is the initial slug temperature. The maximum  $\Delta T$  is determined by the temperature which the transducer materials begin to deteriorate. A nomogram for this equation is presented in Figure 4.



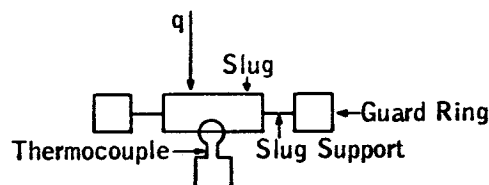
Directions for Use: Connect the points corresponding to  $h$  and  $T_r$  with straight line and find intersection with X. Connect this point with point corresponding to  $t$  with a straight line and find intersection with Y. Connect this point with point corresponding to  $\rho c$  with a straight line and find intersection with  $\delta$ .

FIGURE 4. NOMOGRAM FOR DETERMINING THE SLUG-TYPE CALORIMETER EXPOSED TO CONVECTIVE HEAT FLUX FOR A MAXIMUM TEMPERATURE RISE,  $\Delta T$ , OF 600° F.

5. Heat Losses. The heat losses from the slug are primarily functions of slug temperature, materials used, and the transducer geometry. The contribution of each of the three modes of heat transfer is discussed here with emphasis on preventing heat losses.

a. Conduction Losses. Conduction losses are present through the edge insulation, the thermocouple wires, and the rear surface insulation (if present). It is apparent that these losses may be lessened by reducing the slug temperature, reducing the diameter of the thermocouple wires, and by using materials (insulation and mounting) around the slug with low thermal conductivity and heat capacity.

Another method for reducing heat losses is by employing the "guard-ring" principle illustrated below.



The slug is suspended by supports of high thermal resistance attached to the guard-ring such that the conduction path is from the slug through the slug supports to the guard-ring. The guard-ring is designed so that the temperature difference between the slug and the guard-ring is small, thus making the conduction losses also small.

Appendix C is an analysis of the response to constant heat flux of a slug backed by a semi-infinite imperfect insulator. Correction factors are derived to correct both the temperature rise and the slope for conduction losses.

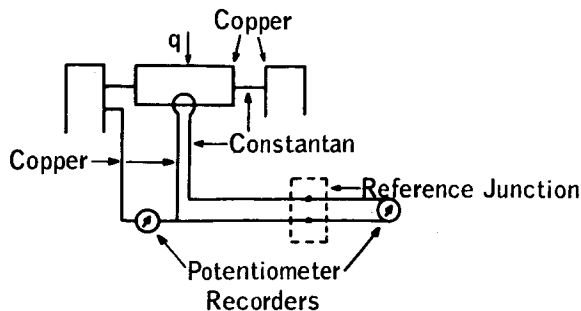
b. Radiation Losses. Rear surface radiation and exposed surface reradiation become significant only with relatively high slug temperatures (greater than about 600° F). Because radiation is proportional to the fourth power of absolute temperature, radiation losses rise rapidly with higher temperatures. At a slug temperature of 700° F, all exposed portions of the slug are emitting nearly 0.8 Btu/ft<sup>2</sup> sec (assuming high emissivity surfaces).

c. Natural Convection. If the space around the slug is not evacuated, losses will occur from natural convection. The convective heat transfer coefficient to an average size slug was estimated by the method of reference 1 to be of the order of 10<sup>-3</sup> Btu/ft<sup>2</sup> -sec °F. Thus, for a slug temperature rise of 500° F,



a possible heat loss on the order of  $1/2 \text{ Btu/ft}^2\text{-sec}$  may be expected from natural convection.

6. The Loss Measuring Slug Transducer. The loss-measuring slug transducer is a modification of the conventional slug transducer with provision for measuring the temperature difference between the slug and casing as well as the temperature of the slug (see sketch below).



Since the heat losses are nearly proportional to the temperature difference between the slug and the casing to which the slug is suspended, a measurement of this temperature difference should give a very accurate correction for heat losses.

7. Desirable Criteria for Slug Transducer Design. The following is a summary of the primary design criteria for slug transducers for all applications (design features for particular applications are discussed in a later section):

- a. The heat losses from the slug should be as small as possible to minimize the effects of losses on the temperature history of the slug.
- b. The slug should have sufficient thermal capacity for the slug temperature to remain below a maximum allowable level (about  $600^\circ \text{F}$  for most calorimeter designs) for the duration of any expected test.
- c. The response of the slope of the temperature history to changes in heat flux should be as rapid as possible.

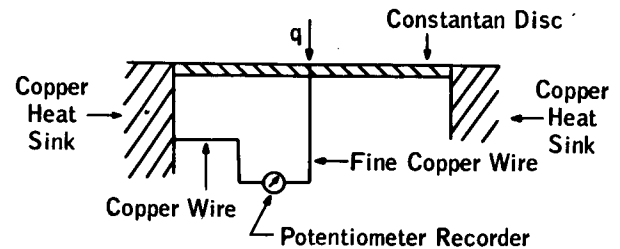
## B. STEADY STATE SENSORS

Steady-state sensors are defined as those sensors which, upon being exposed to a constant heat flux, reach a steady output after a relatively short period of time. Thus, equilibrium output can be related directly (usually proportionately) to the heat flux.

Three types of steady-state sensors are described below: (1) the Gardon type sensor or Gardon Gauge,

(2) a variation of the Gardon principle referred to herein as the Disc-Rod sensor, and (3) the semi-infinite slab sensor.

1. The Gardon Gauge. The Gardon gauge sensor, first described by Robert Gardon in Reference 2, consists basically of a thin constantan disc connected around its edge to a large copper mass, and at its center to a fine copper wire as shown in the following illustration.



This construction results in the formation of a copper-constantan differential thermocouple between the center and the edge of the disc. When the disc is exposed to the heat flux, an equilibrium temperature difference is rapidly established which is proportional to the heat flux being absorbed. Thus, the heat flux to the sensor is obtained directly from the output of the differential thermocouple.

The sensitivity of the Gardon gauge sensor is obtained from the following equation [2]:

$$E/q = 0.03 D^2/\delta, \quad (10)$$

where  $E/q$  is in  $\text{mv/Btu/ft}^2\text{-sec}$  and the disc diameter,  $D$ , and thickness,  $\delta$ , are in inches.

The response time is given by [2]:

$$t^* = 6 D^2, \quad (11)$$

where the response time,  $t^*$ , is in seconds and the diameter,  $D$ , is in inches. The response time as used here is defined as the time required for the output to reach approximately 63 percent steady-state. Equations (10) and (11) are presented graphically in Figure 5.

The ratio of sensitivity to response time depends entirely on the disc thickness,  $\delta$ :

$$\frac{E/q}{t^*} = 0.005/\delta, \quad (12)$$

where, again, the sensitivity,  $E/q$ , is in  $\text{mv/Btu/ft}^2\text{-sec}$ , the response time,  $t^*$ , is in seconds, and the thickness,  $\delta$ , is in inches. Therefore, to increase sensitivity without simultaneously increasing the response time, the disc thickness must be decreased.

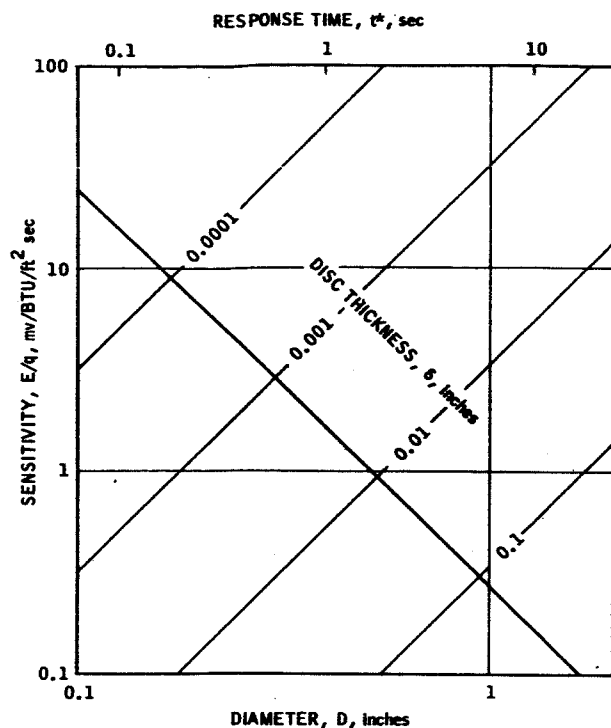
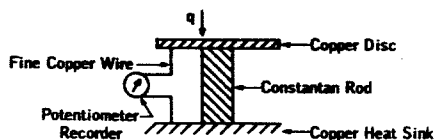


FIGURE 5. GARDON GAUGE SENSITIVITY,  $E/q$ , AND RESPONSE TIME,  $t^*$ , AS FUNCTION OF DISC DIAMETER,  $D$ , AND THICKNESS,  $\delta$ .

2. Disc-Rod Sensor. A variation of the Gardon gauge principle referred to as the disc-rod sensor is illustrated below.



This sensor consists basically of a thin copper heat-receiving disc attached to a constantan wire or rod which in turn is attached to a large copper heat sink. The copper-constantan differential thermocouple is formed in this case between the two ends of the constantan rod. For recording the emf output, copper lead wires are attached to the copper disc and heat sink. The theory of the disc-rod sensor is described in Appendix D.

The sensitivity of the disc-rod sensor is given by the following equation.

$$E/q = 0.5 (D/d)^2 l, \quad (13)$$

where the sensitivity,  $E/q$ , is in  $\text{mv/Btu/ft}^2\text{-sec}$ ,  $D/d$  is the ratio of the diameter of the copper disc to the diameter of the rod, and  $l$  is the length of the rod in inches. Equation (13) is presented graphically in Figure 6.

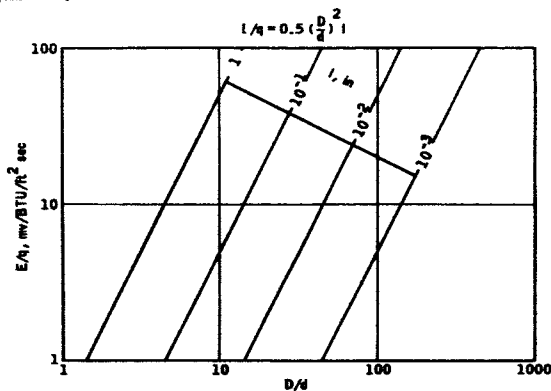


FIGURE 6. SENSITIVITY,  $E/q$ , OF A DISC-ROD SENSOR AS A FUNCTION OF THE RATIO,  $D/d$ , OF DISC TO ROD DIAMETER AND ROD LENGTH,  $l$ .

The response time is given by

$$t^* = 50 [1 + 2 (D/d)^2 (\delta/l)] l^2 \quad (14)$$

where the response time,  $t^*$ , is in seconds,  $D/d$  is the ratio of the diameter of the copper disc to the diameter of the rod,  $\delta/l$  is the ratio of the disc thickness to the length of the rod, and  $l$  is the length of the rod in inches. Equation (14) is presented graphically in Figure 7.

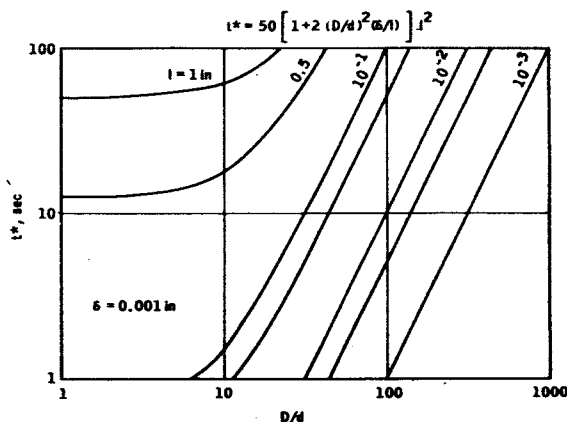
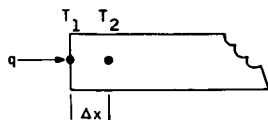


FIGURE 7. RESPONSE TIME,  $t^*$ , OF A DISC-ROD SENSOR AS A FUNCTION OF THE RATIO,  $D/d$ , OF DISC TO ROD DIAMETER AND ROD LENGTH,  $l$ .

3. Semi-Infinite Slab Sensor. The basic features of the semi-infinite slab sensor are illustrated below. Its operation consists of the measurement of temperature difference between two points in the slab near the surface. The theory of this measurement is described in Appendix E.



The equilibrium output of such a measurement is given by the following equation:

$$E/q = \frac{E}{\Delta T} \frac{\Delta X}{144k}, \quad (15)$$

where  $E/q$  is the sensitivity in  $\text{mv/Btu/ft}^2\text{-sec}$ ,  $(E/\Delta T)$  is the ratio of emf output to temperature difference for the thermocouple pair in  $\text{mv/}^\circ\text{F}$ ,  $\Delta X$  is the distance between the two points in inches, and  $k$  is the conductivity of the slab material in  $\text{Btu/in. sec}^\circ\text{F}$ . The sensitivity can be increased by "thermopiling," i.e., using multiple pairs connected in series.

The response time is given by

$$t^* = 6.25 \frac{\Delta X^2}{\alpha} \quad (16)$$

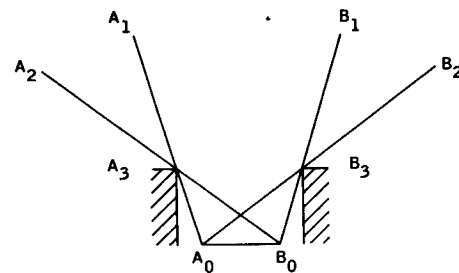
where  $\alpha$  is the thermal diffusivity of the slab material. This response time is defined here as the time required for the output to reach approximately 90 percent steady-state.

### SECTION III. RADIATION MEASUREMENTS

#### A. RECEIVING OF RADIATION BY TRANSDUCER

The amount of radiation absorbed by the sensor depends on (1) the view-angle between the sensing surface and the radiation heat source, (2) the radiation transmission characteristics of the window shielding the sensor from convective heat transfer, and (3) the absorption characteristics sensing surface.

1. View Angle. The view field for the sensing surface is illustrated below.



If the heat source is located entirely within the field enclosed by  $A_0 - A_1$  and  $B_0 - B_1$ , all of the radiation emitted by the source will be "seen" by the sensing surface. If the heat source is located in the fields  $A_2 - A_3 - A_1$  and  $B_1 - B_3 - B_2$ , the source will be "seen" only by a portion of the sensing surface. Any heat source outside of the field enclosed by  $A_2 - A_3$  and  $B_2 - B_3$  will be totally unseen by the sensor. For accurate measurements of the radiant intensity at the transducer location, the view field should be as near 180 degrees as possible.

An ideal window would transmit a high percentage of the incident radiation with no variation in the transmittance with spectrum. Unfortunately, most window materials have good transmission characteristics over only a limited spectral region. Transmittance as a function of wavelength is shown in Figure 8 for several window materials. Because of its mechanical stability, low cost, and availability, as well as transmission characteristics, synthetic sapphire is probably the most commonly used window material for radiation measurements.

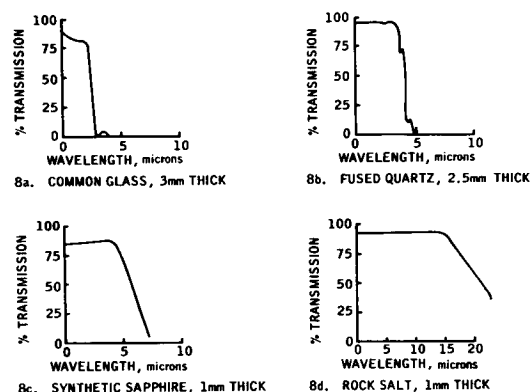


FIGURE 8. TRANSMISSION CHARACTERISTICS FOR TYPICAL OPTICAL MATERIALS

The transmittance for two thicknesses of synthetic sapphire for normal incidence is presented in Figure 9. A fairly uniform transmittance is indicated up to a wavelength of between 5 and 6 microns. Depending on the window thickness, a "cut-off" wavelength may be defined beyond which practically no radiation is transmitted. The curves in Figure 9 were obtained from the following equation:

$$\Phi = (1 - R)^2 e^{-\alpha \tau}, \quad (18)$$

where  $\Phi$  is the transmittance,  $R$  is the reflectivity,  $\alpha$  is the absorption coefficient, and  $\tau$  is the thickness. For normal incidence,  $R$  is obtained from the index of refraction,  $n$ , by Equation (19).

$$R = \frac{(n - 1)^2}{(n + 1)^2}. \quad (19)$$

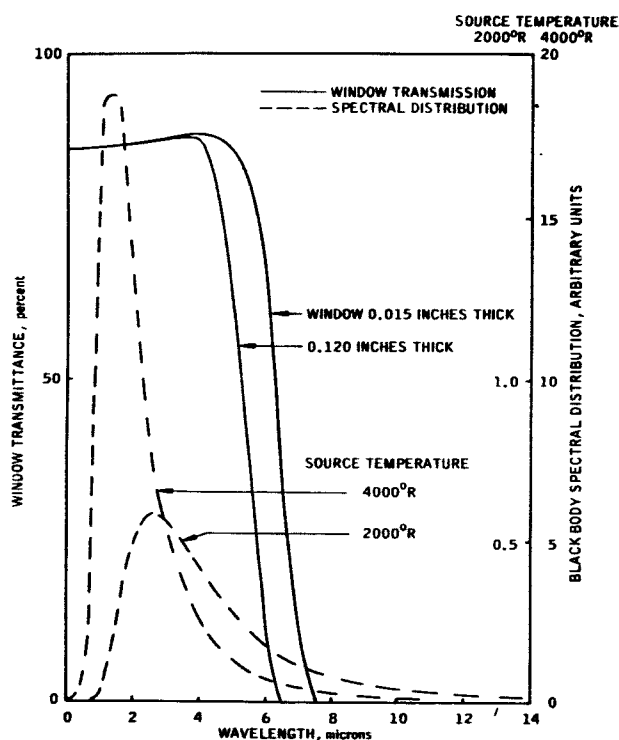
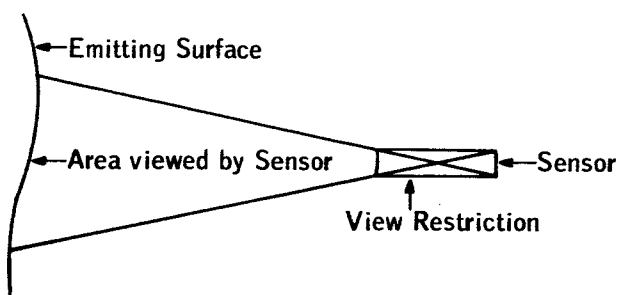


FIGURE 9. TRANSMITTANCE OF SYNTHETIC SAPPHIRE AT ROOM TEMPERATURE FOR NORMAL INCIDENCE AND SPECTRAL DISTRIBUTION OF RADIATION FROM A BLACK BODY.

Occasionally, it is desirable to measure the heat flux emitted from a small area or surface of the heat source. This may be accomplished by intentionally limiting the view field to enclose only a small portion of the emitting surface as illustrated below.



The heat flux,  $q'$ , incident on the sensing surface, is related to the heat flux,  $q$ , emitted from the surface of the heat source, by the following equation:

$$q' = Fq, \quad (17)$$

where  $F$  is the radiation form factor. This factor is usually considered as part of the calibration constant, which is determined when the transducer is calibrated by exposure to a known heat source. It is necessary that the calibration source completely cover the field of view during calibration.

## 2. Window Transmission.

a. Properties of Window Materials. Transducers for radiation measurements usually have an infrared transmitting window to protect the sensor from convective gases. As may be expected, the transmission characteristics of this window are an important consideration in the utilization of the transducer.

The index of refraction,  $n$ , and the absorption coefficient,  $\alpha$ , for synthetic sapphire are given in Figures 10 and 11, respectively.

In using a radiation transducer, it is desirable that the spectrums of both the calibration source and the source to be measured lie within the wavelength region of high window transmittance. If this is not possible, then corrections must be made for the difference in spectrum between the calibration source and the source to be measured. As an example, the spectral distribution of a black body source at 4000°R

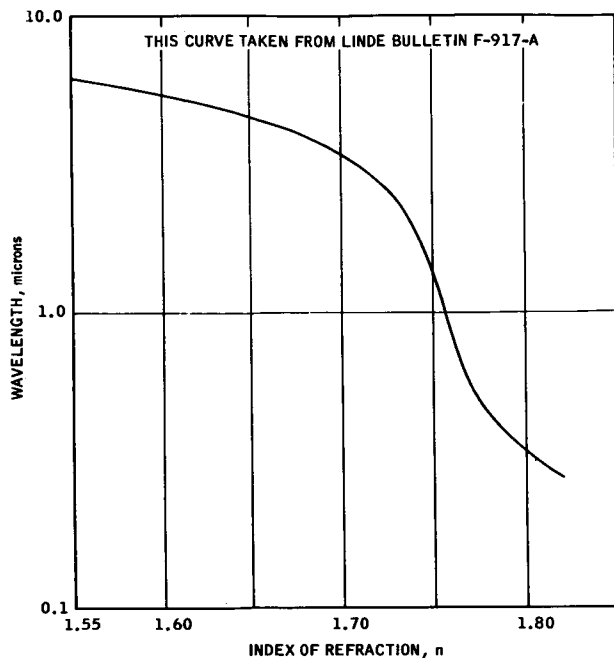


FIGURE 10. INDEX OF REFRACTION FOR SYNTHETIC SAPPHIRE ( $\text{Al}_2\text{O}_3$ ) AT  $24^\circ\text{C}$ .

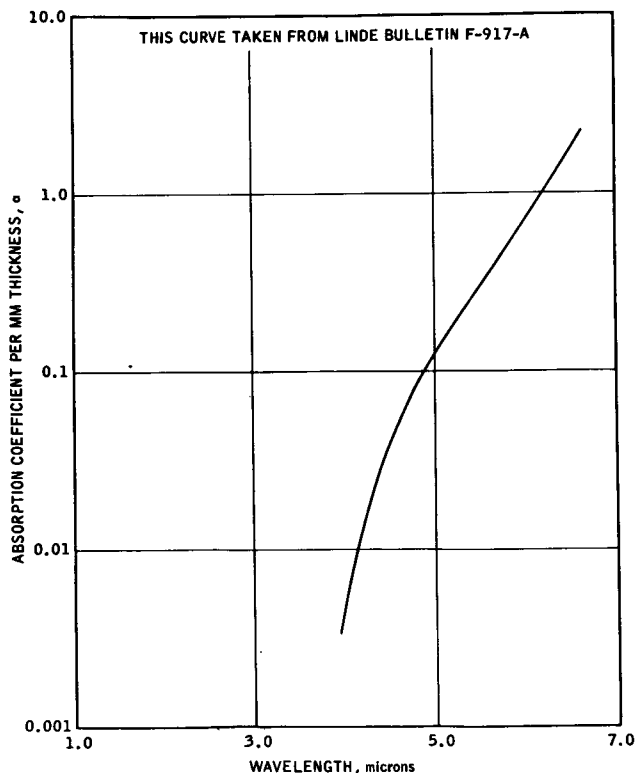


FIGURE 11. ABSORPTION COEFFICIENT,  $a$ , ( $\text{mm}^{-1}$ ) OF CLEAR LINDE SAPPHIRE.

is compared in Figure 9 with a black body at  $2000^\circ\text{R}$ . The  $4000^\circ\text{R}$  source is assumed to be reasonably approximate the spectral distribution from a rocket exhaust plume at sea level, and the  $2000^\circ\text{R}$  source is typical of black body calibration sources. It is seen that the higher temperature source is distributed more in the higher transmitting wavelength region than the lower temperature source. Numerical integration of the product of the window (0.015 inch thick) transmittance and the spectral intensity shows that 84 percent of the radiation from the  $4000^\circ\text{R}$  source is transmitted, whereas only 71 percent of the radiation from the  $2000^\circ\text{R}$  source is transmitted. Thus, the sensitivity of the transducer is about 18 percent greater for radiation from the  $4000^\circ\text{R}$  source than from the  $2000^\circ\text{R}$  calibration source.

b. **Purging the Window Surface.** A secondary problem resulting from the use of infrared transmitting windows is particle accumulation on the window surface during measurements in a smoky or otherwise "dirty" environment. Such an accumulation over the window surface would absorb a large percentage of the incident radiation, preventing transmission through the window.

The most commonly used purging device is a nitrogen flow system designed to prevent the particle containing gases from reaching the window surface. Experience has shown that it is not easy to design a satisfactory gas flow purge system. A poor design will create a low pressure region in the vicinity of the window so that there is a flow of gases containing particles toward the window instead of away from it.

3. **Sensor Absorption.** A statement similar to that applied previously to window transmission characteristics may be applied to sensor absorption; that is, it is desirable to have a high percentage of absorption with very little change in absorption with spectrum. The reason for similarity in desirable window transmission and sensor absorption characteristics is obvious; both determine the amount of the incident radiation to be actually detected by the transducer.

Table I, from Reference 3, gives the absorptivity of various materials as a function of wavelength.

TABLE I. ABSORPTIVITY

Material \ Wavelength, $\mu$	24	8.8	4.4	0.95	0.60
Acetylene soot	.97	.99	.99	.99	.99
Black (Cu O)	.96	-	.85	.76	-
Camphor soot	.94	.98	.99	-	.99
Lampblack paint	.96	.96	.97	.97	.97
Platinum black	.92	.91	.95	.97	.98

Acetylene soot, camphor soot, and lampblack paint are seen to exhibit superior absorption characteristics. However, platinum black is the material most frequently used for transducers because of its stability and bonding characteristics. Also, experience has shown platinum black to maintain essentially constant absorption characteristics up to about 500 - 600°F, which corresponds closely to the sensor temperature of a Gardon gauge transducer at the usual maximum design output of 10 mv.

The vapor-deposited metallic blacks, especially gold black, have been found to exhibit superior absorption characteristics over a very wide wavelength range. The deterioration of these blacks at elevated temperatures, however, renders them unsuitable for most heat flux measurements.

#### B. RECOMMENDED DESIGN AND EXPERIMENTAL RESULTS OF A RADIATION TRANSDUCER

The preceding discussion on radiation measurements has pointed out the following desirable criteria for radiation transducers:

1. a view angle as near 180 degrees as practical,
2. a high percentage window transmission over the wavelength region containing the spectra of the calibration source and the source to be measured.
3. an effective purge system for keeping the window clean, and
4. a receiver coating that will result in a high percentage absorption of the incident radiation.

A schematic of a recommended design which satisfies as much as practicable of each of the above criteria is shown in Figure 12. The relatively narrow view angle (approximately 90°) is a result of the purging requirement. Thus far, an effective gaseous purge has not been developed which has a wide view angle.

The purge system is designed to use gaseous nitrogen at 100 psig with a resulting flow rate of approximately three standard cubic feet per minute. The nitrogen enters the purge tube at the rear of the transducer and flows out over the window and through the front aperture. The purge was tested by exposing the transducer to a large smoky flame created by burning kerosene in a five gallon tub. The transducer was positioned so that the wind constantly directed the flames into the transducer's outer surface. The purge system not only maintained a completely clean window surface, it also cooled the body of the transducer.

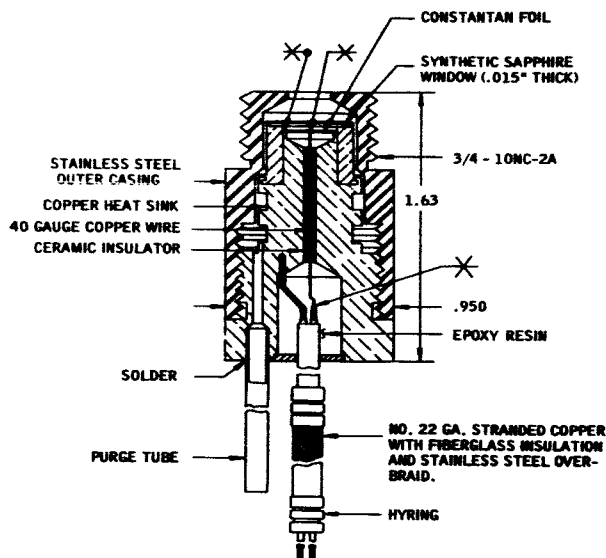


FIGURE 12. RECOMMENDED DESIGN OF A RADIATION TRANSDUCER.

The window material chosen for optimum transmission and mechanical characteristics was synthetic sapphire. Platinum black was chosen for the sensor coating because of its favorable absorption characteristics and stability up to elevated temperatures.

The type of sensor chosen for this application was the Gardon gauge (see preceding section on sensing devices) because of its steady-state output which is proportional to heat flux. Shown in Figure 13 is the

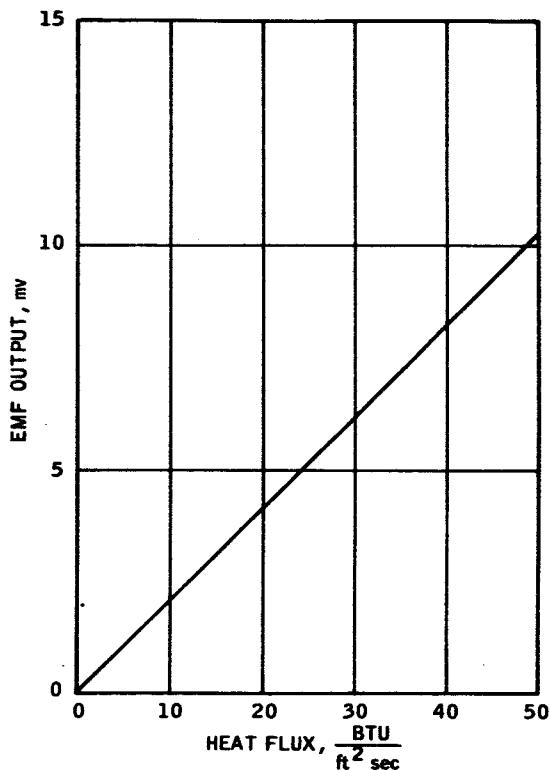


FIGURE 13. EMF OUTPUT OF A RADIATION TRANSDUCER AS A FUNCTION OF HEAT FLUX.

experimentally obtained curve of emf output versus heat flux of the transducer shown in Figure 12. It is seen that the response of the transducer is essentially linear with a sensitivity of about 0.2 mv/Btu/ft<sup>2</sup> - sec. The sensitivity of this instrument may be altered if desired by changing the dimensions of the constantan disc (see Section III. B. 1).

#### SECTION IV. CONVECTION MEASUREMENTS

##### A. PROBLEMS OF CONVECTION MEASUREMENT

Certain problems exist in the measurement of convective heat flux which are not encountered in thermal radiation measurements. The intensity of radiation falling on a given surface is not dependent on the condition of the surface or even whether the surface is material or simply a defined surface in space. This is not true, however, in the case of convection. Convective heat transfer is that heat which is conducted from a moving fluid through a material surface bounding the fluid. The intensity of convective heating is dependent upon the material surface temperature and the fluid flow properties. It is apparent, then, that the presence of a measuring instrument may have a large effect on the intensity of convective heat transfer at the point of measurement. The measurement is usually intended to determine the heat transfer which would exist at the point of measurement if the instrument were not there. It is necessary, therefore, to consider the effect of the presence of the instrument upon the measured heat transfer rate.

The convective heat flux,  $q_c$ , to a surface is found from

$$q_c = h(T_r - T_w) = -k \left( \frac{\partial T}{\partial Y} \right)_{Y=0}, \quad (20)$$

where  $h$  is the local film coefficient,  $T_r$  is the recovery temperature of the fluid,  $T_w$  is the surface temperature,  $k$  is the thermal conductivity of the fluid, and  $(\partial T / \partial Y)_{Y=0}$  is the temperature gradient in the fluid boundary layer at a point on the material surface.

The local film coefficient,  $h$ , depends on the flow conditions in the boundary layer. It is obvious that physical changes in the surface structure cause by the presence of the instrument could greatly alter the fluid flow in the boundary layer, and hence alter the local film coefficient.

A surface temperature discontinuity will likewise alter the local film coefficient because of the finite time required for the temperature gradient in the boundary layer to adjust to a new surface temperature. A method for predicting the change in film coefficient due to a step change in surface temperature on a flat plate is given in [4] for air flowing horizontally across the plate. The following equation is a variation of this method for the case of the plug-in type transducer at a temperature different from its surroundings:

$$h'/h = A(D/L) + B(D/L) \frac{T - T'}{T_g - T'}, \quad (21)$$

where  $h'/h$  is the ratio of the local film coefficient at the center of the transducer surface to the film coefficient for a uniform surface temperature,  $T'$  is the temperature of the transducer surface,  $T$  is the temperature of the surrounding surface,  $T_g$  is the free-stream temperature, and  $A$  and  $B$  are functions of the ratio of transducer surface diameter  $D$  to distance  $L$  from the leading edge. The functions  $A$  and  $B$  are presented graphically in Figure 14. As an example, consider a transducer one inch in diameter mounted in a flat plate at a point nine inches from the leading

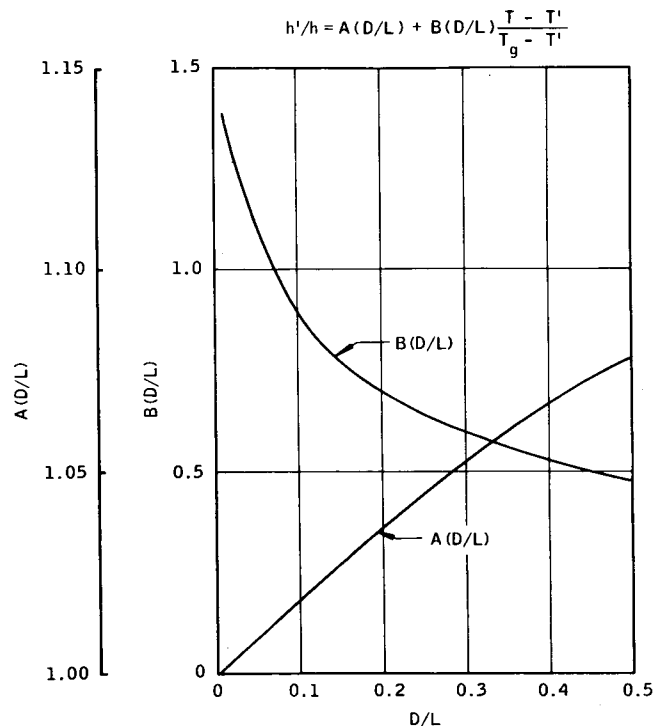


FIGURE 14. PARAMETERS FOR CORRECTING MEASURED HEAT TRANSFER COEFFICIENT FOR SURFACE TEMPERATURE DISCONTINUITY (EQUATION 21).

edge, thus resulting in a ratio,  $D/L$ , of 0.111. Let the free-stream temperature, the flat plate temperature, and the transducer surface temperature be  $200^\circ\text{F}$ ,  $100^\circ\text{F}$ , and  $125^\circ\text{F}$ , respectively. From Figure 14 and equation (21), a ratio,  $h'/h$ , of 0.72 is determined. Thus, the transducer measures a heat transfer rate which is only 72 percent of the rate which would have existed at that point for a uniform plate temperature of  $125^\circ\text{F}$ .

Because plug-in transducers are seldom perfectly installed and nearly always create a surface temperature discontinuity, the suitability of such instruments for convection measurements is highly questionable. In some instances, it may be preferable to determine the convective heat flux to a wall by measuring the temperature history of the wall itself rather than using a transducer.

The heat flux,  $q$ , to a point on the surface of a thermally thin wall of constant thickness,  $\delta$ , is

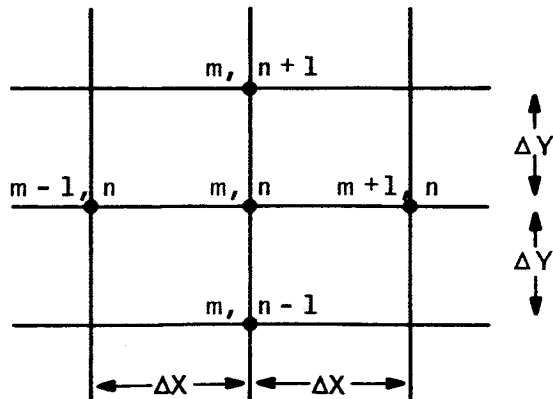
$$q = \rho c \delta \left( \frac{\partial T}{\partial t} \right) - \delta k \nabla^2 T, \quad (22)$$

where  $\rho$ ,  $c$ , and  $k$  are the density, specific heat, and thermal conductivity, respectively, of the wall material;  $\partial T/\partial t$  is the time rate of temperature change at the point of measurement; and

$$\nabla^2 T = \frac{\partial^2 T}{\partial X^2} + \frac{\partial^2 T}{\partial Y^2}, \quad (23)$$

where  $X$  and  $Y$  are rectangular coordinates on the two-dimensional wall.

For an isothermal wall,  $\nabla^2 T$  vanishes, and the measurement of the temperature history at a single point is sufficient to determine the heat flux. For a nonisothermal wall,  $\nabla^2 T$  must be evaluated as well as  $\partial T/\partial t$ . In evaluating  $\nabla^2 T$ , however, the temperature history must be measured at more than one point. Five measurements as shown on the following sketch will suffice for this evaluation.



$\nabla^2 T$  may be determined from equation (23) at any given time by the following approximation:

$$\frac{\partial^2 T}{\partial X^2} \approx \frac{1}{\Delta X^2} [T_{m+1, n} + T_{m-1, n} - 2T_{m, n}] \quad (24)$$

$$\frac{\partial^2 T}{\partial Y^2} \approx \frac{1}{\Delta Y^2} [T_{m, n+1} + T_{m, n-1} - 2T_{m, n}]. \quad (25)$$

## B. CALIBRATION OF CONVECTION TRANSDUCERS

A transducer designed to measure primarily convective heat flux really senses only the heat flux which enters the sensor; it is unable to distinguish between radiation and convection. Therefore, the instrument may be calibrated with any heat source of known intensity, either radiation or convection. The various effects discussed in the preceding section make it extremely difficult, if not impossible, to establish a known intensity of convective heat flux to a transducer. Therefore, the most accurate and practical calibration is achieved by coating the sensor with a material whose absorptivity is known within acceptable limits and exposing the instrument to a radiant heat flux of known intensity.

## C. CONVECTION MEASUREMENTS IN PRESENCE OF THERMAL RADIATION

In many applications involving a measurement of convective heat flux, there is also present a significant amount of thermal radiation; and, although the radiation portion can be measured without sensing the convective portion (see preceding discussion on radiation measurements), the converse is not always possible. Convective measurements have been attempted in which the sensor surface was plated with a highly reflective material such as gold to prevent radiation absorption by the sensor. Particle accumulation and tarnishing in a smoky or otherwise dirty environment, however, tend to increase radiation absorption so that the measurement includes the convective portion of the total heat flux plus an unknown fraction of the radiation portion. The sensors of convective heat flux transducers, therefore, are usually coated with such high absorptivity material that the total heat flux is measured with no attempt to isolate the convective heat flux. The convective heat flux can then be determined by making a separate radiation measurement and subtracting the measured radiation from the measured total heat flux.



#### D. RECOMMENDED DESIGN AND EXPERIMENTAL RESULTS OF CONVECTION TRANSDUCER

As pointed out in the preceding discussion on convection measurement, total heating transducers should be designed so that the surface geometry and temperature distribution at the point of measurement be disturbed as little as possible. The recommended design shown in Figure 15 has an external configuration which allows a minimum disturbance of the surface geometry when the instrument is installed. The surface temperature distribution, however, will be altered somewhat by the instrument.

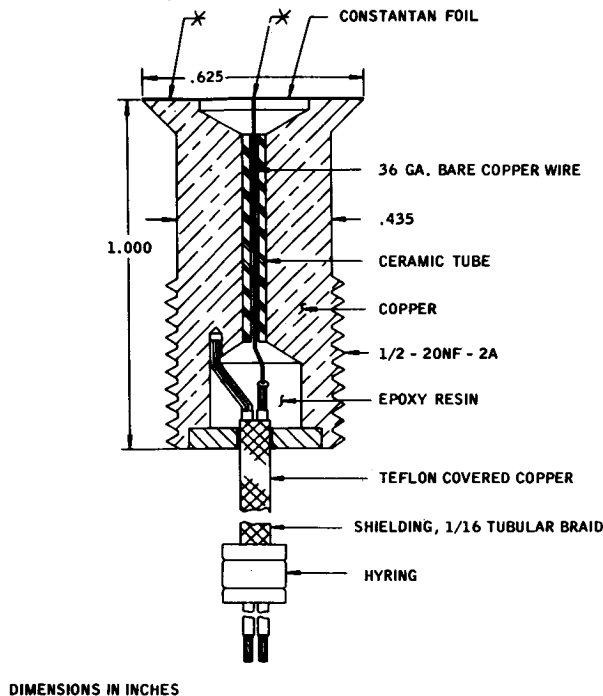


FIGURE 15. RECOMMENDED DESIGN OF A TOTAL HEATING TRANSDUCER.

The sensor surface of the instrument is coated with platinum black so that any significant amount of thermal radiation present will be absorbed by the instrument. As in the case of the recommended radiation transducer design, platinum black was chosen for its favorable absorption characteristics and stability up to elevated temperatures.

Figure 16 shows the experimentally obtained curve of emf output versus heat flux of the transducer in Figure 15. The response is essentially linear with a sensitivity of about 0.3 mv/Btu/ft<sup>2</sup>-sec.

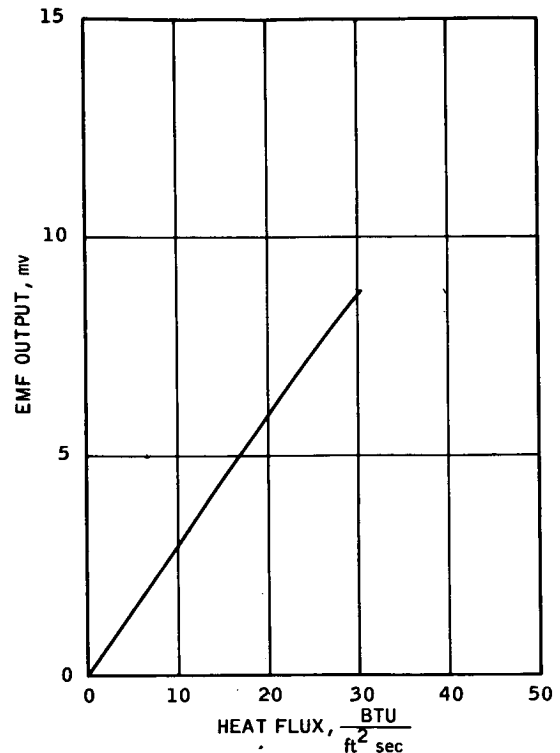


FIGURE 16. EMF OUTPUT OF A TOTAL HEATING TRANSDUCER AS A FUNCTION OF HEAT FLUX.

#### SECTION V. CALIBRATION HEAT SOURCES

##### A. BLACK BODY SIMULATOR

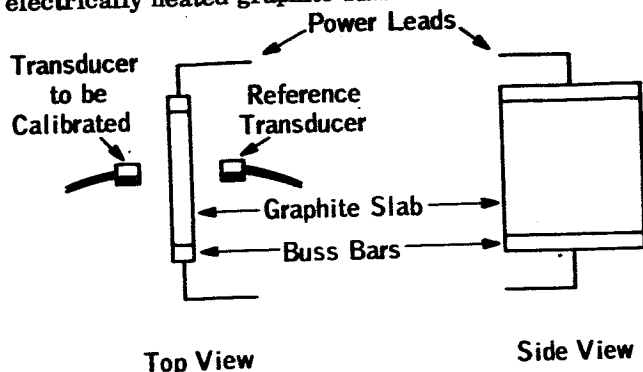
An ideal heat source for accuracy considerations is the black body. Both the spectral distribution and the radiant intensity of a black body heat source are well defined functions of the source temperature.

A perfect black body is one whose surface absorbs all the radiant energy incident upon it; that is, its absorptivity is equal to unity. Likewise, by Kirchhoff's Law its emissivity is unity. Although a perfect black body does not exist in nature, it can be very closely approximated by a small hole in the side of a hollow enclosure. Theoretically, perfect absorption (or emission) will take place only when the area of the hole is infinitely small when compared to the total area of the hollow enclosure. Practically, an approximation sufficiently accurate for experimental purposes is obtained by using a hole in the end of a hollow cylindrical tube with the tube diameter 1/4 the tube length and the hole diameter 1/4 the tube diameter. The variation of temperature over the enclosure surface must be very small.

The black body simulator is generally handicapped by fairly long heating and cooling periods required to maintain the necessary uniform temperature distribution within the heat source. For this reason, most routine calibration is performed with the use of a heat source with rapid response such as a bank of infrared heat lamps or an electrically heated graphite slab.

## B. ELECTRICALLY HEATED GRAPHITE SLAB

Another widely used heat flux simulator is the electrically heated graphite slab illustrated below:



Top View

Side View

The slab is heated internally by electrical conduction. To prevent oxidation of the graphite, an argon purge is provided to eliminate atmospheric oxygen from the slab environment. The heat flux is monitored by a reference transducer positioned symmetrically with the transducer to be calibrated. This type of heat source has been known to achieve heat flux levels on the order of 200 Btu/ft<sup>2</sup>-sec.

The chief disadvantages for this type of source are its expensive construction and spectral distribution over a longer wavelength region than rocket exhaust plumes.

## C. QUARTZ LAMP BANK

Probably the most versatile heat flux source is a bank of quartz infrared heat lamps. The primary assets of a quartz lamp bank are (1) fast response, (2) spectral distribution similar to rocket exhaust plumes, and (3) relatively economical construction.

**1. Description of Lamp Bank Facility.** The quartz lamp bank test facility located at Heat Technology Laboratory, Inc., in Huntsville, Alabama, is made up of five major parts, which are integrated into a test facility having the capability of being continuously controlled from 0-150 Btu/ft<sup>2</sup>/sec. The major components of the facility are (1) the oil-cooled quartz lamp bank, (2) a Thermac temperature and power controller model SPG 5009S with "Data-Track" programmer, (3) an oil cooling system, (4) an x-y plotter, Electronic Associates, Inc., Variplotter model 1100E, and (5) Honeywell strip chart recorders. Figure 17 is a block diagram of the facility.

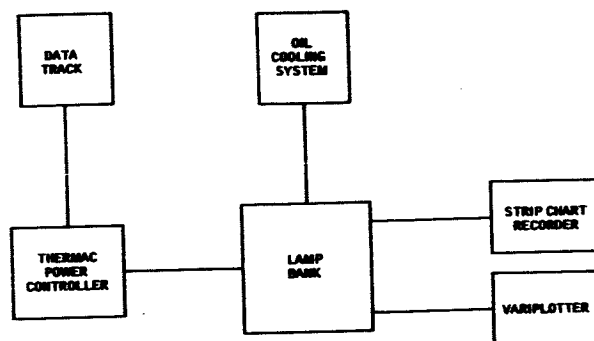


FIGURE 17. BLOCK DIAGRAM OF LAMP BANK FACILITY.

The quartz lamp bank consists of twenty quartz infrared General Electric 2000-T3 230-250V lamps arranged parallel with filaments spaced one-half inch apart. The lamps are held at each end by oil-cooled brass buss bars. The lamps are backed by a gold plated reflector which is also oil cooled. A schematic of the lamp bank is given in Figure 18.

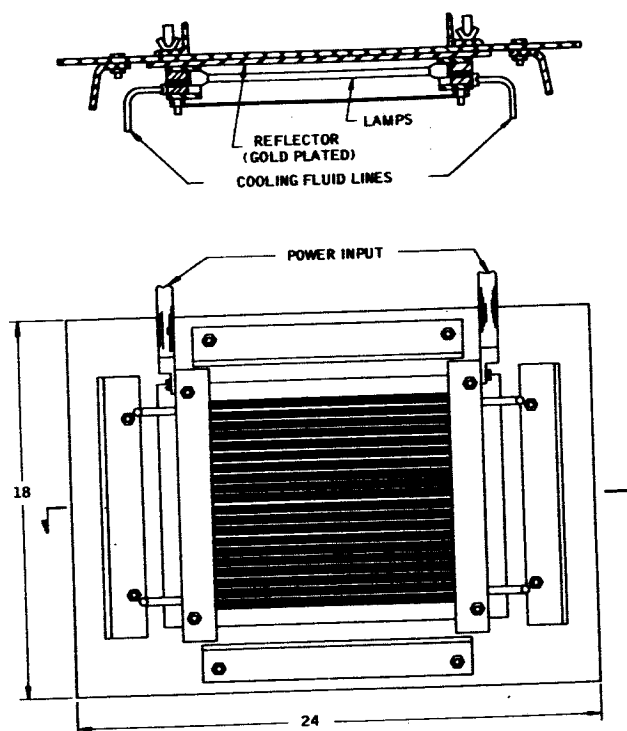


FIGURE 18. SCHEMATIC OF QUARTZ LAMP BANK.

The Thermac power controller, a phase controller power regulator using ignitrons connected in parallel opposition, is capable of controlling the voltage to the lamp bank from 0-400 volts at 130 kw maximum power. This unit can be either manually operated in set point mode or straight manual mode or externally programmed by using the "Data-Track."

The set point control enables the operator to "dial in" a specific value of heat flux, and the unit will

maintain the heat flux independent of the external conditions. The manual control is merely a voltage control.

The "Data-Track" unit permits programming of the voltage to the lamp bank which can be directly related to preprogrammed heat flux for tests to simulate actual conditions. Tests up to 130 seconds can be run.

The cooling system for the lamp bank is used to supplement normal air convective cooling of the lamp holding fixture and the reflector when extra high heat fluxes (for tests of long duration) are being achieved. The cooling system employs a circulating oil system. Transformer grade cooling oil is pumped from a reservoir through fluid passageways provided in the lamp holding fixtures, through heat exchange coils soldered to the bank side of the reflector plate, and back to the reservoir. Neoprene rubber tubing is used to connect the holding fixtures and reflector heat exchanger with the reservoir; this, with the grade of oil used, provides the necessary electrical isolation. A water-cooled heat exchanger inserted in the oil reservoir is used to dissipate the heat removed from the system.

The cooling system has a variable range cooling capacity. This is achieved by a by-pass flow valve which restricts the oil flow to the lamp bank. With the by-pass open the lamp holding fixtures receive one-fourth gallon per minute, and the reflector plate receives one and one-third gallons per minute. Water flow rates of up to one gallon per minute are possible through the water-cooled heat exchanger in the reservoir.

The Variplotter is used for recording output of the instrument being tested versus heat flux exposure. The output of a Gardon gauge type water-cooled reference standard of the appropriate range is connected to the x-axis of the plotter for the measurement of heat flux exposure. The y-axis is generated by the output of a Gardon gauge type test instrument. The performance of the test instrument is evaluated from the resulting curve. In the case of slug type calorimeters, a Gardon gauge type water-cooled reference standard is used to establish heat flux level. The output versus time data for the slug type calorimeter is taken by using a Minneapolis-Honeywell strip chart recorder or the Variplotter utilizing a time base generator which produces voltage input for the x-axis proportional to time. Range calibration for both types of recorders is checked with an Electronic Development, Inc., precision voltage source which is traceable to the Bureau of Standards.

2. Lamp Bank Performance. To determine the operating performance of the lamp bank, an extensive survey of the facility was made. A test survey

was conducted using two 50 Btu/ft<sup>2</sup>/sec Gardon gauge type water-cooled standards. One was placed directly under the center of the lamp bank, mounted in a fixed position in glass rock, and the other was placed in a movable section of glass rock. Both standards were in a plane parallel and two and one-fourth inches below the lamp bank. The 50 Btu/ft<sup>2</sup>/sec stationary standard was used as a reference, and by moving the other standard from the center to the front (from center along a 45 degree diagonal to the corner and from center to right side), different heat flux levels with respect to the center were acquired. The movable standard was initially placed one and five-eighths inches from the stationary standard and then moved to eight different stationary points. The eight stationary testing points were one-half inch apart with reference to the last testing point. With the stationary reference standard connected to the y-axis of the Variplotter and the movable standard connected to the x-axis, heat flux levels were recorded at each test location while applying 0 to 50 Btu/ft<sup>2</sup>/sec of radiant heat to the reference standard.

Figure 19 is a contour plot made from the test data, assuming symmetry for the four quadrants, at the 50 Btu/ft<sup>2</sup>/sec heat flux level. This shows heat flux decreasing from the center to the outer extremities of the lamp bank. The center heat flux is presented in Figure 20 as a function of lamp voltage.

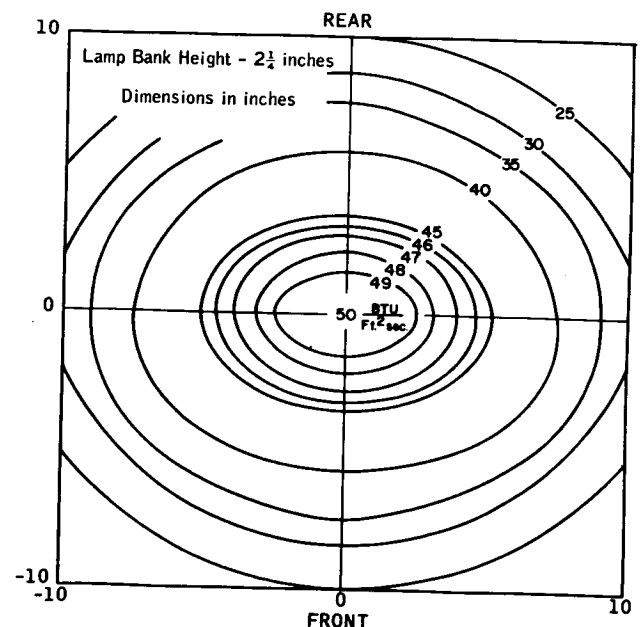


FIGURE 19. HEAT FLUX DISTRIBUTION UNDER LAMP BANK.

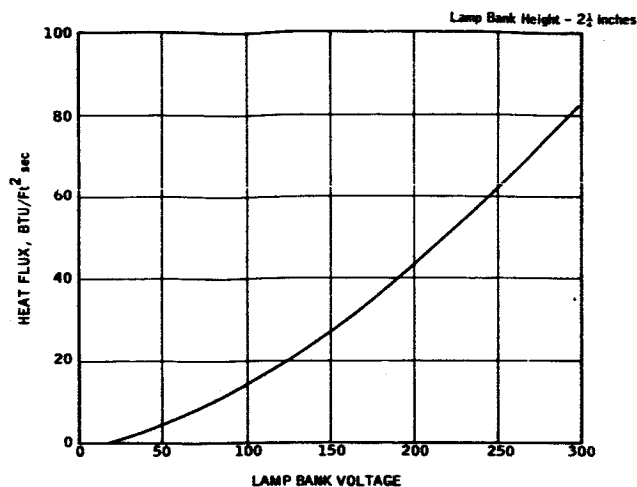


FIGURE 20. CENTER HEAT FLUX UNDER LAMP BANK AS A FUNCTION OF LAMP BANK VOLTAGE.

#### REFERENCES

1. Brown, A. I. and Marco, S. M., Introduction to Heat Transfer, 2nd Ed., McGraw-Hill Book Company (1951).
2. Gardon, Robert, "An Instrument for the Direct Measurement of Intense Thermal Radiation", *Rev. Sci. Instr.*, May, 1953.
3. Hsu, S. T., Engineering Heat Transfer, D. Van Nostrand, Inc., (1963).
4. Rubesin, M. W., "The Effect of an Arbitrary Surface Temperature Variation Along a Flat Plate on the Convective Heat Transfer in an Incompressible Boundary Layer", NACA TN 2345, April, 1951.
5. Carslaw, H. S., and Jaeger, J. C., Conduction of Heat in Solids, 2nd Ed. Oxford University Press (1959).

#### ACKNOWLEDGEMENTS

Several of the personnel of the Aerodynamics Division have contributed in various ways to the accumulation and presentation of the information contained herein.

#### APPENDIX A

##### DERIVATION OF SLUG TRANSDUCER EQUATION

Equation (3) is derived by setting up the following heat balance on the slug:

$$qA\Phi\alpha = C \, dT/dt + (1/R) \, \Delta T, \quad (A-1)$$

where  $q$  is the flux incident to the surface;  $A$ ,  $\alpha$ , and  $C$  are the receiving area, absorptivity, and heat capacitance of the slug, respectively;  $\Phi$  is the fraction of the flux incident on the transducer which actually falls on the slug;  $R$  is the thermal resistance between the slug and its surroundings;  $dT/dt$  is the time rate of slug temperature increase; and  $\Delta T$  is the temperature difference between the slug and its surroundings. For convection measurements,  $\Phi$  and  $\alpha$  are unity.

The above equation may be rearranged as follows:

$$q = (C/A\Phi\alpha) \, dT/dt + (1/RA\Phi\alpha) \, \Delta T \quad (A-2)$$

or

$$q = K \, dT/dt + K\theta\Delta T,$$

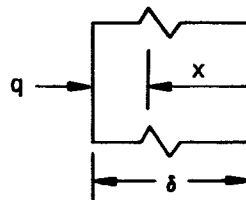
where

$$K = C/A\Phi\alpha \text{ and } \theta = 1/RC.$$

#### APPENDIX B

##### RESPONSE TIME OF SLUG TRANSDUCER

The slug of finite conductivity is usually represented for purposes of analysis as a slab bounded by two parallel planes with one surface heated and the other insulated as shown in the sketch below. This results in a one-dimensional temperature distribution through the slab.



For a constant heat flux,  $q$ , through the exposed surface and an initial slab temperature,  $T$ , of zero, the temperature distribution after exposure time,  $t$ , is shown in [ 5 ] to be

$$T = \frac{qt}{\rho c \delta} \left\{ 1 + \frac{\delta^2}{6\alpha t} \left[ 3 \left( \frac{X}{\delta} \right)^2 - 1 \right] - \frac{2}{\pi^2} \left( \frac{\delta^2}{\alpha t} \right) \sum_{n=1}^{\infty} \frac{(-1)^n}{n^2} \exp. \left( \frac{-n^2 \pi^2 \alpha t}{\delta^2} \right) \cos \frac{n\pi X}{\delta} \right\}, \quad (B-1)$$

where  $\rho$ ,  $c$ , and  $\alpha$  are the slab density, specific heat, and thermal diffusivity, respectively.

Differentiating this expression with respect to time yields

$$\frac{\partial T}{\partial t} = \frac{q}{\rho c \delta} \left[ 1 + 2 \sum_{n=1}^{\infty} (-1)^n \exp. \frac{-n^2 \pi^2 \alpha t}{\delta^2} \cos \frac{n\pi X}{\delta} \right]. \quad (B-2)$$

The series terms are seen to decrease rapidly with increasing  $n$ ; therefore, all terms for  $n$  greater than one are neglected. For a point on the back surface of the slug, equation (B-2) becomes

$$\frac{\partial T}{\partial t} \cong \frac{q}{\rho c \delta} \left[ 1 - 2 \exp. \left( \frac{-\pi^2 \alpha t}{\delta^2} \right) \right]. \quad (B-3)$$

The measured heat flux,  $q_m$ , determined from the temperature-time derivative is

$$q_m = \rho c \delta \left( \frac{\partial T}{\partial t} \right). \quad (B-4)$$

Combining equation (B-3) and (B-4) yields

$$q/q_m = 1 - 2 \exp. \frac{-\pi^2 \alpha t}{\delta^2}. \quad (B-5)$$

It is seen that this ratio depends only on the Fourier number,  $\alpha t/\delta^2$ .

The response time,  $t^*$ , for a slug may be defined as the time required for the measured heat flux,  $q_m$ , to reach  $(1 - 2/e^2)$ , or 73 percent of the actual heat flux. From equation (B-5) it is seen that the Fourier number be  $2/\pi^2$ , or 0.203, to satisfy this criteria. The response time, then, is given by

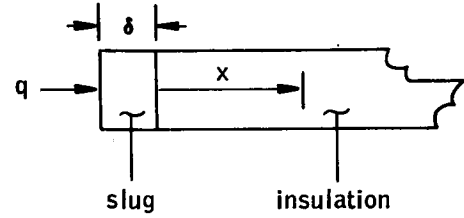
$$t^* = 0.203 \delta^2/\alpha. \quad (B-6)$$

This equation is presented graphically in Figure 2.

## APPENDIX C

### RESPONSE TO CONSTANT HEAT FLUX OF A SLUG BACKED BY A SEMI-INFINITE INSULATOR

A sketch of a slug backed by a semi-infinite insulator is shown below.



The temperature history of this model is obtained from the solution of the one-dimensional Fourier equation:

$$\partial^2 T / \partial X^2 = (1/\alpha) \partial T / \partial t, \quad (C-1)$$

where  $T$  is the temperature at a distance  $X$  into the insulation at time  $t$  and  $\alpha$  is the thermal diffusivity of the insulation material. Equation (1) is subject to the following boundary conditions:

$$q = \rho c \delta \frac{\partial T}{\partial t} - k \frac{\partial T}{\partial X} \text{ at } X = 0 \quad (C-2)$$

$$T = 0 \text{ at } t = 0 \quad (C-3)$$

$$T = 0 \text{ at } X = \infty, \quad (C-4)$$

where  $q$  is the heat flux to the front surface of the slug,  $k$  is the thermal conductivity of the insulation material, and  $\rho$ ,  $c$ , and  $\delta$  are the density, specific heat, and thickness, respectively, of the slug.

Equation (2) is derived from a simple heat balance on the slug assuming that the slug temperature is uniform and equal to the insulator temperature at the interface. The contact resistance at the interface is assumed to be zero, and all thermal properties are assumed to be constant.

The LaPlace transform of equation (C-1), taking into consideration the boundary condition given by equation (C-3), is

$$d^2 \bar{T} / dX^2 = (s/\alpha) \bar{T}, \quad (C-5)$$

where  $\bar{T}$  is the transformed temperature and  $s$  is a constant introduced by the LaPlace Transformation.

Solving for the transformed temperature,  $\bar{T}$ , taking into consideration the boundary condition given by equation (4), yields

$$\bar{T} = A \exp. (-X \sqrt{s/\alpha}) \quad (C-6)$$

where  $A$  is an integration constant. Applying the LaPlace transform to the boundary condition given by equation (2) yields

$$q/s = \rho c \delta s \bar{T} - k d\bar{T}/dt. \quad (C-7)$$

Applying this transformed boundary condition to equation (6) yields

$$\bar{T} = q \exp. (-X\sqrt{s/\alpha}) / [s(\rho c \delta s + K\sqrt{s/\alpha})]. \quad (C-8)$$

This transform is found in the table of LaPlace transforms of [5] to yield the expression:

$$T = \frac{qt}{\rho c \delta} \left[ \frac{2}{\ln \sqrt{\pi \alpha t}} \exp. \left( \frac{-X^2}{4 \alpha t} \right) - \frac{(1+hX)}{h^2 \alpha t} \operatorname{erfc} (X/2\sqrt{\alpha t}) \right. \\ \left. + \frac{1}{h^2 \alpha t} \exp. (hX + h^2 \alpha t) \operatorname{erfc} \left( \frac{X}{2\sqrt{\alpha t}} + \ln \sqrt{\alpha t} \right) \right] \quad (C-9)$$

where  $h = k/\rho c \delta \alpha$ .

The slug temperature history is found from equation (C-9) for  $X$  equal to zero:

$$T = \frac{qt}{\rho c \delta} \left[ \frac{2}{\ln \sqrt{\pi \alpha t}} - \frac{1}{h^2 \alpha t} \left( 1 - \exp. (h^2 \alpha t) \operatorname{erfc} (h\sqrt{\alpha t}) \right) \right] \\ = Z_1 \frac{qt}{\rho c \delta}. \quad (C-10)$$

The slope of the temperature-time curve is found from the first derivative of equation (C-10):

$$dT/dt = (q/\rho c \delta) \exp. (h^2 \alpha t) \operatorname{erfc} (h\sqrt{\alpha t}) = Z_2 q/\rho c \delta, \quad (C-11)$$

or

$$q = \rho c \delta (dT/dt)/Z_2.$$

The conduction correction factors,  $Z_1$  and  $Z_2$ , are presented in Figure (C-1) as a function of the parameter  $h\sqrt{\alpha t}$ . The correction factors are seen to equal unity initially (at  $t = 0$ ), regardless of the thermal diffusivity,  $\alpha$ , of the insulating material. Thus, the heat flux may be determined from the initial slope of

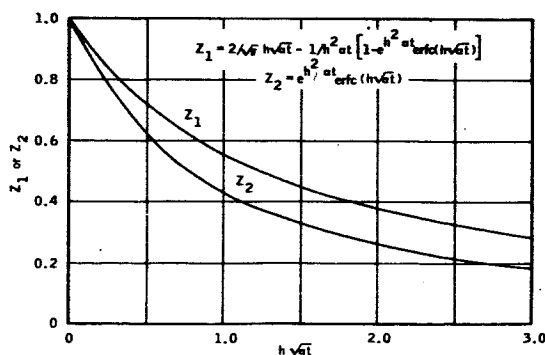


FIGURE C-1. CONDUCTION CORRECTION FACTORS,  $Z_1$  AND  $Z_2$ , AS A FUNCTION OF THE PARAMETER  $h\sqrt{\alpha t}$ .

the temperature-time curve without considering heat losses. Likewise, for a perfect insulator ( $\alpha = 0$ ), the conduction correction factors are equal to unity at any time.

Presented in Figure C-2 is the temperature history calculated from equation (C-10) for a 0.010 inch thick copper slug backed by a semi-infinite glass insulator and exposed to a constant heat flux of 10 Btu/ft<sup>2</sup>-sec. This temperature history is compared to the temperature history of a slug having no heat losses.

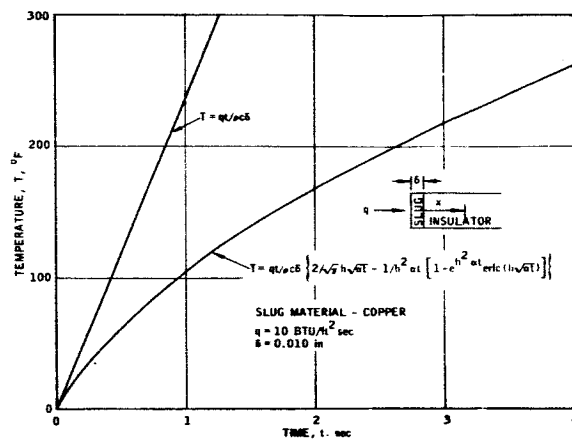
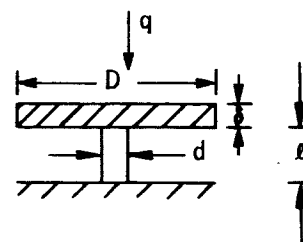


FIGURE C-2. TEMPERATURE HISTORY OF A SLUG BACKED BY SEMI-INFINITE GLASS INSULATOR FOR A CONSTANT HEAT FLUX.

## APPENDIX D

### THEORY OF DISC-ROD SENSOR

The pertinent geometrical dimensions of the disc-rod sensor are shown in the following illustration (see discussion in body of report):



Applying a heat balance to the system yields

$$q \frac{\pi D^2}{4} = \rho_c C_c \frac{\pi D^2}{4} \delta \frac{d\Delta T}{dt} + \frac{1}{2} \rho_K C_K \frac{\pi d^2}{4} l \frac{d\Delta T}{dt} + \frac{K_K \pi d^2}{l} \Delta T, \quad (D-1)$$

where  $q$  is the absorbed heat flux;  $\Delta T$  is the temperature difference between the two ends of the rod; and  $\rho$ ,  $c$ , and  $k$  are the density, specific heat, and thermal conductivity, respectively, of the copper (subscript  $c$ ) and constantan (subscript  $K$ ). A uniform temperature distribution is assumed over the copper disc, and a linear temperature distribution is assumed along the constantan rod with the heat sink at constant temperature.

Rearranging equation (D-2) and integrating yields

$$\Delta T = \Delta T_\infty (1 - e^{-t/t^*}), \quad (D-2)$$

where

$$\Delta T_\infty = q \frac{\left(\frac{d}{\alpha}\right)^2 l}{k} \quad (D-3)$$

and

$$t^* = 0.5 \left[ 2 \left(\frac{D}{\alpha}\right)^2 \frac{\delta}{l} \frac{\rho_c C_c}{\rho_K C_K} + 1 \right] \frac{l^2 \rho_K C_K}{K_K}. \quad (D-4)$$

The sensitivity is found from equation (D-3) by converting the equilibrium temperature difference to thermoelectric emf,  $E$ , for the copper-constantan pair and by substituting into the equation the value of the thermal conductivity,  $k$ :

$$E/q = 0.5 \left(\frac{D}{\alpha}\right)^2 l, \quad (D-5)$$

where the sensitivity,  $E/q$ , is in mv/Btu/ft<sup>2</sup>-sec, and the rod length,  $l$ , is in inches.

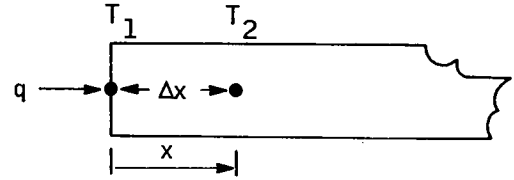
Inserting the copper and constantan properties into equation (D-4) yields the expression for response time,  $t^*$ :

$$t^* = 50 [1 + 2 (D/d)^2 (\delta/l)] l^2. \quad (D-6)$$

## APPENDIX E

### THEORY OF SEMI-INFINITE SLAB SENSOR

This method of determining surface heat flux consists of determining the temperature gradient near the surface by measuring the temperature at the surface and at a position some distance from the surface as shown in the sketch below.



The great heat flux,  $q_m$ , as determined from the temperature measurements, is given by

$$q_m = k(T_1 - T_2)/\Delta X = k\Delta T/\Delta X. \quad (E-1)$$

To gain some indication of the accuracy and response time of such a measurement, an analysis was made of this measurement for the case of a constant heat flux into the surface of a semi-infinite slab. The temperature distribution in a semi-infinite slab exposed to a constant heat flux is given in [5] as follows:

$$T = (2q\sqrt{\alpha t}/k) \operatorname{ierfc}(X/2\sqrt{\alpha t}), \quad (E-2)$$

where  $T$  is the temperature at a distance  $X$  into the slab, and at the time  $t$ ,  $q$  is the heat flux into the front surface,  $\alpha$  is the thermal diffusivity, and  $k$  is the thermal conductivity.

The initial temperature (at  $t = 0$ ) is assumed to be zero at all points.

From equation (E-2), the temperature difference from a point on the surface to a point a distance  $\Delta X$  from the surface is

$$\Delta T = (2q\sqrt{\alpha t}/k) [(1/\sqrt{\pi}) - \operatorname{ierfc}(\Delta X/2\sqrt{\alpha t})]. \quad (E-3)$$

Combining equation (E-1) and (E-3) yields

$$q_m/q = (1/\eta) [(1/\sqrt{\pi}) - \operatorname{ierfc} \eta], \quad (E-4)$$

where

$$\eta = \Delta X/2\sqrt{\alpha t}.$$

The ratio given by equation (E-4) is presented in Figure E-1 as a function of  $\eta$ .

Presented in Figure E-2 is the ratio,  $q_m/q$ , as a function of time for a semi-infinite copper slab exposed to a constant heat flux with  $\Delta X = 0.3$  inches. It

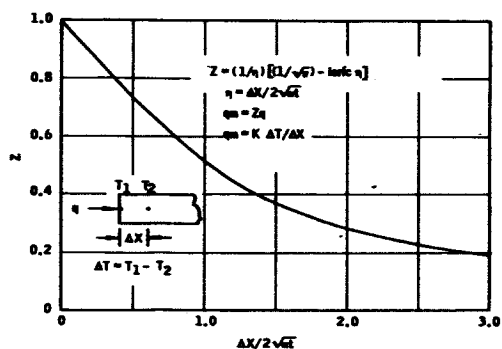


FIGURE E-1. CORRECTION FACTOR,  $Z$ , FOR DETERMINING SURFACE HEAT FLUX FROM TWO TEMPERATURE MEASUREMENTS

is noted that the ratio quickly rises to about 0.9 and then approaches unity very slowly. This is quite different from the exponential curves of Gardon type heat transfer gauges in which unity is approached much more rapidly after the initial rise.

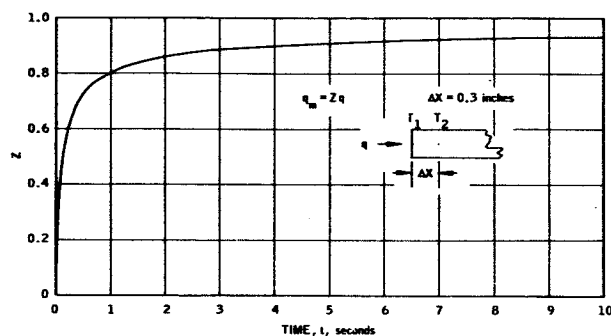


FIGURE E-2. CORRECTION FACTOR,  $Z$ , AS A FUNCTION OF TIME FOR A SEMI-INFINITE COPPER SLAB.



## VI. MATHEMATICS

# A SURVEY OF METHODS FOR GENERATING LIAPUNOV FUNCTIONS

BY

C. C. Dearman, Jr. and A. R. LeMay

## SUMMARY

In 1892, in his now famous memoir, A. M. Liapunov, a Russian mathematician, derived a method for determining stability properties of nonlinear dynamical systems which did not require any knowledge of the solutions of the differential equations that describe the motion of the system.

Liapunov's method consists of generating a function in the state variables which must possess certain properties. If this Liapunov function could be exhibited, certain conclusions could be made concerning the stability properties of the dynamical system. There are as yet no general schemes for constructing these functions, but there are methods for generating Liapunov functions for special cases of certain types and even for classes of certain dynamical systems.

This survey describes those methods which, with possible extensions and modifications, appear to offer the best hope for applications to practical nonlinear dynamical systems.

## I. INTRODUCTION

It is well known that it is possible to obtain information about the stability of a dynamical system without solving the differential equations of motion that describe the behavior of the system. The Routh-Hurwitz criterion is an example of the methods that may be used for this purpose for linear systems. Liapunov's so-called "second" or "direct" method is applicable in this regard to both linear and nonlinear systems. Furthermore, it is the only method known today that is so applicable. The designation "second method" is an unfortunate but apparently firmly entrenched misnomer. It is not really a method at all; it is more a point of view or philosophical approach [28]<sup>1</sup>.

The second method permits the determination of stability properties of dynamical systems by using suitable scalar functions of the state variables that are defined in a phase space or motion space. These functions are called Liapunov functions or  $v$ -functions, and the sign of the time derivative,  $\dot{v}$ , with respect to the equations of motion, has to be considered. Roughly, if  $v\dot{v} \leq 0$ , the motion is stable in some sense; otherwise, it is unstable.

There are many concepts of stability and instability for nonlinear systems, but whatever the concept used the second method requires the generation of a suitable  $v$ -function, and therein lies the principal difficulty in applying the method to practical problems. Presently available methods for generating Liapunov functions lean heavily on the experience, ingenuity, and good fortune of the investigator. No universally applicable methods for generating Liapunov functions are known to exist, but there are techniques that are applicable to particular problems and to some classes of nonlinear systems. Indeed, it might have been more informative if the word "techniques" instead of "methods" had been used in the title of this paper because none of the known procedures for nonlinear systems is entirely methodical.

An extensive study has been made by the authors of methods of generating Liapunov functions and of the various nonlinear differential equations to which they apply. Some of the methods appear to be applicable only to quite special problems. In many cases, they apparently yield Liapunov functions only for the examples given in the paper in which they were presented. Other methods are applicable only if the system is known to have "small nonlinearities," while still others appeared to offer no hope in solving stability problems of interest. The methods that are discussed in this paper are those which seemed to be most interesting and promising of further development toward applicability to practical systems. For an exposition of those methods which are not discussed in this paper, the reader may consult the references in the bibliography.

An example of a nonlinear system which is of immediate interest is the system defined by the equations of motion of a guided space vehicle subject only to

<sup>1</sup>Numbers in square brackets refer to numbered references in the bibliography.

thrust and gravitational forces. At present it appears that the task of generating Liapunov functions for such a system will require extensive exploitation of modern digital and analog computers. Because only initial probing explorations have been made in investigating this possibility, any report of progress at this time would be premature [28].

In this survey only autonomous nonlinear systems will be treated. (The difficulties encountered in generating Liapunov functions for nonautonomous systems have not yet been surmounted except in the simplest cases.) It will be assumed that the equations of motion of the dynamical systems under study may be expressed in vector notation as

$$\dot{\mathbf{X}} = \mathbf{F}(\mathbf{X}), \quad (1.1)$$

where  $\dot{\mathbf{X}} = (\dot{x}_1, \dot{x}_2, \dots, \dot{x}_n)$ ,  $\mathbf{F}(\mathbf{X}) = (f_1(\mathbf{X}), f_2(\mathbf{X}), \dots, f_n(\mathbf{X}))$ , and  $\mathbf{X} = (x_1, \dots, x_n)$ , with  $\mathbf{F}(\mathbf{X})$  possessing those properties which insure the existence and uniqueness of the solution as well as their continuous dependence on the initial values  $\mathbf{X}_0$ . Further, it will be assumed that

$$\mathbf{F}(0) = 0, \quad (1.2)$$

i.e., that equations (1.1) shall have  $\mathbf{X} = 0$  as the trivial or equilibrium solution. This solution may be interpreted as the desired terminal state of the dynamical system. If the system possesses appropriate stability characteristics, its motion will approach this solution or state as a limiting value from some previous state or from some perturbed state. The differential equations (1.1), therefore, will be referred to as the equations of perturbed motion.

Liapunov's theory requires that the  $v$ -function,  $v(\mathbf{X})$ , possess certain properties. These vary with the stability concept under consideration. For example, if it is required that the trivial solution be simply stable, it is sufficient that  $v(\mathbf{X})$  and its first partial derivatives be continuous in some open region  $\Delta$  around the origin, that  $v(0) = 0$ , that  $v(\mathbf{X})$  be positive-definite, and that

$$\dot{v} = \sum_{i=1}^n \frac{\partial v}{\partial x_i} f_i(\mathbf{X}) \quad (1.3)$$

be non-positive. If the trivial solution is to be asymptotically stable, it is sufficient that  $v(\mathbf{X})$  possess the properties enumerated above and that  $\dot{v}$  be negative-definite. According to one concept of instability - due to Liapunov - the trivial solution is unstable if there exists a function  $v(\mathbf{X})$  that has an infinitesimal upper bound, a domain  $v(\mathbf{X}) < 0$ , and whose derivative,  $\dot{v}$ ,

with respect to equation (1.1) is negative-definite. These theorems have been modified and extended by Krasovskii, Zubov, Malkin, La Salle, Kalman, and others.

At present the general questions relating to the existence of  $v$ -functions remain unanswered. However, the question as to whether or not the sufficiency conditions stated in the principal theorems are also necessary has been largely answered in the affirmative although some problems have yet to be resolved [20].

No attempt is made in this survey to extend the theory of the stability of motion according to Liapunov's second method. The aim is the modest one of presenting what our studies have shown to be the most promising methods of generating Liapunov functions for practical nonlinear systems. However, in the interests of brevity and simplicity, only elementary examples have been chosen to illustrate the use of the methods discussed.

## II. DERIVATION OF A LIAPUNOV FUNCTION FOR LINEAR AUTONOMOUS SYSTEMS

Liapunov developed a method for generating  $v$ -functions for linear autonomous systems of differential equations. Several other relatively simple methods now exist for determining stability in these systems. A study of the methods of generating Liapunov functions for linear systems is eminently worthwhile inasmuch as many of the methods of constructing Liapunov functions for nonlinear systems depend upon a knowledge of Liapunov functions for linear systems. One method for constructing Liapunov functions for linear systems of the form  $\dot{\mathbf{X}} = \mathbf{C}\mathbf{X}$ , where  $\mathbf{C}$  is an  $n \times n$  matrix with constant coefficients, is as follows:

(1) Assume  $v(\mathbf{X})$  to be a homogeneous quadratic form defined by the equation

$$v(\mathbf{X}) = \mathbf{X}^T \mathbf{A} \mathbf{X} = \sum_{i=1}^n \sum_{j=1}^n \alpha_{ij} x_i x_j, \quad (2.1)$$

where  $\mathbf{A}$  is an  $n \times n$  symmetric matrix of constant (real) elements  $\alpha_{ij}$ .

(2) Differentiate  $v(\mathbf{X})$  in (2.1) with respect to the equations of motion and get

$$\dot{v}(\mathbf{X}) = \sum_{i=1}^n \frac{\partial v}{\partial x_i} \dot{x}_i = \sum_{i=1}^n \sum_{j=1}^n \beta_{ij} x_i x_j = \mathbf{X}^T \mathbf{B} \mathbf{X}, \quad (2.2)$$

where  $\mathbf{B}$  is an  $n \times n$  matrix with constant elements  $\beta_{ij}$ .

(3) Constrain  $\hat{v}$  to be positive-definite (or negative-definite) and find the elements  $\alpha_{ij}$  and  $\beta_{ij}$  such that  $\hat{v}$  and  $v$  satisfy either a stability or an instability criteria.

Two rather simple examples illustrate the method:

#### Example 1.

Consider the linear differential equation  $\ddot{x} + a\dot{x} + bx = 0$ , where  $a$  and  $b$  are real constants. This equation may be written in matrix form as

$$\begin{bmatrix} \dot{x}_1 \\ \dot{x}_2 \end{bmatrix} = \begin{bmatrix} 0 & 1 \\ -b & -a \end{bmatrix} \begin{bmatrix} x_1 \\ x_2 \end{bmatrix} \leftrightarrow \dot{X} = CX, \quad (2.3)$$

by the usual substitutions,  $x_1 = x$  and  $x_2 = \dot{x}$ . In accordance with step (1) above, let

$$v = \alpha_{11} x_1^2 + 2\alpha_{12} x_1 x_2 + \alpha_{22} x_2^2. \quad (2.4)$$

Then

$$\dot{v} = (-2b\alpha_{12})x_1^2 + (2\alpha_{11} - 2a\alpha_{12} - 2b\alpha_{22})x_1x_2 + (2\alpha_{12} - 2a\alpha_{22})x_2^2. \quad (2.5)$$

If we set

$$2b\alpha_{12} = 1$$

$$2\alpha_{12} - 2a\alpha_{22} = -1 \quad (2.6)$$

$$2\alpha_{11} - 2a\alpha_{12} - 2b\alpha_{22} = 0,$$

then

$$\dot{v} = -x_1^2 - x_2^2. \quad (2.7)$$

The solution of the system (2.6) yields

$$\alpha_{11} = \frac{a^2 + b(b+1)}{2ab} \quad (2.8)$$

$$\alpha_{12} = \frac{1}{2b} \quad (2.9)$$

$$\alpha_{22} = \frac{b+1}{2ab}. \quad (2.10)$$

Thus

$$v = \frac{a^2 + b(b+1)}{2ab} x_1^2 + \frac{1}{b} x_1 x_2 + \frac{b+1}{2ab} x_2^2$$

$$= [x_1 x_2] \begin{bmatrix} \frac{a^2 + b(b+1)}{2ab} & \frac{1}{2b} \\ \frac{1}{2b} & \frac{b+1}{2ab} \end{bmatrix} \begin{bmatrix} x_1 \\ x_2 \end{bmatrix} \quad (2.11)$$

which is of the form  $v = X^T A X$ . According to Sylvester's inequalities,  $v$  is positive-definite if and only if

$$\frac{a^2 + b(b+1)}{2ab} > 0$$

and

$$\left( \frac{a^2 + b(b+1)}{2ab} \right) \left( \frac{b+1}{2ab} \right) - \left( \frac{1}{2b} \right)^2 > 0. \quad (2.12)$$

The inequalities (2.12) require that the relations  $a > 0$  and  $b > 0$  be satisfied. These could also have been found directly by means of the Routh-Hurwitz criteria.

The following example illustrates the increasing difficulties encountered in deriving Liapunov functions for higher order systems.

#### Example 2.

Consider the third order linear differential equations  $\ddot{x} + a\dot{x} + b\ddot{x} + cx = 0$  with constant coefficients  $a, b, c$ . The matrix form of the equation is

$$\begin{bmatrix} \dot{x}_1 \\ \dot{x}_2 \\ \dot{x}_3 \end{bmatrix} = \begin{bmatrix} 0 & 1 & 0 \\ 0 & 0 & 1 \\ -c & -b & -a \end{bmatrix} \begin{bmatrix} x_1 \\ x_2 \\ x_3 \end{bmatrix} \leftrightarrow \dot{X} = CX. \quad (2.13)$$

Let  $v$  be the quadratic form

$$v = X^T A X, \quad (2.14)$$

where  $A$  is a  $3 \times 3$  symmetric matrix with constant coefficients  $\alpha_{ij}$ ;  $i=1,2,3$ ;  $j=1,2,3$ ; and  $X = \text{col}(x_1, x_2, x_3)$ . Differentiating (2.14) with respect to the equations (2.13) gives

$$\dot{v} = X^T [B^T A + AB] X. \quad (2.15)$$

Now, constrain the right member of (2.15) so that

$$\dot{v} = -(x_1^2 + x_2^2 + x_3^2). \quad (2.16)$$

Then,

$$B^T A + AB = -I, \quad (2.17)$$

where  $I$  is a  $3 \times 3$  identity matrix. From equation (2.17), the elements  $\alpha_{ij}$  of  $A$  are obtained.

$$\alpha_{11} = \frac{b(ab-c) + c(ac+a^2 + c^2)}{2c(ab-c)}$$

$$\alpha_{12} = \alpha_{21} = \frac{c^2 + b(a^2 + c^2)}{2c(ab-c)}$$

$$\alpha_{13} = \alpha_{31} = \frac{1}{2c} \quad (2.18)$$

$$\alpha_{22} = \frac{a(a^2 + ac + c^2) + c(b^2 + b + 1)}{2c(ab-c)}$$

$$\alpha_{23} = \alpha_{32} = \frac{ac+a^2+c^2}{2c(ab-c)}$$

$$\alpha_{33} = \frac{bc+c+a}{2c(ab-c)}$$

Sylvester's inequalities become

$$\frac{bc+c+a}{2c(ab-c)} > 0$$

$$\left( \frac{bc+c+a}{2c(ab-c)} \right) \left( \frac{a(a^2+ac+c^2)+c(b^2+b+1)}{2c(ab-c)} \right) - \left[ \frac{ac+a^2+c^2}{2c(ab-c)} \right]^2 > 0 \quad (2.19)$$

$$|A| = \det A > 0.$$

Through tedious but elementary algebraic manipulations, it may be determined that the inequalities (2.19) are satisfied if  $a > 0$ ,  $c > 0$ , and  $ab-c > 0$ . Again, the Routh-Hurwitz criteria would have provided the same result.

### III. AIZERMAN'S METHOD

There are two well-known methods for generating Liapunov functions for systems with "small" nonlinearities. Aizerman's method is one of these. Krasovskii's method is the other; it will be discussed in the section following.

Aizerman proposed a relatively simple procedure for generating Liapunov functions for nonlinear autonomous systems. His method is based on a procedure for generating Liapunov functions for linear systems, and it is applicable to systems containing one or more "slightly" nonlinear elements. For simplification it will be assumed that there is only one nonlinear element in the systems to be discussed.

Aizerman's method consists essentially in approximating the nonlinear element (or elements) of the nonlinear system by linear elements and then finding a Liapunov function for the resulting linear system.

The Liapunov function thus found is then applied to the nonlinear system, and a domain over which stability (or instability) exists is determined. The following example illustrates the method.

Example 1.

Consider the nonlinear differential equation

$$\ddot{x} + a\dot{x} + f(x) = 0, \quad (3.1)$$

where  $a$  is a real constant ( $> 0$ ) and  $f(x)$  is a "slightly" nonlinear element. Further, let  $f(x)$  be expressible in the form

$$f(x) = hx + g(x), \quad (3.2)$$

where  $h$  is a real constant. Then (3.1) may be expressed in the form

$$\begin{bmatrix} \dot{x}_1 \\ \dot{x}_2 \end{bmatrix} = \begin{bmatrix} 0 & 1 \\ -h & -a \end{bmatrix} \begin{bmatrix} x_1 \\ x_2 \end{bmatrix} + \begin{bmatrix} 0 \\ -q(x_1) \end{bmatrix} \quad (3.3)$$

by means of the usual substitutions  $x_1 = x$  and  $x_2 = \dot{x}$ . If  $q(x_1)$  is sufficiently small, equation (3.3) may be approximated by the equations

$$\begin{bmatrix} \dot{x}_1 \\ \dot{x}_2 \end{bmatrix} = \begin{bmatrix} 0 & 1 \\ -h & -a \end{bmatrix} \begin{bmatrix} x_1 \\ x_2 \end{bmatrix}. \quad (3.4)$$

Assume

$$v = \alpha_{11}x_1^2 + 2\alpha_{12}x_1x_2 + \alpha_{22}x_2^2. \quad (3.5)$$

Then

$$\begin{aligned} \dot{v} = & -2\alpha_{12}hx_1^2 + (2\alpha_{11} - 2a\alpha_{12} - 2\alpha_{22}h)x_1x_2 \\ & + (2\alpha_{12} - 2a\alpha_{22})x_2^2. \end{aligned} \quad (3.6)$$

Constrain the right member of (3.6) so that

$$\dot{v} = -x_1^2 - x_2^2. \quad (3.7)$$

Then it may be determined that

$$\alpha_{11} = \frac{a^2 + h(h+1)}{2ah} \quad (3.8)$$

$$\alpha_{12} = \frac{1}{2h} \quad (3.9)$$

$$\alpha_{22} = \frac{h+1}{2ah}. \quad (3.10)$$

Thus, (3.5) becomes

$$v = \frac{a^2 + h(h+1)}{2ah} x_1^2 + \frac{1}{h} x_1 x_2 + \frac{h+1}{2ah} x_2^2, \quad (3.11)$$

which is positive-definite for  $h > 0$ ,  $a > 0$ .

As may be determined from (3.3) and (3.11)

$$-\dot{v} = \frac{f(x_1)}{hx_1} x_1^2 + \left( -\frac{1+h}{a} + \frac{1+h}{ah} \frac{f(x_1)}{x_1} \right) x_1 x_2 + x_2^2. \quad (3.12)$$

By Sylvester's inequalities it may be determined that  $-\dot{v}$  is positive-definite if and only if

$$\frac{f(x_1)}{hx_1} > 0 \quad (3.13)$$

$$\frac{f(x_1)}{hx_1} > \frac{1}{4} \left( -\frac{(hx_1 - f(x_1))(1+h)}{ahx_1} \right)^2. \quad (3.14)$$

The inequality (3.14) is satisfied if and only if

$$\frac{(h+1)^2 + 2a^2 - 2\sqrt{a^4 + a^2(h+1)^2}}{(h+1)^2} < \frac{f(x_1)}{hx_1} < \frac{(h+1)^2 + 2a^2 + 2\sqrt{a^4 + a^2(h+1)^2}}{(h+1)^2} \quad (3.15)$$

It may be noted that (3.15) is but one domain for asymptotic stability. Using the equation (13.1), page 59 of Reference 35, with obvious substitutions, and the procedure on page 60, it may be determined that the domain of stability is given by the relation

$$0 < \frac{f(x_1)}{x_1} < \infty, \quad (3.16)$$

which, of course, is less restrictive than the relation (3.15).

#### IV. KRASOVSKII'S METHOD

Krasovskii considered the autonomous nonlinear system

$$\dot{X} = F(X), \quad (4.1)$$

which possesses the properties of the system (1.1). The Jacobian matrix of  $F(X)$  is

$$J = \begin{bmatrix} \frac{\partial f_1}{\partial x_1} & \dots & \frac{\partial f_1}{\partial x_n} \\ \vdots & \ddots & \vdots \\ \frac{\partial f_n}{\partial x_1} & \dots & \frac{\partial f_n}{\partial x_n} \end{bmatrix} \equiv \frac{\partial F}{\partial X}. \quad (4.2)$$

Krasovskii proposed and proved the following theorem [17]:

"In order that the trivial solution of (4.1) be globally asymptotically stable, it is sufficient that there exist a positive symmetric matrix

$$A = \begin{bmatrix} \alpha_{11} & \dots & \alpha_{1n} \\ \vdots & \ddots & \vdots \\ \alpha_{n1} & \dots & \alpha_{nn} \end{bmatrix} \quad (4.3)$$

with positive eigenvalues, such that the symmetric matrix  $C = (c_{ik})$  where

$$c_{ik} = \sum_{j=1}^n \left( \alpha_{ij} \frac{\partial f_j}{\partial x_k} + \alpha_{kj} \frac{\partial f_j}{\partial x_i} \right) \quad (4.4)$$

has the eigenvalues  $\lambda_i(X)$ , ( $i = 1, \dots, n$ ), which uniformly satisfy the conditions

$$\lambda_i < -\gamma \quad (\gamma > 0, i = 1, 2, \dots, n) \quad (4.5)$$

for all  $x_i$  and  $\gamma$  is a real constant." (For proof, see Reference 31, pages 91-94.)

To apply this theorem to a nonlinear system, it is necessary to exhibit the matrix  $A$  of the theorem. To do this let

$$v = \sum_{i=1}^n \sum_{j=1}^n \alpha_{ij} f_i f_j = F^T A F. \quad (4.6)$$

Then

$$\dot{v} = F^T (AJ + J^T A) F,$$

where  $J$  is the Jacobian matrix of (4.2).

Now,  $v$  can be constrained to be positive-definite, and Sylvester's inequalities can be applied to  $\dot{v}$  to determine the stability bounds.

Although it might appear that Krasovskii's method is basically the same procedure as Aizerman's, there is one major difference. Krasovskii's method makes use of a  $v$  function which is a quadratic form in the components  $f_i$  of  $F$ . These components are the system velocities. Aizerman's method considers  $v$ -functions which are quadratic in the state variables.

As an illustration of the method, consider the example of the previous section that was used to illustrate Aizerman's method:

Example 1.

$$\ddot{x} + a\dot{x} + f(x) = 0, \quad a > 0 \quad (4.7)$$

Let

$$\dot{x}_1 = f_1(X) = x$$

$$\dot{x}_2 = f_2(X) = -ax_2 - f(x_1) \quad (4.8)$$

Then

$$\dot{f}_1(X) = \dot{x}_2 = f_2(X) \quad (4.9)$$

$$\dot{f}_2(X) = -a\dot{x}_2 - \frac{df(x_1)}{dx_1} f_1(X) \quad (4.10)$$

Let

$$v = \alpha_{11}f_1^2(X) + 2\alpha_{12}f_1(X)f_2(X) + \alpha_{22}f_2^2(X) \quad (4.11)$$

Then

$$\dot{v} = \left( -2\alpha_{12} \frac{df(x_1)}{dx_1} \right) f_1^2(X) + 2 \left( \alpha_{11} - a\alpha_{12} - \alpha_{22} \frac{df(x_1)}{dx_1} \right) f_1(X) f_2(X) + 3\alpha_{22} \left( -a\alpha_{22} \right) f_2^2(X) \quad (4.12)$$

Now assume that  $f(x_1)$  can be written in the form

$$f(x_1) = hx_1 + q(x_1), \quad (4.13)$$

with  $q(x_1)$  small so that

$$\frac{df(x_1)}{dx_1} \doteq h. \quad (4.14)$$

In Example 1, Section 2, the right member of (2.5) was constrained so that  $\dot{v} = -x_1^2 - x_2^2$ . In Krasovskii's method the right member of  $\dot{v}$  is constrained so that, analogously, for this example

$$\dot{v} = -f_1^2(X) - f_2^2(X) \quad (4.15)$$

Then, with

$$\frac{df(x_1)}{dx_1} = h,$$

it follows that

$$\alpha_{11} = \frac{a^2 + h(h+1)}{2ah} \quad (4.16)$$

$$\alpha_{12} = \frac{1}{2h} \quad (4.17)$$

$$\alpha_{22} = \frac{h+1}{2ah} \quad (4.18)$$

For the values of  $\alpha_{11}$ ,  $\alpha_{12}$ ,  $\alpha_{22}$ , Sylvester's inequalities show that  $v$  is positive-definite if and only if  $a > 0$  and  $h > 0$ . Likewise, it can be shown that  $\dot{v}$  is negative-definite if and only if

$$h - \frac{df(x_1)}{dx_1} > 0 \quad (4.19)$$

and

$$\frac{df(x_1)}{dx_1} \left( \frac{1}{h} \right) - \left( \frac{h+1}{2ah} \right)^2 \left( h - \frac{df(x_1)}{dx_1} \right)^2 > 0. \quad (4.20)$$

Inequalities (4.19) and (4.20) are satisfied if

$$\frac{(h+1)^2 + 2a^2 - 2\sqrt{a^4 + a^2(h+1)^2}}{(h+1)^4} < \frac{df(x_1)}{dx_1} \left( \frac{1}{h} \right) < \frac{(h+1)^2 + 2a^2 + 2\sqrt{a^4 + a^2(h+1)^2}}{(h+1)^4} \quad (4.21)$$

Inequality (4.21) is a sufficient but not a necessary condition for asymptotic stability of the equilibrium solution of the system (4.7).

Basically, Krasovskii's method possesses most of the advantages and disadvantages of Aizerman's method. However, there are some systems which do not lend themselves to Aizerman's method, whose equilibrium solution can be proven to be asymptotically stable by Krasovskii's method and vice versa.

These two methods are applicable in the study of "slightly" nonlinear systems, but in many practical systems they are not applicable. Of course, what is desired is a method of generating Liapunov functions that is applicable to at least large classes of systems. Some of the methods which appear to offer hope in this problems are discussed in the following sections.

## V. ZUBOV'S METHOD [20], [56], [57]

Zubov's method for constructing Liapunov functions for a given differential equation requires the solution of a partial differential equation which may, in some cases, be obtained in closed form.

Zubov considered the stability of the equilibrium of nonlinear autonomous systems

$$\dot{X} = F(X) \quad (5.1)$$

with the properties described for (1.1). The basis of Zubov's method rests in the following theorem:

Let  $\Delta$  be an open domain of the phase space, an  $n$ -dimensional Euclidean space of the coordinates  $x_1, \dots, x_n$ , and let  $\bar{\Delta}$  be its closure.  $\Delta$  shall contain

the origin. The domain  $\Delta$  is the exact domain of attraction of the equilibrium solution of (5.1) if and only there exist two functions  $v(X)$  and  $\varphi(X)$  having the following properties: (1)  $v(X)$  is defined and continuous in  $\Delta$ , and  $\varphi(X)$  is defined and continuous in the whole of the phase space; (2)  $\varphi(X)$  is positive-definite for all  $X$ ; (3)  $v(X)$  is negative-definite, and, for  $X \in \Delta$ ,  $X \neq 0$ , the relation  $-1 < v(X) < 0$  holds; (4) if  $Y \in \bar{\Delta} - \Delta$ , then  $\lim_{X \rightarrow Y} v(X) = -1$ ; (5)  $\lim_{|X| \rightarrow \infty} v(X) = -1$ , provided that this limit exists for  $X \in \Delta$ ; and

$$(6) \quad \left( \frac{dv(P(X, t, 0))}{dt} \right)_{t=0} = \sum_{i=1}^n \frac{dv}{dx_i} f_i(X) = \varphi(X) [1 + v(X)] \sqrt{1 + F^2(X)}. \quad (5.2)$$

Notice that  $\varphi(X)$  is arbitrary. In any instance it should be chosen so that the partial differential equation (5.2) can be solved in the most convenient way.

An example will illustrate the method. Example 1. Consider the system

$$\begin{aligned} \dot{x}_1 &= -x_1 + 2x_1^2 x_2 \\ \dot{x}_2 &= -x_2 \end{aligned} \quad (5.3)$$

For this system the partial differential equation (5.2) becomes

$$\frac{\partial v}{\partial x_1} (2x_1^2 x_2 - x_1) - \frac{\partial v}{\partial x_2} x_2 = \varphi(x_1, x_2) (1+v) \sqrt{1+x_2^2 + (2x_1^2 x_2 - x_1)^2}. \quad (5.4)$$

If we choose

$$\varphi(X) = \varphi(x_1, x_2) = \frac{x_1^2 + x_2^2}{\sqrt{1+x_2^2 + (2x_1^2 x_2 - x_1)^2}}, \quad (5.5)$$

Then (5.4) becomes

$$\frac{\partial v}{\partial x_1} (2x_1^2 x_2 - x_1) + \frac{\partial v}{\partial x_2} (-x_2) = (1+v) (x_1^2 + x_2^2), \quad (5.6)$$

which has as a solution

$$v(x_1, x_2) = -1 + \exp \left( -\frac{1}{2} x_2^2 - \frac{x_1^2}{2(1-x_1 x_2)} \right). \quad (5.7)$$

From (5.7) it is easily seen that  $v$  is negative-definite and  $\dot{v}$  is positive-definite. Also,  $v$  is a Liapunov function for the system (5.3).

From the condition  $v+1=0$  the boundary of stability is determined to be  $x_1 x_2 = 1$ .

It is not always possible to obtain a closed form solution of the partial differential equation (5.4) in spite of the freedom in the choice of  $\varphi(X)$ . If a closed form solution cannot be found, it may be possible to find an approximation of the domain of attraction of the equilibrium by finding an approximation to the  $v$ -function [57].

## VI. INGWERSON'S METHOD [24], [25], [26]

Ingwerson's method for generating Liapunov functions for nonlinear systems is another example of a method that is based on the derivation of these functions for linear autonomous systems.

Consider the linear system with constant coefficients,  $i = 1, 2, \dots, n$ :

$$x^{(n)} + a_1 x^{(n-1)} + \dots + a_{n-1} \dot{x} + a_n x = 0. \quad (6.1)$$

Make the usual substitutions  $x_1 = x$ ,  $x_2 = \dot{x}$ ,  $\dots$ ,  $x_n = x^{(n-1)}$  and get the system of first-order equations

$$\begin{bmatrix} \dot{x}_1 \\ \dot{x}_2 \\ \vdots \\ \dot{x}_n \end{bmatrix} = \begin{bmatrix} 0 & 1 & \dots & 0 \\ 0 & 0 & \dots & 0 \\ \vdots & \vdots & \ddots & \vdots \\ 0 & 0 & \dots & 1 \end{bmatrix} \begin{bmatrix} x_1 \\ x_2 \\ \vdots \\ x_n \end{bmatrix}, \quad (6.2)$$

which, in matrix notation, may be written

$$\dot{X} = BX. \quad (6.3)$$

The Liapunov function, the quadratic form,

$$v = X^T A X, \quad (A^T = A) \quad (6.4)$$

for this linear system has the time derivative, with respect to the equations of motion (6.3),

$$\dot{v} = X^T (B^T A + AB) X, \quad (6.5)$$

where  $A$  and  $B$  are  $n \times n$  matrices with constant elements. From a theorem by Liapunov [26, 28], the trivial solution  $X = 0$  of equation (6.3) is asymptotically stable if and only if there exists a symmetric, positive-definite matrix  $A$  that is the unique solution of the matrix equation

$$B^T A + AB = -C, \quad (6.6)$$



where  $C$  is any symmetric, positive-definite matrix. Furthermore, it is known [26,28] that  $A$  is positive-definite if and only if the real parts of the eigenvalues of  $B$  are negative.

To find a  $v$ -function to prove asymptotic stability, Ingwerson [25,26] relaxes the restriction of negative-definiteness for  $\dot{v}$  to negative-semidefiniteness. With this less severe condition imposed, only one of the eigenvalues of  $C$  need be nonzero. Now, however, a necessary and sufficient condition that the eigenvalues of  $A$  be positive is no longer that the eigenvalues of  $B$  have negative real parts. The following theorem is required: Let  $B$  be any real matrix which, under any permutation of its rows accompanied by the same permutation of its columns, cannot be partitioned into the form

$$B = \begin{bmatrix} B_1 & B_2 \\ 0 & B_3 \end{bmatrix},$$

where  $B_3$  is a square matrix. Then the solution  $A$  of equation (6.6) is a positive-definite matrix if and only if the eigenvalues of  $B$  have negative real parts and  $C$  is any positive-semidefinite symmetric matrix, [58].

Ingwerson's method for nonlinear systems may now be described as follows:

Let the nonlinear, autonomous matrix differential equation

$$\dot{X} = F(X) \quad (6.7)$$

be differentiated to give

$$\ddot{X} = B(X)\dot{X}, \quad (6.8)$$

where  $B(X)$  is an  $n \times n$  matrix with elements  $\frac{\partial f_i}{\partial x_j}$ ,  $i=1, 2, \dots, n$ ;  $j=1, 2, \dots, n$ . In equation (6.6) Ingwerson replaces the constant matrix  $B$  by  $B(X)$ ,  $A$  by  $A(X)$ , and solves for  $A(X)$ .

In the linear system (6.3),  $A$  is a matrix with elements  $\frac{1}{2} (\partial^2 v / \partial x_i \partial x_j)$ . If by some artifice this could be made true for  $A(X)$ , a Liapunov function could be found by integration. However, for the second partials of a scalar function  $v(X)$  to be the elements of a matrix, the matrix must be symmetric, which  $A(X)$  would be, and the relation

$$\frac{\partial A_{ij}}{\partial x_k} = \frac{\partial A_{ik}}{\partial x_j}; \quad i = 1, 2, \dots, n; \quad j = 1, 2, \dots, n; \quad k = 1, 2, \dots, n \quad (6.9)$$

must hold for all elements  $A_{ij}$ ,  $A_{ik}$  of  $A(X)$ . In general, the relation (6.9) does not hold for matrices satisfying equation (6.6) with  $B(X)$  replacing  $B$ .

A relatively simple stratagem used by Ingwerson which sometimes yields satisfactory results is as follows: Generate a matrix  $A(x_i, x_j)$  from  $A(X)$  by equating to zero all variables  $x_k$  in each element  $A_{ij}$  of  $A(X)$  except those where the index  $k$  is the same as the index of either the row or column of  $A(X)$  in which  $x_k$  appears. Then evaluate

$$\int_0^X A(x_i, x_j) dX \equiv \nabla v \quad (6.10)$$

where it is intended that the integration of each element in the  $j$ th column of  $A(x_i, x_j)$  be made with respect to  $x_j$ ,  $j = 1, 2, \dots, n$ , as the other components of  $X$  are held constant. The result is a vector  $\nabla v$  of  $n$  components and has the property

$$\nabla \times \nabla v = 0. \quad (6.11)$$

Therefore,  $\nabla v$  is the gradient of some scalar function,  $v$ , and  $v$  may be determined from the line integral

$$v = \int_0^X \nabla v \cdot dX \quad (6.12)$$

along any path of integration.

A precise definition of (6.10) and a proof that  $\nabla v$  is indeed a gradient may be found in Reference 26.

A set of  $A$  matrices is derived by Ingwerson for system (6.3) up to the fourth order by setting successively elements on the principal diagonal of the matrix  $C$  equal to unity and the remaining elements equal to zero. Equation (6.6) is then solved for  $A$ . Then both  $A$  and  $C$  are multiplied by the factor found in the denominator of  $A$ .

For example, let

$$C = \begin{bmatrix} 0 & 0 \\ 0 & 1 \end{bmatrix} \quad \text{and} \quad B = \begin{bmatrix} 0 & 1 \\ -a_2 & -a_1 \end{bmatrix} \quad (6.13)$$

Then equation (6.6), for this case, becomes

$$\begin{bmatrix} 0 & -a_2 \\ 1 & -a_1 \end{bmatrix} \begin{bmatrix} A_{11} & A_{12} \\ A_{13} & A_{14} \end{bmatrix} + \begin{bmatrix} A_{11} & A_{12} \\ A_{13} & A_{14} \end{bmatrix} \begin{bmatrix} 0 & 1 \\ -a_2 & -a_1 \end{bmatrix} = - \begin{bmatrix} 0 & 0 \\ 0 & 1 \end{bmatrix} \quad (6.14)$$

from which, by elementary procedures, it may be determined that, for

$$C = \begin{bmatrix} 0 & 0 \\ 0 & 1 \end{bmatrix}, \quad A_1 \equiv 2a_1 A = \begin{bmatrix} a_2 & 0 \\ 0 & 1 \end{bmatrix}$$

$$C_1 \equiv 2a_1 C = \begin{bmatrix} 0 & 0 \\ 0 & 2a_1 \end{bmatrix} \quad (6.15)$$

and for

$$C = \begin{bmatrix} 1 & 0 \\ 0 & 0 \end{bmatrix}, \quad A_2 = \begin{bmatrix} a_1^2 + a_2 & a_1 \\ a_1 & 0 \end{bmatrix} \text{ and } C_2 = \begin{bmatrix} 2a_1 a_2 & 0 \\ 0 & 0 \end{bmatrix}. \quad (6.16)$$

For a third order equation

$$A_1 = \begin{bmatrix} a_3^2 & a_2 a_3 & 0 \\ a_2 a_3 & a_1 a_3 + a_2^2 & a_3 \\ 0 & a_3 & a_2 \end{bmatrix}, \quad C_1 = \begin{bmatrix} 0 & 0 & 0 \\ 0 & 0 & 0 \\ 0 & 0 & 2(a_1 a_2 - a_3) \end{bmatrix} \quad (6.17)$$

$$A_2 = \begin{bmatrix} a_1 a_3 & a_3 & 0 \\ a_3 & a_1^2 + a_2 & a_1 \\ 0 & a_1 & 1 \end{bmatrix}, \quad C_2 = \begin{bmatrix} 0 & 0 & 0 \\ 0 & 2(a_1 a_2 - a_3) & 0 \\ 0 & 0 & 0 \end{bmatrix}, \quad (6.18)$$

$$A_3 = \begin{bmatrix} a_1 a_2^2 - a_2 a_3 + a_1^2 a_3 & a_1^2 a_2 & a_1 a^2 - a_3 \\ a_1^2 a_2 & a_1^3 + a_3 & a_1^2 \\ a_1 a_2 - a_3 & a_1^2 & a_1 \end{bmatrix},$$

$$C_3 = \begin{bmatrix} 2a_3(a_1 a_2 - a_3) & 0 & 0 \\ 0 & 0 & 0 \\ 0 & 0 & 0 \end{bmatrix}. \quad (6.19)$$

For corresponding values for fourth-order equations, see Reference 25.

To illustrate the method consider the simple non-linear equation

$$\ddot{x} + \dot{x} + x^3 = 0, \quad (6.20)$$

which, with the substitutions,  $x_1 = x$  and  $x_2 = \dot{x}$ , may be written as the system

$$\dot{x}_1 = x_2 \quad (6.21)$$

$$\dot{x}_2 = -x_1^3 - x_2$$

or, in vector form, as

$$\dot{X} = F(X), \quad (6.22)$$

where

$$\dot{X} = \begin{pmatrix} \dot{x}_1 \\ \dot{x}_2 \end{pmatrix}, \quad F(X) = \begin{pmatrix} x_2 \\ -x_1^3 - x_2 \end{pmatrix} \quad (6.23)$$

are column vectors.

Differentiating (2.21) gives

$$\ddot{X} = B(X) \dot{X} \quad (6.24)$$

where the matrix

$$B(X) = \begin{bmatrix} 0 & 1 \\ -3x_1^2 & -1 \end{bmatrix}. \quad (6.25)$$

In this simple problem

$$A_1(X) = A_1(x_1, x_2) = \begin{bmatrix} 3x_1^2 & 0 \\ 0 & 1 \end{bmatrix} \quad (6.26)$$

according to the procedure described above. Now,

$$\nabla v_1 = \begin{pmatrix} x_1^3 \\ x_2 \end{pmatrix} \quad (6.27)$$

$$v_1 = \int_0^X (\nabla v_1)^T dX = \int_0^{x_1} x_1^3 dx_1 + \int_0^{x_2} x_2 dx_2 = \frac{x_1^4}{4} + \frac{x_2^2}{2} \quad (6.28)$$

$$\dot{v}_1 = x_1^3 x_2 + x_2 (-x_1^3 - x_2) = -x_2^2. \quad (6.29)$$

$v_1$  is seen to be positive-definite and  $\dot{v}_1$  is negative-semidefinite. According to Liapunov's first theorem on stability, the trivial solution is stable but not asymptotically stable. However, a modification of this theorem by La Salle [35] and others permits the conclusion that (global) asymptotic stability exists even if  $\dot{v}_1$  is semidefinite provided  $v_1(X) \rightarrow \infty$  as  $\|X\| \rightarrow \infty$ , where  $\|X\|$  is the Euclidean norm and  $\dot{v} \neq 0$  along any solution other than  $X = 0$ . Since this condition is satisfied by  $v_1(X)$  in equation (6.28), the trivial solution of the system (6.21) is (globally) asymptotically stable.

Another A matrix, say  $A_2$ , (6.16) might have been chosen. For this example,

$$A_2(X) = A_2(x_1, x_2) = \begin{bmatrix} (3x_1^2 + 1) & 1 \\ 1 & 1 \end{bmatrix} \quad (6.30)$$

and

$$\nabla v_2 = \begin{bmatrix} x_1^3 + x_1 + x_2 \\ x_1 + x_2 \end{bmatrix} \quad (6.31)$$

$$v_2 = \int_0^X (\nabla v_2)^T dX$$

$$= \int_0^{x_1(x_2=0)} (x_1^3 + x_1 + x_2) dx_1 + \int_0^{x_2(x_1=x_1)} (x_1 + x_2) dx_2 \\ = \frac{1}{2} x_1^2 + \frac{1}{4} x_1^4 + \frac{1}{2} x_2^2 + x_1 x_2 \quad (6.32)$$

$$\dot{v}_2 = -x_1^4.$$

Let

$$v = v_1 + v_2 .$$

Then

$$v = \frac{1}{2} \left[ x_1^4 + x_2^2 + (x_1 + x_2)^2 \right] \quad (6.34)$$

and

$$\dot{v} = -x_1^4 - x_2^2 . \quad (6.35)$$

Because  $v$  is positive-definite and  $\dot{v}$  is negative-definite the trivial solution is asymptotically stable.

As an example, consider the system

$$\begin{aligned} \dot{x}_1 &= x_2 \\ \dot{x}_2 &= x_3 \\ \dot{x}_3 &= -(x_1 + cx_2)^3 - bx_3 . \end{aligned} \quad (6.36)$$

Using the same procedure as in the first example, we get

$$B(X) = \begin{bmatrix} 0 & 1 & 0 \\ 0 & 0 & 1 \\ -3(x_1+cx_2)^2 & -3c(x_1+cx_2)^2 & -b \end{bmatrix} \quad (6.37)$$

and

$$A_2(X) = \begin{bmatrix} 3b(x_1+cx_2)^2 & 3(x_1+cx_2)^2 & 0 \\ 3(x_1+cx_2)^2 & b^2+3c(x_1+cx_2)^2 & b \\ 0 & b & 1 \end{bmatrix} . \quad (6.38)$$

Whereupon,

$$A_2(x_i, x_j) = \begin{bmatrix} 3bx_1^2 & 3(x_1+cx_2)^2 & 0 \\ 3(x_1+cx_2)^2 & b^2+3c^3x_2^2 & b \\ 0 & b & 1 \end{bmatrix} \quad (6.39)$$

and

$$\nabla v_2 = \begin{bmatrix} bx_1^3 + (x_1+cx_2)^3/c - x_1^3/c \\ (x_1+cx_2)^3 + b^2x_2 + bx_3 \\ bx_2 + x_3 \end{bmatrix} . \quad (6.40)$$

Then

$$\begin{aligned} v_2 &= \int_0^X (\nabla v_2)^T dX \\ &= \frac{1}{4}bx_1^4 + (x_1+cx_2)^4/4c - x_1^4/4c + \frac{1}{2}b^2x_2^2 \\ &\quad + bx_2x_3 + \frac{1}{2}x_3^2 \end{aligned} \quad (6.41)$$

is positive definite,

and

$$\dot{v}_2 = -(bc-1)(3x_1^2 + 3cx_1x_2 + c^2x_2^2)x_2^2 \quad (6.42)$$

is negative-semidefinite if  $b > 0$ ,  $c > 0$  and  $bc-1 > 0$  as may be verified by Sylvester's theorem. Further,  $v_2(X) \rightarrow \infty$  as  $\|X\| \rightarrow \infty$  so that (global) asymptotic stability is assured.

However Ingwerson in Reference 25 points out that, although the above technique generates a  $v$ -function which provides both necessary and sufficient conditions for (global) asymptotic stability for this particular example, it is not a general method that may be applied to any nonlinear equation with assurance of similar valid results. For one reason, the selection of the  $A(X)$  matrix requires a certain amount of experience and ingenuity. For another, if either of the other two  $A$  matrices  $A_1$  or  $A_3$  above were used, the same result would not be achieved. Frequently, only one of these matrices gives useful information for a nonlinear system. This was true of the preceding example. Often it is necessary to form some linear combinations of  $v$ -functions generated by use of the various  $A$  matrices. Sometimes an  $A$  matrix will have to be determined by selecting some of the off-diagonal elements of the matrix  $C$  to be nonzero.

## VII. THE VARIABLE GRADIENT METHOD OF SCHULTZ AND GIBSON [54]

The variable gradient method of generating  $v$ -functions represents an important step toward reducing the amount and quality of experience and ingenuity required of the investigator attempting to discover the stability properties of nonlinear systems. The method permits the study of systems with one or more single-valued nonlinearities in which the nonlinearities are known as definite functions of the state variables. The method's most significant characteristic is that  $v$ -functions are generated which apply to the particular nonlinear system being investigated. This is in strong contrast to assuming a tentative  $v$ -function and testing it with one or more Liapunov theorems as is the case

when applying the methods of Lur'e, Letov, Krasovskii, Rekasius, and others [54].

As is indicated by its name, the variable gradient method is based on the existence of the gradient of a  $v$ -function  $\nabla v$  with undetermined components. Both  $v$  and  $\dot{v}$  are then determined from this vector. Thus,

$$\dot{v} = (\nabla v)^T \dot{X} \quad (7.1)$$

and

$$v = \int_0^X (\nabla v)^T dX. \quad (7.2)$$

The integral in (7.2) is a line integral, and the upper limit  $X$  is simply an arbitrary point in Euclidean  $n$ -dimensional phase space. In order that  $v$  be uniquely determined from (7.2) it is sufficient that

$$\nabla \times \nabla v = 0. \quad (7.3)$$

This is equivalent to the statement that the matrix

$$M = \begin{bmatrix} \frac{\partial \nabla v_1}{\partial x_1} & \frac{\partial \nabla v_2}{\partial x_1} & \dots & \frac{\partial \nabla v_n}{\partial x_1} \\ \frac{\partial \nabla v_1}{\partial x_2} & \frac{\partial \nabla v_2}{\partial x_2} & \dots & \frac{\partial \nabla v_n}{\partial x_2} \\ \vdots & \vdots & \ddots & \vdots \\ \frac{\partial \nabla v_1}{\partial x_n} & \dots & \dots & \frac{\partial \nabla v_n}{\partial x_n} \end{bmatrix} \quad (7.4)$$

be a symmetric matrix. Thus, the problem of determining a  $v$ -function which satisfies Liapunov's stability criteria is transformed into the problem of finding a  $\nabla v$  such that (7.3) is satisfied.

The vector form of the equations of motion of the dynamical systems whose stability properties are to be investigated is assumed to be of the form

$$\dot{X} = B(X)X; \quad \dot{X}(0) = 0, \quad (7.5)$$

where  $X$  and  $\dot{X}$  are column  $n$ -vectors, and

$$B(X) = \begin{bmatrix} 0 & 1 & \dots & \dots & \dots & 0 \\ 0 & 0 & 1 & \dots & \dots & 0 \\ \vdots & \vdots & \vdots & \ddots & \vdots & \vdots \\ 0 & 0 & \dots & \dots & \dots & 1 \\ b_1(X) & b_2(X) & \dots & \dots & \dots & b_n(X) \end{bmatrix} \quad (7.6)$$

The  $b_i(X)$  are assumed to be continuous over a suitable region of phase space.

The first step in the variable gradient method is to assume  $\nabla v$  to be a column  $n$ -vector of the form

$$\nabla v = \begin{bmatrix} a_{11}x_1 + a_{12}x_2 + \dots + a_{1n}x_n \\ a_{21}x_1 + a_{22}x_2 + \dots + a_{2n}x_n \\ \vdots \\ a_{n1}x_1 + \dots + a_{nn}x_n \end{bmatrix}, \quad (7.7)$$

where the  $a_{ij}$  are restricted to be functions of  $x_i$  alone with the exception of  $a_{nn}$  which is set equal to a constant. Furthermore, the  $a_{ij}$  are chosen to be positive so that  $v$  will have a better chance of being positive-definite. The choice of  $a_{nn}$  to be the constant 2 was made to insure that  $v$ , calculated from equation (7.2), will include a term in  $x_n^2$ . Schultz and Gibson let the remaining terms  $a_{ij}$  be completely undetermined but consisting of a constant part  $a_{ij,c}$  and a variable part  $a_{ij,v}$ . Thus,  $a_{ij}$  is of the form

$$a_{ij} = a_{ij,c} + a_{ij,v}(x_1, \dots, x_{n-1}). \quad (7.8)$$

The above restrictions on the  $a_{ij}$  are made because the  $v$ -functions determined by the method can, at least for the examples treated in Reference 54, be easily tested for positive-definiteness despite the fact that they are sometimes not quadratic forms. The  $v$ -functions generated for the examples are always of the form

$$v(x) = x_n^2 + 2\beta(x_1, \dots, x_{n-1})x_n + \alpha(x_1, \dots, x_{n-1}), \quad (7.9)$$

which may be written

$$v(x) = (x_n + \beta)^2 + \alpha - \beta^2. \quad (7.10)$$

Thus  $v(x)$  is positive-definite if  $\alpha - \beta^2$  is positive-definite.

Substituting from (7.8) into (7.7) gives the general form

$$\nabla v = \begin{bmatrix} (a_{11}, c^{+a_{11}}, v) x_1 + (a_{12}, c^{+a_{12}}, v) x_2 + \dots + (a_{1n}, c^{+a_{1n}}, v) x_n \\ (a_{21}, c^{+a_{21}}, v) x_1 + (a_{22}, c^{+a_{22}}, v) x_2 + \dots + (a_{2n}, c^{+a_{2n}}, v) x_n \\ \vdots \\ (a_{m1}, c^{+a_{m1}}, v) x_1 + (a_{m2}, c^{+a_{m2}}, v) x_2 + \dots + 2x_n \end{bmatrix}. \quad (7.11)$$

where  $a_{ij}, v$  are functions of  $x_i$  alone.  $a_{ij}$  are chosen to be positive, and  $a_{nn} = 2$ . The entire procedure of the variable gradient method may now be summarized as follows:

**Step 1.** Write  $\nabla v$  in the form of equation (7.11).

Step 2. Determine  $\dot{\mathbf{v}}$  from the equation  $\dot{\mathbf{v}} = (\nabla \mathbf{v})^T \dot{\mathbf{X}}$ .

**Step 3.** Constrain  $\tilde{\mathbf{v}}$  to be at least semidefinite.

**Step 4.** Use the  $\frac{1}{2}(\bar{n})(n-1)$  equations implied by the condition  $\bar{\nabla} \times \nabla \mathbf{v} = 0$  to determine the remaining unknown coefficients in  $\nabla \mathbf{v}$  in equation (7.11).

Step 5. Because the addition of terms as a result of performing step 4 may have altered  $\hat{v}$ , it is necessary to determine whether  $\hat{v}$  is still at least semidefinite.

**Step 6. Calculate  $v$  according to the equation**

$$v = \int_0^X (\nabla v)^T dX, \text{ and test for positive-definiteness.}$$

We will use the equations in the first example of Section 6 to illustrate the method. These equations are

$$\begin{aligned}\dot{x}_1 &= x_2 \\ \dot{x}_2 &= -x_1^3 - x_2.\end{aligned}\quad (7.12)$$

**Step 1.** Write  $\nabla v$  in the form of equation (7.7).

$$\nabla v = \begin{bmatrix} a_{11}x_1 + a_{12}x_2 \\ a_{21}x_1 + 2x_2 \end{bmatrix}. \quad (7.13)$$

**Step 2.** Determine  $\dot{\mathbf{v}}$  from equation (7.1).

$$\dot{\mathbf{v}} = (\nabla \mathbf{v})^T \dot{\mathbf{X}} = (a_{11} - a_{21} - 2x_1^2)x_1x_2 + (a_{12} - 2)x_2^2 - a_{21}x_1^4. \quad (7, 14)$$

**Step 3.** Constrain  $\dot{v}$  to be at least negative-semidefinite. This may be done in any one of several ways. For example, set

$$a_{11} - a_{21} - 2x_1^2 = 0 \quad (7.15)$$

$$a_{21} > 0 \quad (7.16)$$

$$0 \leq a_{12} \leq 2. \quad (7.17)$$

Arbitrarily choose  $a_{12} = 1$ , solve for  $a_{11}$  in equation (7.15) and substitute in (7.13). Then

$$\nabla v = \begin{bmatrix} (a_{21} + 2x_1^2)x_1 + x_2 \\ a_{21}x_1 + 2x_2 \end{bmatrix}. \quad (7.18)$$

**Step 4.** Use the condition  $\nabla \times \nabla v = 0$  to get the equation

$$\frac{\partial \nabla v_1}{\partial x_2} = \frac{\partial \nabla v_2}{\partial x_1}, \quad (7.19)$$

which, for this example, gives the equation

$$a_{21} + \frac{\partial a_{21}}{\partial x_1} x_1 = a_{21,c} + a_{21,v} + \frac{\partial a_{21,v}}{\partial x_1} x_1 = 1. \quad (7.20)$$

Equation (7.20) is satisfied if

$$a_{21,c} = 1 \quad (7.21)$$

and

$$a_{21,v} = 0 \quad . \quad (7.22)$$

Then equation (7.18) can be written

$$V_V = \begin{bmatrix} 2x_1^3 + x_1 + x_2 \\ x_1 + 2x_2 \end{bmatrix},$$

and, by line integration,

$$v = \int_0^{x_1(x_2=0)} (2x_1^3 + x_1) dx_1 + \int_0^{x_2(x_1=x_1)} (x_1 + 2x_2) dx_2$$

$$\begin{aligned}
 &= \frac{x_1^4}{2} + \frac{x_1^2}{2} + x_1 x_2 + x_2^2 \\
 &= \frac{1}{2} \left( x_1^4 + x_2^2 + (x_1 + x_2)^2 \right). \quad (7.23)
 \end{aligned}$$

**Step 5.** Determine  $\dot{\mathbf{v}}$ , with respect to equation (7.12), by differentiation of equation (7.23).

$$\dot{V} = -x_1^4 - x_2^2 \quad (7.24)$$

Clearly  $v$  is positive-definite and  $\dot{v}$  is negative-definite. Therefore, asymptotic stability is assured. Further, because

$$v(X) \rightarrow \infty \text{ as } \|X\| \rightarrow \infty$$

and  $\dot{v}$  is not identically zero along any solution other than  $X = 0$ , the trivial solution is globally asymptotically stable according to the modified Liapunov theorem by La Salle [35, 54].

Instead of choosing  $a_{12} = 1$ , any constant value of  $a_{12}$  which would have satisfied the relation  $0 \leq a_{12} \leq 2$  could have been chosen. For  $a_{12} = 0$ ,  $v = x_1^4/2 + x_2^2$ , and  $\dot{v} = -2x_2^2$ . For  $a_{12} = 2$ ,  $v = \frac{1}{4}x_1^4 + x_1^2 + 2x_1x_2 + x_2^2$  and  $\dot{v} = -2x_1^4$ .

As a second example of the application of the variable gradient method consider the system

$$\begin{aligned}\dot{x}_1 &= x_2 - x_1(x_1^2 + x_2^2) \\ \dot{x}_2 &= -x_1 - x_2(x_1^2 + x_2^2)\end{aligned}\quad (7.25)$$

Then

$$\nabla v = \begin{bmatrix} a_{11}x_1 + a_{12}x_2 \\ a_{21}x_1 + 2x_2 \end{bmatrix}\quad (7.26)$$

and

$$\begin{aligned}\dot{v} &= x_1^2 [-a_{21} - a_{11}(x_1^2 + x_2^2)] + x_2^2 [a_{12} - 2(x_1^2 + x_2^2)] \\ &\quad + x_1x_2 [a_{11} - 2(a_{12} + a_{21})(x_1^2 + x_2^2)]\end{aligned}\quad (7.27)$$

As in the first example, set the coefficient of  $x_1x_2$  equal to zero and constrain the coefficients of  $x_1^2$  and  $x_2^2$  to be negative. Thus

$$a_{11} - 2 - (a_{12} + a_{21})(x_1^2 + x_2^2) = 0\quad (7.28)$$

$$-a_{21} - a_{11}(x_1^2 + x_2^2) < 0\quad (7.29)$$

$$a_{12} - 2(x_1^2 + x_2^2) < 0\quad (7.30)$$

Let  $a_{12} = 0$ . Then

$$a_{11} = 2 + a_{21}(x_1^2 + x_2^2)\quad (7.31)$$

and

$$\nabla v = \begin{bmatrix} 2x_1 + a_{21}x_1(x_1^2 + x_2^2) \\ a_{21}x_1 + 2x_2 \end{bmatrix}\quad (7.32)$$

The requirement that

$$\frac{\partial \nabla v_1}{\partial x_2} = \frac{\partial \nabla v_2}{\partial x_1}$$

gives the relation

$$2a_{21}x_1x_2 = a_{21} + x_1 \frac{\partial a_{21}}{\partial x_1}\quad (7.33)$$

which is satisfied for  $a_{21} = 0$ . Thus, with  $a_{12} = a_{21} = 0$

$$\nabla v = \begin{bmatrix} 2x_1 \\ 2x_2 \end{bmatrix}\quad (7.34)$$

and

$$\begin{aligned}v &= \int_0^x (\nabla v)^T dX \\ &= x_1^2 + x_2^2\end{aligned}\quad (7.35)$$

$$\dot{v} = -2(x_1^2 + x_2^2)^2$$

Since, also,

$$v(X) \rightarrow \infty \text{ as } \|X\| \rightarrow \infty,$$

the trivial solution is globally asymptotically stable.

As a third example, consider the system

$$\begin{aligned}\dot{x}_1 &= x_2 \\ \dot{x}_2 &= x_3 \\ \dot{x}_3 &= -3x_3 - 2x_2 - 3x_1^2x_2 - kx_1^3\end{aligned}\quad (7.36)$$

Accordingly,

$$\nabla v = \begin{bmatrix} a_{11}x_1 + a_{12}x_2 + a_{13}x_3 \\ a_{21}x_1 + a_{22}x_2 + a_{23}x_3 \\ a_{31}x_1 + a_{32}x_2 + 2x_3 \end{bmatrix}\quad (7.37)$$

If, now, the usual procedure is followed, it would be seen that  $\dot{v}$ , which must be constrained to be at least negative-semidefinite, could be so constrained in a very large number of ways. Further study would also show that matters could be considerably simplified if, at the beginning,  $a_{32}$  were chosen to be zero. In that case

$$\begin{aligned}\dot{v} &= (a_{23} - 6)x_3^2 + a_{12}x_2^2 - ka_{31}x_1^4 \\ &\quad + (a_{11} - 2a_{31} - 3a_{31}x_1^2)x_1x_2 \\ &\quad + (a_{13} - 4 + a_{22} - 6x_1^2)x_2x_3 \\ &\quad + (a_{21} - 3a_{31} - 2kx_1^2)x_1x_3\end{aligned}\quad (7.38)$$

Because the method recommends that the  $a_{ij}$  should not be negative,  $a_{12}$  should be chosen to be zero so that the bothersome term  $a_{12}x_2^2$  vanishes. In fact, considerable

simplification results if  $\dot{v}$  is constrained to be negative-semidefinite in  $x_1$  and  $x_3$  alone. Thus, let all terms containing  $x_2$  vanish. Therefore,

$$a_{11} - 2a_{31} - 3a_{31}x_1^2 = 0 \quad (7.39)$$

$$a_{13} - 4 + a_{22} - 6x_1^2 = 0. \quad (7.40)$$

Let  $a_{13}$  have a constant part  $a_{13,c}$  and a variable part  $a_{13,v}$ , and let  $a_{13,v} = 6x_1^2$ . Then equation (7.40) becomes

$$a_{22} = 4 - a_{13,c}. \quad (7.41)$$

Equation (7.39) shows that  $a_{31}$  must be a function of  $x_1$  alone inasmuch as the method requires that  $a_{11}$  be a function of  $x_1$  alone. Also, from the first term in equation (7.38), and recalling that the  $a_{ij}$  should not be negative,  $a_{23}$  must have only those values that satisfy the relation

$$0 \leq a_{23} \leq 6. \quad (7.42)$$

With  $a_{12} = 0$ ,  $a_{22} = 4 - a_{13,c}$  and  $a_{11} = a_{31}(2 + 3x_1^2)$ ,

$$\nabla v = \begin{bmatrix} a_{31}x_1(2 + 3x_1^2) + (6x_1^2 + a_{13,c})x_3 \\ a_{21}x_1 + (4 - a_{13,c})x_2 + a_{23}x_3 \\ a_{31}x_1 + 2x_3 \end{bmatrix}. \quad (7.43)$$

The requirement that

$$\frac{\partial \nabla v_1}{\partial x_2} = \frac{\partial \nabla v_2}{\partial x_1}$$

yields the equation

$$x_1 \frac{\partial a_{21}}{\partial x_1} + a_{21} + x_3 \frac{\partial a_{23}}{\partial x_1} = 0, \quad (7.44)$$

which has a solution

$$a_{21} = a_{23} = 0,$$

so that  $\nabla v$  now becomes

$$\nabla v = \begin{bmatrix} a_{31}x_1(2 + 3x_1^2) + (6x_1^2 + a_{13,c})x_3 \\ (4 - a_{13,c})x_2 \\ a_{31}x_1 + 2x_3 \end{bmatrix}. \quad (7.45)$$

The additional requirement that

$$\frac{\partial \nabla v_1}{\partial x_3} = \frac{\partial \nabla v_3}{\partial x_1}$$

yields the equation

$$6x_1^2 + a_{13,c} = a_{31,c} + a_{31,v} + x_1 \frac{\partial a_{31,v}}{\partial x_1}. \quad (7.46)$$

Let  $a_{13,c} = a_{31,c} = 0$ . Then equation (7.46) becomes

$$6x_1^2 = a_{31,v} + x_1 \frac{\partial a_{31,v}}{\partial x_1}, \quad (7.47)$$

which has the solution

$$a_{31,v} = 2x_1^2. \quad (7.48)$$

Whereupon

$$\widehat{\nabla v} = \begin{bmatrix} 6x_1^5 + 4x_1^3 + 6x_1^2x_3 \\ 4x_2 \\ 2x_1^3 + 2x_3 \end{bmatrix} \quad (7.49)$$

and

$$\begin{aligned} v &= \int_0^X (\nabla v)^T dX \\ &= \int_0^{x_1(x_2=x_3=0)} (6x_1^5 + 4x_1^3 + 6x_1^2x_3) dx_1 + \int_0^{x_2(x_1=x_3=0)} 4x_2 dx_2 \\ &\quad + \int_0^{x_3(x_1=x_1, x_2=x_2)} (2x_1^3 + 2x_3) dx_3 \\ &= x_1^6 + x_1^4 + 2x_2^2 + 2x_1^3x_3 + x_3^2 \\ &= x_1^4 + 2x_2^2 + (x_1^3 + x_3)^2 \end{aligned} \quad (7.50)$$

$$\dot{v} = -2(kx_1^6 + 3x_3^2 + x_1^3x_3(k+3)) \quad (7.51)$$

Sylvester's theorem applied to the right member of equation (7.51) shows that  $\dot{v}$  is negative-semidefinite for  $k=3$  and  $v$  is obviously positive-definite. Because, also,  $v(X) \rightarrow \infty$  as  $|X| \rightarrow \infty$  the trivial solution is globally asymptotically stable.

Schultz and Gibson [54] point out that a better result may be obtained if initially  $a_{23}$  is not allowed to be zero. An alternative  $v$  and  $\dot{v}$  are found to be, respectively,

$$\begin{aligned} v &= x_1^6 + \frac{1}{4}(2a_{23} + ka_{23} + 4)x_1^4 + \frac{2}{3}a_{23}x_1^2 \\ &\quad + a_{23}x_1^3x_2 + 2x_1^3x_3 + 2a_{23}x_1x_2 + \frac{2}{3}a_{23} + \frac{1}{6}(a_{23} + 2)x^2 \\ &\quad + a_{23}x_2x_3 + x_3^2 \end{aligned} \quad (7.52)$$

and

$$\dot{v} = -2kx_1^6 - (2k + 6 - a_{23})x_1^3x_3 - x_3^2(6 - a_{23}) - \frac{2}{3}a_{23}kx_1^4. \quad (7.53)$$

If  $a_{23} = -2(k-3)$  then  $\dot{v}$  is negative-semidefinite and  $v$  is positive-definite for all  $k$  satisfying the relation

$$0 < k \leq 3. \quad (7.54)$$

Thus, the trivial solution is globally asymptotically stable not for just  $k=3$  but for the set of all  $k$  satisfying equation (7.54).

## VIII. THE METHOD OF KU AND PURI [51], [52]

The method of Ku and Puri represents another attempt to reduce the kind and magnitude of experience and ingenuity required of the investigator in his attempts to generate Liapunov functions. It might be said that the innovators of the method have tried to assume, by the generation of the form of the elements of an  $S$  matrix, the larger part of the burden of ingenuity and experience normally required of the individual investigator. Whether they have succeeded is problematical. The  $v$ -function is assumed always to be the quadratic form

$$v = X^T S X \quad (8.1)$$

where  $S$  is an  $n \times n$  symmetric matrix. An  $S$  matrix for a fourth order system may have the form

$$S = \begin{bmatrix} \frac{(3c_{11}x_1^2 + Z_{11})}{x_1^2} & \frac{(2c_{12}x_1 + f_{12})}{2x_1} & \frac{(2c_{13}x_1 + f_{13})}{2x_1} & \frac{(2c_{14}x_1 + f_{14})}{2x_1} \\ \frac{(2c_{12}x_1 + f_{12})}{2x_1} & \frac{(3c_{22}x_2^2 + Z_{22})}{x_2^2} & c_{23} & c_{24} \\ \frac{(2c_{13}x_1 + f_{13})}{2x_1} & c_{23} & \frac{(3c_{33}x_3^2 + Z_{33})}{x_3^2} & c_{34} \\ \frac{(2c_{14}x_1 + f_{14})}{2x_1} & c_{24} & c_{34} & \frac{(3c_{44}x_4^2 + Z_{44})}{x_4^2} \end{bmatrix} \quad (8.2)$$

where

$$Z_{jj} = \int_0^{x_j} Z_j(x_j) dx_j, \quad j = 1, 2, 3, 4, \quad (8.3)$$

and  $f_{12}$ ,  $f_{13}$ , and  $f_{14}$  are taken as functions of  $x_1$  only, and the  $c_{ij}$  are constants. It is assumed that the system of nonlinear differential equations has the form

$$\dot{X} = A(X)X, \quad (8.4)$$

where  $A(X)$  is the  $n \times n$  matrix

$$A(X) = \begin{bmatrix} 0 & 1 & . & . & . & 0 \\ 0 & 0 & 1 & . & . & 0 \\ . & . & . & . & . & . \\ . & . & . & . & . & . \\ . & . & . & . & . & . \\ . & . & . & . & . & . \\ 0 & 0 & . & . & . & 1 \\ -a_1(X) & -a_2(X) & . & . & . & -a_n(X) \end{bmatrix} \quad (8.5)$$

Differentiating equation (4.1) gives

$$\dot{v} = X^T (A^T S + SA + \dot{S}) X \quad (8.6)$$

If  $\beta_{ij}$  denotes an element in the  $i^{\text{th}}$  row and  $j^{\text{th}}$  column of the  $S$  matrix, then  $v$  may be written, for a fourth order system, in the form

$$\begin{aligned} v = & \beta_{11}x_1^2 + \beta_{12}x_1x_2 + \beta_{13}x_1x_3 + \beta_{14}x_1x_4 \\ & + \beta_{22}x_2^2 + \beta_{23}x_2x_3 + \beta_{24}x_2x_4 \\ & + \beta_{33}x_3^2 + \beta_{34}x_3x_4 \\ & + \beta_{44}x_4^2 \end{aligned} \quad (8.7)$$

By definition,

$$\dot{v} = (\nabla v)^T \dot{X} \quad (8.8)$$

Ku and Puri set

$$\nabla v = BX \quad (8.9)$$

where  $B$  is the nonsymmetric square matrix

$$B = \begin{bmatrix} \frac{(6c_{11}x_1 + Z_1(x_1))}{x_1} & 2c_{12} + f_{12}(x_1) & 2c_{13} + f_{13}(x_1) & 2c_{14} + f_{14}(x_1) \\ \frac{(2c_{12}x_1 + f_{12}(x_1))}{x_1} & \frac{(6c_{22}x_2 + Z_2(x_2))}{x_2} & 2c_{23} & 2c_{24} \\ \frac{(2c_{13}x_1 + f_{13}(x_1))}{x_1} & 2c_{23} & \frac{(6c_{33}x_3 + Z_3(x_3))}{x_3} & 2c_{34} \\ \frac{(2c_{14}x_1 + f_{14}(x_1))}{x_1} & 2c_{24} & 2c_{34} & \frac{(6c_{44}x_4 + Z_4(x_4))}{x_4} \end{bmatrix} \quad (8.10)$$

Since, from (8.9)

$$(\nabla v)^T = X^T B^T, \quad (8.11)$$

equation (8.8) becomes

$$\dot{v} = X^T B^T \dot{X} = X^T B^T A X \quad (8.12)$$

The matrix  $T$  is then definite by the equation

$$T = B^T A \quad (8.13)$$

Then

$$\dot{v} = X^T T X \quad (8.14)$$

Clearly, also,

$$T = A^T S + SA + \dot{S} \quad (8.15)$$

but the determination of  $T$  according to equation (8.13) is less laborious than by use of equation (8.15). After



the T matrix has been determined, its terms are adjusted to insure that  $\dot{v}$  will be at least negative-semidefinite. This is done by making the sum  $\tau_{ij} + \tau_{ji} = 0$  and  $\tau_{ij}$  negative or zero where the  $\tau_{ij}$  are the elements of the T matrix.

The example in Section 7 will be used to illustrate the method. In that example the nonlinear system used was the following:

$$\begin{aligned}\dot{x}_1 &= x_2 \\ \dot{x}_2 &= x_3 \\ \dot{x}_3 &= -kx_1^3 - (3x_1^2 + 2)x_2 - 3x_3.\end{aligned}\quad (8.16)$$

The A matrix is

$$A = \begin{bmatrix} 0 & 1 & 0 \\ 0 & 0 & 1 \\ -kx_1^2 & -(3x_1^2 + 2) & -3 \end{bmatrix}, \quad (8.17)$$

and the B matrix is

$$B = \begin{bmatrix} \frac{(6c_{11}x_1 + z_1)(x_1)}{x_1} & 2c_{12} + f_{12}(x_1) & 2c_{13} + f_{13}(x_1) \\ \frac{(2c_{22}x_1 + f_{22})(x_1)}{x_1} & \frac{(6c_{22} + z_2)(x_2)}{x_2} & 2c_{23} \\ \frac{(2c_{33}x_1 + f_{33})(x_1)}{x_1} & 2x_{23} & \frac{(6c_{33}x_3 + z_3)(x_3)}{x_3} \end{bmatrix} \quad (8.18)$$

The B matrix could now be simplified according to the method by setting  $c_{11} = c_{12} = c_{13} = c_{23} = z_2 = z_3 = f_{12}(x_1) = 0$  to get a simplified B matrix. The T matrix may be computed according to equation (8.13) to give

$$T = \begin{bmatrix} -2kx_1^4 & 0 & -6x_1^2 \\ 0 & 0 & 4 \\ -2kx_1^2 & -4 & -6 \end{bmatrix}, \quad (8.19)$$

where in the interests of simplicity an arbitrary value of 1 was assigned to  $c_{33}$  which appears as a factor in a term of  $\tau_{32}$ .

Therefore, by equation (8.14)

$$\dot{v} = -2(kx_1^6 + (3+k)x_1^3x_3 + 3x_3^2). \quad (8.20)$$

Using the same substitutions as were used to simplify the B matrix and the values determined for  $z_1(x_1)$ ,  $f_{13}(x_1)$  and  $k_{22}$  in computing T the simplified S matrix becomes

$$S = \begin{bmatrix} x_1^4 + x_1^2 & 0 & x_1^2 \\ 0 & 2 & 0 \\ x_1^2 & 0 & 1 \end{bmatrix}, \quad (8.21)$$

and

$$v = X^T S X = x_1^6 + x_1^4 + 2x_2^2 + 2x_1^3x_3 + x_3^2, \quad (8.22)$$

which is positive-definite.

According to the theorem by La Salle referred to above, the trivial solution is asymptotically stable in the large for  $k = 3$ . It is evident from an examination of the results obtained for the same example in the preceding section that the result obtained by Ku and Puri is too restrictive. However, it is not to be concluded that the method is inherently less powerful than the method of Schultz and Gibson. Further study may reveal modifications which will give the same or even better results.

## BIBLIOGRAPHY

1. Aizerman, M. A. Sufficient Conditions for the Stability of a Class of Dynamic Systems with Variable Parameters. PMM, 15, pp. 382-384, 1951.
2. Aizerman, M. A. On the Determination of the Safe and Unsafe Parts on the Boundary of Stability. PMM 14, pp. 444-448, 1950.
3. Antosiewicz, H. A. A Survey of Liapunov's Second Method. Chapter 8 of the book "Contributions to the Theory of Nonlinear Oscillations." Vol. IV, Princeton University Press. 1958.
4. Auslander, J. and Sievert, P. Prolongations and Stability in Dynamical Systems. RIAS Tech Rept. 63-18. Sept. 1963. 39 pages.
5. Barbashin, E. A. The Construction of Liapunov Functions for Nonlinear Systems. Proceedings First IFAC Congress. 1960. pp. 1637-1640.
6. Barbashin, E. A. and Krasovskii, N. N. The Existence of Liapunov Functions in the Case of Asymptotic Stability in the Large. PMM; 18, 3. 1954. pp. 345-350.
7. Bass, R. W. Zubov's Stability Criterion. RIAS Monograph M59-11. 1959.

8. Bergen, A. R. Verification of Aizerman's Conjecture for a Class of Third Order Systems. California University ERL 60-409 Oct. 12, 1961. 16 pages.
9. Cesari, L. Asymptotic Behavior and Stability Problems in Ordinary Differential Equations. Academic Press, Inc., Publishers. New York. 1963.
10. Chetayev, N. G. The Stability of Motion. Translated from the Russian by M. Nadler. Pergamon Press. New York. 1961.
11. Chzhan, Sui-Ni. Stability of Motion During a Finite Time Interval. PMM. 23. 1959. pp. 230-238.
12. Coddington, E. A. and Levinson, N. Theory of Ordinary Differential Equations. McGraw-Hill Book Co., Inc. New York. 1955.
13. Ergen, W. K., Lipkin, H. J., Nohel, J. A. Applications of Liapunov's Second Method in Reactor Dynamics. J. of Math. and Physics. 36, 1. 1957. pp. 36-48.
14. Erugin, N. P. Liapunov's Second Method and Questions of Stability in the Large. PMM. 17. 1953. pp. 389-400.
15. Gantmacher, F. R. Matrix Theory. Vols. I, II. Chelsea Publishing Co. New York. 1959.
16. Geissler, E. D. Problems in Attitude Stabilization of Large Guided Missiles. Aerospace Engineering. 19, 10. Oct. 1960. pp. 24-29, 68-72.
17. Gibson, J. E. et al. Stability of Nonlinear Control Systems by the Second Method of Liapunov. Air Force Missile Development Center. TR-61-6. July 1961. 137 pages.
18. Grayson, L. P. The Design of Nonlinear and Adaptive Systems via Liapunov's Second Method Polytechnic Institute of Brooklyn. MRI-937-61. 71 pages.
19. Hahn, W. Theorie und Anwendung der Direkten Methode von Liapunov. Springer Verlag. Berlin. 1959.
20. Hahn, W. Theory and Application of Liapunov's Direct Method. Translated from the German by H. H. Hosenthien and S. H. Lehnigk. Prentice-Hall, Inc. Englewood Cliffs, N. J. 1963.
21. Hahn, W. The Present State of Liapunov's Second Method. In the Book "Nonlinear Problems," R. E. Langer, editor. University of Wisconsin Press. Madison, Wisconsin. 1961.
22. Hoelker, R. F. Theory of Artificial Stabilization of Missiles and Space Vehicles with Exposition of Four Control Principles. National Aeronautics and Space Administration TN D-555. June 1961. 22 pages.
23. Hoelker, R. F. and Miner, W. E. Introduction into the Concept of the Adaptive Guidance Mode. Aeroballistics Internal Note No. 21-60. Geo. C. Marshall Space Flight Center, Huntsville, Alabama. Dec. 28, 1960. 14 pages.
24. Ingwerson, D. R. Principal Definitions of Stability. In the book "Proceedings of Workshop Session in Liapunov's Second Method," L. F. Kazda, editor. The University of Michigan, Industry Program of the College of Engineering, Ann Arbor, Michigan. 1962. pp. 53-79.
25. Ingwerson, D. R. A Modified Liapunov Method for Nonlinear Stability Analysis. IRE Transactions on Automatic Control. May 1961. pp. 199-210.
26. Ingwerson, D. R. A Modified Liapunov Method for Nonlinear Stability Problems. Ph.D. dissertation, Stanford University. Stanford, California. Nov. 1960.
27. Kalman, R. E. Liapunov Functions for the Problem of Lur'e in Automatic Control. Proceedings of the National Academy of Sciences. 49, 1963. pp. 201-205.
28. Kalman, R. E., and Bertram, J. E. Control System Analysis and Design via the "Second Method" of Liapunov. I, Continuous-Time Systems. II, Discrete Time Systems. Transactions of the ASME, Journal of Basic Engineering. 82, June 1960. pp. 371-400.
29. Krasovskii, N. N. On the Stability in the Large of a System of Nonlinear Differential Equations. PMM. 18, 1954. pp. 735-737.
30. Krasovskii, N. N. On Stability under Large Perturbations. PMM. 21, 1957. pp. 309-319.
31. Krasovskii, N. N. Stability of Motion. Translated by J. L. Brenner. Stanford University Press, Stanford, California. 1963.

32. La Salle, J. P. The Extent of Asymptotic Stability. Proceedings of the National Academy of Sciences. 46, 3, Mar. 1960. pp. 363-365.
33. La Salle, J. P. Some Extensions of Liapunov's Second Method. IRE Transactions, Vol. CT-7. Dec. 1960. pp. 520-535.
34. La Salle, J. P. Complete Stability of a Nonlinear Control System. Proceedings of the National Academy of Sciences. 48, 1962. pp. 600-603.
35. La Salle, J. P. and Lefschetz, S. Stability by Liapunov's Direct Method with Applications.. Academic Press, Inc. New York. 1961.
36. Lefschetz, S. Differential Equations, Geometric Theory. Interscience. New York. 1957.
37. Lefschetz, S. Liapunov and Stability in Dynamical Systems. Bol. Soc. mat. Mexicana. 2, 3, 1958. pp. 25-39.
38. Lefschetz, S. Controls: An Application of the Direct Method of Liapunov. RIAS TR 59-8. Dec. 1959.
39. Lehnigk, S. H. On Liapunov's Second Method with Parameter-Dependent Quadratic Forms in the Case of Autonomous Non-linear Equations Which Have a Linear Part. Proceedings of the First International Congress of the International Federation of Automatic Control. Moscow, 1960, pp. 971-974.
40. Letov, A. M. Stability in Nonlinear Control Systems. Princeton University Press. 1961.
41. Liapunov, A. M. Probleme General de la Stabilité due Mouvement. Annals of Mathematical Studies, No. 17. Princeton University Press. 1947.
42. Lur'e, A. I. Some Nonlinear Problems in the Theory of Automatic Control. (A translation from the Russian.) Her Majesty's Stationery Office. London. 1957.
43. Lur'e, A. I. and Rozenvasser, E. N. On Methods of Constructing Liapunov Functions in the Theory of Nonlinear Control Systems. Proceedings of the First International Congress of the International Federation of Automatic Control. Moscow. 1960. pp. 1356-1359.
44. Malkin, I. G. Theory of Stability of Motion. AEC Translation 3352. Office of Technical Services Department of Commerce, Washington 25, D.C.
45. Massera, J. L. On Liapunov's Condition of Stability. Ann. of Math. 50, 3. 1949. pp. 705-721.
46. Massera, J. L. Contributions to Stability Theory. Ann. of Math. 64, 2. 1956. pp. 182-206. Correction. Ann. of Math. 68, 2. 1958. page 202.
47. Miner, W. E. and Schmieder, D. H. The Path-Adaptive Mode for Guiding Space Flight Vehicles. Paper 1944-61 Guidance, Control, and Navigation Conference of the ARS. Stanford University, Stanford, California. 1961.
48. Persidskii, S. K. On the Second Method of Liapunov. RMM. 25, 1961. pp. 20-28.
49. Pontryagin, L. S. Ordinary Differential Equations. Translated from the Russian by L. Kacinskas and W. B. Counts, Library of Congress. Addison-Wesley Publishing Co., Inc. Reading, Massachusetts. 1962.
50. Pozarickii, G. K. On the Construction of Liapunov Functions from the Integrals of the Equations of the Perturbed Motion. PMM. 22, 1958. pp. 145-154.
51. Puri, N. N. and Weygandt, C. N. Second Method of Liapunov and Routh's Canonical Form. Journal of the Franklin Institute. 276, 1963. pp. 365-384.
52. Puri, N. N. and Ku, Y. H. On Liapunov Functions of High Order Nonlinear Systems. Journal of the Franklin Institute. 276, 1963. pp. 349-364.
53. Roitenberg, J. N. On a Method for the Construction of Liapunov Functions for Linear Systems with Variable Coefficients. PMM. 22, 1958. pp. 167-172.
54. Schultz, D. G. and Gibson, J. E. The Variable Gradient Method for Generating Liapunov Functions. Transactions of AIEE on Automatic Control. 81, Part II, 1962. pp. 203-210.
55. Yoshizawa, T. Stability and Boundedness of Systems. Arch. rat. Mech. and Anal. 6, 1960. pp. 409-421.
56. Zubov, V. I. Methods of A. M. Liapunov and Their Application. AEC translation 4439. Office of Technical Services, Department of Commerce Washington 25, D. C.
57. Zubov, V. I. Questions in the Theory of Liapunov's Second Method; The Construction of the

General Solution in the Domain of Asymptotic Stability. (English translation.) Military Products Group Research Department, Minneapolis-Honeywell Regulator Co. Minneapolis 40, Minnesota.

58. Vogt, W. G., Li, C. C. and Ingwerson, D. R. Discussion of "A Modified Liapunov Method for

Nonlinear Stability Analysis." IRE Transactions on Automatic Control. Jan. 1962. pp. 85-88.

59. Rodden, J. J. Numerical Applications of Liapunov Stability Theory. In Preprints of Conference Papers 1964 Joint Automatic Control Conference at Stanford University, Stanford, California. June 24-26, 1964.

# AN ORTHONORMALIZATION PROCEDURE FOR MULTIVARIABLE FUNCTION APPROXIMATION

by

Hugo Ingram

## SUMMARY

When a function of several variables is given numerically in tabular form, the orthonormalization technique allows an approximation of the numerical data to be determined in a convenient functional form. A method is described that requires much less computational work than the usual least squares technique, and allows the accuracy of the results to be more easily controlled.

$y_1$	$x_{11}$	$x_{12}$	.....	$x_{1m}$
$y_2$	$x_{21}$	$x_{22}$	.....	$x_{2m}$
.	.	.		.
.	.	.		.
.	.	.		.
$y_n$	$x_{n1}$	$x_{n2}$	.....	$x_{nm}$

## SECTION I. INTRODUCTION

In many types of scientific and engineering problems, a table of two or more columns of data occurs, and it is often desirable to put this data in a more useful form. The methods for performing this task are the many different techniques of multivariable function approximation. The method described in this report is an orthonormalization technique. The approximating functions resulting from this procedure are theoretically equivalent to those obtained by least squares procedures as shown in Reference 2. However, the speed and accuracy with which the coefficients can be computed are much improved. Also, a very clear and useful physical interpretation of the procedure is available to aid in the choice of terms to be included in the approximating formulas.

This report will briefly discuss this procedure by first describing the type of function approximation problem that is of interest, next, outlining the orthonormalization method of solution, and finally, making some consideration of applications.

## SECTION II. GENERAL DISCUSSION

### A. STATEMENT OF THE PROBLEM

A set of  $n$  data points for  $m$  independent variables and one dependent variable  $y$  is defined in the following manner  $(y_i, x_{i1}, x_{i2}, \dots, x_{im})$ , where  $i = 1, 2, \dots, n$ . A schematic representation of this data in tabular form is shown below.

If such a table of data is obtained, then the table is assumed to define a function  $y = f(x_1, x_2, \dots, x_m)$  over some region including the tabulated data points.

The desired form for the approximation to  $y$  is to be a weighted sum of known functions, i.e.,

$$y_a = A_0 f_0(x_1, x_2, \dots, x_m) + A_1 f_1(x_1, x_2, \dots, x_m) + \dots + A_N f_N(x_1, x_2, \dots, x_m),$$

where the  $A_0, A_1, \dots, A_N$  are the coefficients or weighting factors for the  $N+1$  known functions. The magnitude of  $N$  and the form for the functions  $f_0, f_1, \dots, f_N$  are arbitrary except for the restriction that a finite numerical value must be able to be assigned to each of the known functions at all the  $n$  data points. One of the simplest forms for the approximation is the familiar polynomial form

$$y_a = a_0 + a_1 x_1 + a_2 x_2 + \dots + a_m x_m + \dots + a_{m+1} x_1^2 + a_{m+2} x_2 x_1 + a_{m+3} x_2^2 + a_{m+4} x_3 x_1 + a_{m+5} x_3 x_2 + a_{m+6} x_3^2 + a_{m+7} x_4 x_1 + \dots + a_l (x_m)^k.$$

In the above expression,  $k$  is the order of the polynomial and the magnitude of  $l$  depends on  $k$ . The polynomial form is equivalent to the original expression for  $y_a$ , where

$$\begin{aligned}
A_0 &= a_0, & f_0(x_1, x_2, \dots, x_m) &= 1 \\
A_1 &= a_1, & f_1(x_1, x_2, \dots, x_m) &= x_1 \\
&\vdots & & \\
A_m &= a_m, & f_m(x_1, x_2, \dots, x_m) &= x_m \\
A_{m+1} &= a_{m+1}, & f_{m+1}(x_1, x_2, \dots, x_m) &= x_1^2 \\
&\vdots & & \\
A_N &= a_N, \text{ and } f_N(x_1, x_2, \dots, x_m) &= (x_m)^k.
\end{aligned}$$

With the weighted sum type of approximation defined, the problem is now to determine the coefficients or weighting factors for the known functions  $f_0, f_1, \dots, f_N$  by the orthonormalization technique.

## B. METHOD FOR SOLUTION OF THE PROBLEM

After the arbitrary choice of the  $N$  known functions to be used in the approximation, a new data table must be constructed. A schematic diagram of the new table is shown below where  $f_{rs}$  means the numerical value of the function  $f_r$  computed at the  $s$ -th data point.

$y_1$	$f_{01}$	$f_{11}$	.....	$f_{N1}$
$y_2$	$f_{02}$	$f_{12}$	.....	$f_{N2}$
$\vdots$	$\vdots$	$\vdots$		$\vdots$
$\vdots$	$\vdots$	$\vdots$		$\vdots$
$y_n$	$f_{0n}$	$f_{1n}$	.....	$f_{Nn}$

Now each of the columns in the preceding table can be called a vector with  $n$  components, i. e. ,

$$\bar{y} = \begin{bmatrix} y_1 \\ y_2 \\ \vdots \\ y_n \end{bmatrix}, \quad \bar{g}_0 = \begin{bmatrix} f_{01} \\ f_{02} \\ \vdots \\ f_{0n} \end{bmatrix}, \quad \bar{g}_1 = \begin{bmatrix} f_{11} \\ f_{12} \\ \vdots \\ f_{1n} \end{bmatrix}, \quad \bar{g}_N = \begin{bmatrix} f_{N1} \\ f_{N2} \\ \vdots \\ f_{Nn} \end{bmatrix}$$

The set of vectors  $\bar{g}_0, \bar{g}_1, \dots, \bar{g}_N$  is assumed to be linearly independent. With this assumption they can be transformed into a set of orthonormal vectors  $\bar{e}_0, \bar{e}_1, \dots, \bar{e}_N$  by the following Gram-Schmidt process:

$$\begin{aligned}
\text{Define: } \bar{e}_0 &= \frac{\bar{P}_0}{|\bar{P}_0|}, \text{ where } \bar{P}_0 = \bar{g}_0, \\
\bar{e}_1 &= \frac{\bar{P}_1}{|\bar{P}_1|}, \text{ where } \bar{P}_1 = \bar{g}_1 - (\bar{g}_1 \cdot \bar{e}_0) \bar{e}_0, \\
\bar{e}_2 &= \frac{\bar{P}_2}{|\bar{P}_2|}, \text{ where } \bar{P}_2 = \bar{g}_2 - (\bar{g}_2 \cdot \bar{e}_0) \bar{e}_0 \\
&\quad - (\bar{g}_2 \cdot \bar{e}_1) \bar{e}_1, \\
&\vdots \\
\bar{e}_N &= \frac{\bar{P}_N}{|\bar{P}_N|}, \text{ where } \bar{P}_N = \bar{g}_N - (\bar{g}_N \cdot \bar{e}_0) \bar{e}_0 \\
&\quad - (\bar{g}_N \cdot \bar{e}_1) \bar{e}_1 - \dots - (\bar{g}_N \cdot \bar{e}_{N-1}) \bar{e}_{N-1}.
\end{aligned}$$

All the preceding equations are in standard vector notation, i. e. ,

$$\bar{a} \cdot \bar{b} = \sum_{i=1}^n a_i b_i \text{ where } a_i \text{ and } b_i \text{ are the } i\text{-th components of } \bar{a} \text{ and } \bar{b}$$

$$|\bar{a}| = \sqrt{\bar{a} \cdot \bar{a}}.$$

A geometric interpretation of this orthonormalization process is shown in Figure 1.

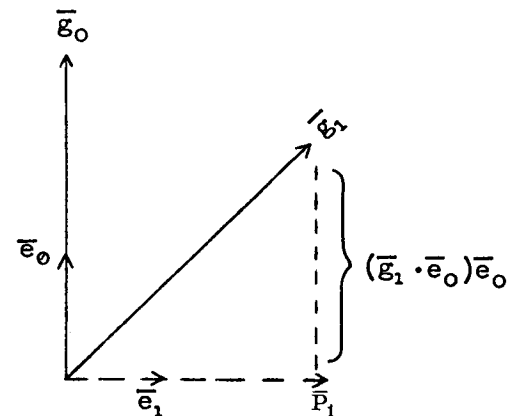


FIGURE 1. A GEOMETRIC INTERPRETATION OF ORTHONORMALIZATION PROCEDURE

After the numerical values of the components of the orthonormal vectors  $\bar{e}_0, \bar{e}_1, \dots, \bar{e}_N$  are computed, an approximation to  $\bar{y}$  could be written as

$$\bar{y}_a = (\bar{y} \cdot \bar{e}_0) \bar{e}_0 + (\bar{y} \cdot \bar{e}_1) \bar{e}_1 + \dots + (\bar{y} \cdot \bar{e}_N) \bar{e}_N.$$

Obviously, the approximation is the vector sum of the projections of  $\bar{y}$  on  $\bar{e}_0, \bar{e}_1, \dots, \bar{e}_N$ . A geometric interpretation is shown in Figure 2. There  $\bar{y} = \bar{y}_a$  if  $n = N+1$ ,

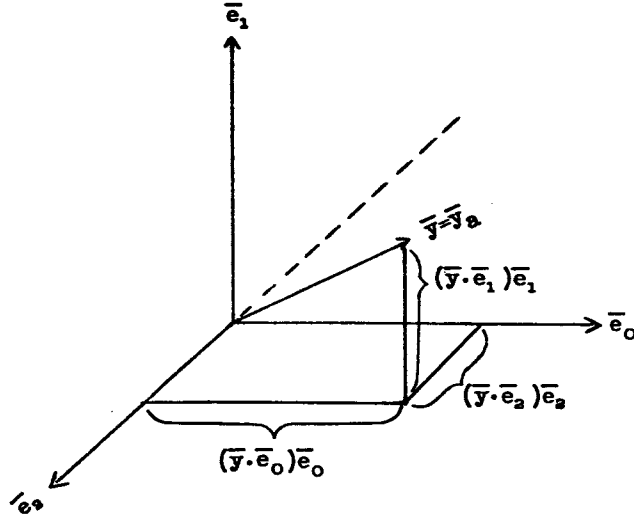


FIGURE 2. A GEOMETRIC INTERPRETATION OF THE SELECTION OF EFFICIENT TERMS

because in this case all of the projections or components of  $\bar{y}$  will be added vectorially to produce  $\bar{y}$  again. Finally, some algebraic manipulations are performed so that  $\bar{y}_a$  can be written in the form

$$\bar{y}_a = A_{00} \bar{g}_0 + A_{11} \bar{g}_1 + \dots + A_{NN} \bar{g}_N$$

as was originally desired. The following equations will give an idea of how the algebraic manipulations are to be performed.

$$(\bar{y} \cdot \bar{e}_0) \bar{e}_0 = (\bar{y} \cdot \frac{\bar{P}_0}{|\bar{P}_0|}) \frac{\bar{P}_0}{|\bar{P}_0|} = \frac{\bar{y} \cdot \bar{P}_0}{(\bar{P}_0 \cdot \bar{P}_0)} \bar{g}_0 = A_{00} \bar{g}_0$$

where

$$A_{00} = \frac{\bar{y} \cdot \bar{P}_0}{\bar{P}_0 \cdot \bar{P}_0}$$

$$(\bar{y} \cdot \bar{e}_1) \bar{e}_1 = (\bar{y} \cdot \frac{\bar{P}_1}{|\bar{P}_1|}) \frac{\bar{P}_1}{|\bar{P}_1|} = \frac{\bar{y} \cdot \bar{P}_1}{(\bar{P}_1 \cdot \bar{P}_1)} \bar{P}_1$$

$$= \frac{\bar{y} \cdot \bar{P}_1}{(\bar{P}_1 \cdot \bar{P}_1)} [\bar{g}_1 - (\bar{g}_1 \cdot \bar{e}_0) \bar{e}_0]$$

$$\begin{aligned} &= \frac{\bar{y} \cdot \bar{P}_1}{(\bar{P}_1 \cdot \bar{P}_1)} \bar{g}_1 - \left( \frac{\bar{y} \cdot \bar{P}_1}{(\bar{P}_1 \cdot \bar{P}_1)} \right) (\bar{g}_1 \cdot \frac{\bar{P}_0}{|\bar{P}_0|}) \frac{\bar{P}_0}{|\bar{P}_0|} \\ &= \frac{\bar{y} \cdot \bar{P}_1}{(\bar{P}_1 \cdot \bar{P}_1)} \bar{g}_1 - \left( \frac{\bar{y} \cdot \bar{P}_1}{(\bar{P}_1 \cdot \bar{P}_1)} \right) \left( \frac{\bar{g}_1 \cdot \bar{P}_0}{(\bar{P}_0 \cdot \bar{P}_0)} \right) \bar{g}_0 = A_{01} \bar{g}_0 \\ &\quad + A_{11} \bar{g}_1 \end{aligned}$$

where

$$A_{01} = - \left( \frac{\bar{y} \cdot \bar{P}_1}{(\bar{P}_1 \cdot \bar{P}_1)} \right) \left( \frac{\bar{g}_1 \cdot \bar{P}_0}{(\bar{P}_0 \cdot \bar{P}_0)} \right)$$

and

$$A_{11} = \frac{\bar{y} \cdot \bar{P}_1}{(\bar{P}_1 \cdot \bar{P}_1)}.$$

The above process is continued until the following table can be constructed.

$$(\bar{y} \cdot \bar{e}_0) \bar{e}_0 = A_{00} \bar{g}_0$$

$$(\bar{y} \cdot \bar{e}_1) \bar{e}_1 = A_{01} \bar{g}_0 + A_{11} \bar{g}_1$$

$$(\bar{y} \cdot \bar{e}_2) \bar{e}_2 = A_{02} \bar{g}_0 + A_{12} \bar{g}_1 + A_{22} \bar{g}_2$$

⋮  
⋮  
⋮

$$(\bar{y} \cdot \bar{e}_N) \bar{e}_N = A_{0N} \bar{g}_0 + A_{1N} \bar{g}_1 + A_{2N} \bar{g}_2 + \dots + A_{NN} \bar{g}_N$$

Adding each column in the preceding table shows that

$$\begin{aligned} \bar{y}_a &= (\bar{y} \cdot \bar{e}_0) \bar{e}_0 + (\bar{y} \cdot \bar{e}_1) \bar{e}_1 + \dots + (\bar{y} \cdot \bar{e}_N) \bar{e}_N \\ &= A_{00} \bar{g}_0 + A_{10} \bar{g}_1 + \dots + A_{N0} \bar{g}_N, \end{aligned}$$

where

$$A_0 = A_{00} + A_{01} + A_{02} + \dots + A_{0N}$$

$$A_1 = A_{11} + A_{12} + \dots + A_{1N}$$

$$A_2 = A_{22} + \dots + A_{2N}$$

⋮  
⋮  
⋮

$$A_N = A_{NN}$$

All of the  $A_0, A_1, A_2, \dots, A_N$  can be computed by using only the following list of dot products:

$$(\bar{g}_0 \cdot \bar{g}_0)$$

$$(\bar{g}_1 \cdot \bar{g}_0), (\bar{g}_1 \cdot \bar{g}_1)$$

$$(\bar{g}_2 \cdot \bar{g}_0), (\bar{g}_2 \cdot \bar{g}_1), (\bar{g}_2 \cdot \bar{g}_2)$$

$$\begin{matrix} \cdot & \cdot & \cdot \\ \cdot & \cdot & \cdot \\ \cdot & \cdot & \cdot \end{matrix}$$

$$(\bar{g}_N \cdot \bar{g}_0), (\bar{g}_N \cdot \bar{g}_1), (\bar{g}_N \cdot \bar{g}_2), \dots, (\bar{g}_N \cdot \bar{g}_N)$$

and

$$(\bar{y} \cdot \bar{g}_0), (\bar{y} \cdot \bar{g}_1), (\bar{y} \cdot \bar{g}_2), \dots, (\bar{y} \cdot \bar{g}_N).$$

All of the listed dot products are computed from the second data table. The recursion relations (determined as described previously) are then used to compute the  $A_{00}, A_{01}, A_{11}, A_{02}, A_{12}, \dots, A_{NN}$  which are summed to yield the desired results, i.e.,  $(A_0, A_1, \dots, A_N)$ .

### C. APPLICATIONAL CONSIDERATIONS

In the previous subsection, the procedure was explained for the weighted sum of all the  $N$  (arbitrary) functions. Often it is desirable to construct in an efficient manner a sufficiently good approximation which uses as few as possible of the arbitrary functions. This is accomplished by letting each of the functions be used as  $\bar{g}_0$  and computing the corresponding  $(\bar{y} \cdot \bar{e}_0)$ . The particular function which makes  $(\bar{y} \cdot \bar{e}_0)$  the largest is used as the actual  $\bar{g}_0$ , and then the remaining functions are each used as  $\bar{g}_1$  to compute  $(\bar{y} \cdot \bar{e}_1)$ . The function which makes  $(\bar{y} \cdot \bar{e}_1)$  the largest is used as the actual  $\bar{g}_1$ . The process is continued until as many of the arbitrary functions are used as desired. As shown in Figure 2,  $\bar{y}$  has three components. The components are given by the expressions  $(\bar{y} \cdot \bar{e}_0)\bar{e}_0$ ,  $(\bar{y} \cdot \bar{e}_1)\bar{e}_1$ , and  $(\bar{y} \cdot \bar{e}_2)\bar{e}_2$ . If only two of the components of  $\bar{y}$  could be used to write an approximation to  $\bar{y}$ , then it would seem reasonable to use the two biggest components, i.e.,  $(\bar{y} \cdot \bar{e}_0)\bar{e}_0$  and  $(\bar{y} \cdot \bar{e}_1)\bar{e}_1$ . This is the basis for using this particular selection procedure. The process is very rapid because the recursive property of the orthonormalization method allows all work done in one step to be used on the next step.

If at any point during the computational procedure the absolute value of one of the  $\bar{P}$ 's becomes zero or approximately zero, the  $\bar{g}$  used to compute that particular  $\bar{P}$  is linearly or nearly linearly dependent on the previous  $\bar{g}$ 's. This indicates that, to achieve good accuracy in the approximation, the  $\bar{g}$  which causes a particular  $\bar{P}$  to be zero or near zero must not be used at that point in the process, although it may be saved for later use.

The final consideration to be made in this report concerns a method for weighting the constructed data table so that the partials of the approximation to  $\bar{y}$  will also approximate  $\frac{\partial \bar{y}}{\partial x_1}, \frac{\partial \bar{y}}{\partial x_2}, \dots, \frac{\partial \bar{y}}{\partial x_m}$ . This is done simply by including values for the  $\frac{\partial y}{\partial x_1}, \frac{\partial y}{\partial x_2}, \dots, \frac{\partial y}{\partial x_m}$  in the  $\bar{y}$  column of the data table, including values of  $\frac{\partial f_0}{\partial x_1}, \frac{\partial f_0}{\partial x_2}, \dots, \frac{\partial f_0}{\partial x_m}$  in the  $\bar{g}_0$  column, etc. The procedure is reasonable because  $y_{ia} = A_0 f_{0i} + A_1 f_{1i} + \dots + A_N f_{Ni}$ , where  $i$  is the number of the data point; and therefore,

$$\begin{aligned} \frac{\partial y_{ia}}{\partial x_j} &= A_0 \frac{\partial f_{0i}}{\partial x_j} + A_1 \frac{\partial f_{1i}}{\partial x_j} + \dots \\ &+ A_N \frac{\partial f_{Ni}}{\partial x_j} \quad (j = 1, \dots, m). \end{aligned}$$

Naturally, the additions to the data table must be available. They will usually decrease the accuracy of the approximation to  $\bar{y}$ , but the approximation will more nearly satisfy the partial derivatives of the function that is assumed to have produced  $\bar{y}$ .

### SECTION III. CONCLUSIONS

The preceding sections give a brief outline of the orthonormalization procedure with a few computational considerations. More detail on the mathematical basis for the procedure can be found in the references. An IBM 7094 computer program incorporating most of the features described has been successfully used to develop polynomial type approximations using 45 of the 220 functions that are generated by 9 variables ( $m=9$ ) each to the 3rd order ( $k=3$ ). The appendix is a listing of the computational procedure used to construct the computer program.

### REFERENCES

1. Dupree, Daniel E., "Existence of Multivariable Least Squares Approximating Polynomials," Progress Report No. 2 on Studies in the Fields of Space Flight and Guidance Theory.
2. Dupree, et.al, "A Recursion Process for the Generation of Orthogonal Polynomials in Several Variables," Progress Report No. 3 on Studies in the Fields of Space Flight and Guidance Theory.



# APPENDIX

## COMPUTATIONAL PROCEDURE

(1) Preload is the table of dot products

$$\bar{g}_0 \cdot \bar{g}_0,$$

$$\bar{g}_0 \cdot \bar{g}_1, \bar{g}_1 \cdot \bar{g}_1$$

$$\bar{g}_0 \cdot \bar{g}_2, \bar{g}_2 \cdot \bar{g}_1, \bar{g}_2 \cdot \bar{g}_2$$

...

$$\bar{g}_N \cdot \bar{g}_0, \bar{g}_N \cdot \bar{g}_1, \bar{g}_N \cdot \bar{g}_2, \dots, \bar{g}_N \cdot \bar{g}_N$$

$$\bar{y} \cdot \bar{g}_0, \bar{y} \cdot \bar{g}_1, \bar{y} \cdot \bar{g}_2, \dots, \bar{y} \cdot \bar{g}_N, \bar{y} \cdot \bar{y}$$

(2) Start Computation Procedure

$$\bar{P}_0 \cdot \bar{P}_0 = \bar{g}_0 \cdot \bar{g}_0$$

$$H_0 = \frac{1}{\sqrt{\bar{P}_0 \cdot \bar{P}_0}} \bar{y} \cdot \bar{g}_0$$

$$A_{00} = \frac{1}{\sqrt{\bar{P}_0 \cdot \bar{P}_0}} H_0$$

$$(3) B_{10} = \frac{\bar{g}_1 \cdot \bar{g}_0}{\bar{P}_0 \cdot \bar{P}_0}$$

$$\bar{P}_1 \cdot \bar{P}_1 = \bar{g}_1 \cdot \bar{g}_1 - 2B_{10} \bar{g}_1 \cdot \bar{g}_0 + (B_{10})^2 \bar{g}_0 \cdot \bar{g}_0$$

$$H_1 = \frac{1}{\sqrt{\bar{P}_1 \cdot \bar{P}_1}} [\bar{y} \cdot \bar{g}_1 - B_{10} \bar{y} \cdot \bar{g}_0]$$

$$A_{10} = \frac{-1}{\sqrt{\bar{P}_1 \cdot \bar{P}_1}} (B_{10} H_1)$$

$$A_{11} = \frac{1}{\sqrt{\bar{P}_1 \cdot \bar{P}_1}} H_1$$

(4) Start loop now with  $(i = 2, 3, \dots, N)$  where  $N+1$  is the number of functions to be used in the approximation.

$$(a) \bar{g}_i \cdot \bar{P}_0 = \bar{g}_i \cdot \bar{g}_0$$

$$(b) \bar{g}_i \cdot \bar{P}_m = \bar{g}_i \cdot \bar{g}_m - \sum_{j=0}^{m-1} B_{mj} \bar{g}_i \cdot \bar{g}_j \quad (m=1, 2, \dots, i-1)$$

$$(c) B_{ik} = \frac{\bar{g}_i \cdot \bar{P}_k}{\bar{P}_k \cdot \bar{P}_k} - \sum_{j=k+1}^{i-1} \frac{\bar{g}_i \cdot \bar{P}_j}{\bar{P}_j \cdot \bar{P}_j} B_{jk} \quad (k=0, 1, 2, \dots, i-2)$$

$$(d) B_{i(i-1)} = \frac{\bar{g}_i \cdot \bar{P}_{i-1}}{\bar{P}_{i-1} \cdot \bar{P}_{i-1}}$$

$$(e) \bar{P}_i \cdot \bar{P}_i = \bar{g}_i \cdot \bar{g}_i + \sum_{r=0}^{i-1} [(B_{ir})^2 \bar{g}_r \cdot \bar{g}_r - 2B_{ir} \bar{g}_i \cdot \bar{g}_r] + 2 \sum_{j=1}^{i-1} \sum_{r=0}^{j-1} B_{ir} B_{ij} \bar{g}_r \cdot \bar{g}_j$$

$$(f) H_i = \frac{\bar{y} \cdot \bar{g}_i}{\sqrt{\bar{P}_i \cdot \bar{P}_i}} - \frac{1}{\sqrt{\bar{P}_i \cdot \bar{P}_i}} \sum_{r=0}^{i-1} B_{ir} \bar{y} \cdot \bar{g}_r$$

$$(g) A_{ir} = -\frac{1}{\sqrt{\bar{P}_i \cdot \bar{P}_i}} (B_{ir} H_i) \quad (r=0, 1, 2, \dots, i-1)$$

$$(h) A_{ii} = \frac{1}{\sqrt{\bar{P}_i \cdot \bar{P}_i}} H_i$$

$$(i) A_0 = A_{00} + A_{10} + \sum_{i=2}^N A_{i0}$$

$$A_1 = A_{11} + \sum_{i=2}^N A_{i1}$$

$$A_i = \sum_{q=i}^N A_{qi} \quad (i=2, 3, \dots, N)$$

$$(j) \bar{d} \cdot \bar{d} = \bar{y} \cdot \bar{y} - H_0^2 - \sum_{i=2}^N H_i^2$$

$$(k) \text{R.M.S.} = \sqrt{\frac{\bar{d} \cdot \bar{d}}{n}} \quad \text{where } n \text{ is the number of points and must be preloaded.}$$

(5) To select only  $L$  of the  $N+1$  functions for the approximation, the following procedure is used.

(a) Use each of the  $\bar{g}$ 's as  $\bar{g}_0$  and use the  $\bar{g}$  that produces the largest  $H_0$  as the actual  $\bar{g}_0$ .

- (b) With the  $\bar{g}_0$  determined by (a), use each of the remaining  $\bar{g}$ 's as  $\bar{g}_1$  and use the  $\bar{g}_1$  that produces the largest  $H_1$  as the actual  $\bar{g}_1$ .
- (c) With the  $\bar{g}_0$  and  $\bar{g}_1$  determined by (a) and (b), use each of the remaining  $\bar{g}$ 's as  $\bar{g}_2$  and use the  $\bar{g}_2$  that produces the largest  $H_2$  as the actual  $\bar{g}_2$ .
- (d) If at any point in parts (b) or (c) one of the  $\bar{g}$ 's produces a  $\bar{P}$  less than a prespecified tolerance, that particular  $\bar{g}$  is not used in the procedure, although it may be saved for use as a  $\bar{g}$  later in the process.
- (e) Continue this process until  $L$  terms are contained in the approximation to  $\bar{y}$ .

## VII. ORBIT THEORY

ANALYSIS OF THE INFLUENCE OF VENTING AND GAS LEAKAGE  
ON TRACKING OF ORBITAL VEHICLES

By

A. R. McNair and P. E. Dreher

SUMMARY

The results of a study of the effects on earth orbits of leakage and venting of propellant gases are discussed. Two types of propulsive thrusts, continuous and intermittent, which might result from such venting and leakage, are treated considering the orbit and tracking effects. Integrated and analytic formulations have been made. The following conclusions result from the analysis for a continuous thrust. The only significant effect of out-of-plane thrust is in the out-of-plane direction. The only significant effects of in-plane thrusts are in-plane. The downrange effect of an in-plane thrust is larger than the radial effect after about half an orbit. Downrange thrust gives the largest effects of any thrust in both the radial and downrange direction. The analytic formulation compares well with the integrated effects as long as the orbit is near circular. The altitude of the orbit affects the position change due to the thrust. An intermittent thrust causes more pronounced short period effects than a continuous thrust, with the short period being sensitive to the frequency of the thrust. The orbits which result from the initial conditions determined with tracking data are influenced by the thrusts. Considering the case that no attempt is made to solve for the thrust, a downrange thrust in the downrange direction gives the largest tracking effects, although some in-plane effect is observed. The error during the period when tracking data are available is smaller than the error after the interval because the orbit determination model has no information about errors where there are no observations. As more passes are used, the error becomes larger during the tracking interval, since the actual thrusting orbit is approximated by a nonthrusting orbit. This, of course, assumes that no attempt is made to solve for the thrust.

I. INTRODUCTION

This paper presents some of the results of a study on the effect of gas leakage and venting of gases on earth orbits performed by Thompson Ramo Wooldridge, Inc., Space Technology Laboratories, for the George C. Marshall Space Flight Center under National Aeronautics and Space Administration Contract Number

NAS8-11073. A more detailed analysis of the results appears in "Investigation and Analysis of the Influence of Perturbing Forces on Tracking of Orbital Vehicles," STL Report Number 4103-6011-RU-000, extracts of which have been used in this paper. Studies have also been performed by the Goddard Space Flight Center concerning the influence of venting on Apollo earth parking orbits [1].

Because of the heat input to the tanks in which propellant remains, gases must be vented from vehicles during orbital operations. Such phenomena are characteristic of the Saturn class vehicles where an orbiting stage is approximately two-thirds filled with liquid hydrogen and oxygen, and where propellant loss must be minimized. The gaseous venting also results from trapped or residual propellants after final burning of the stage is completed. This gas leakage or venting may impart a small propulsive thrust to the vehicle, either continuous or intermittent, both types of which are studied.

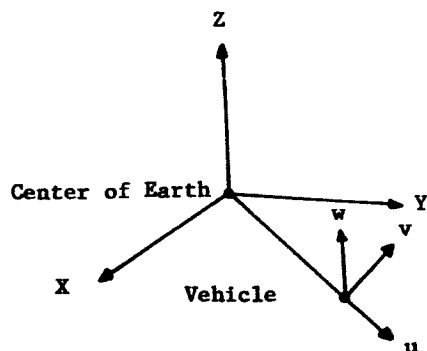
The effects of a propulsive thrust on earth orbits are of two types: orbit and tracking. The orbit effects are the changes in vehicle coordinates that result from the application of the thrust. The tracking effects are the errors in prediction of the vehicle coordinates caused by the thrust effects on the orbit determination model and the tracking data.

Two methods of determining the effects of a propulsive thrust on earth orbits have been used. Most of the results presented were obtained from an integrating trajectory program, since this allowed the generation of radar data to be used in the calculation of tracking effects. Analytic expressions and sample results are also presented because they allow a simpler method of calculation under certain conditions.

II. COORDINATE SYSTEMS AND REFERENCE ORBIT

The effective differences between the coordinates of a thrusting vehicle and a nonthrusting vehicle with the same initial conditions have been studied in a coordinate system centered at the nonthrusting vehicle which defines the position of one vehicle relative to the other. The axes are defined with the u-direction

radial, the v-direction horizontal in the direction of motion (downrange), and the w-direction out-of-plane.



A nominally circular orbit was chosen as the reference orbit for the studies of the effects of low thrust. This orbit is equatorial, with its initial position on the X-axis and its initial velocity in the Y-direction, where the XYZ coordinates form an earth-centered inertial system with X toward the vernal equinox and Z toward the north pole. Thus, the Z-direction and the w-direction coincide.

### III. CONTINUOUS THRUST

A. Integrated Effects. The orbital position differences between a nonthrusting vehicle and one thrusting with a continuous acceleration of  $5(10^{-5})$  g were determined using a Space Technology Laboratory integrating trajectory program. The  $5(10^{-5})$  g acceleration corresponds to a thrust level for a Saturn V type orbiting vehicle of approximately 62 newtons (14 lb). The thrusting vehicle in a 200-km circular orbit was given the acceleration of  $5(10^{-5})$  g in each of the u, v, and w directions separately, and the effects in each of the directions were analyzed. Figures 1-3 show results of these fixed thrusts. For the particular thrust level and orbit used, the following conclusions can be drawn from the curves:

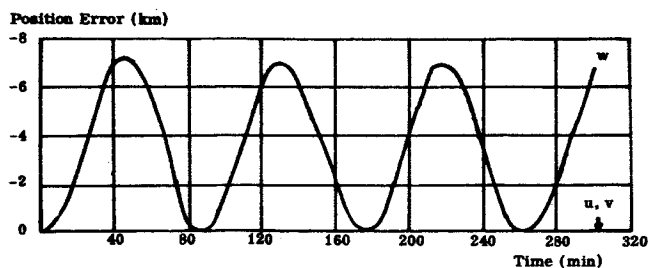


FIGURE 1. EFFECT OF  $5(10^{-5})$ g CONTINUOUS THRUST, w EFFECT OF u, v, w THRUST

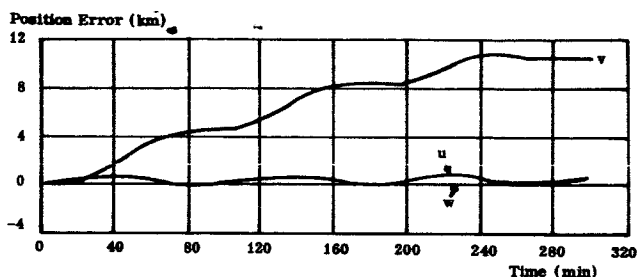


FIGURE 2. EFFECT OF  $5(10^{-5})$ g CONTINUOUS THRUST, u EFFECT OF u, v, w THRUST

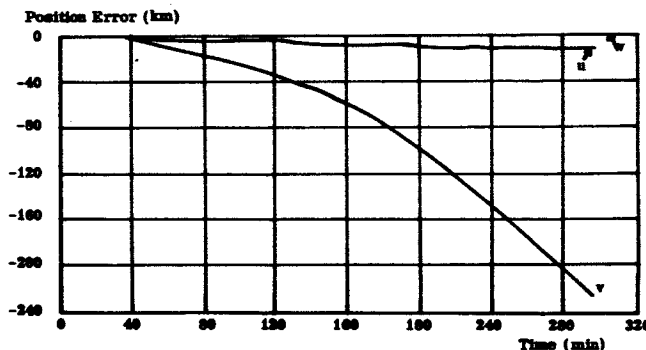


FIGURE 3. EFFECT OF  $5(10^{-5})$ g CONTINUOUS THRUST, v EFFECT OF u, v, w THRUST

a. The only significant effect of out-of-plane thrust is in the out-of-plane direction (Fig. 1).

b. The only significant effects of in-plane thrusts are in-plane (Fig. 2, 3).

c. The downrange effect of an in-plane thrust is larger than the radial effect after about half an orbit (Fig. 2, 3).

B. Analytic Comparison. Analytic expressions, derived for the effects of continuous low thrust, are based on linear perturbations of a nominally circular orbit. In the uvw-coordinate system, the differential equations are

$$a_u = \ddot{u} - 3\omega^2 u - 2\omega \dot{v}$$

$$a_v = \ddot{v} + 2\omega \dot{u}$$

$$a_w = \ddot{w} + \omega^2 w,$$

where

$$\omega = \text{angular frequency, } \omega = \frac{2\pi}{P} \quad (P = \text{orbital period})$$

and

$a_u, a_v, a_w$  = acceleration in the  $u, v, w$  directions.

A comparison between the integrated and the analytic method is shown as solid curves in Figures 4 through 7.

The analytic formulation depends on the orbit being nearly circular. The approximations involve setting  $\cos e = 1$  and  $\sin e = 0$ , where  $e$  is the eccentricity of the orbit. For elliptical orbits in the range of 150 to 700-km altitude,  $e < .05$ , the approximation is good enough for results that are to be presented graphically.

C. Altitude Variation Effects. The altitude of the nominal circular orbit affects the position deviation caused by a continuous low thrust. Figures 4 through 7 show some typical examples of the effects

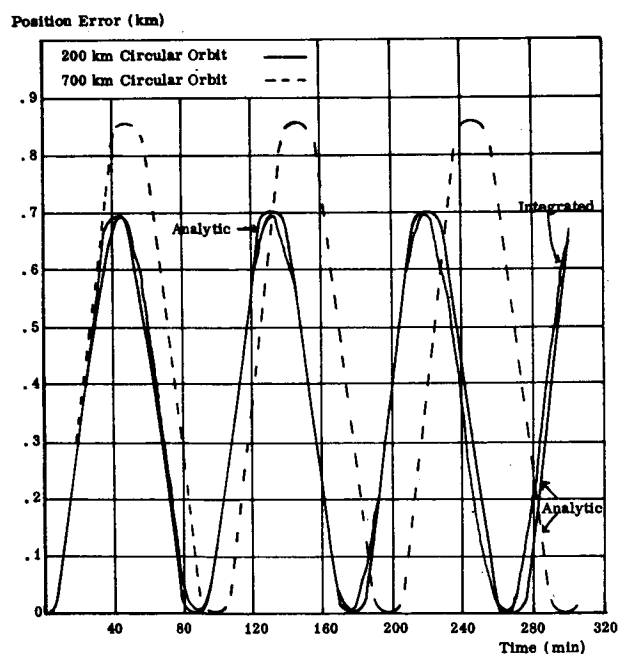


FIGURE 4. COMPARISON OF INTEGRATED AND ANALYTIC RESULTS,  $w$  EFFECT OF  $u$  THRUST,  $5(10^{-5})g$  CONTINUOUS

of changing the altitude from 200 km to 700 km. The amplitude of the effect of a thrust in the  $w$  (out-of-plane) direction is inversely proportional to the square

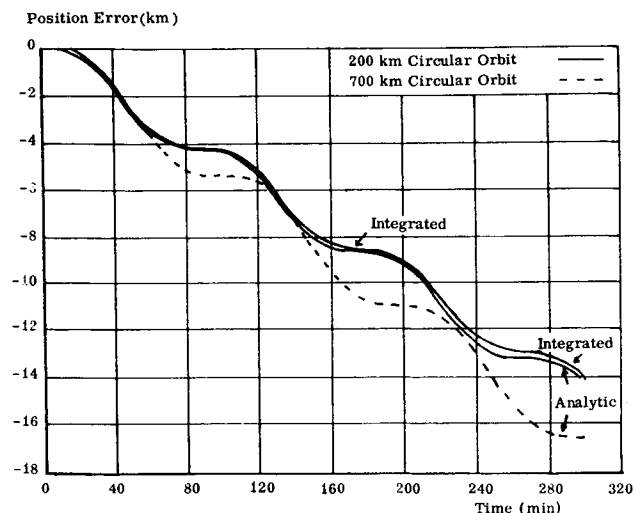


FIGURE 5. COMPARISON OF INTEGRATED AND ANALYTIC RESULTS,  $v$  EFFECT OF  $u$  THRUST,  $5(10^{-5})g$  CONTINUOUS

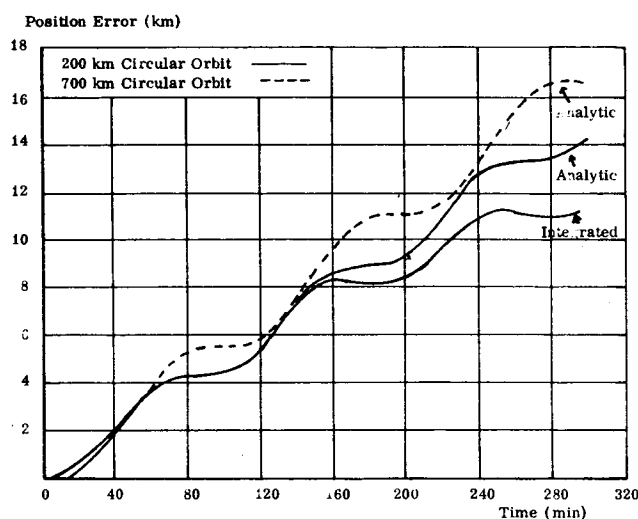


FIGURE 6. COMPARISON OF INTEGRATED AND ANALYTIC RESULTS,  $u$  EFFECT OF  $v$  THRUST,  $5(10^{-5})g$  CONTINUOUS

of the angular frequency, as seen in the equations of paragraph B. The  $v$  (downrange) effect of a downrange thrust is essentially independent of altitude (Fig. 7).

D. Tracking Effects. The effects of continuous low thrusts on the tracking of earth orbits were determined with Space Technology Laboratory programs by doing actual fits to noise-free tracking data generated by the perturbed trajectories, and then comparing the

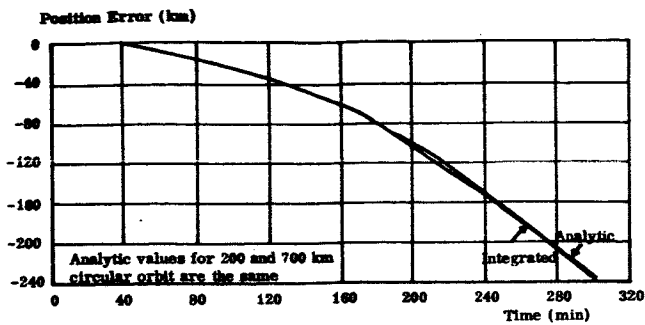


FIGURE 7. COMPARISON OF INTEGRATED AND ANALYTIC RESULTS,  $v$  EFFECT OF  $v$  THRUST,  $5(10^{-5})g$  CONTINUOUS

resulting estimated orbits with the actual orbits. The observations were generated and processed to obtain the initial conditions of the nonthrusting orbits which best fit the data in a least squares sense. The differences between the original thrusting orbits and the orbits resulting from the initial conditions found by the tracking analysis were calculated.

The orbit used was nominally circular at an altitude of 200 km with zero inclination and was perturbed by an acceleration of  $5(10^{-5})g$  in various directions. Observations were made by three tracking stations located at one degree north latitude and 15, 135, and 255 degrees east longitude. Range, azimuth, and elevation observations were taken every ten seconds during the period of visibility of the vehicle to each station. The one-sigma uncertainties were assumed to be 10 meters in range and .015 degrees in azimuth and elevation.

Figures 8 through 10 show the  $u$ ,  $v$ , and  $w$  effects of  $u$ ,  $v$ , and  $w$  thrust on the prediction of the orbit from three tracking passes. These curves show that downrange thrust gives the largest in-plane tracking effects, just as it gives the largest in-plane orbit effects. Also, in-plane thrusts give an out-of-plane tracking error even though they cause no out-of-plane perturbations of the orbit. This is a result of using tracking data from stations out of the orbit plane.

Because downrange thrust in the downrange direction gives the largest tracking effects, it was chosen for more detailed study, the results of which are shown in Figure 11. In this figure the error in the prediction of the vehicle downrange position is presented with the number of tracking passes as a parameter. The error during the tracking interval is smaller than the error after the interval, because the fitting procedure has no information about errors where

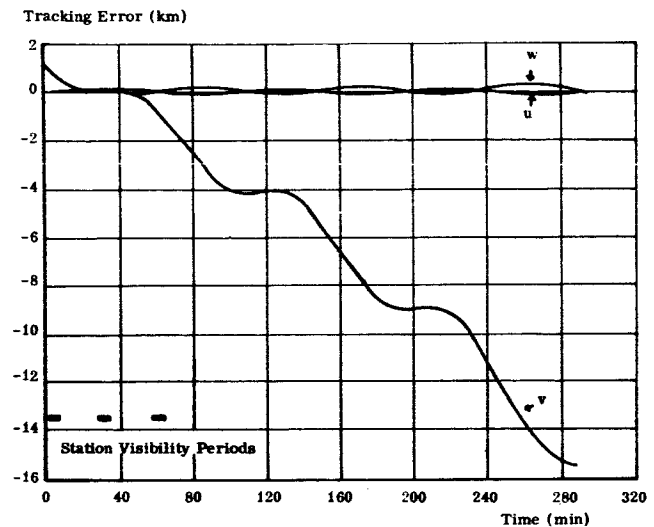


FIGURE 8. TRACKING EFFECT,  $u$  EFFECT OF  $u$ ,  $v$ ,  $w$  THRUST,  $5(10^{-5})g$  CONTINUOUS

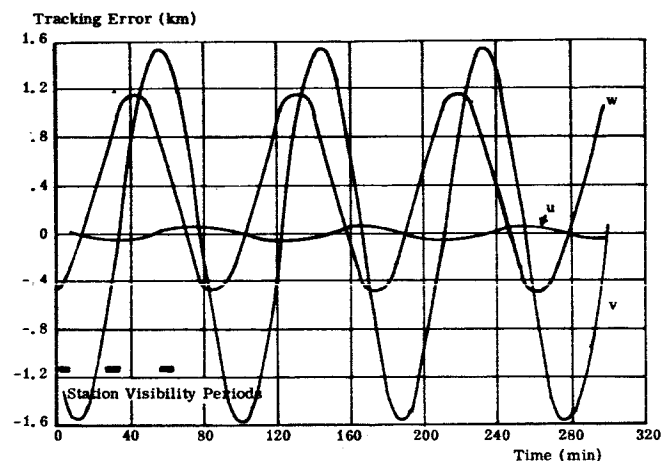


FIGURE 9. TRACKING EFFECT,  $w$  EFFECT OF  $u$ ,  $v$ ,  $w$  THRUST,  $5(10^{-5})g$  CONTINUOUS

there are no observations. As more passes are used, the fit during the tracking interval has more error, since the actual thrusting orbit is approximated by a nonthrusting orbit in the tracking program.

Figure 12 shows the downrange tracking estimate error for downrange thrust as a function of time after the last observation. The best prediction occurs when only the last radar pass is used in the fit.

One technique by which the error caused by the thrust can be reduced is to introduce it as an unknown

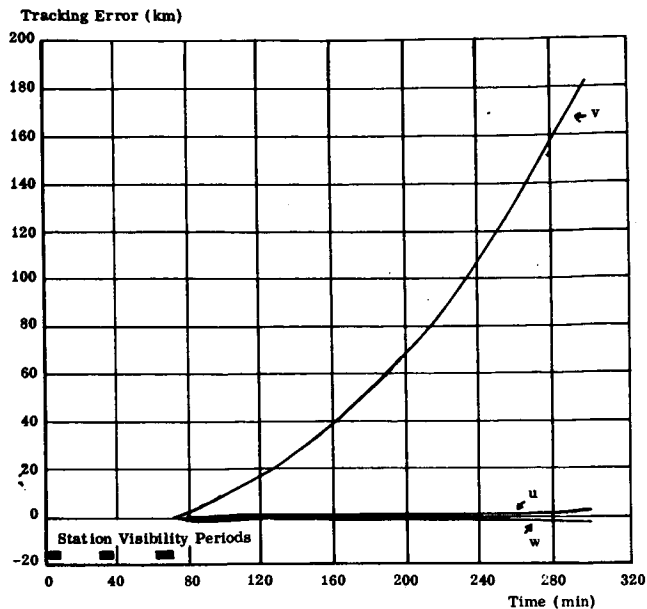


FIGURE 10. TRACKING EFFECT,  $v$  EFFECT OF  $u$ ,  $v$ ,  $w$  THRUST,  $5(10^{-5})g$  CONTINUOUS

in the orbit determination process. All available tracking data can then be used to predict the magnitude and direction of the thrust. The actual application of such a technique could be a problem if the thrust is small. No investigations of this approach have been made.

#### IV. PERIODIC THRUST

A. Vent Interval Effect. The effects of a random type low thrust on a nominally circular 200-km orbit have been studied. A random low thrust may result from gas leakage, from uncertainties in continuous venting, or from a combination of the two. No matter what the cause, in this study the uncertain thrust is assumed to be fixed in magnitude and direction relative to the body axes. The effects can then be analyzed with the analytic expressions developed for the position errors resulting from a fixed thrust. The

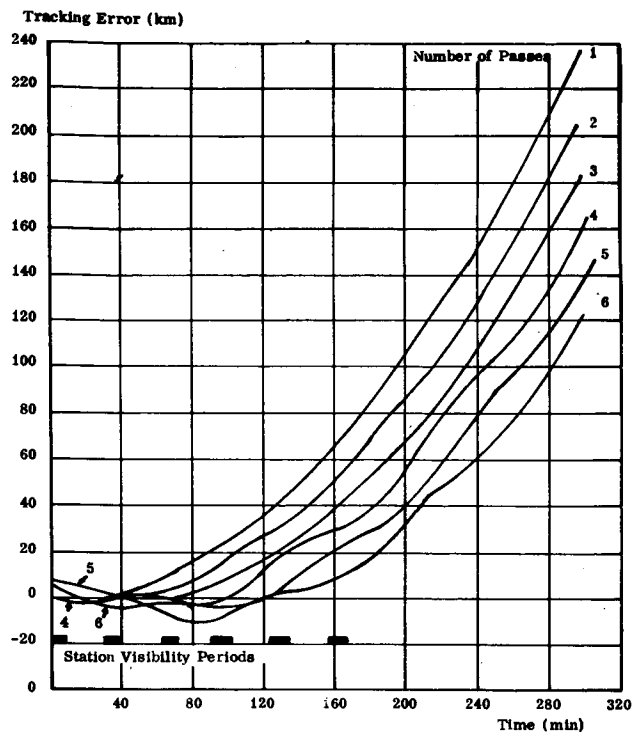


FIGURE 11. EFFECT OF VARIATION IN NUMBER OF TRACKING PASSES  $v$  EFFECT OF  $v$  THRUST,  $5(10^{-5})g$  CONTINUOUS

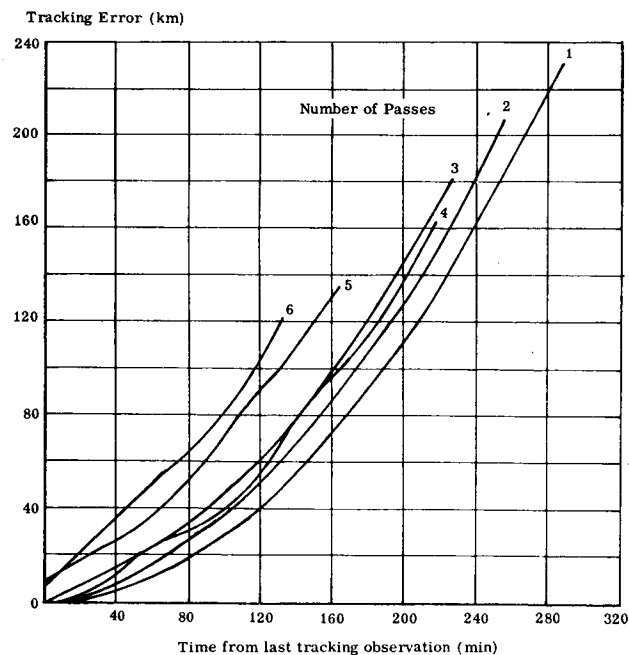


FIGURE 12.  $v$  TRACKING PREDICTION ERROR FROM,  $v$  THRUST,  $5(10^{-5})g$  CONTINUOUS



effects of intermittent venting can be divided into orbit effects and tracking effects just as for continuous low thrust.

The velocity addition from the venting and the duration of venting are proportional to the interval between ventings. The case considered is as follows:

$$V = \frac{1.5 \text{ m/s}}{80 \text{ min}} \quad T \text{ and } \tau = \frac{3.0 \text{ min}}{80 \text{ min}} \quad T,$$

where

$V$  = velocity added by the venting in m/sec

$\tau$  = duration of the venting in minutes

$T$  = interval between ventings in minutes.

The duration of venting for the nominal case is 3.0 minutes; the velocity, 1.5 m/sec; and the vent interval, 80 minutes. According to this model the average acceleration is the same for all intervals and is  $.0081 \text{ m/sec}^2 = .00083 \text{ g}$ .

Regardless of the frequency or duration of venting, an ullage firing must occur immediately before each venting to settle the propellants in the tank. The ullage firing is assumed to have the following characteristics: duration, 30 seconds; velocity addition, .34 m/sec; average acceleration,  $.011 \text{ m/sec}^2 = .0011 \text{ g}$ .

Figures 13 through 15 show the position error

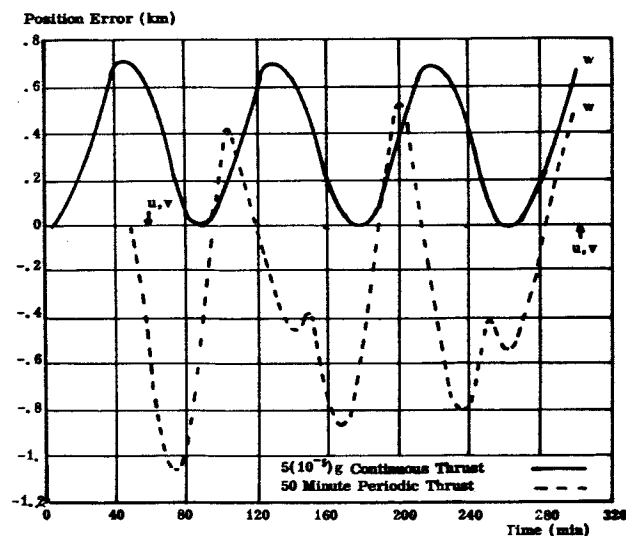


FIGURE 13. COMPARISON OF CONTINUOUS AND PERIODIC THRUSTS, w. EFFECT OF  $u, v, w$  THRUST, 200 km CIRCULAR ORBIT

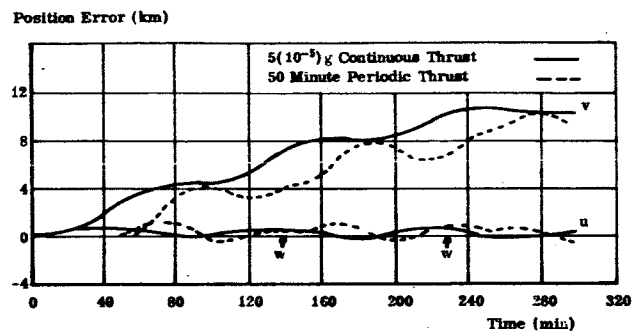


FIGURE 14. COMPARISON OF CONTINUOUS AND PERIODIC THRUST  $u$  EFFECT OF  $u, v, w$  THRUST, 200 km CIRCULAR ORBIT

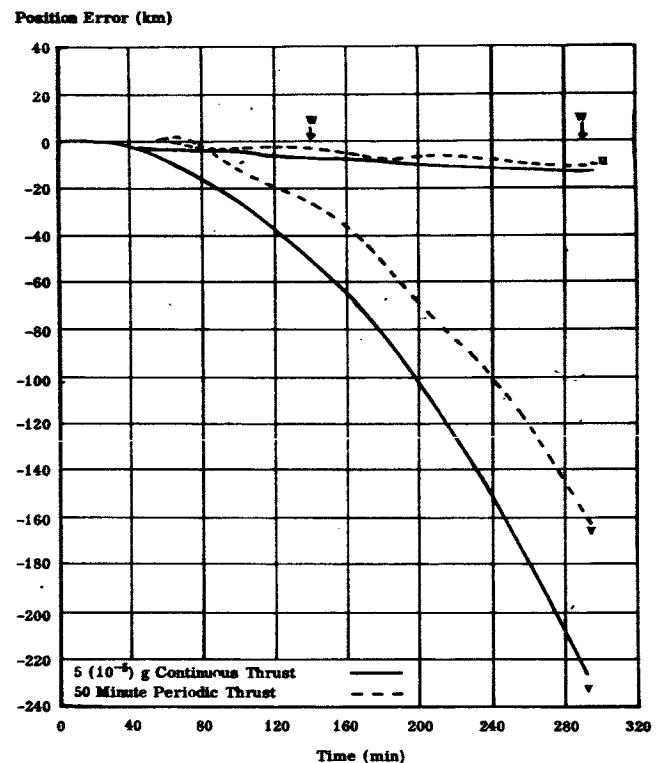


FIGURE 15. COMPARISON OF CONTINUOUS AND PERIODIC THRUST,  $v$  EFFECT OF  $u, v, w$  THRUST, 200 km CIRCULAR ORBIT

caused by intermittent thrust (50 minute periodic) compared with those caused by continuous thrust. The intermittent thrust causes more pronounced short period effects than the continuous thrust. The effects of intermittent venting can be approximated by considering the sum of the effects of a series of velocity impulses. The response to each impulse can be calculated with the velocity components as initial condi-

tions. Figures 16 and 17 show two typical examples of the effects of varying the vent period. The short period effects are quite sensitive to the frequency of venting.

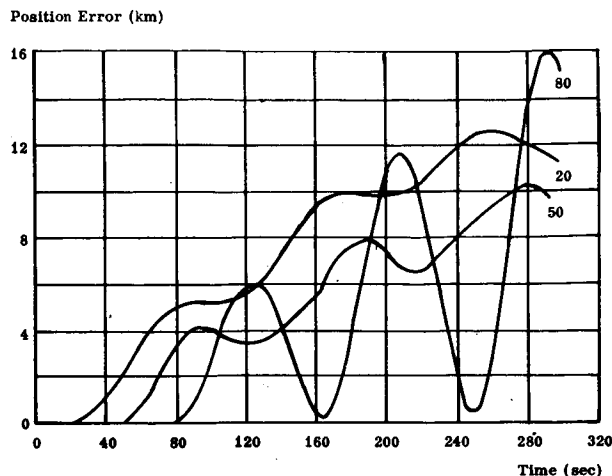


FIGURE 16. EFFECT OF VARIATION IN VENT INTERVAL, u EFFECT OF  $v$  THRUST, 20, 50, 80 MINUTE PERIODIC

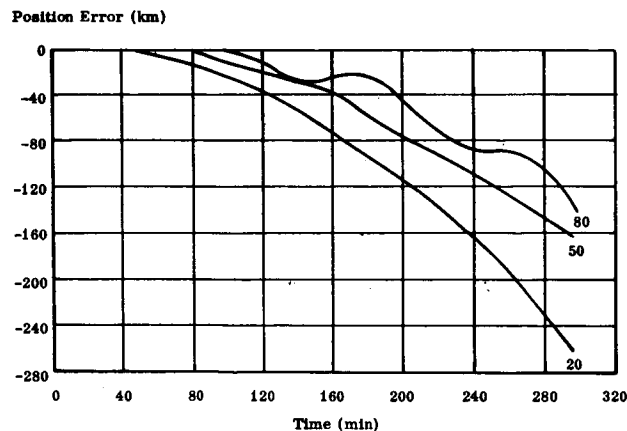


FIGURE 17. EFFECT OF VARIATION IN VENT INTERVAL, v EFFECT OF  $v$  THRUST, 20, 50, 80 MINUTE PERIODIC

B. Tracking Effects. The effects of intermittent venting on the prediction of earth orbits from tracking data were analyzed with the same procedure and tracking model used for continuous thrust. Since it is the largest, the downrange error due to a downrange thrust is shown for illustration. The error is plotted in Figure 18 with the number of tracking passes as a parameter. Just as for continuous thrust, the prediction error increases as more radar passes are used.

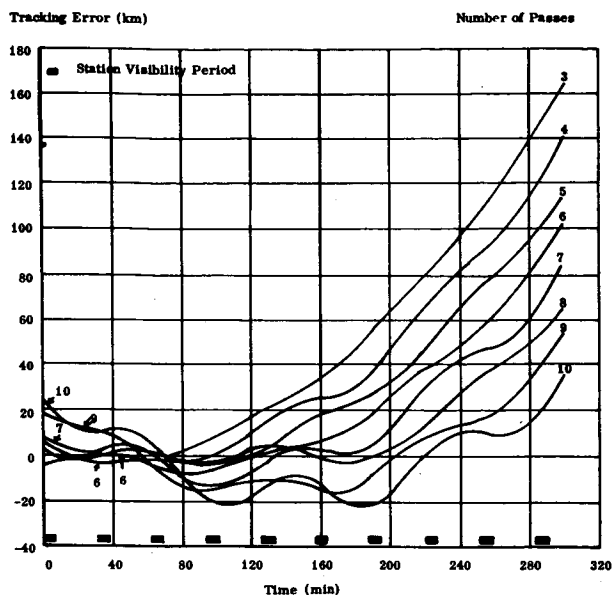


FIGURE 18. EFFECT OF VARIATION IN NUMBER OF TRACKING PASSES, v EFFECT OF  $v$  THRUST, 50 MINUTE PERIODIC

It is best, therefore, to use only the latest pass as long as the random errors associated with it are small enough (Fig. 19) and as long as the thrust is not solved for in the orbit determination process.

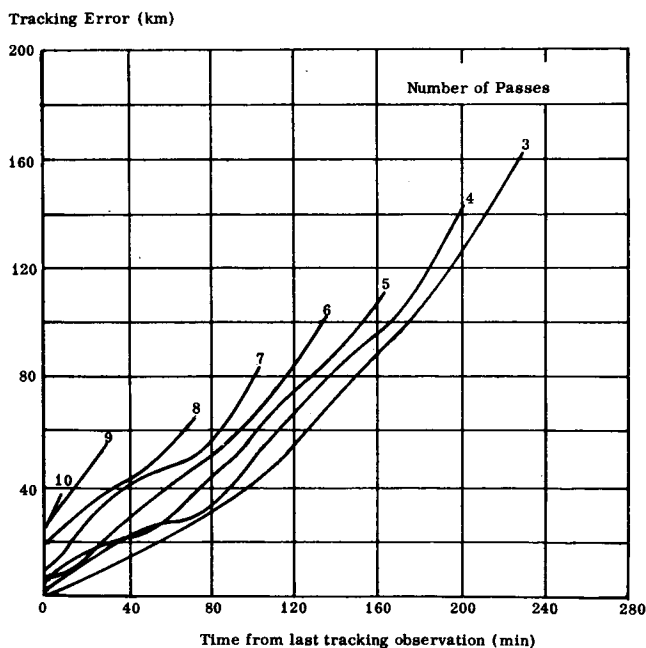


FIGURE 19. TRACKING PREDICTION ERROR FROM  $v$  THRUST, 50 MINUTE PERIODIC

#### REFERENCES

1. Cooley, J. L., "The Influence of Venting on Apollo Earth Parking Orbits," GSFC Report X-513-64-359, November 24, 1964.

## VIII. PUBLICATIONS AND PRESENTATIONS

## PUBLICATIONS AND PRESENTATIONS

### A. PUBLICATIONS

#### TECHNICAL MEMORANDUM X-53034

October 13, 1964

#### THE EFFECT OF LOCATION AND SIZE OF PROPELLANT TANKS ON THE STABILITY OF SPACE VEHICLES CONSIDERING SLOSHING IN TWO OR THREE TANKS

By

Alberta C. King

George C. Marshall Space Flight Center  
Huntsville, Alabama

#### ABSTRACT

The effect of propellant oscillations on the response and stability of a space vehicle is of major importance. The main contributing factors are (1) tank location, (2) tank geometry, which determines natural frequency and sloshing mass, and (3) propellant damping (due to wall friction and antislosh devices). This report contains a study of the effect of these contributing factors on the stability of a rigid space vehicle with an ideal control system. The results are given as root locus plots with tank location as parameter.

#### TECHNICAL MEMORANDUM X-53053

June 2, 1964

#### BOOSTER PARAMETRIC DESIGN METHOD FOR PERFORMANCE AND TRAJECTORY ANALYSIS

#### PART II: PROPULSION

By

V. Verderaine

George C. Marshall Space Flight Center  
Huntsville, Alabama

#### ABSTRACT

Approximate equations for large, liquid chemical rocket engine mass and space envelope are presented

in parametric form. Well known propulsion performance equations are given with modifications to admit programming of mixture ratio shifts and throttling of propellant mass flow rate. Parameters used in mass and space envelope equations were nominal input design parameters in common with the propulsion performance equations such that their interdependence could be manifested in a vehicle trajectory and performance optimization study. Though results are based on current type engines, it is expected that coefficients and exponents used may be readily modified to define mass and size of moderately advanced rocket engines.

#### TECHNICAL MEMORANDUM X-53054

June 2, 1964

#### STABILITY ANALYSIS OF SATURN SA-6 WITH RATE GYRO FOR S-IV CONTROL DAMPING

By

Philip J. Hays

George C. Marshall Space Flight Center  
Huntsville, Alabama

#### ABSTRACT

A control feedback stability analysis was performed on Saturn SA-6 during S-I and S-IV stage powered flight. Predicted flight damping values were used in the sloshing stability analysis for both stages of flight. Stability was achieved for both stages of flight although marginal stability was observed in the S-IV LOX tank during booster flight. The marginal stability is due to the interaction between the sloshing and vehicle structure.

Theoretical and experimental bending frequencies were compared during booster flight using the experimentally obtained structural damping. Theoretical bending data were used for the S-IV flight with one percent structural damping assumed.

Bending mode stability was achieved by two methods: phase stabilization and gain stabilization. Gain stabilization was employed for all elastic modes in the roll and  $\alpha$ -channels. The  $\phi$ -channel phase stabilized the first lateral bending mode and gain sta-

bilized the higher modes. The elastic modes in the  $\phi$ -channel were gain stabilized for the S-IV flight.

#### TECHNICAL MEMORANDUM X-53055

June 3, 1964

#### STUDY OF MANNED INTERPLANETARY FLY-BY MISSIONS TO MARS AND VENUS

By

Rodney Wood, Bobby Noblitt, Archie C. Young, and  
Horst F. Thomae

George C. Marshall Space Flight Center  
Huntsville, Alabama

#### ABSTRACT

This report contains the results of an "in depth" mission analysis study of manned interplanetary fly-by missions to Mars and Venus during the 1970's using Apollo technology and hardware wherever possible. The usual conic and impulsive velocity techniques were used in this study; however, a precision integrated fly-by trajectory to Mars during the 1975 opposition is included.

#### TECHNICAL MEMORANDUM X-53056

June 4, 1964

#### THE AERODYNAMIC CHARACTERISTICS OF SATURN I/APOLLO VEHICLES (SA-6 AND SA-7)

By

Billy W. Nunley

George C. Marshall Space Flight Center  
Huntsville, Alabama

#### ABSTRACT

This report presents the final aerodynamic characteristics of the Saturn/Apollo vehicles. These data are based on wind tunnel tests of scale models. Normal force coefficient gradient, normal force coefficient, center of pressure, total power-on and power-off drag coefficient, power-on and power-off base drag coefficient, and forebody drag coefficient are presented

for the Mach number range from 0 to 10. Local force coefficient distributions are presented for various Mach numbers ranging from 0.20 to 4.96. These data are for zero angle of attack with the exception of the gradients, which are slopes at zero angle of attack, and the normal force coefficients, which are a function of angle of attack.

#### TECHNICAL MEMORANDUM X-53059

June 8, 1964

#### SPACE VEHICLE GUIDANCE - A BOUNDARY VALUE FORMULATION

By

Robert W. Hunt and Robert Silber

George C. Marshall Space Flight Center  
Huntsville, Alabama

#### ABSTRACT

A mathematical formulation of the problem of guiding one stage of a space vehicle is given as a boundary value problem in differential equations. One approach to the solution of this problem is to generate the Taylor's series expansion (in several variables) about a known solution. The theoretical nature of such solutions is discussed, and a method for numerically computing them is presented. This method entails the numerical integration of an associated system of differential equations, and can be used to obtain the solution to any desired degree of accuracy for points in a region to be defined. An extension of the method to the problem of guiding several stages of a space vehicle is also given, employing fundamental composite function theory.

#### TECHNICAL MEMORANDUM X-53060

July 22, 1964

#### SA-5 FLIGHT TEST DATA REPORT

By

H. J. Weichel

George C. Marshall Space Flight Center  
Huntsville, Alabama

## ABSTRACT

This report is a presentation of certain flight mechanical data obtained from the SA-5 flight test. Digitized data are presented in graphical form. Also included are oscillograms of the flight measurements.

The intention of the report is to present the digitized data in an easy-to-read form for use by design and technical personnel. This report is to supplement the Saturn SA-5 Flight Evaluation Report and many other reports published by the various laboratories.

### TECHNICAL MEMORANDUM X-53062

June 10, 1964

#### AN AUTOMATED MODEL FOR PREDICTING AEROSPACE DENSITY BETWEEN 200 AND 60,000 KILOMETERS ABOVE THE SURFACE OF THE EARTH

By

Robert E. Smith

George C. Marshall Space Flight Center  
Huntsville, Alabama

## ABSTRACT

This paper describes the derivation of a computer routine for predicting the vertical distribution of aerospace density in the terrestrial space environment above the surface of the earth. Solar activity, geomagnetic storm, diurnal heating, latitude, and the earth's orbital eccentricity effects are included in this model. Densities can be predicted for any time through December 1992.

### TECHNICAL MEMORANDUM X-53064

June 16, 1964

#### LATEST WIND ESTIMATED FROM 80 KM TO 200 KM ALTITUDE REGION AT MID-LATITUDE

By

W. T. Roberts

George C. Marshall Space Flight Center  
Huntsville, Alabama

## ABSTRACT

The data from a total of forty rocket launches fired specifically to determine wind characteristics by the release of chemiluminescent trails have been compiled and studied in an attempt to clarify seasonal and diurnal trends in upper atmospheric winds above 80 kilometers. From a series of graphs taken at 10-kilometer intervals a general picture of the change in wind vectors with height is determined.

Below 120 kilometers there appears to be extreme variation in speed and direction with very little correlation with season or time of day discernible. Above 120 kilometers, however, the winds appear to orient more with season, and above 150 kilometers, some diurnal variations become apparent.

More experiments of this type, particularly in the summer and winter months, are needed to establish confidence in the seasonal and diurnal trends.

### TECHNICAL MEMORANDUM X-53071

June 24, 1964

#### SA-7 PRELIMINARY PREDICTED STANDARD TRAJECTORY

By

Jerry D. Weiler

George C. Marshall Space Flight Center  
Huntsville, Alabama

## ABSTRACT

This report presents the preliminary predicted standard trajectory for Saturn I vehicle SA-7 to be flown over the Atlantic Missile Range. The nominal impact area of the S-I booster, the recoverable camera capsules, and launch escape system are also presented.

A brief discussion of the trajectory shaping and a description of the vehicle configuration are presented.

The nominal trajectory will insert the S-IV stage and payload into a near-circular orbit with a perigee and apogee of 185 km and 217-km altitude, respectively. The nominal lifetime of the orbit is 3.0 days.

The final predicted standard trajectory and dis-

persion analysis will be published approximately 30 days prior to launch date.

#### TECHNICAL MEMORANDUM X-53072

June 24, 1964

#### MULTIPLE BEAM VIBRATION ANALYSIS OF SATURN I AND IB VEHICLES

By

Larry Kiefling

George C. Marshall Space Flight Center  
Huntsville, Alabama

#### ABSTRACT

A method is described for finding the natural modes and frequencies of a Saturn I or IB vehicle. The vehicle is idealized as a system of nine connected beams, one beam consisting of the booster center tank and upper stages, and each of the other eight beams consisting of a booster outer tank. A vibration analysis is first made on each individual beam by a modified Stodola method. The equations for the connected systems are then derived using Lagrange's equations. A method for reducing a three-dimensional model to three two-dimensional models and equations for finding the third dimension component for the two-dimensional problem solved are given.

A sample comparison is made with dynamic test data.

#### TECHNICAL MEMORANDUM X-53077

July 6, 1964

#### A METHOD FOR THE DETERMINATION OF CONTROL LAW EFFECT ON VEHICLE BENDING MOMENT

By

Don Townsend

George C. Marshall Space Flight Center  
Huntsville, Alabama

#### ABSTRACT

The determination of bending moments which occur as the vehicle encounters predicted in-flight wind conditions is an important phase of vehicle design studies. Presently this information is required to determine if the moments induced by these winds are within the structural design limits of the vehicle. One means by which the vehicle's flight through these winds may be assured is the optimization of the control system to reduce bending moments. This analysis is conducted to develop program for computing the coefficients necessary to accomplish this optimization.

The relative merits of two different approaches for calculation of vehicle bending moments are presented. The two approaches considered are the direct summation of moments acting on the vehicle, and the mode displacement method. These are used in conjunction with existing programs for the elastic response of a vehicle to winds.

The mode displacement method was first used for determination of bending moments. It required a large number of bending modes to obtain accurate results. The summation of moments was then investigated and found to give adequate results which were in a readily usable form for control law studies.

The results indicate that a decrease in control frequency results in a decrease in bending moment. An increase of the ratio  $b_0/a_0$  from that of drift minimum control, holding the control frequency constant, results in a decrease in bending moment.

#### TECHNICAL MEMORANDUM X-53079

October 7, 1964

#### AN EXPLICIT SOLUTION FOR LARGE SYSTEMS OF LINEAR DIFFERENTIAL EQUATIONS

By

Robert E. Cummings and Lyle R. Dickey

George C. Marshall Space Flight Center  
Huntsville, Alabama

#### ABSTRACT

A practical method of obtaining an explicit solution to an inhomogeneous system of linear differ-



tial equations with constant coefficients is described. The method is readily adaptable to solving large systems on high speed digital computers and is particularly efficient when a large number of solutions are desired for the same set of equations with different initial conditions and forcing functions. The problem that often arises when large eigenvalues are present is overcome by a unique feature. The solution is obtained for an exceptionally small integration step, and a process is described whereby the step can be doubled. Successful applications of this process provide a solution over an interval which increases exponentially in size with each step; whereas, the work involved increases only in a linear fashion. This is particularly advantageous since standard techniques require that special provisions must be made for any system which has exceptionally large eigenvalues.

#### TECHNICAL MEMORANDUM X-53081

October 12, 1964

#### CALCULATION OF TRANSONIC NOZZLE FLOW

By

Joseph L. Sims

George C. Marshall Space Flight Center  
Huntsville, Alabama

#### ABSTRACT

An approximate solution of the transonic throat flow in a DeLaval nozzle is found by expanding the potential function in a power series about the critical line. Five terms were used in the present series expansion, and the complete potential flow equation of motion was used.

Solutions of the present set of equations are functions of two independent parameters: the radius of curvature of the nozzle wall and the ratio of specific heats of the fluid medium. The solution of the resultant equations is complex enough to make an electronic computer program desirable. For this reason, basic results of a series of solutions over a wide range of the two independent parameters are given in tabular form. From these tabulated results, any quantities of interest in the flow field may be rapidly computed.

TECHNICAL MEMORANDUM X-53088

July 16, 1964

#### THE REDUCED THREE-BODY PROBLEM: A GENERALIZATION OF THE CLASSICAL RESTRICTED THREE-BODY PROBLEM

By

Gary P. Herring

George C. Marshall Space Flight Center  
Huntsville, Alabama

#### ABSTRACT

The restricted three-body problem is generalized to include the motion of the earth and moon on coplanar Keplerian ellipses of eccentricity  $\epsilon$ , ( $0 \leq \epsilon < 1$ ). The equations of motion are written in a space-fixed coordinate system. After accomplishing a normalization of the equations in this system, the normalized equations are transformed to a rotating coordinate system. Transformations of the results to several other systems of interest are given.

#### TECHNICAL MEMORANDUM X-53089

July 27, 1964

#### STUDY OF SPHERE MOTIONS AND BALLOON WIND SENSORS<sup>1</sup>

By

Paul B. MacCready, Jr.<sup>2</sup>  
and Henry R. Jex<sup>3</sup>

<sup>1</sup>This study was performed by Meteorology Research, Inc., Altadena, California, as part of NASA Contract NAS8-5294 with the Aero-Astrodynamics Laboratory, Aero-Astrophysics Office, Marshall Space Flight Center, Huntsville, Alabama. Final Report MR164 FR-147, April 1964.

<sup>2</sup>Meteorology Research, Inc.

<sup>3</sup>Systems Technology, Inc., Inglewood, California, as consultant to Meteorology Research, Inc.

## ABSTRACT

July 24, 1964

### COMPARISON OF MISSION PROFILE MODES FOR ACHIEVING TEST OBJECTIVES ON SATURN V REENTRY QUALIFICATION FLIGHTS

By

John B. Winch, Roy C. Lester and Frank M. Graham

George C. Marshall Space Flight Center  
Huntsville, Alabama

## ABSTRACT

Balloons ascending in still air typically exhibit lateral movements which introduce errors when the balloons are tracked as sensors of wind motion. This report examines some of the fundamentals of the fluid flows and associated motions and net drag coefficients of free-moving spheres. The flows and motions depend directly on Reynolds number ( $R_d$ ) which determines the flow regime; depend on the relative mass of the sphere to the fluid it displaces ( $RM$ ) because, for a given  $R_d$ , the lower the  $RM$  values the greater the lateral motions and thus the larger the total wake size and drag; and also depend on the sphere rotational inertial and minute details of surface roughness, sphericity, and random orientation. Because of these complex interactions, no unique drag coefficient ( $C_D$ ) vs  $R_d$  curve can be found for free-moving spheres. The separate effects of the main factors are described as they might affect an idealized  $C_D$  vs  $R_d$  curve for a perfectly smooth free-moving sphere of infinite  $RM$ .

Observations were made of the mean vertical and velocity and the magnitude of the lateral motions as spherical balls and balloons ascended and descended through both water and air, covering wide ranges of  $R_d$  and  $RM$ . The results are in general agreement with the physical concepts developed, and the water experiments give results consistent with the tests in air. In the subcritical  $R_d$  regime, where the wake separation is laminar, the motion tends to be a fairly regular zigzag, or spiral, of wave length on the order of 12 times the diameter. The magnitude of the lateral motion is roughly related to the factor  $(1 + 2RM)^{-1}$ . In the supercritical  $R_d$  regime, where the wake separation is turbulent and the wake is smaller, the motion tends to be an irregular meandering spiral. In the critical range of  $R_d$  the shift from subcritical to supercritical (and vice versa) flows and drags is rather abrupt; if sufficiently abrupt, there is a hysteresis effect with increasing and decreasing Reynolds number, and two stable velocities exist.

Tests were also made in air with spheres to which skirts, vanes, and/or drag chutes were affixed in an effort to stabilize the motion.

It is concluded that balloon motion can be smooth enough for most needs for high resolution atmospheric wind data if spherical or semi-spherical balloons are used operating always in the subcritical range, or certain balloons are used with roughness elements or other attachments operating at even higher Reynolds number.

The more optimum mission profile modes for achieving the launch vehicle and the spacecraft test objectives on Saturn V missions prior to manned Apollo flights have been critically investigated and analyzed. The vast number of possible profiles have been reduced to five principal methods.

Method one, which is essentially a lob shot, is unacceptable since it would require trajectory reshaping and extensive payload off-loading.

The method two profile permits incorporation of all available propulsion systems and uses a circular parking orbit as will the operational vehicle; however, it is unacceptable due to unfavorable maneuvers required to achieve an adequate coast prior to satisfying reentry conditions.

Methods three, four, and five are acceptable profiles, but method four is not recommended primarily due to unmanned operation of the midcourse guidance system, long flight time, and two propulsion periods required of the service module.

In this report, methods three and five are presented in detail. Method five differs principally from method three and the operational flight by replacing the circular parking orbit with an elliptical parking orbit and not requiring any burns of the service module's propulsion system.

Of all the methods investigated, the method three profile offers the most satisfactory solution to the reentry problem.

TECHNICAL MEMORANDUM X-53098

TECHNICAL MEMORANDUM X-53097

July 16, 1964

THREE-DIMENSIONAL MULTIPLE BEAM ANALYSIS  
OF A SATURN I VEHICLE

By

James L. Milner

George C. Marshall Space Flight Center  
Huntsville, Alabama

ABSTRACT

A normal mode vibration analysis was made of a Saturn I vehicle using a newly developed lumped parameter multiple beam representation incorporating coupling of the center tank motion in pitch, yaw, and roll with the motion of the outer tanks. The analysis demonstrates the uncoupling of motions in pitch, yaw, and roll for a vehicle having a symmetrical distribution of mass and stiffness. A few cases of nonsymmetry were examined and numerical results were obtained which show the effect of vehicle nonsymmetry on the natural frequencies of the vehicle.

TECHNICAL MEMORANDUM X-53100

July 28, 1964

SPACE VEHICLE GUIDANCE - A BOUNDARY VALUE  
FORMULATION

PART II:

BOUNDARY CONDITIONS WITH PARAMETERS

By

Robert Silber

George C. Marshall Space Flight Center  
Huntsville, Alabama

ABSTRACT

This report contains an extension of the results presented in NASA Technical Memorandum X-53059, "Space Vehicle Guidance - A Boundary Value Formulation," by Robert W. Hunt and Robert Silber, June 8, 1964. In that memorandum, the control laws for space vehicle guidance were formulated as a set of functions implicitly defined by a set of boundary conditions. In this report the domain of the control laws is augmented

to contain mission parameters. In this way, the control laws are defined for a family of missions rather than for a single mission.

TECHNICAL MEMORANDUM X-53104

August 10, 1964

AN AUTOMATED MODEL FOR PREDICTING THE  
KINETIC TEMPERATURE OF THE AEROSPACE  
ENVIRONMENT FROM 100 TO 60,000 KILOME-  
TERS ABOVE THE SURFACE OF THE EARTH

By

Robert E. Smith

George C. Marshall Space Flight Center  
Huntsville, Alabama

ABSTRACT

This paper describes the derivation of a series of equations capable of predicting the kinetic temperature of the aerospace environment from 100 to 60,000 kilometers above the surface of the earth. The equations, which are programmed on a GE 225 computer, can be used to predict temperature-height profiles for any time through December 1992.

TECHNICAL MEMORANDUM X-53108

August 17, 1964

CHARACTERISTIC FEATURES OF SOME PERIODIC  
ORBITS IN THE RESTRICTED THREE-BODY  
PROBLEM

By

Wilton E. Causey

George C. Marshall Space Flight Center  
Huntsville, Alabama

ABSTRACT

Earth-moon orbits are presented which, when referred to a rotating coordinate system, return periodically to their original set of state variables. Information concerning the period of the orbit, time spent

in the region between earth and moon, close approach distance to the moon, and closest approach distance to the earth is given for various families of periodic orbits. These orbits have periods of 1 to 4 months, and they have at least one perpendicular crossing of the earth-moon line on the back side of the moon.

TECHNICAL MEMORANDUM X-53109

August 19, 1964

NUMERICAL PROCEDURES FOR STABILITY STUDIES

By

Robert S. Ryan

George C. Marshall Space Flight Center  
Huntsville, Alabama

ABSTRACT

This report presents the numerical procedures used by the Aero-Astroynamics Laboratory in performing stability analysis for large space vehicles with a more complex control system, and wherein a large number of modes of oscillation must be considered. The modes of oscillation included in the system are (1) bending, (2) translation, (3) pitching, (4) sloshing, and (5) swivel engine. Equations describing the characteristics of the control sensors are included for rate gyros, accelerometers, and angle of attack meter. Two numerical methods for solving the system for its eigenvalues are presented: the characteristic equation and the matrix iteration approach. Finally, a plan for using the procedures in evaluating a vehicle for stability, filter design, and propellant damping is also developed.

TECHNICAL MEMORANDUM X-53112

August 20, 1964

MONTE CARLO SOLUTIONS OF KNUDSEN AND NEAR-KNUDSEN FLOW THROUGH INFINITELY WIDE, PARALLEL AND SKEWED, FLAT PLATES

By

James O. Ballance

George C. Marshall Space Flight Center

Huntsville, Alabama

ABSTRACT

This study presents the results of an investigation of Knudsen flow and near-Knudsen flow through infinitely wide, parallel and skewed, flat plates. Monte Carlo computer techniques were used. Two simple models for considering molecule-molecule interactions, as well as molecule-surface interactions, were used to examine the near-Knudsen flow regime. Transmission probabilities for various length-to-entrance ratios and for various angles of skewness are presented. The influence of mean free path and length-to-entrance ratios on Knudsen flow determination is discussed.

TECHNICAL MEMORANDUM X-53113

August 20, 1964

CALIBRATION TESTS OF THE MSFC 14 x 14-INCH TRISONIC WIND TUNNEL

By

Erwin Simon

George C. Marshall Space Flight Center  
Huntsville, Alabama

ABSTRACT

This report presents calibration data obtained from the MSFC 14 x 14-inch trisonic wind tunnel for the Mach range of .2 through 5.0. Pressure distribution data for the 20° cone-cylinder are presented for the Mach range of .90 through 5.00. Static pipe Mach number surveys are presented for the entire calibrated Mach range of .2 through 5.0. Flow inclinations are presented for the Mach range of .2 through 5.00.

TECHNICAL MEMORANDUM X-53115

August 24, 1964

DETAILS OF WIND STRUCTURE FROM HIGH RESOLUTION BALLOON SOUNDINGS

By

August 27, 1964

## ABSTRACT

The tracking of spherical superpressure balloons by an FPS-16 radar has generated accurate data concerning the winds in the upper troposphere and lower stratosphere. Above about 11 km the winds are obtained to high resolution, while below this altitude spurious balloon motions mask the fine structure of the wind although the gross features of the wind are still accurately displayed. At Cape Kennedy 87 soundings are investigated, with most attention being focused on 2 series of 9 and 18 soundings spaced approximately 45 minutes apart.

All the soundings, covering various meteorological situations, show a large amount of microstructure in the wind field above the tropopause, with shears of 2 mps/100 m being observed on all soundings, shears exceeding 5 mps/100 m being observed occasionally, and with the speed (and direction) variations tending to occur with vertical wave lengths of 0.5 to 2 km. The shears occur at an altitude range and are of a magnitude and wave length where they can significantly affect vertically rising rocket launch vehicles.

The sequence soundings show that the large measured individual speed variations tend to persist for a matter of hours, sometimes exceeding 6 hours. Thus, the variations are not turbulence but are instead manifestations of an intricate vertical layering of the air at these levels. The persistence is such that a forecast of the major shears, based on a one- to three-hour extrapolation of a sounding, appears moderately reliable.

Three possible physical models for mesoscale circulation to explain the observed shears are selected for special consideration: (1) stacked layers of alternating inertial oscillations, (2) phase shifts with height of standing gravity waves (lee waves) in successive atmospheric layers, and (3) paired longitudinal vortices (helicanes). Each model is supported by some segments of the data and contradicted by others. It is concluded that more measurements with FPS-16 radar and other tools are needed before a decision can be reached as to the exact physical cause of the observed shearing phenomena.

TECHNICAL MEMORANDUM X-53116

\* Meteorological Research Corporation

## AN EMPIRICAL ANALYSIS OF DAILY PEAK SURFACE WIND AT CAPE KENNEDY, FLORIDA, FOR PROJECT APOLLO

By

J. David Lifsey

George C. Marshall Space Flight Center  
Huntsville, Alabama

## ABSTRACT

A fourteen-year serially complete data sample of daily peak surface wind at Cape Kennedy, Florida, was obtained from historical weather records. After adjusting speed values to a reference height of 10 meters above the ground and removing "hurricane-associated" peak winds, monthly, seasonal and annual values were computed for the following: selected percentiles and statistics; bivariate empirical percentage frequency distributions of (1) speed versus direction, (2) speed versus hour of occurrence, and (3) hour of occurrence versus direction; and exposure period probabilities (empirical percentage frequencies) of equaling or exceeding peak wind speeds of various magnitudes during consecutive-day time intervals. Use of the results is aided by specific examples and a further development of theoretical frequency distributions is proposed. This study is unique in terms of the data sample and the amount of information presented. The results can be used in many areas of research and operation.

TECHNICAL MEMORANDUM X-53118

August 28, 1964

## DISTRIBUTION OF SURFACE METEOROLOGICAL DATA FOR CAPE KENNEDY, FLORIDA

By

J. W. Smith

George C. Marshall Space Flight Center  
Huntsville, Alabama

## ABSTRACT

Thermodynamic surface data for Cape Kennedy, Florida, have been analyzed, and are presented graphically in this study. The medians and extremes, plus the cumulative percentage frequency levels of 0.135, 2.28, 15.9, 84.1, 97.72, and 99.685 percent, are shown for temperature, pressure, density, vapor pressure, mixing ratio, enthalpy, refractivity, and relative humidity. These data are presented for hourly, monthly and annual periods, and are discussed briefly.

**TECHNICAL MEMORANDUM X-53119**

August 28, 1964

**PRELIMINARY CAPE KENNEDY ATMOSPHERIC  
DATA FOR NUCLEAR OR TOXIC PARTICLES  
DISPERSIVE STUDIES  
(August 1962 - July 1963)**

By

Charles K. Hill

George C. Marshall Space Flight Center  
Huntsville, Alabama

**ABSTRACT**

This presentation of one year of climatic data (August 1962 - July 1963) for the lowest 1524 meters (5000 feet) at Cape Kennedy, Florida, is the most complete to date. Some monthly statistical values (daytime and nighttime) of the following parameters have been plotted in Figures 1 - 56: wind roses, scalar wind speeds, dewpoint, ambient temperature, density and pressure. Rawinsonde observations were used to obtain the measurements for each 152-meter (500-foot) level from 152 to 1524 meters (500 to 5000 feet). Surface measurements were recorded from local ground instrumentation. Not all levels of wind rose and pressure data were used, but these and all data appearing herein plus additional statistics on vertical wind shears and absolute and relative humidity may be obtained in tabulated form upon request to the Aero-Astrophysics Office of Marshall Space Flight Center.

**TECHNICAL MEMORANDUM X-53120**

August 13, 1964

**FINAL PREDICTED TRAJECTORY AND DISPERSION  
STUDY FOR SATURN I VEHICLE SA-7**

By

Jerry D. Weiler and Onice M. Hardage, Jr.

George C. Marshall Space Flight Center  
Huntsville, Alabama

**ABSTRACT**

This report presents the final predicted standard trajectory and dispersion analysis for Saturn I vehicle SA-7 to be flown over the Atlantic Missile Range. The nominal impact area of the S-I booster and the recoverable camera capsules is presented, along with a discussion of the trajectory shaping and a description of the vehicle configuration.

The nominal trajectory will insert the S-IV stage and payload into a near-circular orbit with a perigee and apogee of 182 km and 229-km altitude, respectively. The nominal lifetime of the orbit is 3.2 days.

**TECHNICAL MEMORANDUM X-53123**

August 21, 1964

**SATURN SA-6 POSTFLIGHT TRAJECTORY (U)**

By

Gerald R. Riddle and Robert H. Benson

George C. Marshall Space Flight Center  
Huntsville, Alabama

**ABSTRACT**

This report presents the postflight trajectory for the Saturn SA-6 test flight. Trajectory dependent parameters are given in earth-fixed, space-fixed, and geographic coordinate systems. A complete time history of the powered flight trajectory is presented at 1.0 sec intervals from first motion through insertion. Tables of insertion conditions and various orbital parameters are included in a discussion of the orbital portion of flight. A comparison between nominal and actual trajectory dependent parameters is also presented.

**TECHNICAL MEMORANDUM X-53124**

September 3, 1964

# LUNAR ENVIRONMENT: AN INTERPRETATION OF THE SURFACE OF THE MOON AND ITS ATMOSPHERE

By

John R. Rogers\* and Otha H. Vaughan, Jr.

George C. Marshall Space Flight Center  
Huntsville, Alabama

## ABSTRACT

This MSFC report on the lunar environment represents the first of a series of reports entitled Space Environment Criteria Guidelines. Subsequent reports will discuss matters pertinent to other space environments including (1) the earth's atmosphere above 100 km; (2) the atmosphere and surface of Mars; (3) the atmosphere of Venus; (4) the radiation environment of space; (5) the meteoroid environment of space; and (6) the magnetic and gravitational fields of the earth, moon, and the planets. The present study and these future studies are intended for use by MSFC in future lunar and space programs. These studies as presently envisaged will complement work being done on space environments at other government and contractor facilities.

Under the heading of lunar topographic features comparative analyses have been made of several geological classifications of lunar features based on inferred age relationships. Also, a discussion of the major landforms, Continents and Maria, is included. The genetic classification, based on inferred geological origin of the various lunar landforms, attempts to compare by analogy certain lunar features with their interpreted terrestrial counterparts.

A deliberate attempt has been made to be objective and to draw from the entire spectrum of lunar geological knowledge some specific conclusions regarding the somewhat controversial origins of lunar features. A practical approach has been taken in identifying certain features as predominantly impact in origin versus volcanic since it is realized that many decisions have to be made now regarding future lunar surface vehicles and missions. An independent judgment has been made concerning the genetic significance of certain lunar features and in such cases the authors of this report assume full responsibility for their tentative conclusions.

\* Engineering Specialist, Brown Engineering Company.

Since design criteria for a stationary vehicle will not suffice for future missions involving mobility, this report provides design criteria parameters for both mobile and stationary vehicles. A need exists for reliable small scale data to obtain lunar surface criteria based on "real-case" conditions instead of "worst-case" assumptions.

## TECHNICAL MEMORANDUM X-53128

August 25, 1964

## AERODYNAMIC EVALUATION OF SA-6 FLIGHT

By

Fernando S. Garcia

George C. Marshall Space Flight Center  
Huntsville, Alabama

## ABSTRACT

This report presents results from the aerodynamic evaluation of SA-6, the second flight test of the Saturn I Block II series. Evaluation of telemetered data included stability analyses, fin loading calculations and environmental pressure analyses. Environmental pressure data from SA-5 are also shown for comparison.

The flight-determined center of pressure and normal force for the vehicle agreed well with predicted, and deviations fell within the telemetry error margins. Localized pressure loadings obtained by measurements located on Fin II were in poor agreement with theory.

Heat shield pressures measured on SA-6 for the most part agreed well with SA-5 results. Flight results were higher than wind tunnel data from hot jet tests, especially at transonic Mach numbers.

Inside the tail compartments, a uniform pressure distribution (which was generally near the predicted level) was observed throughout. This is in contrast to what was measured on SA-5 where a large variation within the same compartment was noted.

## TECHNICAL MEMORANDUM X-53130

September 17, 1964

**A SYSTEM OF EQUATIONS FOR OPTIMIZED  
POWERED FLIGHT TRAJECTORIES**

By

Gary McDaniel

George C. Marshall Space Flight Center  
Huntsville, Alabama

**ABSTRACT**

The equations of motion for a vehicle with thrust, lift, and drag forces, and a Newtonian gravitational force are derived in an earth-fixed polar coordinate system. This system of equations forms the differential equations of constraint in the calculus of variations formulation of minimizing flight time between two sets of boundary conditions with inequality constraints imposed on the magnitude of the angle of attack or the product of the dynamic pressure and the magnitude of the angle of attack. The necessary conditions for optimality are given exclusive of derivation. Also, a computational scheme is given suitable for a digital computer program.

**TECHNICAL MEMORANDUM X-53132**

September 3, 1964

**STABILITY CONDITIONS OF THE LOWER ATMOS-  
PHERE AND THEIR IMPLICATIONS REGARDING  
DIFFUSION AT CAPE KENNEDY, FLORIDA**

By

James R. Scoggins and Margaret B. Alexander

George C. Marshall Space Flight Center  
Huntsville, Alabama

**ABSTRACT**

This report describes the atmospheric stability conditions at Air Force Station 700 on Cape Kennedy. The data are presented by time of day, month, season, and annually. Results are categorized and presented graphically and tabularly to indicate qualitatively the diffusion conditions and best months and hours for handling toxic fuels or launching vehicles that use fuels.

**TECHNICAL MEMORANDUM X-53133**

September 16, 1964

**SA-6 FLIGHT TEST DATA REPORT**

By

H. J. Weichel

George C. Marshall Space Flight Center  
Huntsville, Alabama

**ABSTRACT**

This report is a presentation of certain flight mechanical data obtained from the SA-6 flight test. Digitized data are presented in graphical form. Also included are schematic drawings showing the instrument location on the vehicle.

The intention of this report is to present the digitized data in an easy-to-read form for use by design and technical personnel. This report is to supplement the Saturn SA-6 Flight Evaluation Report and many other reports published by the various laboratories.

**TECHNICAL MEMORANDUM X-53134**

September 21, 1964

**PROBABILITY OF S-IVB/IU LUNAR IMPACT DUE  
TO GUIDANCE ERRORS AT TRANSLUNAR INJECTION**

By

Roy C. Lester

George C. Marshall Space Flight Center  
Huntsville, Alabama

**ABSTRACT (U)**

Using a Monte Carlo random sampling technique for the guidance errors at translunar injection, a probability distribution of radii at lunar arrival is generated. From this distribution the probability of lunar impact is determined.

**TECHNICAL MEMORANDUM X-53139**



September 23, 1964

A REFERENCE ATMOSPHERE FOR PATRICK AFB,  
FLORIDA, ANNUAL (1963 REVISION)

A REFERENCE ATMOSPHERE FOR CAPE KENNEDY,  
FLORIDA, DEFINED TO 90-Km ALTITUDE  
EXTENDED TO 700-Km ALTITUDE

By

O. E. Smith and Don K. Weidner\*

George C. Marshall Space Flight Center  
Huntsville, Alabama

ABSTRACT

The reference atmosphere established by this study is based on the most current annual statistical parameters of pressure-height, temperature, and relative humidity for the constant pressure levels from 0 to 28-km altitude and on a defined temperature versus altitude relationship from 28 to 90-km altitude. It is also extended to 700-km altitude by the technique given in the U.S. Standard Atmosphere, 1962 with latitude adjustments so that it is directly applicable to Cape Kennedy. This technique was defined by simplification of the expression for geopotential height. Computed values of pressure, kinetic temperature, virtual temperature, molecular temperature, density, coefficient of viscosity, kinematic viscosity, speed of sound, molecular weight, pressure ratio, density ratio, viscosity ratio, and pressure difference are tabulated from 0 to 700-km altitude.

TECHNICAL MEMORANDUM X-53142

September 30, 1964

SPACE ENVIRONMENT CRITERIA GUIDELINES FOR  
USE IN SPACE VEHICLE DEVELOPMENT

By

Robert E. Smith

George C. Marshall Space Flight Center  
Huntsville, Alabama

---

\* Senior Mathematician, Brown Engineering Company, Inc., Huntsville, Ala.

ABSTRACT

This document provides guidelines on interplanetary space, terrestrial space, near-Venus space, near-Mars space, lunar atmosphere and surface, Venus atmosphere and surface, and Mars atmosphere and surface environmental data applicable for Marshall Space Flight Center space vehicle development programs and studies related to future NASA programs.

This report established design guideline values for the following environment parameters: (1) meteoroids, (2) secondary ejecta, (3) radiation, (4) gas properties, (5) magnetic fields, (6) solar radio noise, (7) winds, (8) wind shear, (9) clouds, (10) ionosphere, (11) albedo, (12) planetary surface conditions, (13) planetary satellites, (14) composition of the planetary atmospheres, (15) temperature, and (16) astrodynamic constants. Additional information may be located in the references cited.

Extensive use was made of the data prepared by the Planetary Atmosphere Section, ASTD, Space Environment, Manned Spacecraft Center, Houston, Texas to insure compatibility of both development and study effort between Marshall Space Flight Center and the Manned Spacecraft Center, especially in those areas where there are insufficient data to make definite conclusions.

TECHNICAL MEMORANDUM X-53147

October 5, 1964

AN ULTRA-LOW FREQUENCY ELECTROMAGNETIC  
WAVE FORCE MECHANISM FOR THE IONOSPHERE

By

J. M. Boyer\* and W. T. Roberts

George C. Marshall Space Flight Center  
Huntsville, Alabama

ABSTRACT

Present theoretical explanations of the ionospheric behavior encounter certain difficulties in accounting for observed geographic, diurnal, and seasonal anom-

---

\* Principal Investigator, Northrop Space Laboratories, under NASA contract NAS-11138.

alies. Section II discusses, in particular, the two nocturnal maximum electron density concentrations which occur approximately 12 degrees above and below the geomagnetic equator, their seasonal variation and the sudden height increases, which occur in the F2 layer soon after twilight. In Section III a theoretical force mechanism for ionospheric matter, originated by J. M. Boyer, is briefly described. Such a model uses a mechanical potential geometry derived from electromagnetic standing waves generated by Mie scattering of ultra-low frequency energy from the sun incident on the earth. The importance of the  $1/\omega^2$  dependence of the time average Lorentz force on charged matter within such a standing wave gradient is emphasized, weighing first order effects toward the first few dipole multipole resonances of the earth in the region 7.0 to 70.0 cps. Some computer results for plane wave scattering from the earth in the above spectral region are displayed to show that the result is the erection of a complex wave geometry of three-dimensional potential wells for charged matter. Anomalies in the standing electromagnetic wave field are found to correspond well with observed ionosphere anomalies in the F2 region, when translation between the wave coordinate frame and the geographic frame is made.

#### TECHNICAL MEMORANDUM X-53148

October 5, 1964

#### A FORTRAN PROGRAM TO CALCULATE AN ENGINEERING ESTIMATE OF THE THERMAL RADIATION TO THE BASE OF A MULTI-ENGINE SPACE VEHICLE AT HIGH ALTITUDES

By

E. R. Heatherly, M. J. Dash, G. R. Davidson, and  
C. A. Rafferty

George C. Marshall Space Flight Center  
Huntsville, Alabama

#### ABSTRACT

A method of estimating the radiant heat flux in a base of arbitrary shape from intersection regions caused by the interaction of hydrogen-oxygen engine exhaust jets is presented. An approximate method of generating the intersection region shape and temperature-pressure profiles is discussed. A computer program incorporating both of the above is described and instructions are given for its loading and use. The accuracy of this program is expected to yield within

an order of magnitude of true value of thermal radiation.

#### TECHNICAL MEMORANDUM X-53150

October 16, 1964

#### PROGRESS REPORT NO. 6 on Studies in the Fields of SPACE FLIGHT AND GUIDANCE THEORY

Sponsored by

Aero-Astroynamics Laboratory of Marshall Space  
Flight Center  
Huntsville, Alabama

#### ABSTRACT

This paper contains progress reports of NASA-sponsored studies in the areas of space flight and guidance theory. The studies are carried on by several universities and industrial companies. This progress report covers the period from December 18, 1963 to July 23, 1964. The technical supervisor of the contracts is W. E. Miner, Deputy Chief of the Astro-dynamics and Guidance Theory Division, Aero-Astro-dynamics Laboratory, Marshall Space Flight Center.

#### TECHNICAL MEMORANDUM X-53151

October 21, 1964

#### A COMPREHENSIVE ASTRODYNAMIC EXPOSITION AND CLASSIFICATION OF EARTH-MOON TRANSITS

By

Gary P. Herring

George C. Marshall Space Flight Center  
Huntsville, Alabama

#### ABSTRACT

The restricted three-body model is used to develop a geometrical and topological taxonomy of the field of earth-moon transits (both directions) which is based on conditions at the terminals (perigee and periselenium). It is presented in such a way as to promote mental control of the subject.

The classifying techniques are then employed in the analysis of free-return transits as well as such problems as the lighting conditions upon landing.

The report provides convenient reference material for the engineer involved in the layout of Apollo type missions.

#### TECHNICAL MEMORANDUM X-53156

November 2, 1964

#### A STUDY OF DENSITY VARIATIONS IN FREE MOLECULAR FLOW THROUGH CYLINDRICAL DUCTS DUE TO ACCOMMODATION COEFFICIENTS

By

S. J. Robertson\*

George C. Marshall Space Flight Center  
Huntsville, Alabama

#### ABSTRACT

A theoretical investigation was made of free-molecule flow through a duct of circular cross section. The molecular flux to the duct wall and exit plane was calculated along with the total flow rate through the duct. The density field was calculated at the duct exit and along the centerline for various duct wall temperatures and thermal accommodation coefficients. It was concluded that an experimental determination of the thermal accommodation coefficient can be made by measuring the effect of the duct wall temperature on the density field.

#### TECHNICAL MEMORANDUM X-53166

November 27, 1964

#### GUIDANCE APPLICATIONS OF LINEAR ANALYSIS

By

Lyle R. Dickey

---

\* Mr. Robertson is associated with the Heat Technology Laboratory, Inc., Huntsville, Alabama. This work was performed under NASA Contract NAS8-11558.

George C. Marshall Space Flight Center  
Huntsville, Alabama

#### ABSTRACT

The application of linear analysis in determining a guidance function is investigated. The differential equations of motion are linearized about a nominal calculus of variations solution. The result is an explicit expression for the cutoff radius error,  $\Delta r$ , and cutoff angle error,  $\Delta \theta$ , as a linear operation on deviations in initial conditions and several nonlinear functions of thrust angle deviations and thrust acceleration deviations along the trajectory. With this expression available, a suitable form is selected for a function to determine thrust angle,  $\chi$ . The coefficients of this function are mathematically determined from the explicit solution obtained for  $\Delta r$  and  $\Delta \theta$  under the constraint that these values be as near zero as feasible for deviations in initial conditions and thrust acceleration whose values are arbitrary within their expected range of variation.

The results of employing this function to determine  $\chi$  for a number of examples are shown. These results emphasize the advantage of mathematically imposing the mission criteria in determination of guidance coefficients as well as illustrate the value of linearization techniques in guidance analysis.

#### TECHNICAL MEMORANDUM X-53167

November 19, 1964

#### THE MARTIAN ENVIRONMENT

By

Robert B. Owen

George C. Marshall Space Flight Center  
Huntsville, Alabama

#### ABSTRACT

An intensive literature survey has been made of the present consensus on the surface and atmospheric conditions of Mars. Knowledge of the gross features of the Martian surface appears to be fairly complete, but there is sharp disagreement on the atmospheric conditions. While estimates of the surface tempera-

ture are in fairly close agreement and estimates of the surface pressure range from 10 to 150 millibars, other phenomena such as the blue haze are inexplicable. Formal design criteria for entry vehicles cannot yet be finalized because of the wide range of the environmental parameter values.

#### TECHNICAL MEMORANDUM X-53169

November 23, 1964

#### SA-7 FLIGHT TEST DATA REPORT

By

H. J. Weichel

George C. Marshall Space Flight Center  
Huntsville, Alabama

#### ABSTRACT

This report is a presentation of certain flight mechanical data obtained from the SA-7 flight test. Digitized data are presented in graphical form. Also included are schematic drawings showing the instrument location on the vehicle.

The intention of this report is to present the digitized data in an easy-to-read form for use by design and technical personnel. This report is to supplement the Saturn SA-7 Flight Evaluation Report and many other reports published by the various laboratories.

#### TECHNICAL MEMORANDUM X-53171

December 1, 1964

#### SATURN SA-7/BP-15 POSTFLIGHT TRAJECTORY

By

Gerald R. Riddle and Robert H. Benson

George C. Marshall Space Flight Center  
Huntsville, Alabama

#### ABSTRACT

This report presents the postflight trajectory for the Saturn SA-7/BP-15 test flight. Third of the Block

II series, SA-7 was the second of the Saturn class vehicles to carry an Apollo boilerplate, BP-15, payload. Trajectory dependent parameters are given in earth-fixed, space-fixed ephemeris, and geographic coordinate systems. A complete time history of the powered flight trajectory is presented at 1.0 sec intervals from S-I S-IV separation to insertion. Tables of insertion conditions and various orbital parameters are included in a discussion of the orbital portion of flight.

#### TECHNICAL MEMORANDUM X-53176

December 10, 1964

#### SA-9 PRELIMINARY PREDICTED TRAJECTORY

By

Gerald Wittenstein

George C. Marshall Space Flight Center  
Huntsville, Alabama

#### ABSTRACT

This report presents the preliminary predicted trajectory for SA-9. The SA-9 vehicle is to be flown over the Eastern Test Range with a flight azimuth of 105°. Also included are a discussion of the vehicle and mission objectives, the trajectory shaping and constraints, and a brief description of the vehicle configuration. The primary objectives are further flight testing of the vehicle system and to further man-rate the Saturn class vehicle. The primary payload, the Pegasus (Micrometeoroid) satellite, is to obtain information on micrometeoroids for near-earth orbits.

A depleted S-IV stage and payload, which includes the Pegasus satellite, are to be inserted in an elliptical, low-earth orbit, with a perigee altitude of 500 km and an apogee altitude of 750 km. The nominal lifetime for this orbit is well in excess of one year.

The information contained in this report may be considered applicable until superseded for SA-8 and SA-10 flight profiles.

#### TECHNICAL MEMORANDUM X-53185

December 22, 1964

THE GEORGE C. MARSHALL SPACE FLIGHT CENTER'S 14 x 14 INCH TRISONIC WIND TUNNEL  
TECHNICAL HANDBOOK

By

Erwin Simon

George C. Marshall Space Flight Center  
Huntsville, Alabama

ABSTRACT

This handbook is intended to be informative presentation of the George C. Marshall Space Flight Center's 14 x 14 inch trisonic tunnel capabilities to the potential user personnel. The information presented allows more thorough preliminary test planning to be carried out.

The following items are presented to illustrate the capabilities and operation of the tunnel: (1) facility description, (2) performance and operational characteristics, (3) model design, (4) instrumentation and data recording equipment, (5) data processing and presentation, (6) preliminary test information required.

TECHNICAL MEMORANDUM X-53186

December 23, 1964

RADIOSONDE AUTOMATIC DATA PROCESSING  
SYSTEM

By

Robert E. Turner and Richard A. Jendrek\*

George C. Marshall Space Flight Center  
Huntsville, Alabama

ABSTRACT

This report describes an operational Automatic Radiosonde Data Processing System developed for use with the AN/GMD-2 RawinSet. The method of reliably identifying the time-shared temperature, humidity and reference frequency information from a modified AN/AMQ-9 Radiosonde is described.

This report shows that automatic reduction of ra-

diosonde data by the described method possesses operational capabilities as demonstrated by more than 300 balloon-borne meteorological soundings from September, 1963 to November 1964.

B. PRESENTATIONS

ALLEVIATION OF AERODYNAMIC LOADS ON  
SPACE VEHICLES

By

Mario H. Rheinfurth

The effect of different control modes on the response of space vehicles due to basic wind and wind shear characteristics is analyzed. The equations for planar rigidbody motion are linearized in space-fixed and body-fixed coordinate systems and resulting differences in stability and response behavior are discussed. The analysis includes nomograms which allow the quick determination of gain settings for accelerometer-controlled vehicles if the gain values are known for angle-of-attack control and vice versa. General design criteria are presented for the prediction of trends under changes of system parameters and/or input characteristics.

Paper presented July 15-17, 1964

Aerospace Industries Association  
New York, N. Y.

A SURVEY OF FREE RETURN TRANSITS IN EARTH-MOON SPACE

By

A. J. Schwaniger

This paper presents the results of an extensive survey of free return transits which have properties that make them suitable for application to lunar exploration missions. It shows that there is a continuous region of such transits and notes that there are also other transits satisfying the definition of free return, but not in the region of transits of immediate interest for application.

The method of conducting the survey was numerical

and experimental. The mathematical model of the restricted three-body problem was employed, and the trajectory calculations were done by Cowell's method. Geometric notions and systematic management of the transit parameters are used to make the results of the survey more easily understood and remembered. For the purposes of this paper, a free return transit is defined as one which starts at a perigee of chosen radius from the earth's center, passes arbitrarily near the moon and terminates at another perigee of radius equal to the first.

Trajectories are characterized by their position and velocity components at the close approach points to both earth and moon. The transits are classified by the direction of departure from earth and the distance of close approach to the moon.

---

Presented at the XVth International Astronautical Congress in Warsaw, Poland, September 1964.

#### NONLINEAR TWO-DEGREES-OF-FREEDOM RESPONSE WITH SINUSOIDAL INPUTS

By

Robert S. Ryan

The study of forced vibrational systems is very difficult if the system is nonlinear. This becomes apparent because the principle of superposition does not hold as it does for linear systems.

In studying the behavior of linear systems, it is useful to deal with sinusoidal inputs and resulting outputs which are harmonic. By definition the complex ratio of the output to input is called a transfer function. This transfer function, since it is complex, can be written as two parts: the modulus and the argument. The first describes the so-called response curves, and the second the phase angle between the two harmonic oscillations. Because of the property of superposition inherent in linear systems, these transfer functions become the basis for a complete description of the system.

In the nonlinear system, the output of the system to sinusoidal inputs is no longer sinusoidal, but contains harmonics of both higher and lower frequencies. Neither does the superposition principle hold; therefore, a study using sinusoidal inputs does not yield the wide scope of information obtained in the linear case. There are other shortcomings in studying the system using sinusoidal inputs; nevertheless, the sinusoidal input functions provide a convenient way of studying the

nonlinear system.

This analysis proposed to solve the nonlinear forced oscillation of a vehicle using air springs for vibration isolation. Both a single and a two-degrees-of-freedom system will be studied where the force applied is considered to be sinusoidal in nature. The single-degree-of-freedom system is also solved in the free vibration state using phase plane methods.

---

Presented in partial fulfillment for M.S. at University of Alabama, Tuscaloosa, Alabama, on August 21, 1964.

#### AN ULTRA-LOW FREQUENCY ELECTROMAGNETIC WAVE FORCE MECHANISM FOR THE IONOSPHERE

By

J. M. Boyer\* and W. T. Roberts

Present theoretical explanations of the ionospheric behavior encounter certain difficulties in accounting for geographic, diurnal, and seasonal anomalies. Section II discusses, in particular, the two nocturnal maximum electron density concentrations which occur approximately 12 degrees above and below the geomagnetic equator, their seasonal variation, and the sudden height increases which occur in the F2 layer soon after twilight. In Section III a theoretical force mechanism for ionospheric matter, originated by J. M. Boyer, is briefly described. Such a model uses a mechanical potential geometry derived from electromagnetic standing waves generated by Mie scattering of ultra-low frequency energy from the sun incident on the earth. The importance of the  $1/\omega^2$  dependence of the time average Lorentz force on charged matter within such a standing wave gradient is emphasized, weighing first order effects toward the first few dipole/multipole resonances of the earth in the region 7.0 to 70.0 cps. Some computer results for plane wave scattering from the earth in the above spectral region are displayed to show that the result is the erection of a complex wave geometry of three-dimensional potential wells for charged matter. Anomalies in the standing electromagnetic wave field are found to correspond well with observed ionosphere anomalies in the F2 region, when translation between the wave coordinate frame and the geographic frame is made.

---

Presented at the Ultra Low Frequency Symposium in Boulder, Colorado, August 1, 1964.

---

\* Principal Investigator, Northrop Space Laboratories, under NASA contract NAS-11138.

## MEASUREMENT OF GAS TEMPERATURE AND THE RADIATION COMPENSATING THERMOCOUPLE

By

Glenn E. Daniels

The theory and errors of gas temperature and measurements are discussed. To achieve a high degree of accuracy in gas temperature measurement, a method is described whereby several thermocouples may be wired together to make the Radiation Compensating Thermocouple. This thermocouple is designed such that the errors of measurement from the radiation environment will cancel out. Results of test, equations, and information are presented to aid in fabrication of the Radiation Compensating Thermocouple.

Presented at the National Conference on Micro-meteorology Sponsored by the American Meteorological Society, Salt Lake City, Utah, October 13-16, 1964.

## REVIEW OF RANGER 7 PHOTOGRAPHS

By

Otha H. Vaughan, Jr.

A review of the Ranger photographic mission is presented. Topics discussed are earth-based (Mt. Wilson photographs) resolution photographs versus Ranger 7 photographs. Photographs show the areas of impact prior to the Ranger landing so that one might compare the difference in details which were obtained by the Ranger 7. Postulated lunar surface models (three different types of lunar terrain - volcanic terrain, meteoroid bombarded terrain, and comparison of both volcanic terrain and meteoroid bombarded terrain) are shown and are to be discussed.

Although the Ranger mission was a success as a photographic mission, it still leaves many questions to be answered as to the origin of the moon, as well as the lunar bearing strength, which can be critical for design of landing vehicles or roving vehicles.

Presented to the Rocket City Astronomical Society, November 1964.

## THE ALLEVIATION OF AERODYNAMIC LOADS ON RIGID SPACE VEHICLES

By

Mario H. Rheinfurth

### ABSTRACT

A necessary condition for the successful flight of a space vehicle through atmospheric disturbances is to maintain stability at all flight times. It is, however, equally important to keep the responses within the design limits of control deflections and structural loads of the vehicle. The following study demonstrates how the control systems engineer can assist in this task by a judicious choice of the control system parameters. To this effect several typical control modes (drift-minimum, velocity feedback control, etc.) are analyzed for some basic wind profiles. The extent to which a reduction of aerodynamic loads and control excursions can be expected is discussed for various wind, wind shear, and gust conditions. By restricting the analysis to planar and linearized motion of the vehicle, it is possible to derive a set of preliminary design rules, which allow one to predict the relative merits of the discussed control principles when system parameters and/or wind structure are changed. In addition, the study provides nomograms for the quick determination of gain settings for accelerometer-controlled vehicles if the gain values are given for angle-of-attack control and vice versa.

Presented at AIA Dynamics and Aero-elasticity Research Panel Meeting, July 15-17, 1964, New York, N. Y.

## VARIABLE POROSITY WALLS FOR TRANSONIC WIND TUNNELS

By

A. Richard Felix

### ABSTRACT

Recently variable porosity walls were installed in the transonic test section of the 14 x 14 Inch Transonic Tunnel at Marshall Space Flight Center. Evaluation tests indicated that use of these walls greatly

improves the ability of this facility to produce reasonably accurate model pressure distribution data throughout the critical and difficult Mach range from 1.0 to 1.25. The evaluation was accomplished by comparing pressure distributions for a 20° cone-cylinder model with interference free data for the

same model. The range of porosities utilized is between 0.5% and 5.4% with the holes being 60° slanted.

---

Presented at the Supersonic Tunnel Associations' Meeting in Brussels, Belgium, September 1964.